Surfaces & Interfaces in Thin-Film & Conventional Li-ion Batteries

Jokin Rikarte Ormazabal

Supervisor: Miguel Ángel Muñoz Márquez

Universidad del País Vasco
Euskal Herriko Unibertsitatea

2019

Txerrikito originalari.

Laburpena

XXI. mendeko erronka nagusietako bat etengabe gorantz doan energia kontsumoarena izango da. Horri era sustengarri batean aurre egiteko energia berriztagarrietan oinarritutako eredu bat garatu beharko da. Energia berriztagarriek, zoritxarrez, ez dute energia era jarraian sortzen eta, normalean, eskaerak eta produkzioak ez dute bat egiten denboran. Hori dela eta, sorburu berriztagarrietan oinarritutako energia eredu baterako trantsizioa egiteko energia biltegirazeko sistemak garatzea beharrezko baldintza da. Hainbat modu dauden arren, bateriak dira energia pilatzeko sistema ohikoenak aplikazio gehienetan, teknologia eraginkorrena baita. Sareko energia pilatzeko ez ezik, bateriak dira nagusi ere auto elektrikoetan, gailu elektroniko eramangarrietan eta beste hainbat eta hainbat aplikazio ezberdinetan. Hortaz, gaur egungo gizartean bateriek garrantzi handia dute, eta teknologia hori garatu eta hobetzea ezinbestekoa da.

Gaur egun, bateria mota ezberdinen artean Litio-ioi bateriena (LIB) da nagusi beste teknologiekin konparatuz gero, hark eskaintzen duen energia dentsitate altuago eta eraginkortasun hobean oinarrituta. Bateria bat zelda elektrokimiko ezberdinez osaturiko sistema bat da, non elektrizitatea energia kimiko gisa pilatzen den behar den heinean hornitzeko. Zelda bat, era berean, hainbat elementuz dago osatuta: bi elektrodo (anodo eta katodoa), elektrolitoa eta korronte kolektoreak. Elektrolitoa bi elektrodoen artean kokatzen da, eta korronte kolektoreak, berriz, elektrodo bakoitzaren atzealdean. Hortaz, LIB zelda batean hainbat elementu ezberdinen arteko muga edo gainazal dago. Azken hamarkadetan ikerkuntza materialen hobekuntzan eta material berrien garapenean oinarritu da, baterien energia dentsitatea hobetzeko. Hala ere, hobekuntza horiek ez dira erabilgarriak zelda barneko prozesu elektrokimikoa elementu ezberdinen arteko gainazaletan mugatua bada. Beraz, aipatutako elementu ezberdinen arteko mugetan gertatzen diren prozesuak ikertzea behar-beharrezkoa da LIB baterien garapenerako, eta, horretarako, elektrodoen gainazalak ikertzea ezinbestekoa da.

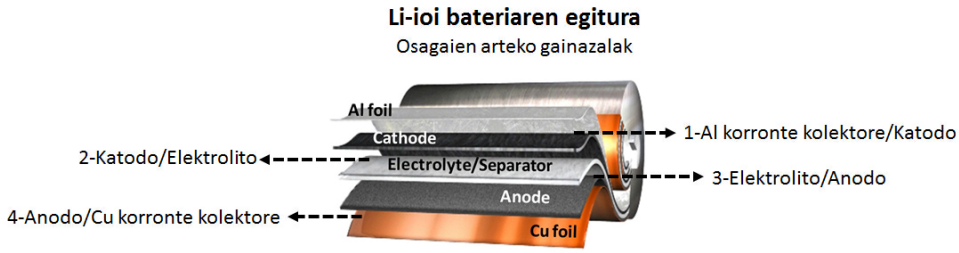

Figure 1: LIB baterietako osagai eta gainazalen deskribapena.

Testuinguru honetan, aurrean daukagun doktoretza tesi honetan aurkezten den lana LIB teknologiaren garapenerako garrantzitsuak izango diren hainbat materialen ikerketan oinarritu da, aipatutako bateria barneko gainazalen analisian eta haien hobekuntzan zentraturik. Emaitzen lehen kapituluan $Li_4Ti_5O_{12}$ (LTO) materiala izan da aztergai. Izan ere, LTO materialean oinarritutako elektrodoak euren hainbat propitetate onuragarriengatik ikertuak izan dira azken urteotan, haien artean elektrodo-elektrolito arteko mugaren egonkortasunagatik. Hori dela eta, lan honetan, kargatze-deskargatze zikloek LTO elektrodoen gainazalean duten eragina ikertu da, gainazal horien eboluzioa aztertuz. Helburu horrekin, literaturan deskribatutako prozesu berezi bat jarraituz prestatutako LTO kapa finen sintesi eta karakterizazioa deskribatzen da kapitulu honetan. Erresoluzio handiko X-izpien difrakzio eta mikroskopia elektroniko teknika aurreratuak erabiliz, ziklatzean LTO gainazalean konposatu kristalino berririk sortzen ez dela konfirmatu da. Zehazki, $\alpha - Li_2TiO_3$ konposatuaren presentzia sintesian sortzen dela frogatu da, eta ez ziklo elektrokimikoetan zehar, uste zen bezala. Halaber, konposatu honen presentzia gainazaleko lehen 15 nm inguruan mugatuta dagoela ikusi da. Horretaz gain, LTO gainazalean kargatze-deskargatze prozesuak eragindako tentsioaren areagotze bat neurtu da, gainazalaren uzkurdurarekin erlazionatuta egon daitekeena.

LTO elektrodoen ikerketarekin jarraituz, Magnetron Sputtering teknikaren bitartez elektrodoen gainazalean depositatutako geruza finen era- gina aztertu da lan honetan. Geruza finekin babestutako elektrodoen erantzun elektrokimikoa babestu gabeko elektrodo soilekin konparatu da, geruza fin horiek eduki ditzaketen onurak aztertzeko. Hasiera batean, geruza fin babesgarrien eragina elektrodo konbentzionaletan aztertu da. Babestutako elektrodo eta elektrodo soilen arteko gainazaleko konposizio kimikoa espezifikoki gainazalak aztertzeko erabiltzen diren tekniken bitartez analizatu dira, bai ziklatu aurretik baita ziklatu ostean ere. Izatez, bai karbonozko bai aluminio oxi-

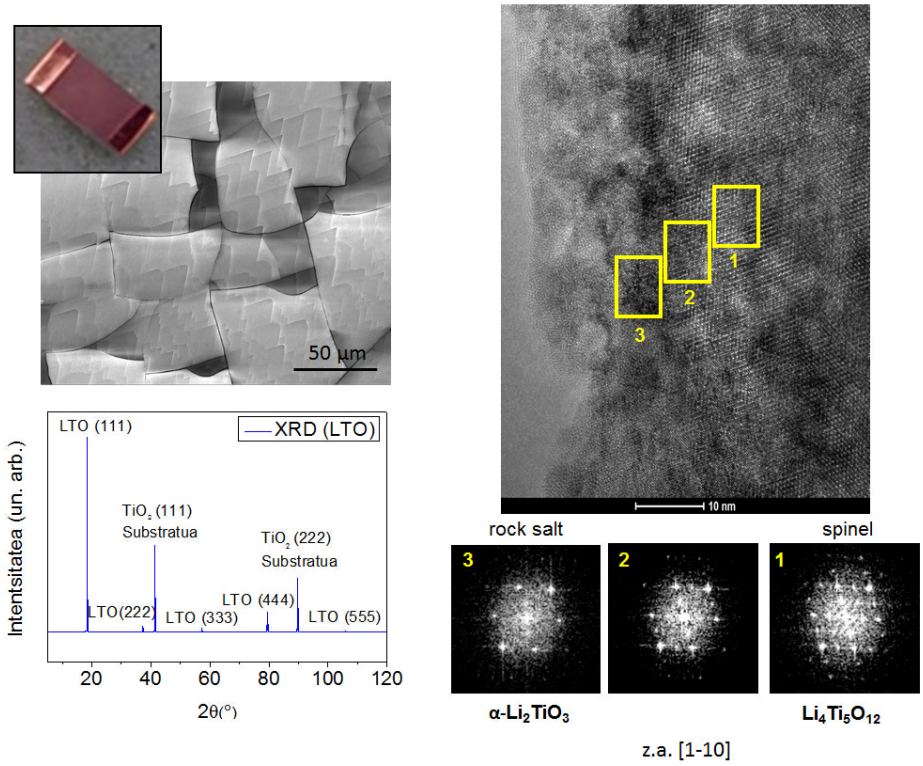

Figure 2: 3. kapituluko emaitzen laburpena: LTO elektrodoaren gainazalaren analisia.

dozko geruza finek LTO elektrodo konbentzionalen erantzun elektrokimikoa hobetzen dutela frogatu da, efektua nabariago izanik Al_2O_3 geruzen kasuan. Hobekuntza are agerikoagoa da korronte intentsitate altuagoak erabiltzen direnean, %30 hobekuntza lortzen delarik probatutako korronte intentsitate altuenaren kasuan. Elektrodo konbentzionaletan ez ezik, kapa fineko LTO elektrodoetan ere aztertu da Al_2O_3 geruza babesgarrien efektua. Izan ere, kapa fineko elektrodoak plataforma ideala dira gainazaletan gertatzen diren efektuak aztertzeko, eta, beraz, Al_2O_3 geruza babesgarriaren funtzioa ulertzeko kasu zehatz honetan. Al_2O_3 geruza finez babestutako LTO elektrodo konbentzionalak eta kapa fineko elektrodoak konparatzerako orduan, ordea, erantzun elektrokimiko ezberdina ikusi dira. Kapa fineko LTO elektrodoek ez dute erakutsi elektrodo konbentzionaletan frogatutako hobekuntza nabaria. Egindako karakterizazio lan sakonaren emaitzek iradokitzen dute ezberdintasun hori bi elektrodo moten arteko diferentzia geometrikoen ondorioa dela.

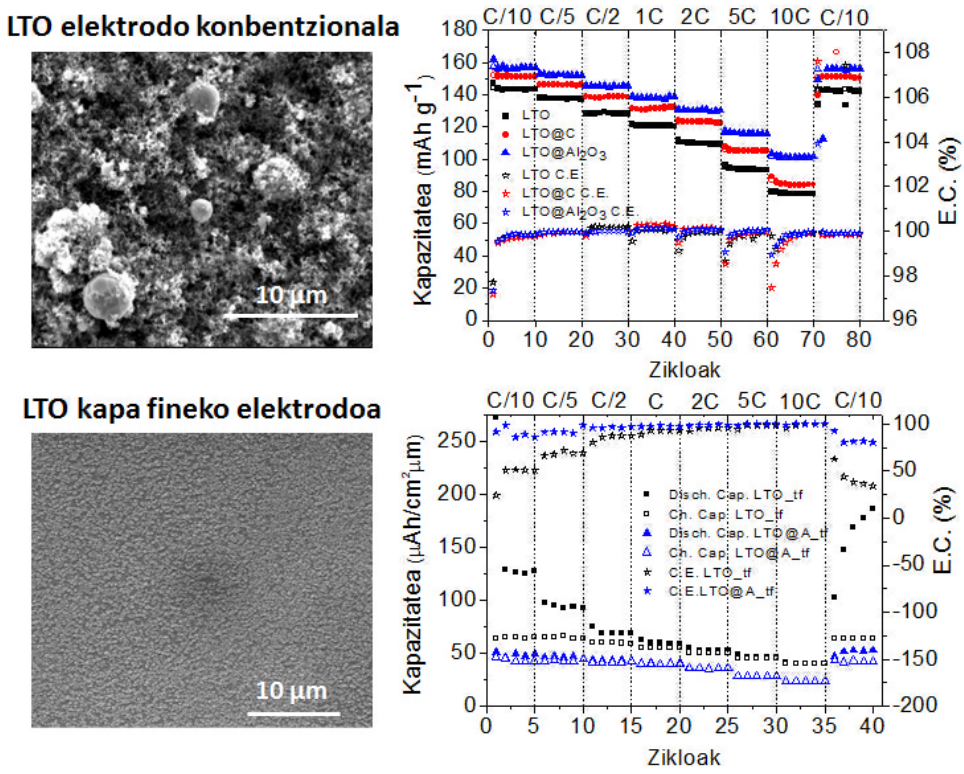

Figure 3: 4. kapituluko emaitzen laburpena: geruza babesgarrien eragina LTO elektrodoetan.

Kapa fineko elektrodoen ildotik jarraituz, lan honetako azken kapitulu esperimentalean $LiNi_{0.5}Mn_{1.5}O_4$ (LNMO) materialaz osatutako kapa finak aztertzen dira, katodo bezala erabiltzeko. Izan ere, gainazala aztertzeko plataforma ideala izateaz gain kapa fineko elektrodoak baterietako elementu gisa ere erabiltzen dira, kapa fin ezberdinez osatutako mikrobaterietan, alegia. Guztiz solidoak diren (hau da, osagai likidorik gabeko) mikrobateria hauek hainbat abantaila dituzte bateria konbentzionalekin alderatuta: energia espezifiko eta energia dentsitate altuagoa, tenperatura tarte zabalagoan erabiltzeko aukera, bizitza luzeagoa eta segurtasun handiagoa, besteak beste. Guzti horretan oinarrituz, europar mailako lankidetza proiektu baten testuinguruan, kapa fineko LNMO elektrodoak ikertu dira produkzio prozesuko hainbat parametrok LNMO kapa finen ezaugarrietan duten eragina ezagutzeko. Karakterizazio tresna mota ezberdinen konbinazioan oinarrituz, elektrodo

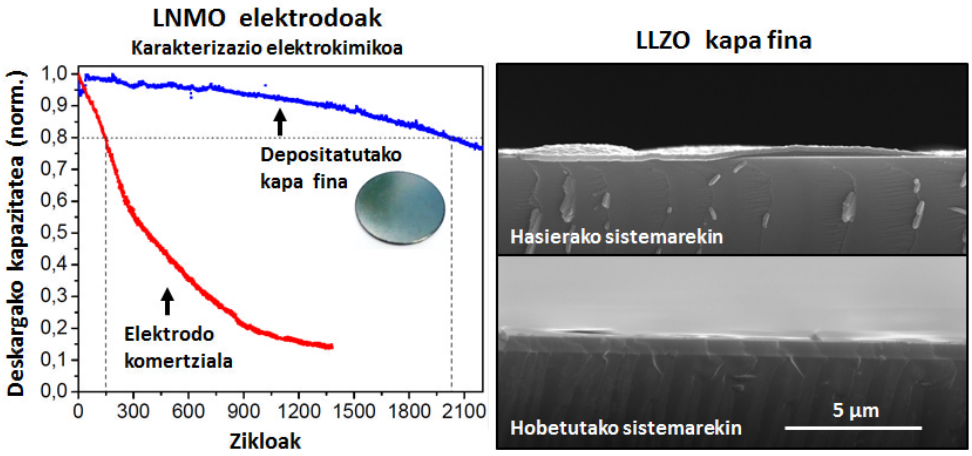

Figure 4: 5. kapituluko emaitzen laburpena: LNMO eta LLZO kapa finak.

hauen estruktura kristalografikoa, konposizio kimikoa, gainazaleko morfologia eta propietate elektrokimikoak aztertu dira, besteak beste. Karakterizazio analisi zabal horren bitartez deposizio osteko prozesu termiko baten beharra konfirmatu da, LNMO materialaren fase eta estruktura egokia lortzeko. Are gehiago, atmosfera ezberdinetan garatutako prozesu termikoen ondorioz, pausu hau airean (atmosfera berezirik aplikatu gabe) egin behar dela ikusi da; atmosfera inertea erabiliz gero (argon gasa) ez baita produktu egokia lortzen. Berotze prozesuaren tenperaturari dagokionez, tenperatura egokiena 600°C dela frogatu da, bai konposizio kimiko eta baita estruktura kristalografikoari dagokionez ere. Optimizatutako elektrodoen erantzun elektrokimikoari dagokionez, berriz, kapa finaren lodieraren eragina argi ikusi da, kapa finenetan kapazitate hobea lortzen delarik korronte intentsitate altuak aplikatzean, batik bat. Proiektu honetan garatutako kapa fineko elektrodoak LNMO elektrodo komertzialekin konparatzerako orduan, lan honetan garatutako elektrodoen propietate hobeak frogatu dira. Baldintza berdinetan ziklatzean, elektrodo komertzialek 150 ziklora iritsi ez diren bitartean, kapa fineko LNMO elektrodoek 2000 ziklotik gora egin dituzte.

Horrez gain, gainazaletan arreta berezia jarri da kapa finen bi mugak aztertu direlarik: LNMO elektrodo eta substratuaren artekoa batetik eta LNMO elektrodo eta elektrolitoaren artekoa bestetik. Lehenengo kasuan, metalezko substratuak erabili dira substratu izateaz gain ziklatzerako orduan korronte kolektore funtzioa izan zezaten. LNMO elektrodoak sortzeko prozesuan substratu-LNMO arteko gainazalean korrosio prozesu bat gertatzen

dela frogatu da, prozesuan beharrezko den tratamendu termikoan, alegia. Gainera, karakterizazio teknika ezberdinak erabiliz, metalezko substratutik LNMO elektrodora eta elektrodoan zeharreko difusio prozesu bat ikusi da, elektrodoen erantzun elektrokimikoan eragina izan dezakeena. LNMO kapa finen beste gainazalari dagokionez, $Li_7Zr_2La_3O_{12}$ (LLZO) materialez osatutako kapa finen deposizioa aztertu da. LLZO materiala magnetron sputtering teknikaren bitartez depositatzeko aukera ikertu da elektrolito solidoaren funtzioa betetzeko helburuarekin. Hortaz, LLZO kapa finaren deposizioa baldintza ezberdinetan egin da. Depositatutako LLZO kapa finak karakterizatu egin dira eta baldintzon eragina aztertu da deposiziorako balio optimoak definitu direlarik. Horretaz gain, deposizio sistema bera garatu egin da, prozesuaren kontrol hobea edukitzeko eta kalitate hobeko kapak sortzeko. Garapen horren eraginez, LNMO eta LLZO kapa finen arteko adhesioan hobekuntza nabaria lortu da.

Orohar, lan honetan aurkeztutako tesi proiektuan litio-ioi baterien garapenerako garrantzitsuak izango diren hainbat elektrodo material aztertu dira, gainazalen analisian bereziki zentratuz. Elektrodoen gainazalek ziklatzean jasaten duten eboluzioa ikusi da, eta gainazal horiek manipulatu edota babesteak baterien portaera elektrokimikoan dituen onurak frogatu dira.

Contents

List of Figures

Chapter 1

Introduction

Dealing with the constantly increasing energy demand will be one of the most important challenges in the XXI century, and, hence, accomplishing an environmentally sustainable energy supply will be of paramount importance. In fact, global energy consumption increased 1% in 2016 [1] and it is expected to rise 28% by 2040, mainly driven by the energy demand increase in Asia [2]. Renewable sources, despite being a constantly increasing source of energy during the last years [2,3], are still far from the dominating position that the non-renewable energy sources have currently (figure 1.1). Therefore, their use should be further boosted if a sustainable electric grid is to be developed in the future. One of the main limitations of renewable energy sources is their non constant and controllable production rate which leads to a significant mismatch between production and demand while destabilizing the grid. Hence, integration of energy storage technologies is critical for the transition to renewable energy sources as main suppliers to the grid.

Despite the existence of many different energy storage technologies, batteries are one of the most common ones in a wide range of applications, since they are the most efficient. Among different energy storage technologies, rechargeable batteries are the ones that have most attracted commercial interest for grid storage [3]. Besides, batteries are also the main option when portable energy storage is needed. With electric passenger vehicles accounting for 1% of global passenger car sales in 2016 [3], the already on-going electrification of the road transport sector is also based on rechargeable batteries as energy storage system. Portable electronics, which have become necessary tools in our daily life, need batteries for powering them as well [4]. Therefore, modern society relies on the performance of batteries, and the improvement of current technology is urgently needed.

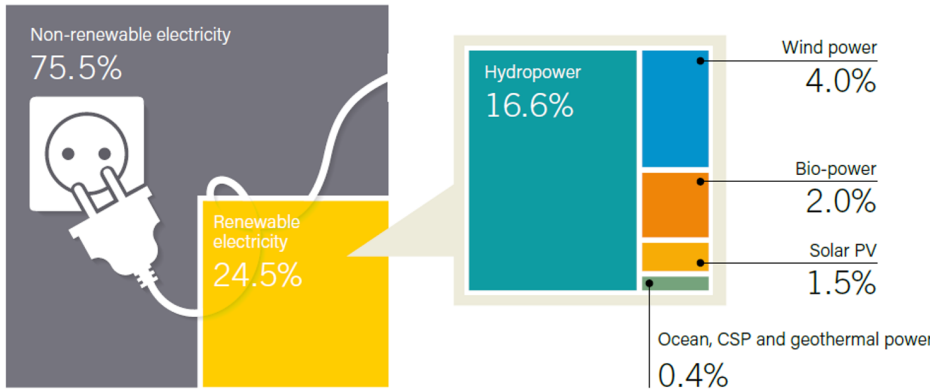

Figure 1.1: Renewable energy share of global electricity production (2016) [5].

There are many different types of batteries that have been developed upon the time, based on different chemistry. In general, batteries can be classified in primaries or secondaries, depending on if they are non-rechargeable or rechargeable, respectively. Carbon-zinc, manganese alkaline, different kind of zinc anode and lithium anode cells are the most common examples of primary batteries. Among the different secondary battery technologies the most relevant ones are described in table 1.1, where their general properties are indicated. Lithium-ion batteries, which are described in next section, stand out between the different type of technologies available up to date. Within this technology, thin-film Li-ion microbatteries are a subfamily that is of particular interest due to its properties, which are describe later in this chapter. Beyond Li-ion, there are also other new battery technologies that are being developed, such as, Li-O_2, Li-S and Na-S, which are also mentioned along this introductory chapter.

1.1 Li-ion batteries

A battery is a system composed of several electrochemical cells, that is able to store electricity as chemical energy and deliver it when needed [9]. It is formed by different elements, namely electrodes, electrolyte and current collectors. In conventional Li-ion batteries electrodes are composed by the active material (which makes possible the storage mechanism), binder (for good mechanical cohesion of the electrode), and a conductive additive (usually carbon) when needed. The electrolyte is situated in between the electrodes, and must be good Li-ion conductor and electronic insulator. Commonly it is

Table 1.1: Properties of the most important rechargeable battery technologies [6–8].

Type	E density(Wh/kg)	Efficiency (%)	Life (cycles)
Pb-Acid	2440	50-75	1000
Ni-Cd	30-45	55-70	2000
Ni-MH	60-75	75-80	2000
Redox flow	10-20	75-80	3000
Li-ion	125-250	94-99	4000
Thin-film Li-ion	250-400	99	45000

based on lithium salt and organic electrolytes. To physically separate both electrodes, a porous separator is also included between them in most of the cases. Electrodes are cast on current collectors which will be the external part in each side of the cell; the current collector role is to work as electrical contact between the electrode and the external circuit. Thus, different interfaces are present in Li-ion batteries (electrode-electrolyte and electrode-current collector), which importance is detailed later on the text.

Electric energy is transformed into chemical energy via oxidation and reduction (redox) reactions of the active material within the electrodes . The one with the lower redox potential is known as the negative electrode, while the one with the higher potential is the positive electrode, although, usually, they are referred as anode and cathode, respectively. During discharge, the active material on the positive electrode is reduced, at the same time that negative electrode is oxidized. On charge, just the opposite process occurs. However, this redox reactions can not always take place in both directions, and batteries are classified in primary and secondary depending on the reversibility of the process, as described before. Primary batteries are those in which the reaction is not reversible, whereas, secondary batteries are rechargeable, in such a way that can be continuously charged and discharged reversing the redox reactions within the cells.

Lithium-ion batteries [10] correspond to the secondary batteries family. In this system, Li-ions reversibly travel from one electrode to the other through the electrolyte, which separates both electrodes. The electrolyte must be good ionic conductor to facilitate Li-ion transport between electrodes, but, good electronic insulator to force the electrons go to the external circuit, and, thus, generate electric current. Lithium is the most favorable mobile ion species for batteries, since it is the lightest metal and has the highest electrochemi-

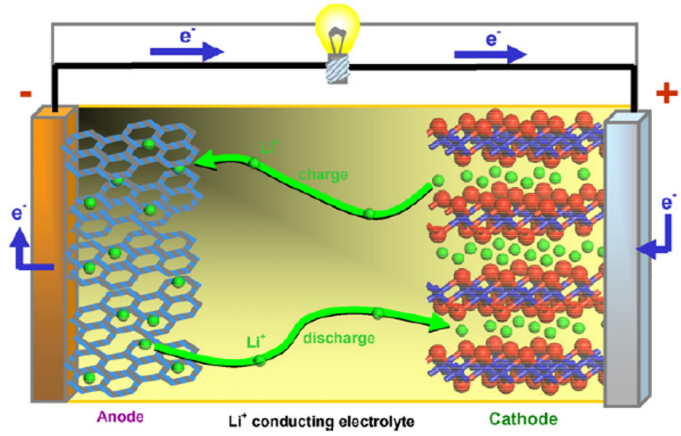

Figure 1.2: Schematic representation of Li-ion cell [6].

cal potential, providing the largest gravimetric energy density. A schematic representation of Li-ion cell is shown in figure 1.2.

Since their commercialization in the 1990s by SONY company [11], the most popular Li-ion batteries were composed by graphite as anode and $LiCoO_2$ (LCO) as cathode materials [10]. However, during the last two decades, many other electrode materials have been studied, developed and sometimes commercialized [12, 13]. The most relevant ones, included in figure 1.3, are classified by their discharge potential and specific capacity.

The success of Li-ion batteries relies on their high energy and power density (figure 1.4), high efficiency, high voltage and good cycle life [14], as well as the negligible self-discharge and absence of memory effect [15], in contrast with other battery technologies. Based on these advantageous properties, Li-ion batteries have become the power source of choice for portable electronics and power tools, with a production in the order of millions of units per year [4, 14]. Moreover, Li-ion technology has also become the preferred one for powering electric vehicles (EV) [16, 17]. In grid storage, they have the potential to become the main energy storage system, due to the longer cycle life, high energy and power density with respect to other battery technologies [18, 19]. Indeed, batteries for grid storage applications have already been launched [20].

Nevertheless, Li-ion technology is not free from limitations. Main draw-

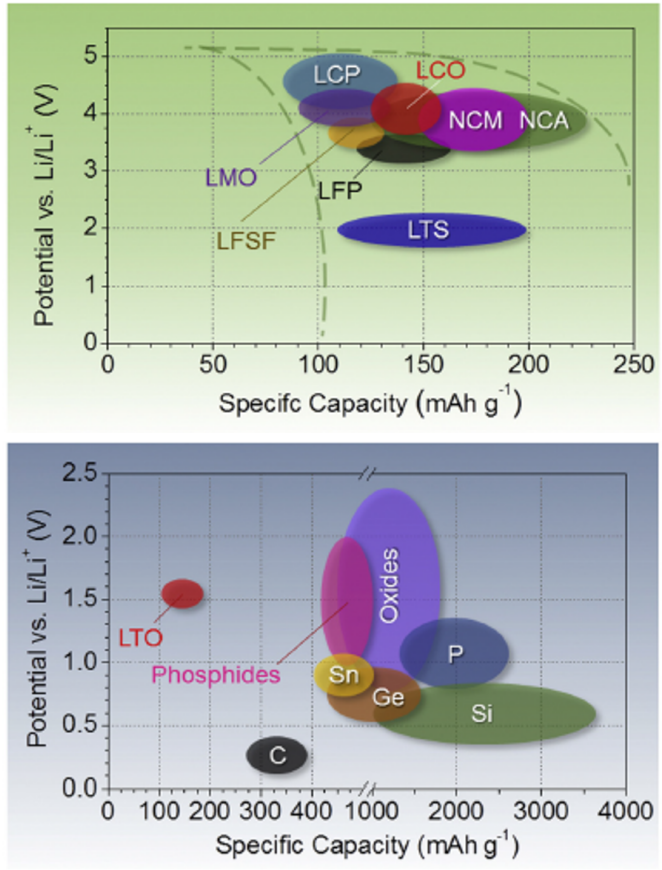

Figure 1.3: Approximate range of average discharge potentials and specific capacity of some of the most common negative (bottom) and positive (top) electrodes for Li-ion batteries [13].

backs are safety issues related to the presence of flammable organic liquid electrolytes, cost and uneven distribution of Li resources that are concentrated in a few countries. In order to make Li-ion batteries safer and avoid any risk of thermal runaway producing fire or explosions, big effort is being devoted to the development of solid electrolytes, based on both polymeric and ceramic materials (or even composites) among others [21–24]. Issues related to the cost, which some years ago seemed to be unaffordable, look today not to be such a big issue, since the costs rapidly declined during the last years principally pushed by the rapidly falling costs of battery packs for electric vehicles [16, 25]. However, the uneven distribution of lithium, with all the supply controlled by only four companies in the world, makes any forecast

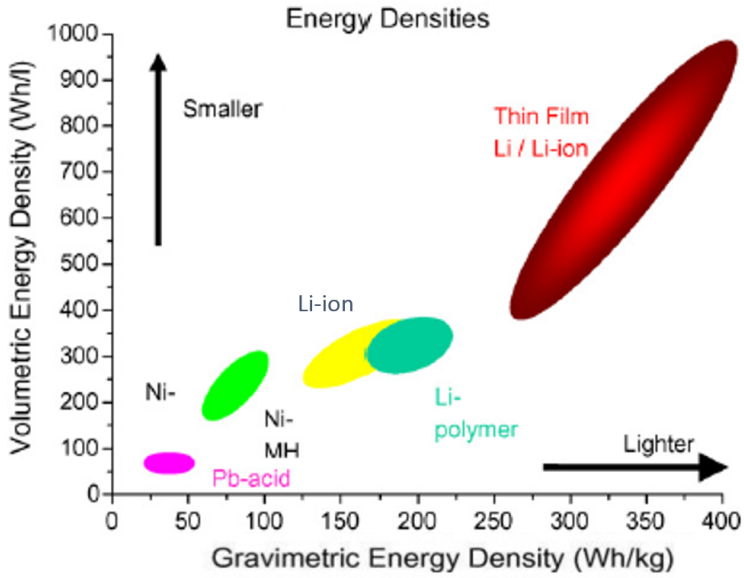

Figure 1.4: Energy density of Li-ion and thin film Li-ion batteries compared to previous technologies [6].

about the Li price evolution is uncertain [26]. Finally, based on last reports scarcity of lithium should not be a problem [26,27]. Moreover, recycling of Li-ion batteries could play an important role in the future, whilst the possibility of automotive Li-ion batteries towards second life in stationary applications would be really interesting from the point of view of sustainability and optimal use of resources [28]. Besides, the possibility of recovering the lithium from seawater [29], would increase the amount of available resources considerably.

Beyond Li-ion, batteries based in other chemistries are also being investigated. Among the most relevant, Li-O_2 (also known as Li-air) and Li-S stand out due to their higher theoretical capacity, while Na-ion system is being studied as a low cost alternative to Li-ion due to the abundance of sodium. However, it is becoming increasingly evident that the short lifetime is a serious problem for these post Li-ion technologies [30]. Li-S batteries, despite the fact that have been recently commercialized [31], are limited to specific applications in which gravimetric energy density is critical and limited cyclibility is tolerable. Reversibility, charge-discharge efficiency and long term cyclability are unsolved issues in Li-O_2 batteries, and are unlikely to have commercial

success. Na-ion system, on the other hand, is usually presented as the cheaper alternative to Li-ion for grid-scale energy storage. Although energy density is not a critical parameter in stationary storage, energy-normalized cost is calculated to be lower for Li-ion compared to Na-ion [30]. Hence, in spite of being based on cheaper raw materials, Na-ion batteries must improve their energy density to compete with their Li-ion counterparts.

1.2 Role of surfaces and interfaces

As stated before, during the last decades, big efforts have been devoted to the development of novel materials and improvement of existing ones in Li-ion technology. However, the research activity has been mainly focused on increasing the capacity and energy density of batteries, and achieved advances would be useless if kinetics are limited on the interfaces. Despite having outstanding electrode and electrolyte materials independently, it would not be translated to overall cell performance unless good interfacial stability and Li-ion diffusion is ensured.

Most evident example of the importance of the interface phenomena is in conventional Li-ion batteries. Indeed, the formation of a passivation layer on the negative electrode from the partial decomposition of organic electrolytes mostly during the first electrochemical cycles is recognized [34]. This layer behaves like a solid electrolyte interphase (figure 1.5), so it is named SEI [35], and its formation, nature and behavior have determinant effect on important properties for batteries, such as cycle life, life time, power capability, and even their safety.

Formation of SEI via reductive decomposition of organic electrolyte occurs when the electrochemical potential of the negative electrode is below the Electrochemical Stability Window (ESW) of the electrolyte. If the electrochemical potential of the anode is not within ESW, it will continuously reduce the electrolyte unless this process leads, within a few cycles, to the formation of a stable passivation layer that creates a barrier between the anode and the electrolyte [36]. Most common positive electrode materials are within the ESW of conventional electrolyte, whereas negative ones are mostly out of it. Thus, electrolyte decomposition is usually more prominent in negative electrodes than in positive electrodes. However, some high voltage cathodes which have always been of interest considering the significant increase in energy density they can trigger, are out of ESW and electrolyte is oxidized in these cases. Formation of a stable SEI layer, which is sometimes

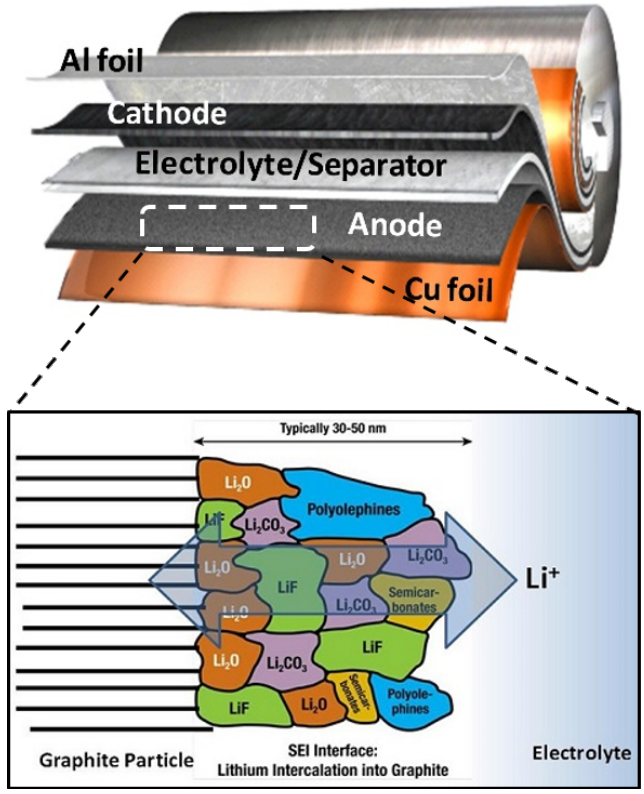

Figure 1.5: Representation of the different interfaces present in a Li-ion battery (top) and the SEI formed on conventional negative electrode (bottom). Modified from [32] and [33].

called solid permeable interphase (SPI) in the cathode's side, is also needed to avoid continuous decomposition of the electrolyte. Moreover, even the electrode materials within the ESW are not free from interfacial reactions with the electrolyte [37]. Despite the fact that the effect in the later case is much less pronounced, a good understanding of these interfacial processes would help to improve the electrochemical performance of the electrode materials.

Moreover, the implementation of certain solid electrolytes under study would be really interesting, since it would widen the electrochemical window [38], enabling the use of electrodes that are out of the ESW with current liquid electrolytes, and would also overcome safety concerns related to such liquid flammable electrolytes. Nonetheless, in the all solid state configuration, interfaces also play a critical role, as poor interfaces are very often the

responsible of hindering the performance of potential solid electrolyte alternative materials.

Finally, it is worth noting that electrode-electrolyte interfaces are not the only ones present in a cell. Electrode-current collector interfaces should also be considered, as formation of interphases could involve an increase of internal resistance that would hamper the proper operation of the battery. Therefore, understanding the processes occurring on different interfaces at cell level is essential, and build-up of appropriate interphases would help to enhance the electrochemical performance of Li-ion batteries.

To elucidate interface processes, study of surfaces in the electrodes is necessary. Although the surface study of conventional electrodes is possible and very useful, thin-film electrodes offer an ideal system to investigate interface reactions, since they are characterized by the absence of any additive and the flat surfaces they contain [39]. Besides, thin film electrodes and electrolytes can also be used to conform a microbattery, which is, in fact, a system with a great potential as it will be described in next section.

1.2.1 Thin-film Li-ion microbatteries

All solid state thin-film Li-ion battery concept (figure 1.6) was demonstrated many years ago [40, 41], and microbatteries based on that idea have been commercialized since then [42–44]. Most of them are based, as in the case of the conventional batteries, on the LCO as cathode material. The difference is on the use of metallic lithium as anode material, which use is possible due to the stability of the glassy electrolyte that is most commonly used in thin-film batteries, namely, LiPON [45].

Thin-film batteries have many advantages compared to their bulky counterparts in Li-ion batteries. Since the solid electrolytes used in thin-film batteries have a much wider electrochemical voltage window, very low voltage anodes and high voltage cathodes can be used [47]. Moreover, the use of conductive additives and binders (always present in conventional electrodes) is avoided, as well as the separator, since the electrolyte plays the role of both ionic conductor and physical barrier between the electrodes. Based on these particularities, thin-film batteries have upgraded specific energy and energy density [6] (figure 1.4). Even more, it is worth noting that the much wider temperature window of solid electrolytes (-40<T<150°C) compared to common liquid electrolytes (most fading at T>60°C), improves the response of Li-ion batteries in extreme conditions. Other beneficial properties are the

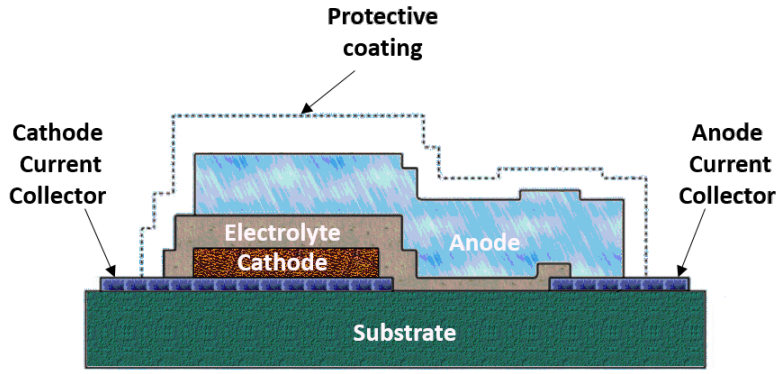

Figure 1.6: Typical scheme of a thin-film battery (modified from [46]).

longer cycle life (>45000 cycles have been demonstrated [44]), the safety (including compatibility vs metallic lithium and absence of any risk related to leakages [48]), and the possibility of integrating the battery directly with micro-electromechanical devices (MEMS) [48, 49].

Indeed, on coming Internet of Things (IoT) and new industrial (I4.0) revolutions lay on the continuous miniaturisation of autonomous (wireless) sensors and electronic devices. One of the limiting factors in this technological revolution is the need for high performance power sources at the same miniaturization scale. Here, the role of thin-film Li-ion batteries will be of paramount importance, as far as the energy density and overall performance of current microbatteries is improved to meet the requirements of this technology (such as geometry, energy density and power capability). The range of possibilities in terms of applications is incredibly wide (figure 1.7), including, portable electronics (wearable devices, smart cards, RF ID tags, wireless sensors and energy harvesting devices), health (biosensors, pacemakers, drug delivery systems and body monitoring systems), robotics, automotive, industrial and even spaceship applications [50]. In industry, for instance, machine to machine connectivity is often done using cabled devices and conventional batteries, which is sometimes inconvenient also involve a significant cost in wiring and connections. All solid state thin-film batteries could play an important role when connectivity is needed in places difficult to reach or extreme temperature conditions, among others. Besides, in the automotive industry, smart transportation is becoming a reality. Modern cars have up to 100 sensors nowadays, and that number will grow in the future based on the increased use of wireless systems and devices with added functionality [51].

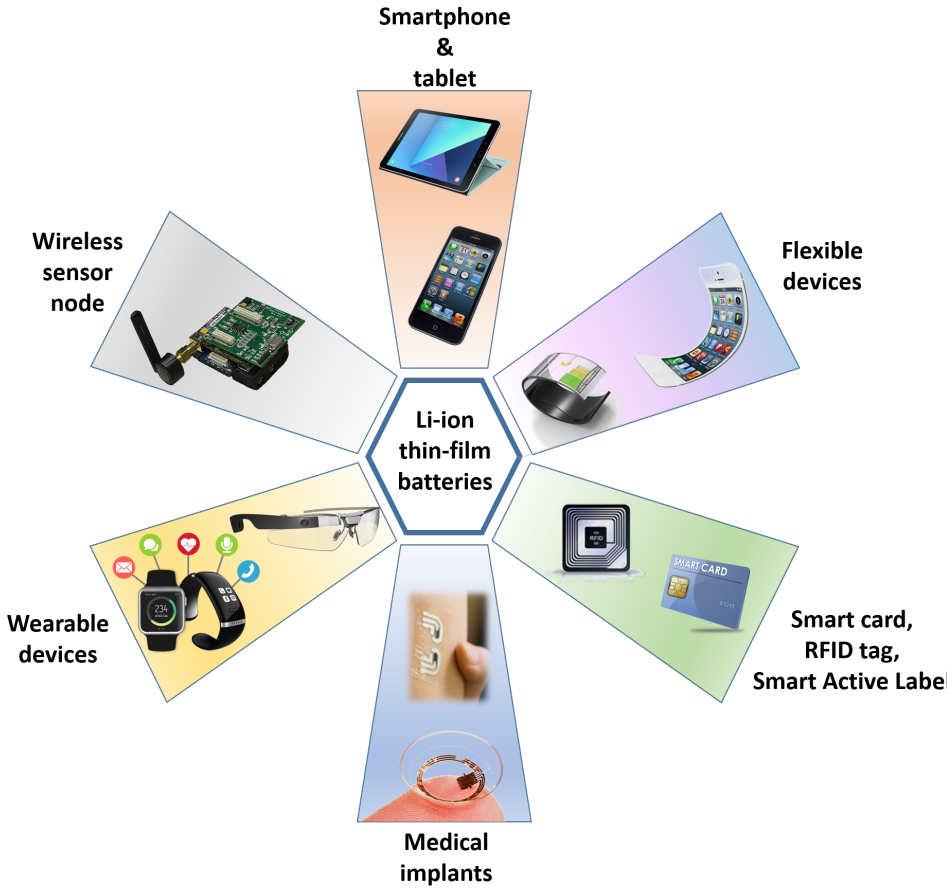

Figure 1.7: Some of the potential applications for Li-ion thin-film batteries.

Taking into account that cabling is currently the third heaviest component in a car, thin-film batteries integrated in the sensors would potentially be the enabling technology for a distributed energy storage that would reduce the cabling. Medical applications are another field in which thin-film batteries can offer unique opportunities. Implantable or ingestible smart devices powered by a thin-film battery may be used to collect patient data and support drug delivery, and this microbatteries could also be directly part of wearable devices such as smart contact lenses [52].

1.3 Scope of the thesis

Along this introductory chapter, the importance of storage technology in general, and Li-ion batteries in particular has been presented. The relevance of investigating interfacial phenomena has been highlighted, since the knowledge of the processes occurring at different cell surfaces and interfaces will most probably be one of the keys for the development of batteries with upgraded performance. Based on this assumption, the thesis work presented here has been focused on the study of surfaces, interfaces and thin-films of different materials that will play an important role within Li-ion technology in the near future.

After a brief description of the experimental techniques used to develop this work (chapter 2), surface evolution study upon electrochemical cycling of Lithium Titanate (LTO) electrode material was carried out in chapter 3. LTO is, in fact, a material that attracted great interest at research level during the last years, partially nested in its particular properties regarding the electrode-electrolyte interface. The work developed in this chapter, was performed within the framework of SIRBATT FP7 European project (Stable Interfaces for Rechargeable Batteries, No 608502), aiming to elucidate the behavior of LTO (111) surface during discharge-charge cycles. Additionally, evolution of surface strain over such surface during electrochemical cycles has been analyzed.

In chapter 4 the effect of different coatings applied by Physical Vapour Deposition (PVD) techniques was investigated. Electrochemical cycling of coated LTO electrodes was compared to non-coated ones to identify the benefits that could stem from the surface coatings, enhancing the performance of the electrodes. Differences on the chemical composition of surface species formed on the electrode-electrolyte interface for coated and non-coated electrodes was analyzed by means of surface specific techniques. In addition, due to the complex composition of conventional electrodes, thin-film LTO electrodes were studied, as a system that could give better insight of the phenomena taking place on electrode surface upon cycling. Thus, the study of the surface composition evolution was repeated on thin-film electrodes in the case of the most promising coating material.

Continuing with thin-film studies, in chapter 5 Lithium Nickel Manganese Oxide (LNMO) cathode material was investigated as alternative thin-film electrode for Li-ion microbatteries, which potential for a wide range of applications was described before. For the optimization of LNMO thin-film

production, several parameters were studied, such as annealing atmosphere and temperature, which were analyzed by means of a large set of techniques for a comprehensive characterization at different levels. Electrochemical performance of LNMO thin-films was also presented, elucidating the effect of parameters like the thickness and the temperature. Besides, interfaces were also investigated at both sides, namely electrode-current collector and electrode-electrolyte interfaces. In the former case, possible oxidation and diffusion phenomena were analyzed, while, in the later case, a sputterability study of $Li_7Zr_2La_3O_{12}$ (LLZO) ceramic material was described, as alternative thin-film solid electrolyte. The research work presented in chapter 5 was carried out within the framework of MONBASA H2020 European project (Monolithic Batteries for Spaceship Applications, No. 687561).

Finally, in chapter 6, overall conclusions drawn from the whole research work were presented. Future perspectives, with questions that remain open and research activities that can be continued, along with possible new studies that could be raised were also described in this final chapter.

Bibliography

[1] BP company. BP statistical review of world energy 2017, June 2017.

[2] U.S. Energy Information Administration. International energy outlook 2017. www.eia.gov/ieo, September 14, 2017.

[3] World Energy Council. World energy resources 2016.

[4] J.M. Tarascon and M. Armand. Issues and challenges facing rechargeable lithium batteries. *Nature*, 414(6861):359-367, 2001.

[5] REN21. Renewable Energy Policy Network for the 21st Century. Renewables 2017 global status report, 2017.

[6] A. Patil, V. Patil, D.W. Shin, J.W. Choi, D.S. Paik, and S.J. Yoon. Issue and challenges facing rechargeable thin film lithium batteries. *Materials Research Bulletin*, 43(8):1913-1942, 2008.

[7] J. Li, L. Baggetto, S. Martha, G.M. Veith, J. Nanda, C. Liang, and N.J. Dudney. An artificial Solid Electrolyte Interphase enables the use of a $LiNi_{0.5}Mn_{1.5}O_4$ 5V cathode with conventional electrolytes. *Advanced Energy Materials*, 3(10):1275-1278, 2013.

[8] M. Zarrabeitia-Ipiña. Low and high voltage stability of Na-ion battery materials: study of structural, transport and interfacial properties. Doctoral Thesis. 2016.

[9] G. Pistoia. Batteries for portable devices. Elsevier, 2005.

[10] K. Ozawa. Lithium Ion Rechargeable Batteries: Materials, Technology, and New Applications. John Wiley & Sons, 2012.

[11] K. Ozawa. Lithium-ion rechargeable batteries with $LiCoO_2$ and carbon electrodes: the $LiCoO_2$/C system. *Solid State Ionics*, 69(3-4):212-221, 1994.

[12] M.S. Whittingham. Ultimate limits to intercalation reactions for lithium batteries. *Chemical Reviews*, 114(23):11414-11443, 2014.

[13] N. Nitta, F. Wu, J.T. Lee, and G. Yushin. Li-ion battery materials: present and future. *Materials Today*, 18(5):252-264, 2015.

[14] B. Scrosati and J. Garche. Lithium batteries: Status, prospects and future. *Journal of Power Sources*, 195(9):2419-2430, 2010.

[15] Y. Nishi. Lithium-ion secondary batteries; past 10 years and the future. *Journal of Power Sources*, 100(1):101-106, 2001.

[16] B. Nykvist and M. Nilsson. Rapidly falling costs of battery packs for electric vehicles. *Nature Climate Change*, 5(4):329-332, 2015.

[17] A. Opitz, P. Badami, L. Shen, K. Vignarooban, and A.M. Kannan. Can Li-ion batteries be the panacea for automotive applications? *Renewable and Sustainable Energy Reviews*, 68:685-692, 2017.

[18] B. Dunn, H. Kamath, and J.M. Tarascon. Electrical energy storage for the grid: a battery of choices. *Science*, 334(6058):928-935, 2011.

[19] B. Diouf and R. Pode. Potential of Lithium-ion batteries in renewable energy. *Renewable Energy*, 76:375-380, 2015.

[20] Saft to deliver MW-scale Li-ion battery for the largest storage project in nordic countries. https://www.saftbatteries.com/press-releases/saft-deliver-megawatt-scale-li-ion-battery-system-fortum-largest-electricity-storage, April 26, 2016. Accessed: January 2018.

[21] V. Thangadurai, S. Narayanan, and D. Pinzaru. Garnet-type solid-state fast Li-ion conductors for Li batteries: critical review. *Chemical Society Reviews*, 43(13):4714-4727, 2014.

[22] J.G. Kim, B. Son, S. Mukherjee, N. Schuppert, A. Bates, O. Kwon, M.J. Choi, H.Y. Chung, and S. Park. A review of lithium and non-lithium based solid state batteries. *Journal of Power Sources*, 282:299-322, 2015.

[23] L. Chen, Y. Li, S.P. Li, L.Z. Fan, C.W. Nan, and J.B. Goodenough. PEO/garnet composite electrolytes for solid-state lithium batteries: from Ceramic-in-Polymer to Polymer-in-Ceramic. *Nano Energy*, 2017.

[24] A. Manthiram, X. Yu, and S. Wang. Lithium battery chemistries enabled by solid-state electrolytes. *Nature Reviews Materials*, 2:16103, 2017.

[25] G. Berckmans, M. Messagie, J. Smekens, N. Omar, L. Vanhaverbeke, and J. Van-Mierlo. Cost projection of state of the art lithium-ion batteries for electric vehicles up to 2030. *Energies*, 10(9):1314, 2017.

[26] M.A. Muñoz-Márquez, D. Saurel, J.L. Gómez-Cámer, M. Casas-Cabanas, E. Castillo-Martínez and T. Rojo. Na-ion batteries for large scale applications: A review on anode materials and solid electrolyte interphase formation. *Advanced Energy Materials*, 7(20):1700463, 2017.

[27] E.A. Olivetti, G. Ceder, G.G. Gaustad, and X. Fu. Lithium-ion battery supply chain considerations: analysis of potential bottlenecks in critical metals. *Joule*, 1(2):229-243, 2017.

[28] L. Ahmadi, S.B. Young, M. Fowler, R.A. Fraser and M.A. Achachlouei. A cascaded life cycle: reuse of electric vehicle Lithium-ion battery packs in energy storage systems. *The International Journal of Life Cycle Assessment*, 22(1):111-124, 2017.

[29] T. Hoshino. Innovative lithium recovery technique from seawater by using world-first dialysis with a lithium ionic superconductor. *Desalination*, 359:59-63, 2015.

[30] J.W. Choi and D. Aurbach. Promise and reality of post-lithium-ion batteries with high energy densities. *Nature Reviews Materials*, 1:16013, 2016.

[31] Sion Power announces launch of its groundbreaking Licerion rechargeable lithium battery. http://www.sionpower.com/media-center.php?code=production-rampup, January 31, 2018. Accessed: February 2018.

[32] University of Liverpool Hardwick Group. Peled model of the Solid Electrolyte Interphase. : www.liverpool.ac.uk/chemistry/research/hardwick-group/research/. Accessed: January 2018.

[33] Phys.org. Conventional battery. https://phys.org/news/2012-06-paintable-battery-technique-surface-lithium-ion.html. Accessed: February 2018.

[34] W.Y. Xuan et al. *Lithium-ion batteries: Solid-Electrolyte Interphase*. World Scientific, 2004.

[35] E. Peled. The electrochemical behavior of alkali and alkaline earth metals in nonaqueous battery systems-the Solid Electrolyte Interphase model. *Journal of The Electrochemical Society*, 126(12):2047-2051, 1979.

[36] J.B. Goodenough and Y. Kim. Challenges for rechargeable Li batteries. *Chemistry of Materials*, 22(3):587-603, 2009.

[37] M.S. Song, R.H. Kim, S.W. Baek, K.S Lee, K. Park and A. Benayad. Is Li_4Ti5O_{12} a Solid Electrolyte Interphase-free electrode material in Li-ion batteries? Reactivity between the Li_4Ti5O_{12} electrode and electrolyte. *Journal of Materials Chemistry A*, 2(3):631-636, 2014.

[38] T. Thompson, S. Yu, L. Williams, R.D. Schmidt, R. Garcia-Mendez, J. Wolfenstine, J.L. Allen, E. Kioupakis, D.J. Siegel, and J. Sakamoto. Electrochemical window of the Li-ion solid electrolyte $Li_7La_3Zr_2O_{12}$. *ACS Energy Letters*, 2(2):462-468, 2017.

[39] L. Baggetto, R.R. Unocic, N.J. Dudney, and G.M. Veith. Fabrication and characterization of Li-Mn-Ni-O sputtered thin film high voltage cathodes for Li-ion batteries. *Journal of Power Sources*, 211:108-118, 2012.

[40] J.B. Bates, N.J. Dudney, G.R. Gruzalski and C.F. Luck. Thin film battery and method for making same, August 16 1994. US Patent 5,338,625.

[41] J.B. Bates, N.J. Dudney, G.R. Gruzalski, R.A. Zuhr, A.Choudhury, C.F. Luck and J.D. Robertson. Fabrication and characterization of amorphous lithium electrolyte thin films and rechargeable thin-film batteries. *Journal of Power Sources*, 43(1-3):103-110, 1993.

[42] M.L. Jenson and V.H. Weiss. Thin-film battery having ultra-thin electrolyte and associated method, March 27 2007. US Patent 7,194,801.

[43] S. Oukassi. Process for realizing an electrode based on Vanadium Oxide and battery comprising such an electrode, May 9 2008. US Patent App. 12/118,036.

[44] NanoMarkets Report. Thin-film and printed batteries market. *White Paper*, 2008.

[45] J.B. Bates, N.J. Dudney, G.R. Gruzalski, R.A. Zuhr, A. Choudhury, C.F. Luck and J.D. Robertson. Electrical properties of amorphous lithium electrolyte thin films. *Solid State Ionics*, 53:647-654, 1992.

[46] N.J. Dudney. Solid-state thin-film rechargeable batteries. *Materials Science and Engineering: B*, 116(3):245-249, 2005.

[47] J. Li, C. Ma, M. Chi, C. Liang and N.J. Dudney. Solid electrolyte: the key for high-voltage lithium batteries. *Advanced Energy Materials*, 5(4), 2015.

[48] J. Oudenhoven, L. Baggetto and P. Notten. All-solid-state Lithium-ion microbatteries: A review of various three-dimensional concepts. *Advanced Energy Materials*, 1(1):10–33, 2011.

[49] M.J. Hundt, H. Du, K. Kelappan and F. Sigmund. Integrated circuit package including embedded thin-film battery, July 1 2014. US Patent 8,766,435.

[50] MONBASA H2020 project. Monolithic batteries for spaceship applications. http://www.monbasa.eu/, 2016-2018. Accessed: January 2018.

[51] Automotive sensors and electronics expo 2017. www.automotive sensors2017.com, June 14, 2017. Accessed: September 2018.

[52] H. Lee, S. Kim, K.B. Kim and J.W. Choi. Scalable fabrication of flexible thin-film batteries for smart lens applications. *Nano Energy*, 53:225–231, 2018.

Chapter 2

Experimental techniques

For the development of the research work described in this thesis a wide range of experimental techniques were used, which are briefly described in this chapter divided in three sections. Firstly, the method used for the deposition of thin-films is presented, followed by a set of techniques used for the structural, morphological and compositional characterization of the materials in the second section. Finally, in the last section, the electrochemical characterization methods are described.

2.1 Thin-film growth by Magnetron Sputtering

Sputtering is a thin-film deposition technique that outperforms the film deposition process compared to other Physical Vapour Deposition (PVD) techniques, such as thermal evaporation or Pulsed Laser Deposition (PLD). Indeed, sputtering has been successfully used at industrial level for the production of high quality films in very different applications like food packaging, hard coatings, low friction coatings, architectural glass, decorative, PV cells, microelectronics, and, also, thin-film batteries [1].

In the conventional sputtering process, a target (or cathode) of a chosen material is bombarded by ions from a plasma (figure 2.1). This plasma is generated when electrons in the proximity of the target are accelerated towards the anode by an externally applied voltage and collide with neutral atoms, ionizing them. The ions are accelerated by the same voltage towards the target, while the electrons will collide other neutral gas atoms creating a cascading process. The bombardment process causes removal, i.e. sputtering, of target atoms, which then condense on a substrate as a thin-film [2, 3]. Ejected material arrives at the substrate mostly in atomic or molecular form.

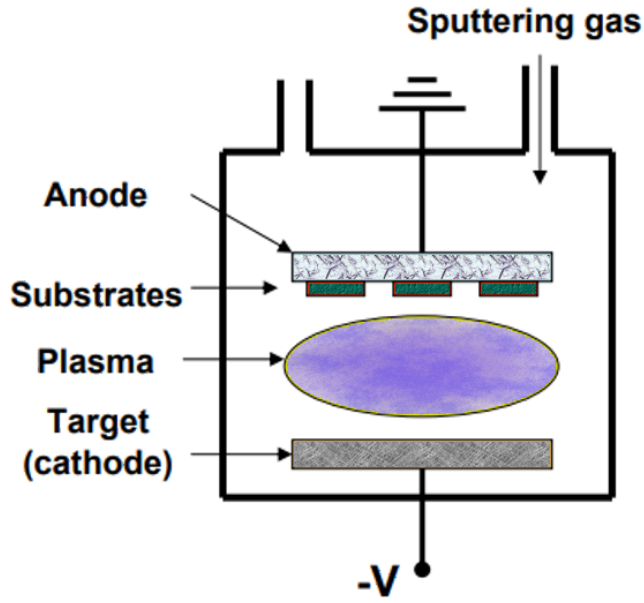

Figure 2.1: Schematic representation of conventional sputtering process.

The atom diffuses across the substrate due to its kinetic energy, until at some point it either evaporates or joins another diffusing atom to form a doublet. When a third atom joins triplets is formed, and then quadruplets and so on. This process, referred as nucleation stage, leads to the formation of quasi-stable islands, which will grow in size following to the coalescent stage, until the film becomes continuous (figure 2.2).

For the sputtering process good vacuum level is needed to maintain high ion energies and to prevent too many atom-gas collisions after ejection from the target. Unfortunately, the gas pressure needed to sustain the plasma is too high to allow transfer of the sputtered material without significant scattering. This results in low deposition rates, low ionisation efficiencies in the plasma, and high substrate heating effects. Such limitation is overcome by magnetron sputtering configuration (figure 2.3), where magnetrons take advantage of the fact that a magnetic field can constrain secondary electron motion to the vicinity of the target, thus, facilitating the control of the plasma. The magnets are arranged placing one pole at the central axis of the target and the second pole forming a ring of magnets around the outer edge of the target. In this way electrons are confined in a small volume over the target which substantially increases the ionisation probability (figure 2.4). This results

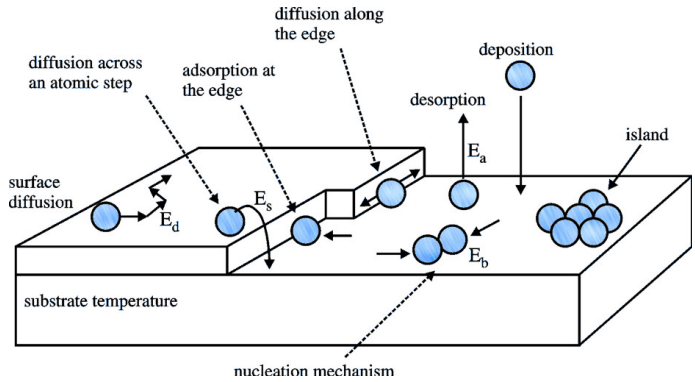

Figure 2.2: Schematic representation of film nucleation and growth (modified from [4]).

in an increase of ion bombardment of the target material, giving upgraded sputtering and deposition rates. Besides, the use of magnetron configuration enables lower working pressures and operating voltages compared to conventional sputtering.

There are two main modes in sputtering, based on the power source used: DC and RF [5]. In DC sputtering a direct voltage is applied between cathode (target) and the anode (substrate, in the most basic configuration), being this method limited only to conducting materials. RF mode, on the other hand, was developed as a way to enable the sputtering of insulating compounds. In RF sputtering, an RF frequency (typically 13.56 MHz) is coupled to the target by means of an impedance matching box, which blocking capacitor contained within this system ensures that the time average net current to each electrode is zero. When the RF power is applied, electrons oscillate between the two electrodes with the frequency set, while ion mobility is too low and they remain mainly in the center of the plasma. During one half of the cycle the target will act as anode and will attract the electrons, whereas the counter-electrode will not acquire as many ions, due to the reduced mobility mentioned. During the other half of the cycle, just the opposite process will occur, and, hence, both electrodes will be negatively biased with respect to the plasma. At some point, due to the negative charge accumulation, the target will capture less electrons during the first half of the cycle and it will start acquire enough ions during the second half of the cycle to cancel any electron gain. Therefore, since the target will have a net negative DC bias, gas ions will be attracted towards the target, producing the sputtering process. It is worth noting the symmetry of this process, since if the target (cathode) and

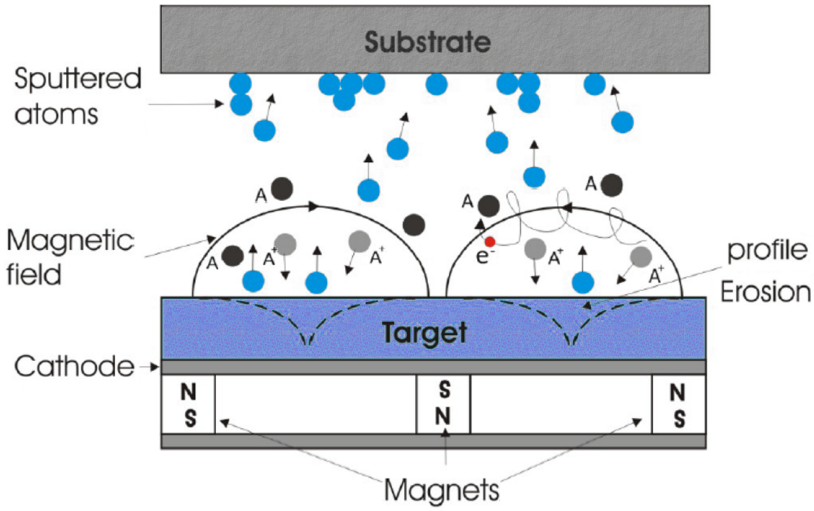

Figure 2.3: Schematic representation of magnetron sputtering (modified from [6]).

substrate (anode) are the same size, none of the electrodes will acquire negative bias relative to each other. Nevertheless, this limitation can be solved by non-symmetric cathode-anode configuration, where the whole chamber acts as the anode. If the anode area is big enough, relative cathode (target) potential will increase, and the sputtering of the anode (chamber) will be negligible. Despite it allows the sputtering of insulating materials, main limitation of RF mode is that the effective power at the target is typically only the 50% of the delivered power, hence,considerably lowering deposition rates. Another intermediate mode is the Mid-Frequency AC power supply. This method is essentially based on the DC method concept, except that cathode and anode switch their polarity every half cycle allowing the deposition of insulating materials. If two targets of the same material are used as anode and cathode, AC sputtering also provides a more efficient use of the power compared to RF sputtering, since half of the cycle one of the targets will be sputtered and on the other half of the cycle (when polarity is switched) the other one. This results in better deposition rates. Moreover, Mid-Frequency AC sputtering operates in the kHz rather than MHz range typically used in RF counterpart, requiring less sophisticated and expensive power sources.

Depending on the gas used in the process, two different types of sputtering

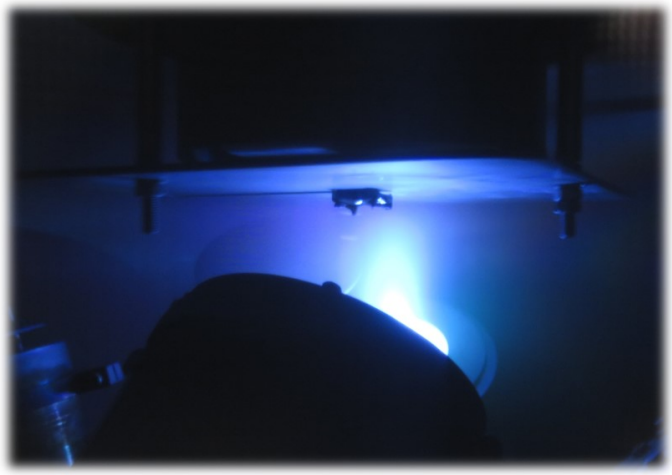

Figure 2.4: Picture of a magnetron and the plasma during the sputtering process.

are defined: non-reactive and reactive sputtering. In the first one, an inert gas (Ar typically) is used, while if a chemically reactive gas is used (O_2, N_2 or other) the process is referred as reactive sputtering. There are several parameters that affect to the sputtering and deposition rates, as well as to the quality of deposited films. Among others, base chamber pressure, sputtering pressure and partial pressure of reactive gas, target to substrate geometry, power and substrate temperature have a direct effect on the process.

For the thin-films grown along the work presented here, Pfeiffer Classic 500 SP instrument was used, with magnetron sputtering method with a magnetron head coupled to a RF power source. For each material deposited, process parameters were scanned and optimized. LNMO thin-films described in chapter 5, were deposited in Tecnalia by AC magnetron sputtering, within the collaborative framework of MONBASA European project (Grant Agreement No. 687561).

2.2 Characterization techniques

Many different techniques were used in order to characterize the materials studied along this research work at different levels. X-ray diffraction and Raman spectroscopy were used to obtain structural information of the materials, while X-ray Photoelectron Spectroscopy (XPS) was used to study the composition and Atomic Force Microscopy (AFM) to characterize the surface

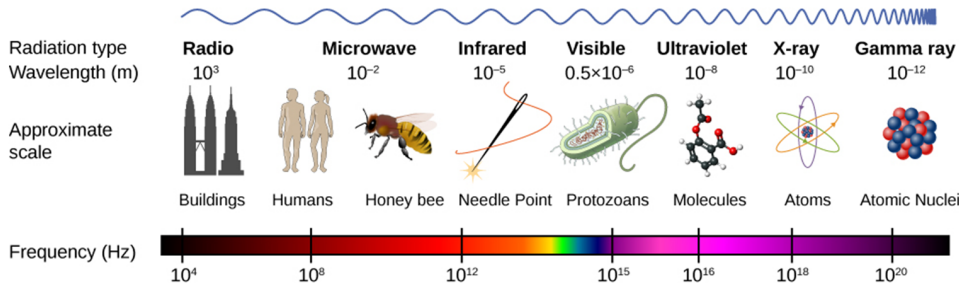

Figure 2.5: Electromagnetic spectrum [8].

morphology. Different techniques within Electron Microscopy were also used as suitable methods to have an insight on the structure, composition and morphology of the materials. The use of the wide range of techniques mentioned above facilitated the comprehensive characterization of the different materials studied in this work.

2.2.1 X-Ray Diffraction

X-ray diffraction (XRD) [7] is one of the principal techniques for phase identification and structure determination of crystalline materials. With this technique different crystalline phases present on the sample can be detected, and accurate data analysis can provide concentration of each phase and structural information, including lattice parameters and atomic positions among others. It is based on the light diffraction phenomena, which occurs when light is elastically scattered by matter, producing constructive interferences of the electromagnetic waves. Since the technique is used to obtain structural information of the phase under study, incident radiation must have a wavelength comparable to the spacing between atomic planes within the crystallographic structure. Hence, X-rays are used as high energy radiation with a low wavelength in the size range of the interplanar distances of typical crystalline structures (figure 2.5).

$$n\lambda = 2d_{hkl}sin\theta \tag{2.1}$$

The basics of the diffraction process is described by Bragg's law (equation 2.1), where θ is the incident angle with respect to the surface plane, d is the spacing between the atomic planes corresponding to (hkl) Miller index, λ is the wavelength of the incident light and n an integer. This equation can be derived applying constructive interference condition to the rays reflected

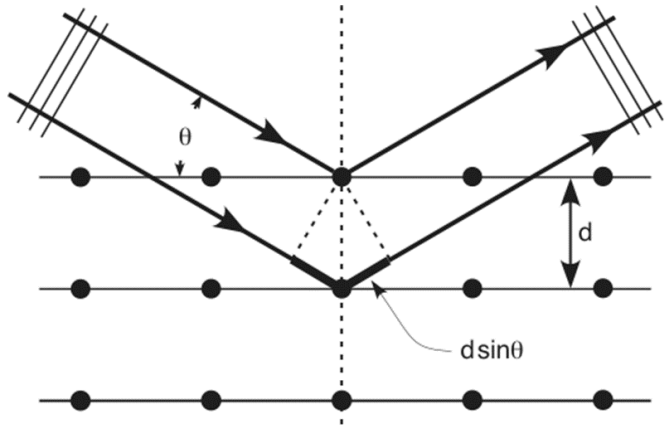

Figure 2.6: Bragg's law [9].

by a set of consecutive reticular planes, labeled as (hkl). If θ is the incidence and reflection angle, constructive interference (diffraction) will occur if the distance traveled by incident and reflected beams is proportional to the wavelength (figure 2.6). Thus, measuring the angle at which diffraction condition is fulfilled, determination of the distance between each plane is possible.

From the experimental point of view, during an XRD measurement, position between X-ray source, sample and detector are progressively changed (figure 2.7), in such a way that X-ray intensity at different angles is recorded. By scanning θ, a diffraction pattern is obtained, with peaks corresponding to interplanar distances (d) where Bragg's condition is satisfied. From the analysis of the angular position of reflections, Miller index can be obtained, leading to the determination of the lattice parameters.

XRD experiments performed during the development of the thesis work presented here, were performed by means of two different diffractometers, both from Bruker company: non-monochromatic D8 Advance (Cu $K_{\alpha 1,2}$, λ= 1.5406 Å, 1.5444 Å), and monochromatic D8 Discover (Cu $K_{\alpha 1}$, λ= 1.5406 Å). Temperature analysis reported in chapter 5, was carried out using a Anton Paar HTK 1200 (Rigaku) high-temperature oven chamber integrated in the D8 Advance diffractometer. Peak matching and phase identification was done comparing our experimental results with documented ones that are included in ICSD (FIZ Karlsruhe) database. In the cases that XRD results were analyzed with more detail, Rietveld analysis using the FullProf software [10] was performed.

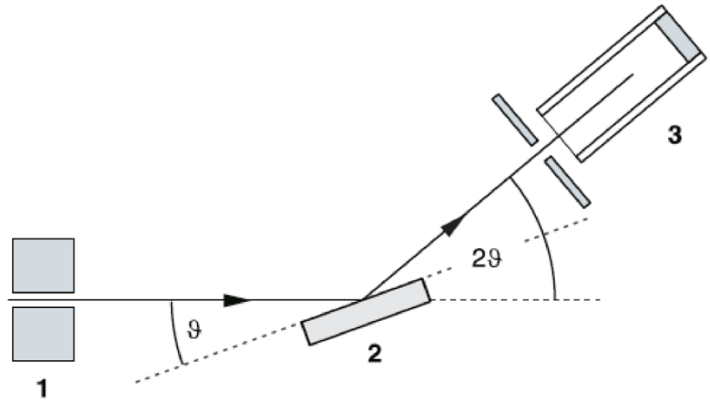

Figure 2.7: Schematic diagram of XRD measurement setup: 1) X-ray source, 2) sample, 3) X-ray detector.

Synchrotron radiation

Beyond the use of diffractometers, synchrotron radiation is very useful as X-ray source for material characterization, since it delivers much greater intensity, collimation and energy than can be obtained from conventional laboratory sources. Thus, this technique was also used along this work in order to obtain higher resolution X-ray diffraction patterns of the materials under study. The generation of synchrotron radiation stems from the laws of electromagnetism, which state that electromagnetic waves will be emitted from an accelerating charged particle. The energy of such radiation will be dependent of the degree of acceleration of the particle. In a synchrotron facility, the generation of radiation is nested on the acceleration of electrons in high vacuum around the curved orbits produced by the presence of a magnetic field. An installation for the generation of synchrotron radiation consists of a linear accelerator and a booster in which the particles are accelerated to several GeV, followed by a storage ring where the electrons move in circular orbits, providing the source of synchrotron radiation. The ring is not perfectly circular, as it consists of a series of straight sections consisting on insertion devices in the form of magnetic arrays called wigglers or undulators, together with short arcs in between the straight sections. The arcs contain a sequence of dipole magnets which bend the particles around the curved trajectory (bending magnets), and quadrupole magnets which keep the particles together. The instruments which exploit synchrotron radiation are situated tangentially to the storage ring, and are called beamlines.

As stated before, main advantages of using synchrotron radiation in comparison to conventional X-ray source are the higher intensity and the collimation of the beam among others, which provide, for instance, diffraction patterns with much higher resolution. On the results presented in chapter 3, synchrotron radiation source was used to take advantage of these useful properties. Measurements were performed in the BM25 Spanish CRG Beamline, at the European Synchrotron (ESRF, in Grenoble), with a radiation energy of 20 keV (λ=0.62 Å).

2.2.2 Electron Microscopy

Electron Microscopy (EM) is a common characterization technique in material science, used to obtain morphological, structural, and even compositional information from the material under study. It is based on the wave-particle duality of matter proposed by L. de Broglie, and, thus, takes advantage of this dual nature of free electrons so their energy is modulated in order to set their wavelength to be in the range of the atomic distances of the material under study. The higher the energy of the electrons, the shorter is their wavelength, and, hence, the higher is the spatial resolution. Indeed, one of the main advantages of EM stems from the higher magnification and spatial resolution that can be obtained compared to that of optical microscopy. Usual voltage range in different electron microscopes is 5-300 kV, which results in a wavelength of 0.20-0.5 Å, far below the wavelength of visible light (400-700 nm).

Therefore, in an electron microscope, an electron gun is used to generate and accelerate an electron beam, which is then bent and focused by means of electromagnetic lenses towards the sample to be studied. High vacuum is needed in the system, for the proper functioning of the electron gun and to avoid interactions of the electrons with the atoms in the air. When the incident electron beam interacts with the sample, various effects occur, as can be observed in figure 2.8. The use of different configurations and detectors allows getting morphological, structural, compositional, and other information of the sample from those effects. There are two main configurations, namely, Scanning Electron Microscope and Transmission Electron Microscopy.

Scanning Electron Microscope

Scanning Electron Microscope (SEM) [12] is used for observation and characterization of specimen surfaces. This technique uses the secondary and

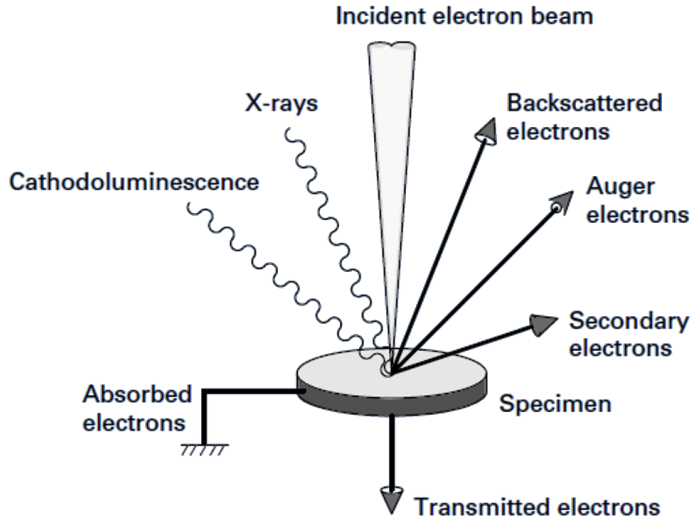

Figure 2.8: Electron Microscopy. Different effects that occur from the interaction between the incident electron beam and sample [11].

backscattered electrons that are emitted from the sample surface when it is irradiated by an electron beam with certain spot size and energy. Morphology of the surface can be observed by two dimensional scanning of the electron beam over the surface and acquisition of an image from the detected electrons. Schematic view of an SEM is represented in figure 2.9.

Secondary electrons (SE) are produced from the emission of valence electrons of the constituent atoms in the sample. SE generated at an inner region are quickly absorbed by the sample, since their energy is very low. Thus, only those generated at the outermost surface of the specimen are emitted, meaning that SE microscopy is a surface sensitive technique. Backscattered electrons (BE), on the other hand, are those scattered backward and emitted out of the sample. Information from a relatively deeper region is obtained from BE, since they possess higher energy than SE. Moreover, BE are sensitive to the composition of the specimen, as their scattering energy depend on the atomic number of the elements composing the sample.

In this work, SEM was routinely used for the surface morphology characterization of the different samples studied; data were collected with a FEI Quanta-200FEG microscope, at accelerating voltages between 10-30 kV. Sam-

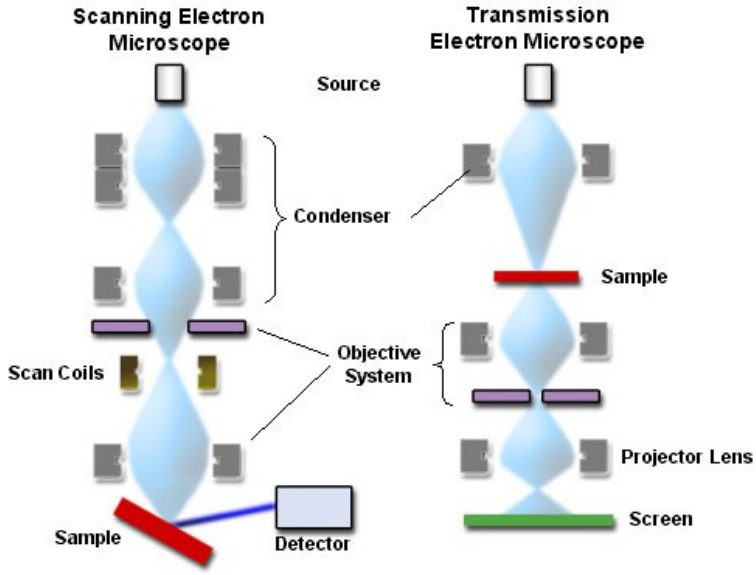

Figure 2.9: Schematic description of the configuration relative to SEM (left) and TEM (right) microscopes [13].

ples were mounted with carbon tape in aluminum stubs. Thin gold coating was used when needed, to avoid loss of resolution due to charging effects nested in the insulating nature of certain samples. Such coating was deposited using SPI module TM Super Coater, based on sputter coating technology. Cross-sectional analysis was also performed in thin film samples, in order to get information related to thickness and homogeneity. Special stubs designed for such kind of configuration were used. Samples were cut with diamond tip, except in the case of LNMO thin films in chapter 5, for which more complex method was followed. In such cases, sample was embedded in an epoxy resin and polished, after being cut with a diamond saw exposing the cross-section.

Transmission Electron Microscope

Transmission Electron Microscope (TEM) [14] is an analytical tool allowing visualization and analysis of specimens at very high magnifications (from micron to nanometer), being possible even the detection of single columns of atoms. It allows detailed micro-structural examination of the material under study through high resolution and high magnification imaging. The word *transmission* means *to pass through*, which indicates that it produces images from a sample by detecting the electrons that are transmitted through the material, when it is illuminated by an electron beam. Since the electrons have to

pass through the material under study, the preparation of thin samples (usually below 100 nm) is required. On the way through the specimen, different parts of the material stop or deflect electrons differently. The electrons are collected from below the sample onto a phosphorescent screen or through a CCD camera. In the regions where electrons do not pass through the sample the image is dark. Where electrons are not scattered, the image is brighter, and there are a range of grays in between depending on the way the electrons interact with and are scattered by the sample. Adjusting the magnetic lenses properly, an electron diffraction pattern can also be generated. Components and configuration of TEM is represented in figure 2.9.

Along the research work presented here, TEM was used for cross sectional analysis of thin film samples produced and studied. Images and diffraction data were obtained using a FEI Tecnai G2 TEM instrument, with a 200kV field emission gun. Sample preparation procedure was carried out in four steps. First, a piece of the sample was cut and glued (using an epoxy) to a silicon piece. This procedure allows to handle and to protect the sample for the next preparation steps. Secondly, a slice from the specimen parallel to the face of interest was cut by using a wheel diamond cutter, and then fixed onto a Cu grid. The next step was the reduction of the specimen thickness by mechanical polishing, initially down to 500-600 μm by using the grinding discs, and then down to 200 μm by means of the dimpling grinder technique. The final step consisted on making the sample transparent to the electrons, for what the thickness had to be reduced to the range of some tens of nanometers. To achieve the last an additional polishing was carried by means of the ion milling technique.

Energy Dispersive X-ray Spectrometry

Energy Dispersive X-ray Spectrometry (EDS) [15] makes use of the X-ray photons emitted from a specimen illuminated by a focused electron beam (figure 2.8), in order to obtain a localized compositional information of the sample. When electrons in the inner shells are emitted from the constituent atoms in the sample due to the irradiation of the incident electrons, the vacant orbits are filled with outer-shell electrons, and the substance emits X-rays whose energies correspond to the energy difference between the outer-shell electrons and the inner-shell electrons. Thus, energy of such X-rays are characteristic of the element. Qualitative and also quantitative analysis (determination of the concentrations of the elements present) is possible with this technique. By scanning the beam and displaying the intensity of a selected X-ray line, element distribution images can be produced. SEM and TEM are

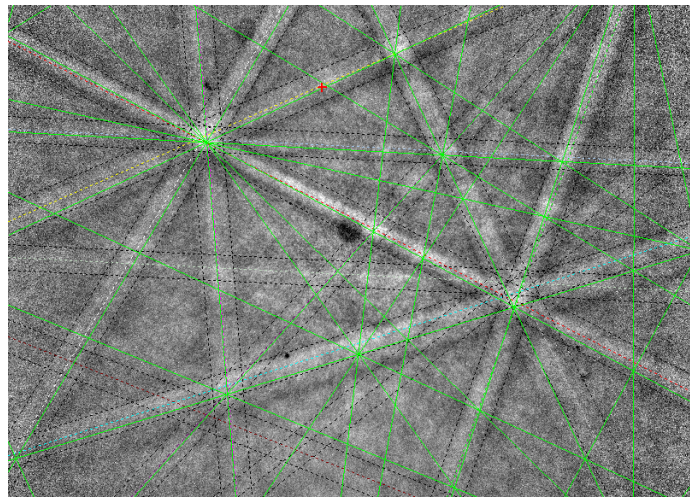

Figure 2.10: Kikuchi pattern obtained when a sample is characterized by High Resolution EBSD and indexation of detected phases by the corresponding software.

designed primarily for producing electron images, although they can also be used for compositional analysis, if an X-ray spectrometer is incorporated. In this work, EDS was used for the compositional analysis along the section of thin-film LNMO electrode, in chapter 5.

Electron Backscattered Diffraction

Electron Backscattered Diffraction (EBSD) [16, 17] is a widespread SEM technique that allows obtaining microstructural information of most inorganic crystalline materials, based on the accurate identification of diffraction patterns with the help of appropriate software. It reveals grain size, grain boundary character, grain orientation, texture, and phase identity of the sample under the beam. EBSD spatial resolution is related to the resolution of the SEM. EBSD operates by arranging the sample at a shallow angle to the incident electron beam (usually 20°). Using an accelerating voltage of 10–30 kV, and incident beam currents of 1–50 nA, electron diffraction occurs from the incident beam point on the sample surface. With the beam stationary an EBSD pattern is produced, which is measured by the detector. Specialized computer software analyzes the pattern by detecting a number of Kikuchi bands (figure 2.10) using an optimized Hough transform. With information from a database, the software determines all possible orientations with each phase and reports the best fit as the identified phase and orientation, being

the pattern indexed once its orientation and phase are known (coloured dash lines in figure 2.10). EBSD maps can also be used to obtain long range surface information, such as overall preferred orientation (texture), prevalence and distribution of grains in specific orientations, phase distribution, state of strain and local variations in residual strain, and character and distribution of grain boundaries. In this work, High Resolution Electron Backscattered Diffraction (HREBSD) measurements were performed on LTO samples described in chapter 3, within a collaboration with the Department of Materials at University of Oxford.

2.2.3 Atomic Force Microscopy

Atomic Force Microscopy (AFM) [18] is a type of Scanning Probe Microscopy (SPM) that can reach sub-nanometric spatial resolution. It provides a 3D topographic information of the surface, by measuring the oscillations of a sharp probe on surface at very short distance (0.2-10 nm probe-sample separation). The probe is commonly made of Si and supported on the edge of a flexible cantilever. The force between the probe and the sample can be described using Hook's law (equation 2.2), since it is dependent on the stiffness of the cantilever and the distance between the probe and the surface,

$$F = -k \cdot x \tag{2.2}$$

where F is the force, k is the stiffness (spring constant), and x the cantilever deflection. Hence, when the probe is approached to the surface, cantilever is bent, and the motion of the probe across the surface is monitored using feedback loop and piezoelectric sensors. A diode laser is bounced off the back of the cantilever onto a position sensitive photodiode detector, which measures the bending of cantilever while the tip is scanning sample surface (figure 2.11). Then, a dedicated control unit and software generate a surface topography map, based on measured cantilever deflections.

At short probe-sample distances at which the AFM operates, Van der Waals interactions are dominant, which can be either repulsive or attractive depending on the distance. There are three primary working modes in AFM. On *contact mode*, where probe-surface distance is below 0.5 nm, forces are repulsive, whereas in *non-contact mode* with separations of 0.1-10 nm, attractive forces dominate. There is a third mode called *intermittent contact mode* (or *tapping mode*), where the cantilever is oscillated at its resonant frequency, contacting the surface at the bottom of its swing.

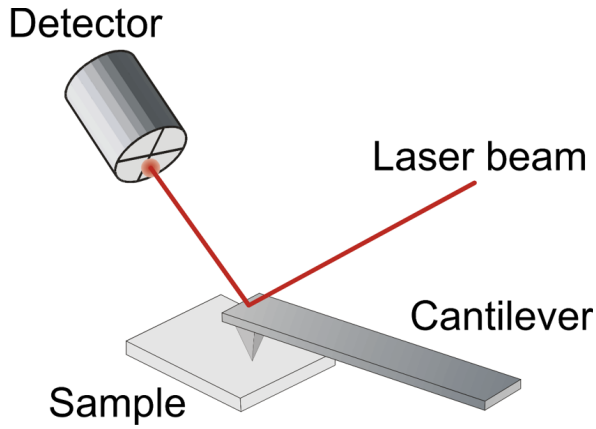

Figure 2.11: Schematic description of the set up in an AFM [19].

Surface topography characterization of the samples performed during this work was carried out using an Agilent 5500 microscope, in tapping mode (tapping mode), and with Si probe (NT-MDT). Analysis of the images and roughness calculation was done using Gwyddion program.

2.2.4 Raman Spectroscopy

Raman spectroscopy [20, 21] is a characterization technique based on Raman effect, which is an inelastic light scattering phenomena nested in the excitation or de-excitation of vibrational modes. When an incident photon interacts with a material it can be scattered either elastically or inelastically, which will correspond to Rayleigh scattering and Raman scattering, respectively. In fact, in Rayleigh scattering, the incident photon excites the system to a virtual state before decaying back to the ground state, while in Raman scattering, it decays to an excited vibrational state. In the later case, two different options are possible. When the scattered photon has lower energy than the incident one, energy transference occurs from the incident photon to the system, and is referred as Stokes scattering. On the other hand, when scattered photon energy is higher than for the incident one, energy transference occurs from the system to the scattered photon, and is called Anti-Stokes scattering (figure 2.12). Anti-Stokes scattering is a much weaker effect than Stokes scattering, so it is customary practice to measure Stokes lines in Raman spectroscopy, and spectra is represented as a shift taking Rayleigh line as the origin of the axis.

Raman scattering is an effect with very low probability of occurrence,

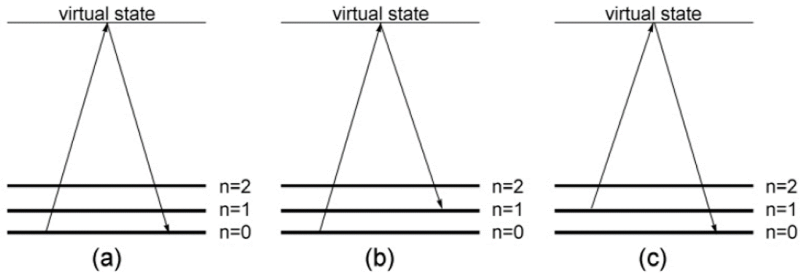

Figure 2.12: Schematic description of different possible scattering processes: a) Rayleigh scattering; b) and c) Raman scattering, Stokes and anti-Stokes, respectively. [22]

since only one in 10^6 of incident photons is inelastically scattered. Hence, a strong excitation source and good filters (to remove Rayleigh scattering) are needed if Raman scattering is to be measured and analyzed. In that sense, lasers are an optimum excitation source since they provide strong, coherent monochromatic light in a wide range of wavelengths, whilst notch filters effectively suppress stray light and the Rayleigh line. Moreover, Raman effect depends on the polarizability of the material, since it is not Raman-active unless the polarizability changes during the scattering process. However, Raman scattering is related to the chemical composition and bond configuration of the material and is a non destructive process. Therefore, Raman spectroscopy is a very useful technique to characterize a wide range of materials.

In this work, inVia Renishaw confocal microscope was used for Raman characterization. Confocal Raman microscopy enables spatial control of the sample during the analysis, both in xy (lateral) and z (depth) axes, thus, increasing considerably the spatial resolution in comparison to conventional Raman spectroscopy. A schematic representation of the instrumentation is shown in figure 2.13. 532 nm wavelength laser was used as light source, with an spot size below 2.0 μm. In all the materials characterized by means of Raman spectroscopy, first a general spectra was acquired, followed by a set of more accurate measurement at different points of the sample, adjusting the measuring region to the range of interest.

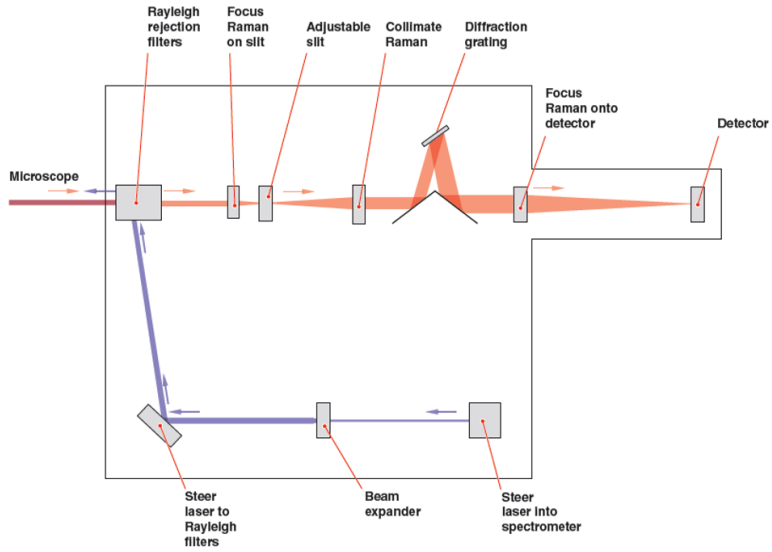

Figure 2.13: Diagram of the confocal Raman microscope used in this work.

2.2.5 X-ray Photoelectron Spectroscopy

X-ray Photoelectron Spectroscopy (XPS) [23, 24], also known as ESCA (Electron Spectroscopy for Chemical Analysis), is a surface specific technique for qualitative and quantitative analysis, based on the photoelectric effect. As shown in figure 2.14, when a surface is irradiated by X-rays, core level electrons from surface atoms are ejected out of the sample with a kinetic energy E_k determined by the following equation:

$$E_k = h\nu - E_B - \phi \tag{2.3}$$

where E_k is the kinetic energy of the emitted electron, $h\nu$ is the energy of the incident photon, E_B is the binding energy of the electron, and ϕ is the work function of the spectrometer. Therefore, based on this equation, considering that $h\nu$ and phi are known and measuring E_k, the binding energy of the core electron can be determined. Since photoelectron signal would be significantly decreased by scattering in a gas phase, ultra high vacuum conditions are needed to maximize the traveling length of photoelectrons. Besides, high vacuum is also needed if sample surface is to be kept clean, as gas molecules have high sticking coefficient at higher pressures.

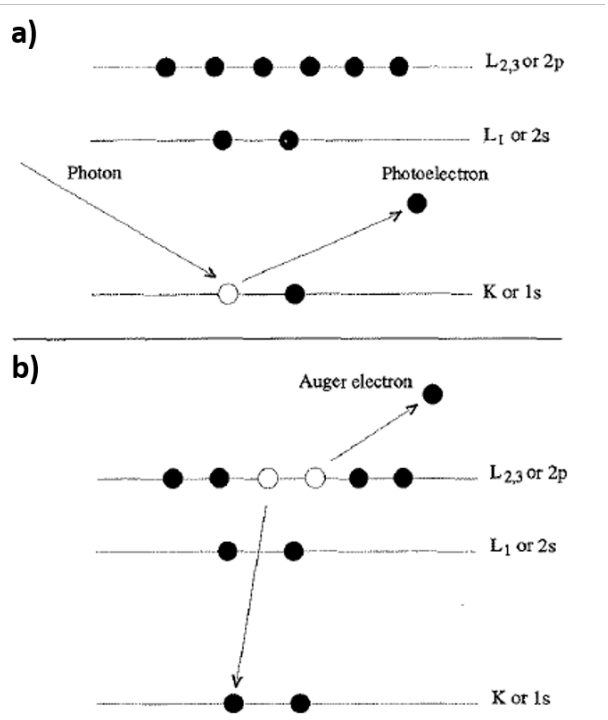

Figure 2.14: Photoelectric effect (a) and Auger electron emission (b) [23].

Basic elements of XPS spectrometer are the X-ray source, the electron analyzer and the electron detector. At laboratory level, the X-ray source is a X-ray tube, typically with Al or Mg cathode that lead to K_α emission at 1486 and 1253 eV, respectively. Although X-rays penetrate at least several hundred of nm on the irradiated sample, only photoelectrons escaping from the surface are detected. Hence, information obtained by XPS is limited to around the outermost 10 nm, since photoelectrons ejected from deeper regions are stopped by inelastic scattering processes within the material. With higher photon energies, the kinetic energy of the photoelectrons can be increased, thus, increasing their mean free path and the penetration depth of the technique. Among the different analyzer designs available, hemispherical analyzer is the most common one nowadays, due to its better resolution characteristics. Photoelectrons ejected from a sample surface are focused towards the entrance slit of the hemispherical analyzer by means of electrostatic lenses. Energies of the photoelectrons are retarded to a fixed energy, called pass energy (E_p), before entering to the analyzer. Once inside the analyzer the photoelectrons travel between two metallic hemispheres, with focusing potentials -U and U (

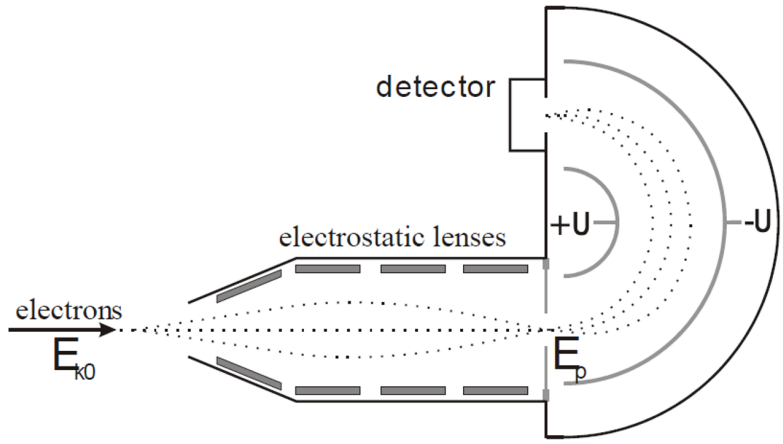

Figure 2.15: Schematic representation of the analyzer in a XPS spectrometer [25].

figure 2.15). The instrument transmission function, which refers to the fraction of the total number of photoelectrons ejected from the sample that will pass through the analyzer and reach the detector, is dependent on the slit width, analyzer radius and the initial E_k of the photoelectrons. The lower the pass energy, the higher will be the resolution of the measurement. However, an increase in the resolution implies a loss of signal intensity, since more photoelectrons are dispersed around the exit slit. Final element, the detector, consists of an electron multiplier of the channeltron type and a multichannel plate.

Recorded data is plotted as a function of photoelectron intensity versus binding energy, obtained from the kinetic energy from equation 2.3. XPS spectra consists of narrow core-level photoelectron peaks, broader Auger transition peaks, valence band, and other features such as background (from inelastically scattered electrons) and satellites. The very first ones are the signal of interest in XPS analysis. The binding energy of a particular core electron signal, will depend not only on the element but also on the chemical environment and energy state of the emitting atoms. Energy level of the atom will be perturbed by any change in the chemical environment or state, which results in corresponding variation of the binding energy measured. This effect is referred as chemical shift, and enables the identification of the chemical environment at the surface. Quantitative analysis of the concentration of each

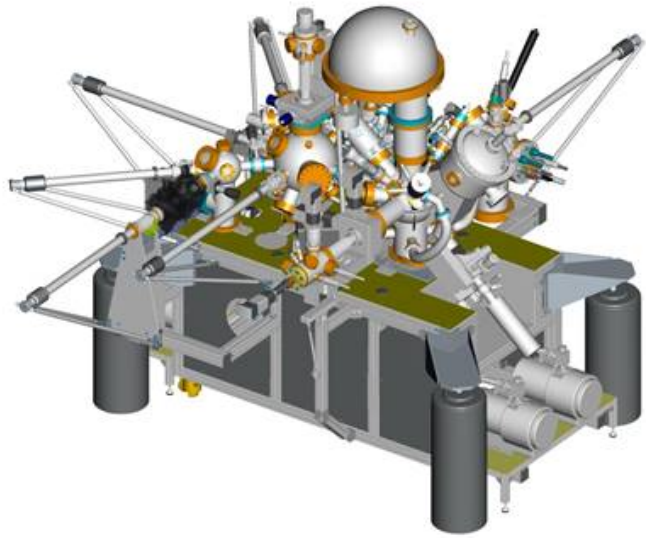

Figure 2.16: Schematic representation of the XPS instrument used in this work.

element can be calculated from the intensity (or the area) of the corresponding peak.

In addition to photoelectron peaks, useful information can also obtained from Auger emission (figure 2.14) [26]. This process stems from the transition of an electron from a higher orbital to occupy the vacancy originated by the emitted photoelectron, with the subsequent Auger electron ejection to compensate the energy excess. With the binding energy of the photelectron and the kinetic energy of the Auger electron corresponding to the same atom, Auger parameter can be calculated, which is characteristic of each phase. Moreover, in contrast to photoelectron signal, Auger parameter is independent of any surface charging effect that could influence the XPS spectra. Such surface charging effect might occur on insulating materials due to continued exposure to X-ray radiation, and can be compensated by a flood gun of low energy electrons oriented towards the sample.

In this work, SPECS Phoibos 150 XPS spectrometer (figure 2.16) was used for qualitative and quantitative surface composition analysis, using a non monochromatic Mg Kα source (hν =1253.6 eV). For every sample an-

alyzed, first low resolution survey spectra was measured in order to detect all the elements present on the surface, followed by higher resolution regions corresponding to the core electron signals of interest. Data analysis was performed using CasaXPS software [27]. Calibration of the spectra was based on aliphatic carbon (284.8 eV), unless some other reference is specified. Background was subtracted using Shirley type background, although Tougaard type was also used in particular cases. Peaks were fitted using Gauss-Lorentz (Voight) functions.

2.3 Electrochemical characterization

During the development of the research activities reported in this thesis work, broad electrochemical characterization was carried out. Several electrochemical cycling protocols were used, different kind of electrochemical cells were used, and a range of parameters were analyzed. Most relevant concepts are described in this section.

2.3.1 Electrochemical cells

Two different types of cells were used along this project, depending on the needs of the particular research activity being developed at each point. On the one hand, Swagelok type two electrode configuration cells were used, and, on the other hand, commercially available coin cells (CR2032 type) were utilized. For all of them half cell setup was used, meaning that metallic Li was always used as counter electrode (and reference electrode). Thus, active material under study was always mounted as positive electrode, although in some cases, namely lithium titanate (LTO) electrodes, in real application it would be used as negative electrode. $LiPF_6$ EC:DMC (1:1 v/v) was used as electrolyte (Solvionic, 99.9%), and glass fiber (GE Healthcare, GF/D grade) or Celgard2400 membrane as separator, depending on the case. Cells were assembled in inert atmosphere glove box (Ar filled, with H_2O and O_2 values below 0.1 ppm) since both metallic lithium and liquid electrolyte are moisture sensitive. Biologic VMP3 potentiostats and Maccor Series 4000 battery tester were used as platforms for the electrochemical characterization.

Swagelok cell

Swagelok cell is formed by a cylindrical polypropylene body, where the different elements of the battery are introduced, and sealed by two stainless steel plungers tightened with their corresponding nut and ferrule which ensure air tightness. The good mechanical and electronic contact are granted by a

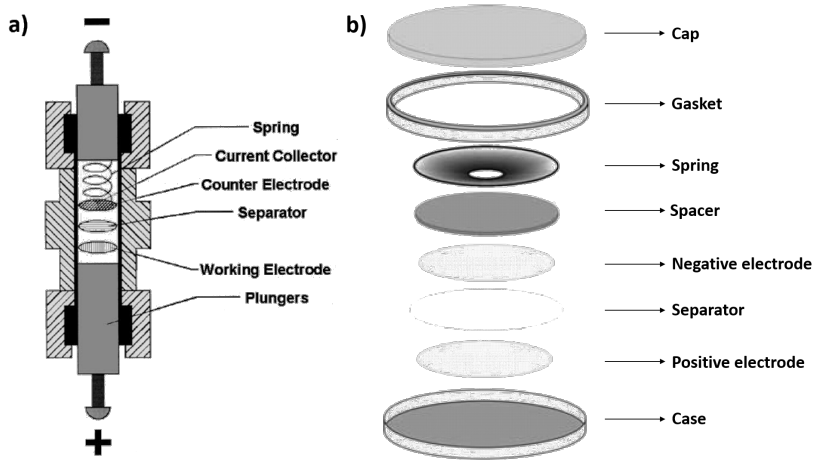

Figure 2.17: Configuration and elements of the electrochemical cells: Swagelok type cell (a), and the coin cell type (b).

spring and a metallic current collector. Schematic structure of the Swagelok cell is represented in figure 2.17a. This kind of cells were cycled in Biologic VMP3 potentiostats.

Coin cell

Coin cell configuration was composed by the case and an electronic insulator gasket (to avoid short circuiting the cell), where the different elements were introduced (electrodes, separator and electrolyte), along with the spacer, the spring and the cap which were put on the back. Schematic view of the cell is shown in figure 2.17b. CR2032 type coin cells were used in this work. Cells were sealed within the glove box by means of a manual clamper, and cycled both in Biologic VMP3 Potentiostats and Maccor Series 4000 battery tester, depending on the case.

2.3.2 Electrochemical analysis concepts

Main concepts related with the electrochemical characterization of the materials are described herein. Most relevant concepts are:

Open Circuit Voltage

Open Circuit Voltage (OCV) refers to potential difference between the two electrodes before connecting to any circuit, that is to say with no exter-

nal load connected.

Voltage Hysteresis

Voltage hysteresis is the difference between redox voltage during charge and discharge processes. The lower the difference, the higher the efficiency of the process, and the lower will be the energy loss.

Theoretical Capacity

The theoretical capacity of an electrode is the magnitude that determines the total quantity of electricity involved in the electrochemical reaction, and is dependent on the amount of active material that the electrode contains. It can be derived from Faraday's law, and is expressed as:

$$C_t = \frac{nF}{3600M} \tag{2.4}$$

where n is the number of electrons involved in the electrochemical reaction, F is Faraday constant (96485.33289 Cmol^{-1}), and M is the molecular weight of the active material. Ampere-hours units are usually used to define this magnitude.

Current Capability (C-rate)

Current capability, in the following called C-rate, indicates the value of the current at which the cell will be charged or discharged. Usually is indicated as C/n, where C is the cell capacity and n the number of hours to deliver or recover such capacity.

Coulombic Efficiency

Coulombic Efficiency (CE) is defined as the ratio of the total charge extracted from the battery to the total charge put into the battery over a full cycle. It is calculated dividing the discharge capacity by the charge capacity, and expressed in percentage. This magnitude is used to study the reversibility of the redox process taking place in the cell at each cycle.

Cycle Life

Cycle life refers to the number of times that a cell can be cycled before its capacity drops to 80% of initial capacity. This limit is commonly accepted as

the end of cell life.

2.3.3 Electrochemical measurements

Electrochemical characterization methods are classified as potentiostatic and galvanostatic techniques, depending on the voltage and current conditions used.

Potentiostatic techniques

Potentiostatic techniques are those in which a voltage is applied while generated current is tracked. Although it does not fit the definition given, Cyclic Voltammetry (CV) is usually considered as a potentiostatic technique. In a CV (figure 2.18a), voltage is constantly changed at a certain rate within chosen voltage window repeatedly, in order to record the generated current at different voltage values. Voltage window is selected based on the voltage values where redox activity is expected, and, low rate values are usually set (below mVs^{-1}). Equivalent current peaks, with opposite sign, are obtained at the voltages where oxidation and reduction occur in reversible processes. CV is a useful technique for the identification of redox reactions and determination of the voltage value in which they take place, for the study of the reversibility of the processes, and even for quantitative analysis of the current.

Galvanostatic techniques

Galvanostatic techniques are the ones in which a constant current is applied between the two electrodes, while voltage change upon time is monitored. Thus, in galvanostatic cycling, certain current is applied and the evolution of the voltage is tracked within given voltage limit. Then, the current is reversed, and voltage evolves until the other limit of the voltage window selected is reached. These charge-discharge cycles (figure 2.18b) are useful to obtain information of the redox reactions occurring in the electrode, which will appear either as a *plateau* (for two phase reactions) or as a sloppy curve (for solid solution reactions). Results are usually plotted as the voltage versus time, or also versus the capacity. With the latter, apart from the capacity retention of the material, CE of the process can also be calculated.

In addition, results can be plotted as differential capacity against the voltage ($\delta Q/\delta V$), which gives similar information to the CV measurements (figure 2.18c), although it is sometimes easier to determine the voltage of the redox reactions by this method. Besides, depending on the current applied, mate-

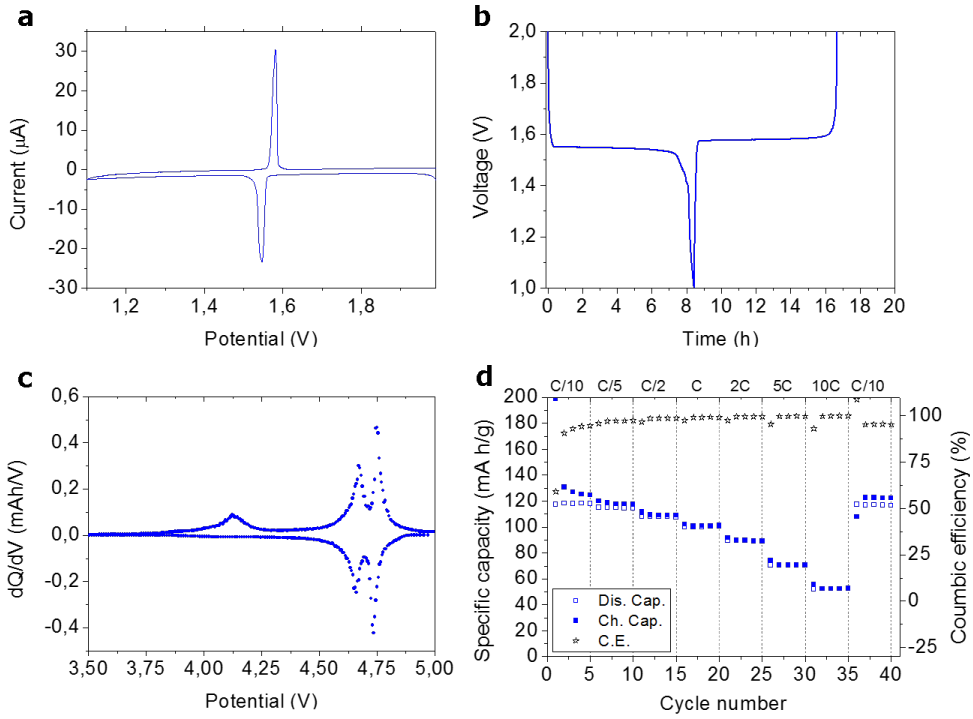

Figure 2.18: Examples of the different kind of electrochemical measurments: Cyclic Voltammetry (a), Galvanostatic charge-discharge (b), differential capacity (c), and, C-rate capability (d).

rial will be cycled at a certain C-rate. Indeed, C-rate capability test (figure 2.18d) are quite common to study the response of the material at different currents. In these tests, a series of charge-discharge cycles at different currents are programmed (from lower to higher), finishing the test setting back the lowest current.

Bibliography

[1] J.E. Greene. Tracing the recorded history of thin-film sputter deposition: From the 1800s to 2017. *Journal of Vacuum Science & Technology A: Vacuum, Surfaces, and Films*, 35(5):204, 2017.

[2] S. Swann. Magnetron sputtering. *Physics in Technology*, 19(2):67, 1988.

[3] P.J. Kelly and R.D. Arnell. Magnetron sputtering: a review of recent developments and applications. *Vacuum*, 56(3):159-172, 2000.

[4] Molecular beam epitaxy. www.physik.uni-kl.de/hillebrands/research/methods/molecularbeam-epitaxy/. Accessed: January 2018.

[5] M.M. Waite, S.I. Shah and D.A. Glocker. Sputtering sources. *Ch*, 15:108, 2010.

[6] M. Vorokhta. Investigation of magnetron sputtered $PT-CeO_2$ thin film catalyst for fuel cell applications. Doctoral Thesis, 2013.

[7] C. Hammond. Basics of crystallography and diffraction, volume 214. Oxford, 2001.

[8] phys.libretexts.org. The electromagnetic spectrum. https://phys. libretexts.org. Accessed: January 2018.

[9] compmatsci.org. Simulating powder X-ray diffraction in Python with Pymatgen and Xrayutilities. https://compmatsci.org/. Accessed: January 2018.

[10] L.C. Chapon and J. Rodrıguez-Carvajal. Fullprof: a program of the fullprof suite developed for Rietveld analysis of neutron or X-ray powder diffraction data. *https://www.ill.eu/sites/fullprof/php/ programs8809.html?pagina=FullProf.*

[11] JEOL. Scanning Electron Microscope a to z: basic knowledge for using the SEM. www.jeol.co.jp/en/applications/pdf/sm/sematozall.pdf. Accessed: January 2018.

[12] P. Echlin, C.E. Fiori, J. Goldstein, D.C. Joy and D.E. Newbury. Advanced Scanning Electron Microscopy and X-ray microanalysis. Springer Science & Business Media, 2013.

[13] McGill University Barrett Research Group. Nanotechnology: A brief overview. http://barrett-group.mcgill.ca/tutorials/nanotechnology/nano02.htm. Accessed: January 2018.

[14] M. De Graef. Introduction to conventional transmission electron microscopy. Cambridge University Press, 2003.

[15] D.C. Bell and A.J. Garratt-Reed. Energy Dispersive X-ray analysis in the electron microscope, volume 49. Garland Science, 2003.

[16] W. Zhou and Z.L. Wang. Scanning microscopy for nanotechnology: techniques and applications. Springer science & business media, 2007.

[17] J. Alkorta. Erresoluzio angeluar handiko EBSD teknika berriak. Materialen Zientzia eta Teknologia Kongresua, 2012.

[18] J.C. Vickerman and I. Gilmore. Surface analysis: the principal techniques. John Wiley & Sons, 2011.

[19] ETH Zurich Department of Materials. Scanning Probe Microscopy. http://www.ferroic.mat.ethz.ch/research/methods/atomic-force- microscope.html. Accessed: January 2018.

[20] L.A. Nafie. Theory of Raman scattering. *Practical Spectroscopy Series*, 28:1-10, 2001.

[21] F. Adar. Evolution and revolution of Raman instrumentation-application of available technologies to spectroscopy and microscopy. *Practical Spectroscopy Series*, 28:11-40, 2001.

[22] B.D. Hosterman. Raman spectroscopic study of solid solution spinel oxides. Doctoral thesis. 2011.

[23] J. Chastain, R.C. King and J.F. Moulder. Handbook of X-ray Photoelectron Spectroscopy: a reference book of standard spectra for identification and interpretation of XPS data. Physical Electronics Division, Perkin-Elmer Corporation Eden Prairie, Minnesota, 1992.

[24] D.P. Woodruff and T.A. Delchar. Modern techniques of surface science. Cambridge Solid State Science Series, 1994.

[25] E. Kleimenov. High-pressure X-ray Photoelectron Spectroscopy applied to Vanadium Phosphorus Oxide catalysts under reaction conditions. Doctoral thesis. 2005.

[26] C.D. Wagner and A. Joshi. The auger parameter, its utility and advantages: a review. *Journal of Electron Spectroscopy and Related Phenomena*, 47:283-313, 1988.

[27] J. Walton, P. Wincott, N. Fairley and Alan Carrick. Peak fitting with CasaXPS: A casa pocket book. Acolyte Science, 2010.

Chapter 3

Elucidating $Li_4Ti_5O_{12}(111)$ Surface Evolution Upon Electrochemical Cycling

3.1 Introduction

As stated in chapter 1, Li-ion batteries are widely known to be the dominant energy storage system for electronic devices and tools [1, 2], they are currently the best option for Electric Vehicles (EV) [3, 4], and they are also used for grid storage [5, 6]. Although the most common Li-ion battery is composed by graphite as anode and $LiCoO_2$ as cathode materials [2], during the last years, other electrode materials have been studied and commercialized [7, 8]. Among them, $Li_4Ti_5O_{12}$ (LTO) [9, 10] is one of the alternatives to the graphite as negative electrode material.

LTO has a defective spinel structure (Fd-3m space group, figure 3.1a) with the oxygen atoms forming an fcc lattice, half of the octahedral sites occupied by titanium and lithium cations in a ratio 5:1 and the remaining lithium ions occupying one eighth of the tetrahedral sites. Upon lithiation, three lithium ions per formula unit are intercalated to form $Li_7Ti_5O_{12}$ (figure 3.1b). The tetrahedrally coordinated 8a lithium ions and the intercalated lithium occupy the octahedral 16c sites, whereas the octahedral 16d sites keep the original titanium/lithium occupation, forming a rock-salt analogue structure [11, 12].

Typically, along with the Li insertion/deinsertion process, there is an inherent volume change of the electrode material. Such a change, affects the electrode degradation in the long term cycling. However, in the LTO case,

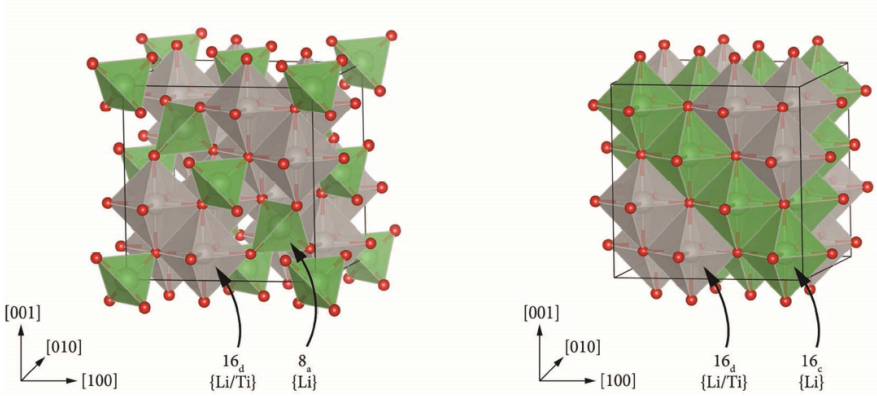

Figure 3.1: Structure of Lithium Titanate, a) in the non-inserted form, $Li_4Ti_5O_{12}$; and, b) in the Li inserted form, $Li_7Ti_5O_{12}$.

the volume change is very small, less than 0.1% [12–16], which minimizes the electrode degradation caused by mechanical strain and enables the long and stable cycle life that LTO electrodes display [17–19]. Another interesting feature of LTO is its insertion potential, 1.55 V vs Li/Li^+. Although this voltage could be considered high for a negative electrode and will certainly impact on decreasing the energy density, the positive aspect is that prevents the organic electrolyte reduction that occurs below 1.0 V vs Li [20–22]. Thus, the formation of the SEI layer (described in section 1.2) known to be formed in lower voltage insertion electrodes is avoided. Sustained on these properties LTO electrodes perform better than other electrode materials in high current and long cycling conditions. Hence, LTO is an interesting alternative for Li-ion batteries in general, and for high power applications and long cycle life applications [17, 23–27] in particular. In fact, LTO is already being used in commercial batteries by Toshiba ($SCiB^{TM}$ rechargeable battery).

Large variety of studies can be found in the bibliography related to synthesis paths of LTO [28–38], coatings [39–42] and dopings [43–45] for improving the cycling performance of LTO material. Regarding the surface study of the LTO electrodes, it did not attract much interest in the beginning, as it was thought to be SEI-free electrode due to its high insertion potential. However, during the last years, different studies confirmed that LTO is not free from surface reactions [46–55].

Besides the formation of new surface species in the interphase via electrolyte decomposition reactions, evolution of the LTO material's surface itself

has also attracted the attention. Kitta and co-workers described the possible formation of $\alpha-Li_2TiO_3$ phase on the surface of LTO (111) upon first Li-ion insertion-extraction, on the grounds of experimental TEM data, electron energy loss spectroscopy (EELS) and atomic force microscopy (AFM) investigation, claiming that it works as a protective layer [56].

Based on theoretical ab-initio calculations performed within European project SIRBATT (Stable Interfaces for Rechargeable Batteries, FP7 European Project, No 608502), the formation of this lithium metatitanate phase on top of the lithium titanate could occur under certain conditions. Starting from $Li_4Ti_5O_{12}$, the $\alpha-Li_2TiO_3$ phase could be formed either during the first Li-insertion, or during the first Li-extraction, following reaction with Li_2O formed during the first Li-insertion. Furthermore, the presence of a surface corrugation was also predicted in the same work.

In this study, highly oriented LTO (111) films were synthesized and cycled electrochemically, in order to verify the formation of $\alpha-Li_2TiO_3$ phase on the surface upon cycling, using long range surface sensitive characterization techniques. In addition, evolution of the outermost surface strain during electrochemical cycling was analyzed. The research study presented in this chapter, was developed within the framework of European project SIRBATT.

3.2 Synthesis and Characterization

Due to the requirements of this study which demands of a single crystal layer of LTO, instead of the usual $Li_4Ti_5O_{12}$ synthesis path (using TiO_2 and Li_2CO_3 powders as raw materials), rutile TiO_2 (111) single crystal was used, following a solid state synthesis reported before [57]. Pre-treatment was done in rutile TiO_2 (111) single crystal (SurfaceNet, 5 mm x 5 mm x 0.5 mm) by ultrasonic cleaning both in acetone and ethanol, followed by a calcination process in air at 800°C for 12 hours. For the synthesis process, the precursor was put in an alumina crucible along with LiOH (Sigma-Aldrich,$\geq$ 98%) and heated up to 900°C for 24 hours in air, in order to obtain $Li_4Ti_5O_{12}$ (111) layer on its surface.

Characterization of the synthesized sample was performed once the product was obtained. Phase and structure was checked by out of plane X-ray Diffraction (XRD) using Bruker Advance D8 instrument with Cu radiation (Cu $K_{\alpha1,2}$, λ= 1.5406 Å, 1.5444 Å). The X-ray diffraction pattern obtained for the first sample synthesized is shown in figure 3.2. Two narrow reflec-

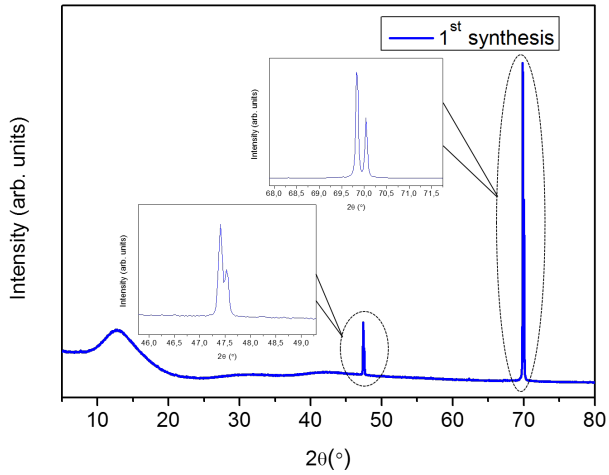

Figure 3.2: XRD pattern corresponding to the first synthesized highly oriented LTO layer sample.

tions were observed, the most intense one around $2\theta = 70°$ and a second less intense at about $2\theta = 47.5°$. Another broad peak was also present at low angle, which was produced by the sample holder used for the measurement. The narrowness of the peaks indicated the high crystallinity of the phase or phases present on the sample. If any of the two peaks is zoomed in, in order to observe them more in detail, it is observed that the peaks are clearly splitted in two, being this double peak more separated in the case of the most intense peak, which is at higher angles. This splitting of the angle is caused by the use of non-monochromatic incident radiation, and is another evidence of the high crystallinity of the product obtained in the synthesis.

The reflections that we would expect from a successful synthesis, were those corresponding to LTO (111) plane family, and same orientation peaks for the TiO_2 rutile substrate, as far as the formed LTO layer was thin enough to have signal from the substrate. LTO (111) plane should show a diffraction line at $2\theta = 18.4°$ whereas the TiO_2 (111) plane should appear at $2\theta = 41.3°$. Clearly, this was not what the diffraction pattern showed. Surprisingly, the most intense reflection at $2\theta = 70°$ would be in good agreement with the TiO_2 (112) reflection position, while the peak at $2\theta = 47.5°$ was where LTO (331) diffraction line should appear. To verify this hypothesis, as acquired TiO_2 (111) single crystal was characterized by XRD under the same condi-

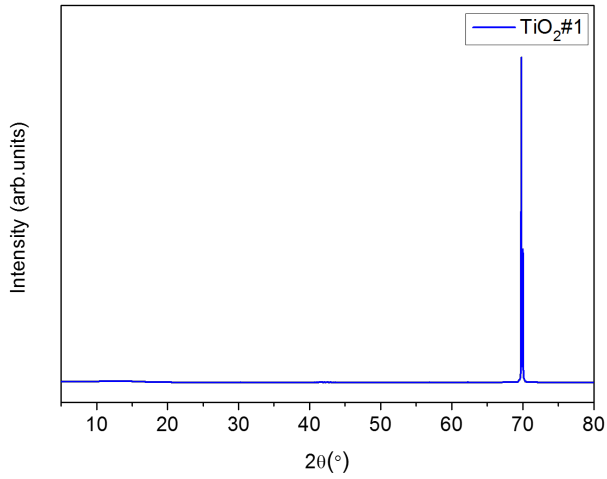

Figure 3.3: XRD pattern corresponding to as acquired TiO_2 single crystal.

tions. The result is shown in figure 3.3. In this case, only one reflection was present, exactly at the same position as the most intense peak of the previous diffraction pattern. This was a confirmation that the purchased single crystals used as substrate did not have the expected (111) orientation, but the (112) orientation instead, and thus, this was the reason for not obtaining the desired product from the initial synthesis process.

Once the second batch of commercial TiO_2 single crystals was acquired, first, XRD characterization was performed in order to verify their actual orientation and purity. Diffraction pattern obtained is shown in figure 3.4. In this occasion, two reflections were present, main at $2\theta = 41°$, and less intense one at $2\theta = 90°$. This two reflections corresponded to the expected (111) and (222) reflections for TiO_2 rutile, while same orientation higher order diffraction lines were out of the measured range.

The synthesis process described before, was repeated for the new raw TiO_2 crystals, and the XRD characterization of the new product, showed a completely different result (figure 3.5). In this case, more reflections were present, with different intensities. The most intense one, at $2\theta = 18°$, would match with the expected position for LTO (111) diffraction line. Moreover, the other new reflections shown in the pattern, were at the angles where same plane higher order reflections would be expected; peaks at $2\theta = 37°, 2\theta =$

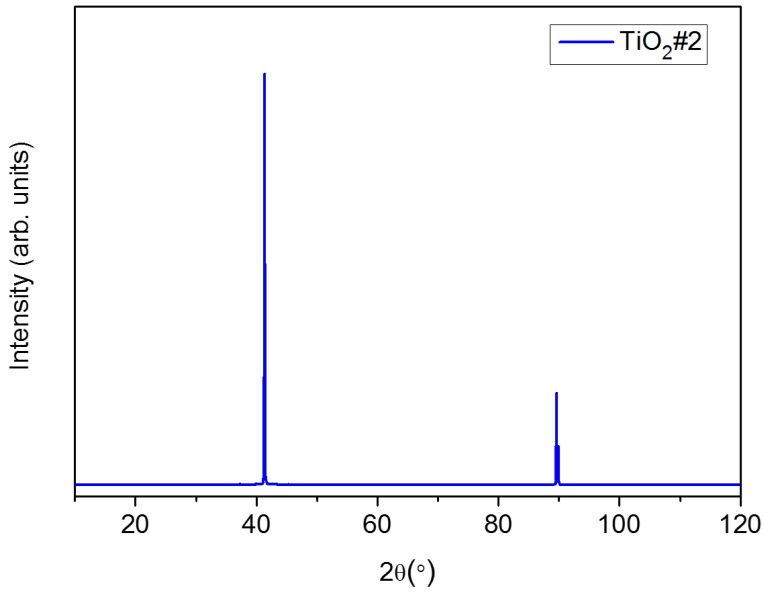

Figure 3.4: XRD pattern corresponding to TiO_2 (111) single crystal.

$56°, 2\theta = 79°$, and $2\theta = 106°$, correspond to LTO (222), (333), (444) and (555) respectively. This was a clear proof that not only the synthesis was successful, but also that the formed LTO layer was highly oriented in the desired (111) orientation, as only those reflections related to this plane were detected. The last two peaks that were observed, at $2\theta = 41°$ and $2\theta = 90°$, were those already present in the previous pattern (figure 3.5), corresponding to the rutile substrate. The presence of those lines, could mean either that the formed LTO layer was not uniformly created along the substrate's surface, or that the penetration depth of the x-ray diffraction process was deeper than the LTO layer itself. In both cases, the signal related to the substrate should be seen.

In order to check the mentioned layer homogeneity and make a general analysis of the surface, samples were characterized by a set of different techniques. The overall appearance of the surface was characterized by means of ZEISS Axio ScopeA1 Optical Microscope. The surface of the synthesized sample showed regular structure all across the surface, with two main characteristic features (figure 3.6): 1) Randomly directed semi straight or slightly

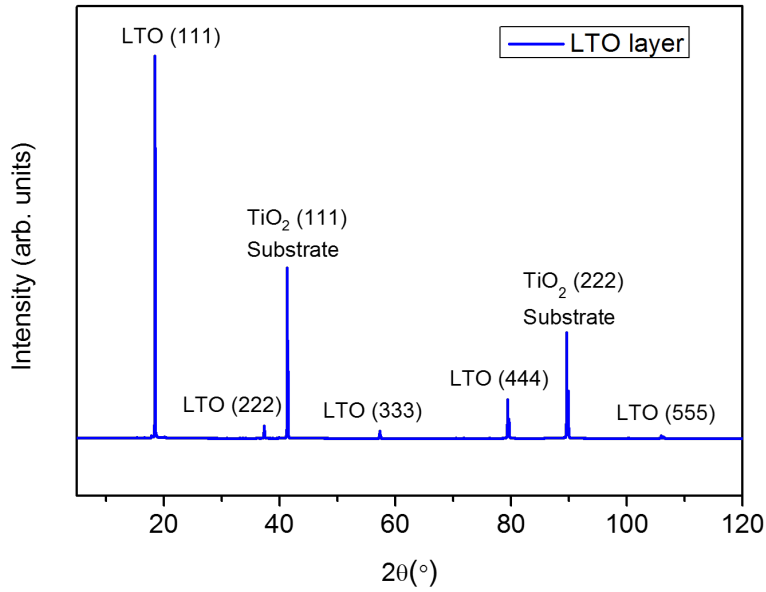

Figure 3.5: XRD pattern obtained from the synthesis process of the second batch of samples.

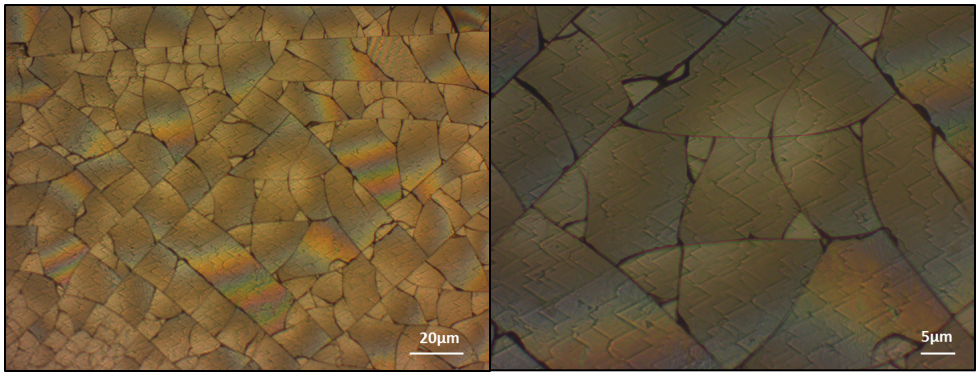

Figure 3.6: LTO (111) layer characterized by optical microscopy.

curved lines (boundaries), dividing the sample in many differently shaped areas; and, 2) very regular and equally oriented triangular shapes, within the mentioned areas.

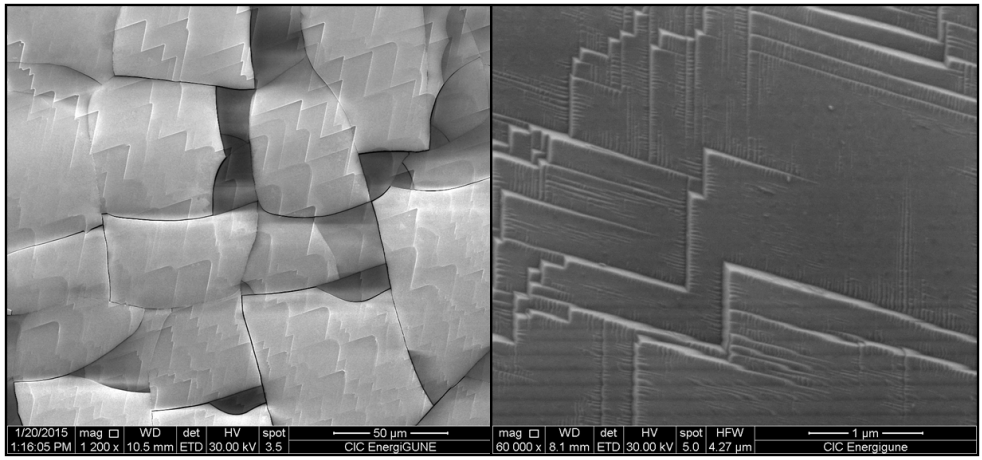

Figure 3.7: LTO (111) layer surface, as seen by SEM.

A detailed view of these surface features was obtained using a Quanta 200 FEG (FEI) Scanning Electron Microscope (SEM), at 30 kV accelerating voltage (figure 3.7). The first of these two features, looked to be a kind of cracking of the sample, due to some strain suffered at some point of the synthesis process. The second, on the other hand, was the presence of growing terraces, owing its triangular shape to the three-fold symmetry of the (111) surface in cubic spinel structure.

Details of the triangular terraces were examined by Agilent 5500 Atomic Force Microscope (AFM), in tapping mode. Scans were represented for different magnitudes, namely, phase, amplitude and topography. Topography was used for quantifying surface roughness, but, as phase and amplitude images may highlight physical properties that are not readily discernible in the topographic map, all of them were compared. For example, fine morphological features are, in general, better distinguished in amplitude and phase images. In figure 3.8, AFM images of the sample are shown, both before and after the synthesis process. In the case of the pristine sample, as it was a polished TiO_2 rutile single crystal, surface was extremely smooth, with an average roughness (R_a) of 0.10 nm and a root mean square roughness (R_q) of 0.17 nm (table 3.1). Only some small features are present, most probably being related to powder particles coming from the air or imperfections of the polishing process.

On the other hand, for the synthesized sample, perfectly triangular shapes were present, with different sizes and overlapped one over the other, resulting in a surface with facets at different levels. Overall roughness values measured

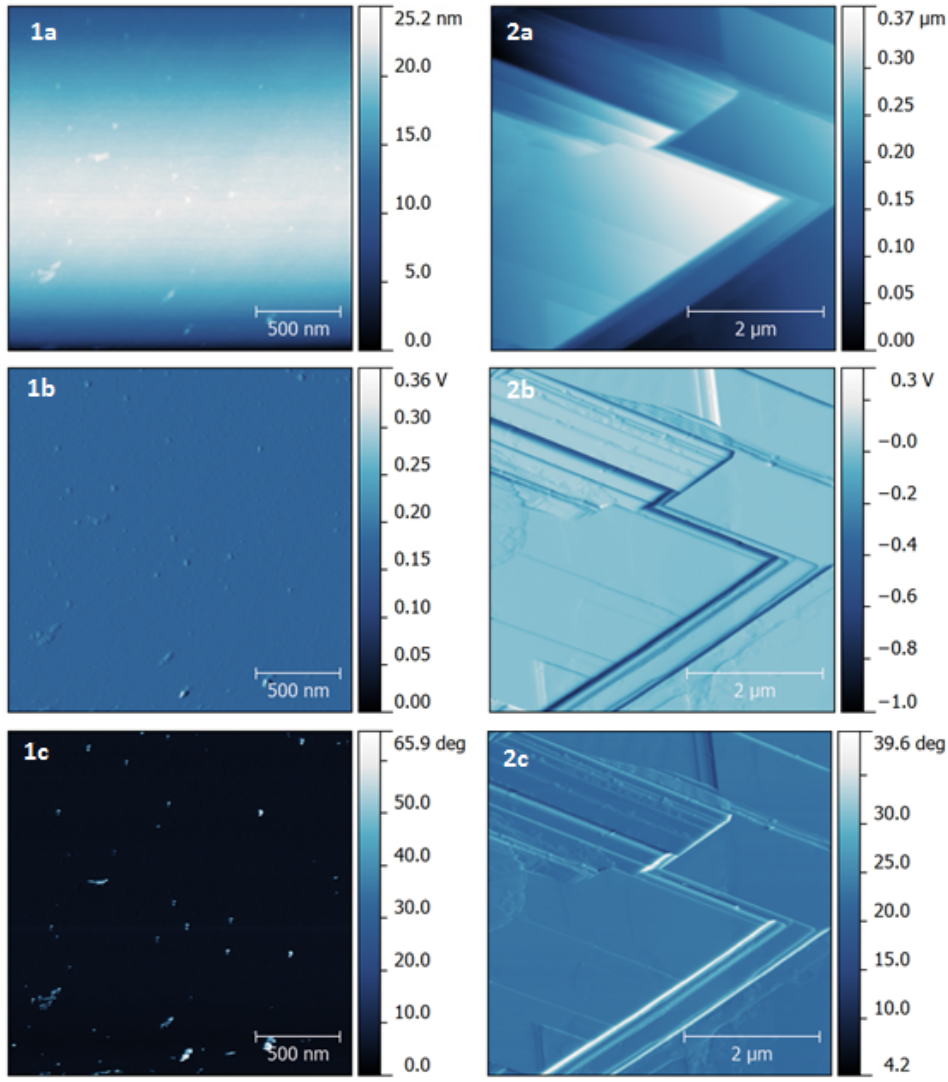

Figure 3.8: AFM images of the single crystal before (1) and after (2) the synthesis, representing the topography (a), amplitude (b), and phase (c) values measured.

for the scanned area in figure 3.8 are indicated in table 3.1. Most of these triangular growing terraces present on the sample surface, were formed by several layers, leading to steps from around a nanometer to several hundreds of nanometers. However, some of the terraces correspond to a single layer,

Table 3.1: Surface roughness values for rutile substrate and synthesized LTO sample.

Sample	R_a(nm)	R_q(nm)
TiO_2 (111)	0.10±0.02	0.17±0.03
LTO (111)	1.9±0.3	3.0±0.8

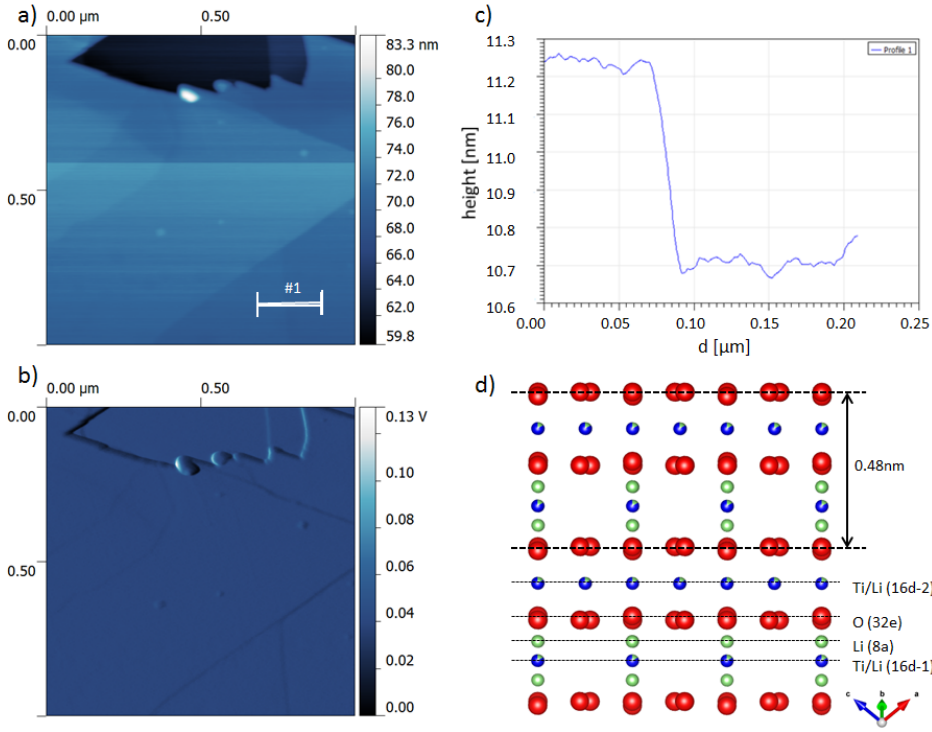

Figure 3.9: AFM topography (a) and amplitude (b) images of the growing terraces, the profile (c) of the line indicated in (a), and representation of out-of-plane structure of (111)-layer stacking in LTO, viewed from the $[1\bar{2}1]$ direction.

meaning by single layer the (111) inter-planar spacing of the spinel LTO structure. Figure 3.9 shows one of these single layers, along with the profile of the step. Profile was measured in topography image, but amplitude image is also shown, as edges are better observed in this mode. Such step was of around 0.5 nm, which is in good agreement with the expected distance in the (111) direction for LTO [57], as represented in the same figure 3.9d.

Analysis of the chemical composition of the synthesized layer, as well as the presence of possible impurities, was done by means of X-ray Photoelectron Spectroscopy (XPS) technique. Measurements were performed using a Phoibos 150 XPS spectrometer and a non monochromatic Mg Kα source (hν =1253.6 eV). Survey spectra was obtained with 0.5 eV step size, pass energy value of 60 eV, dwell time of 0.1 seconds and 1 scan. The result is represented in figure 3.10, where the different signals detected are indicated. Apart from the elements expected for the synthesized sample, namely titanium (Ti), oxygen (O) and lithium (Li), other two elements were detected. The first of them is carbon (C), which, in fact, is always present in samples exposed to air as adventitious carbon (also called ubiquitous carbon). Indeed, this signal is commonly used as charge reference in insulating materials for calibrating the binding energy of the XPS spectra [58, 59]. Therefore, this carbon was unavoidable as surface contamination. The second unexpected element detected was sodium (Na), which presence was indicated by Na 1s photoelectron, as well as the KLL Auger electron lines. Although at the beginning we were not sure about the origin of this contamination, we finally concluded that it could stem from the use of alumina crucible as container for the synthesis process.

In order to overcome the Na contamination, a simple physical approach was raised. 1 mm thick Ti foil pieces (Alpha Aesar, 99.2%), were cut with the proper size to fit in the alumina crucible as base and cap, as shown in figure 3.11. The aim of these Ti sheets was to work as a physical barrier, to the Na diffusion through the alumina in the case of the base, and to powder particles from the ambient in the case of the cap. The proof that this method was successful is in figure 3.12, where the XPS survey spectra of the LTO sample synthesized using these Ti protective layers is shown. Neither Na 1s photoelectron, nor the KLL Auger electrons signals were present, indicating that Na diffusion was stopped.

For the quantification of the concentrations of the different elements present on the surface, and, in particular, to verify that ratios were according to those expected for the LTO, specific regions were recorded with higher resolution.These regions were measured with Mg Kα source, step size of 0.1 eV, pass energy value of 40 eV, dwell time of 0.3 seconds and 3 scans. In the case of the region corresponding to Li 1s, 10 scans were recorded, due to the lower sensitivity of this element [60]. Results obtained for O 1s, Ti 2p, C 1s and Li 1s photoelectron signals are represented in figure 3.13. All the spectra were calibrated based on the aliphatic carbon peak (284.8eV) from the carbon signal, which was present as adventitious carbon as explained before. Data

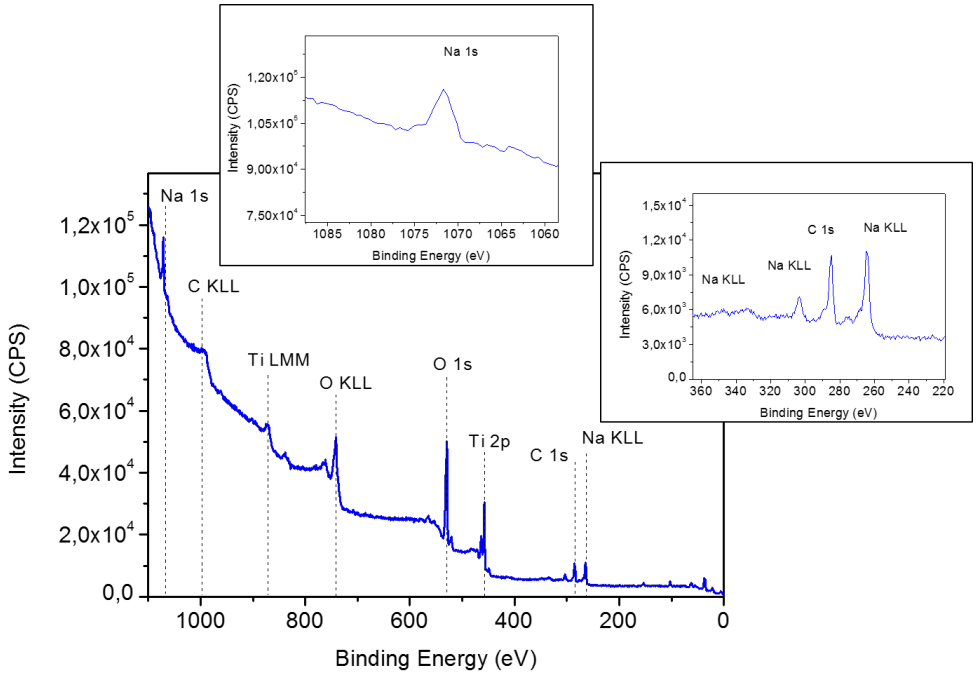

Figure 3.10: Survey XPS spectra corresponding to the synthesized LTO layer. The two inset correspond to the region where the Na 1s photoelectron and KLL Auger electron signals are detected.

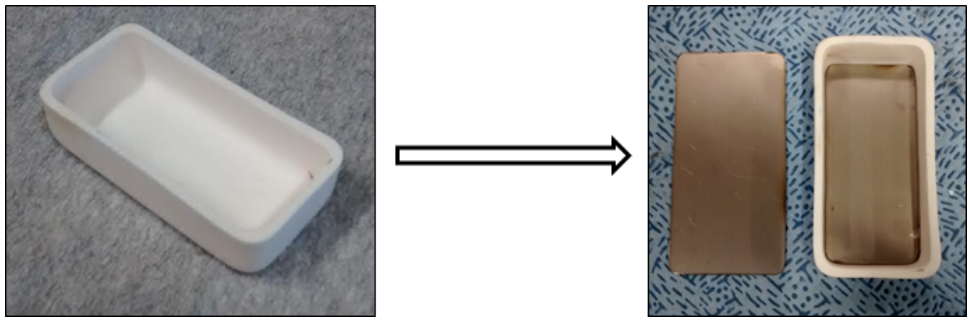

Figure 3.11: Picture of the alumina crucible itself (left), and Ti foil pieces used as base and cap in the alumina crucible (right).

was fitted using CasaXPS software, and deconvolution of overlapping peaks are represented in different colors and straight lines, while experimental data is represented in dotted curves.

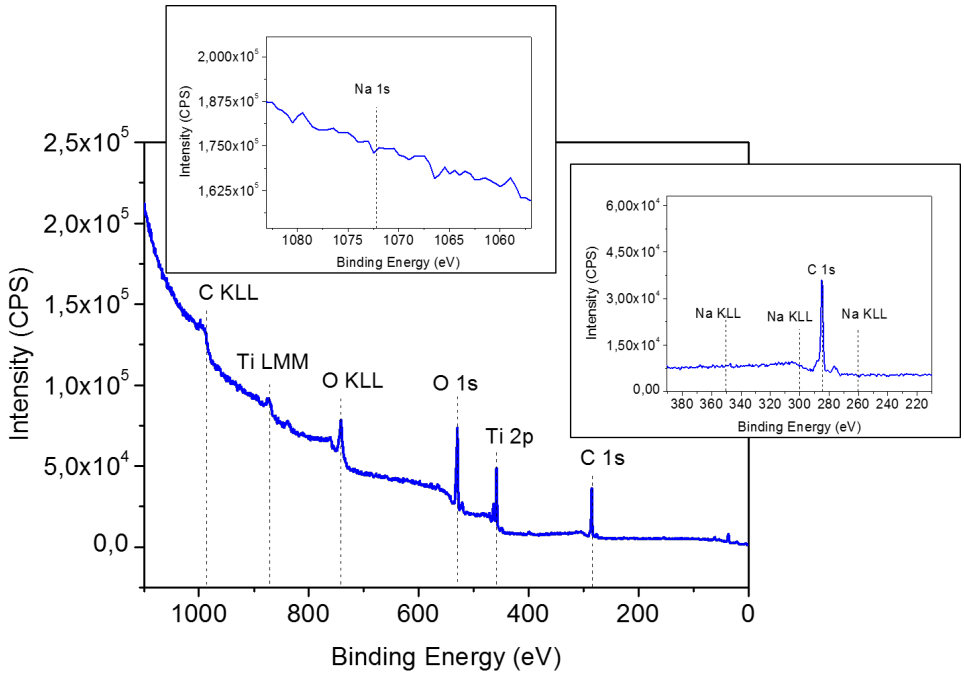

Figure 3.12: Survey spectra of the LTO sample synthesized using Ti foil layers. Insets indicate the regions where Na 1s photoelectron and KLL Auger electron signals should appear.

O 1s spectra was composed by a main peak, at a binding energy of 529.3 eV which is typical energy for metal oxide compounds [61, 62], with a clear broadening to higher energies. Oxide peak corresponded in this case to the oxygen signal from LTO, while the broadening was deconvoluted in two peaks related to hydroxides and carbonates (peak around 531 eV), and adsorbed water and organic oxygen (peak over 532 eV) [48, 53–55, 63]. Ti 2p signal showed the typical splitting of 2p1/2 and 2p3/2 peaks, situated at 463.6 eV and 457.9 eV respectively, in good agreement with the position and splitting values expected for a Ti(IV) oxide [64]. C 1s core electron showed the typical adventitious carbon signal mentioned before, with main peak related to aliphatic carbon (C-C and C-H bondings, at 284.8 eV). Successive peaks at 286.3 eV, 287.8 eV and 289.4 eV were hydroxides and ethers (C-OH and C-O-C), carbonyl group (C=O), and carbonates (CO_3^{2-}) respectively [63]. Last region analyzed, associated with Li 1s, showed a broad peak not as well defined as the previous ones, due to the lower relative sensitivity factor of this

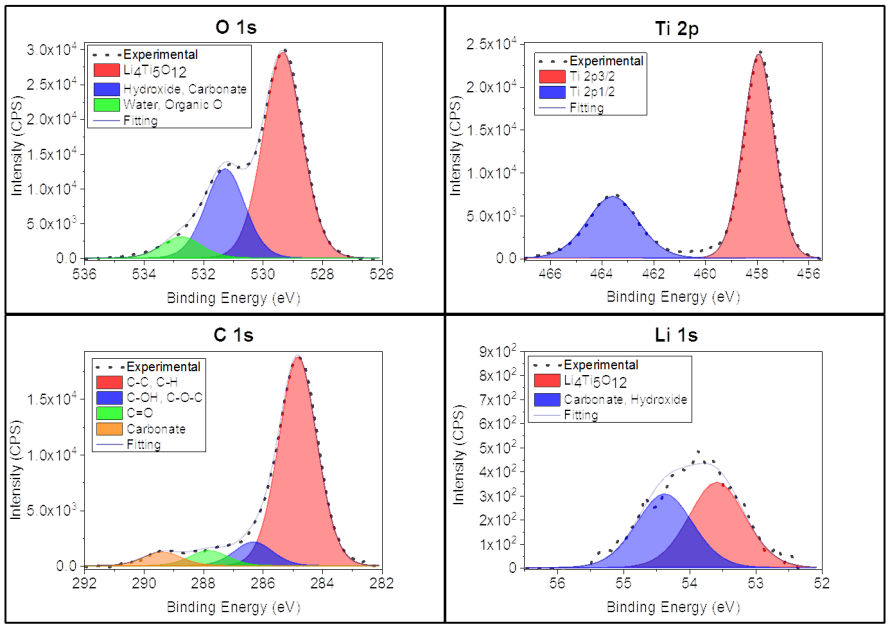

Figure 3.13: XPS spectra of the LTO sample showing the O 1s (a), Ti 2p (b), C 1s (c) and Li 1s (d) regions.

photoelectron. The peak was formed by two different contributions. Lithium from LTO phase (53.6 eV), on the one hand , and lithium in form of carbonate and/or hydroxides (54.4 eV), on the other hand. These values are slightly lower than the ones reported before, although peak assignments and relative peak distances are similar [55].

In regard to the details of the different values obtained from the XPS data fitting, they are all indicated in table 3.2. There, the different peaks deconvoluted for each orbital are specified, along with their measured binding energy (B.E.), the Full Width at Half Maximum (FWHM), the atomic concentration, and the assignment done for each peak. The relative concentration for oxygen, titanium and lithium contributions related to LTO phase, were very close to the stoichiometric ones (table 3.3). Thus, from a compositional point of view also, the results confirmed the success of LTO phase formation on the synthesis process.

Cross-section analysis of the sample was performed by means of SEM,

Table 3.2: Values obtained from the LTO sample XPS data fitting.

Orbital	**B.E.(eV)**	**FWHM**	**at.%**	**assignment**
O 1s	529.3	1.5	21.7	LTO
O 1s	531.2	1.5	9.4	OH, CO_3^{2-}
O 1s	532.7	1.5	2.2	H_2O, organic O
Ti 2p3/2	457.9	1.4	8.6	LTO
Ti 2p1/2	463.6	2.3	8.6	LTO
C 1s	284.8	1.5	35.7	C-C, C-H
C 1s	286.3	1.5	4.1	C-OH, C-O-C
C 1s	287.8	1.5	2.6	C=O
C 1s	289.4	1.5	2.3	Carbonates
Li 1s	53.6	1.0	7.2	LTO
Li 1s	54.4	1.0	6.2	Carbonate, hydroxide

Table 3.3: Relative concentrations of O, Ti and Li for the synthesized LTO, calculated from XPS data.

$Li_4Ti_5O_{12}$	**O/Ti**	**O/Li**	**Ti/Li**
Theoretical	2.4	3.0	1.25
Experimental	2.5	3.0	1.2

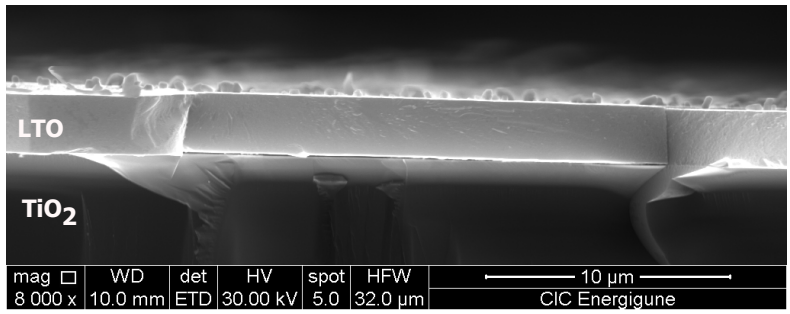

Figure 3.14: Cross-section analysis of the synthesized LTO layer by means of SEM.

with the aim of determining the thickness of the layer grown. Sample was cut in half by a diamond tip, and put in a cross section stub for SEM analysis. The presence of an homogeneous layer was verified all over the sample, with a thickness of around 2-3 μm, as can be seen in figure 3.14. The features that can be observed on the surface are particles deposited during the cutting process.

Once the sample was successfully synthesized and characterized, next step was to check its electrochemical properties. It is worth noting that, the sample was a single crystal LTO layer, which is an insulating material, on top of a rutile single crystal, which is even more insulating material. Therefore, cycling it looked a bit challenging, as LTO surface layer had to be electronically connected somehow, in order to allow the electron flow from and to the external circuit during electrochemical cycles. To do so, the sample was wrapped in a piece of copper foil (as shown in figure 3.15a), in such a way that the surface of the sample was electronically connected to the back side of the sample, which would be the part in contact with the current collector of the electrochemical cell.

Electrochemical characterization was done by means of Cyclic Voltammetry (CV) and Galvanostatic charge-discharge cycles, in Swagelok type two electrode configuration cells, described in chapter 2. LTO samples were cycled versus metallic lithium (Rockwood Lithium, battery grade, 99.8%), with glass fiber as separator (GE Healthcare, GF/D grade) and 1M $LiPF_6$ EC:DMC (1:1 v/v) as electrolyte (Solvionic, 99.9%). Cells were assembled in MBraun Ar filled globe box (H_2O and O_2 values below 0.1 ppm) and cycled in Biologic VMP3 Potenciostats. CV was performed for the synthesized samples at different rates, and different C rates were also used in the case of Galvanostatic

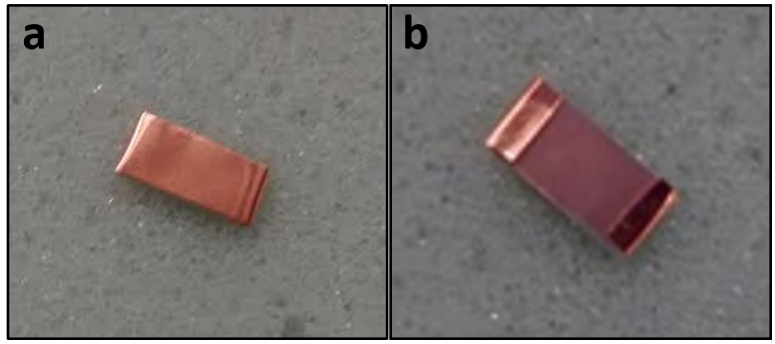

Figure 3.15: Details of Cu current collector contact: contact on the back side of the sample (a), and on LTO surface (b).

cycles.

The response obtained for the CV can be observed in figure 3.16. Current peaks related to the redox reactions occurring in LTO material are expected around 1.55 V [12, 41]. In this case, reduction and oxidation peaks were situated at 1.44 V and 1.66 V respectively, thus, symmetrically displaced 0.11 V from the expected voltage. This hysteresis effect was, most probably, due to the limited electronic conductivity on the system, which origin would be two-fold: first, the intrinsic insulating nature of LTO, which in the sample was not mixed with any conductive additive, as is usually done for conventional electrodes; and, secondly, from the difficulties arisen from the configuration of the active-material/current-collector connection. As the LTO layer lies on top of non-conductive TiO_2 substrate, this connection was made with a direct contact of copper current collector at the edges of the LTO surface as explained before. Even though the configuration and characteristics of the system are not the most convenient for an optimal electrochemical performance, the absence of any kind of additive, along with the high crystallinity and orientation of the LTO layer, made it the most suitable for this study. The oxidation peak in the CV is more intense than the reduction one, phenomenon that is designated to the lower reduction rate comparing to the oxidation rate, caused by the different conductivity properties between $Li_4Ti_5O_{12}$ and Li inserted $Li_7Ti_5O_{12}$ [57], which are insulator and conductive respectively [65, 66]. The small peak around 1.30 V during the first reduction might be related to surface lithium storage process corresponding to the Faradaic reaction, as reported before [67]. Rutile TiO_2 single crystal was also tested under the same conditions, confirming that no electrochemical activity can be ascribed to the

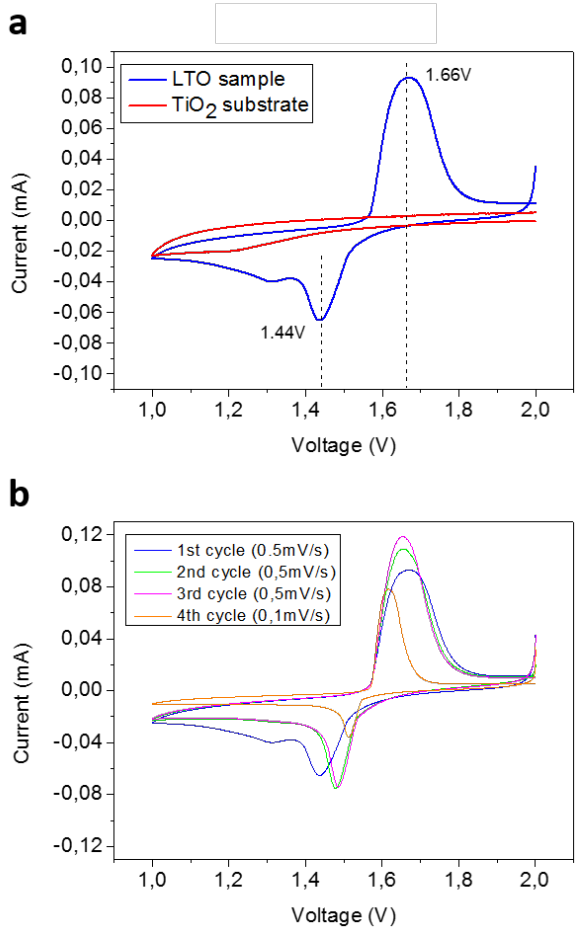

Figure 3.16: Results of the CV test on LTO samples. Comparison of the first cycle for LTO sample compared to bare TiO_2 rutile substrate (a); and, comparison of the first four CV cycles for the LTO sample (b).

substrate (red line in figure 3.16a).

Figure 3.17 shows the results of the Galvanostatic discharge-charge curves for the LTO sample, cycled at a rate of approximately C/10. As can be observed, reversible Li insertion/extraction was obtained. During the first discharge (figure 3.17a), a voltage plateau began to appear at 1.55 V, indicating the insertion of Li ions in the LTO structure, which after a short period evolved to a descending curve until the end of the discharge, set at 1.1 V to avoid organic electrolyte decomposition which typically starts below 1 V.

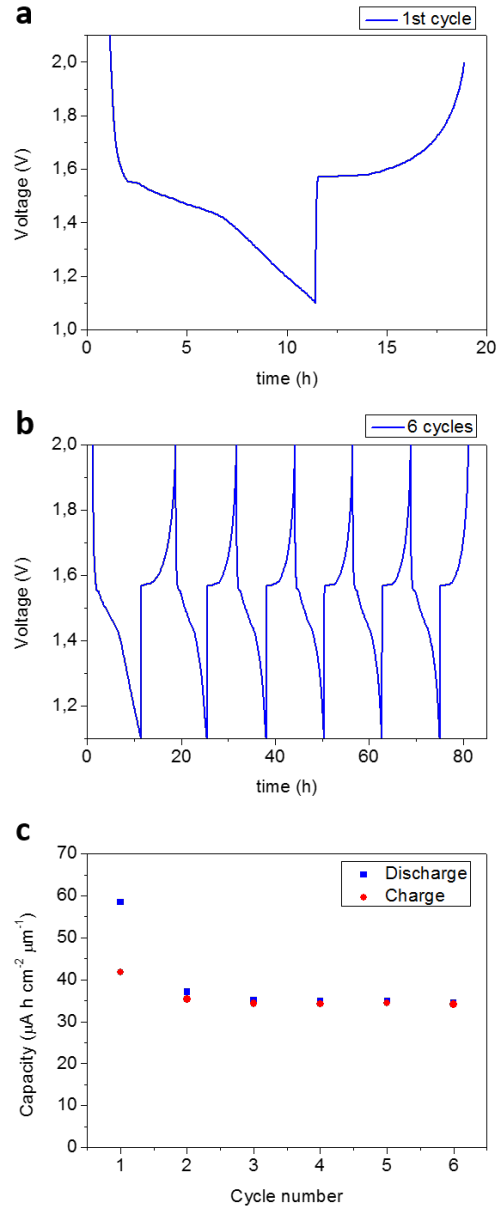

Figure 3.17: Results of the Galvanostatic discharge-charge cycles on LTO samples. Time vs Voltage evolution of the first cycle (a); the first six cycles (b); and, discharge and charge capacity evolution over the same cycles (c).

During the charge, Li ion de-insertion started slightly above 1.55 V, and was present as flatter but shorter plateau. The fact that the charge voltage curve was smoother, suggests that the electrochemical process was easier developed during the de-insertion (charge) than in the insertion (discharge). This phenomenon could be related, again, with the insulating (conductive) nature of the sample at the de-inserted (inserted) state, as well as with the complicated set up used to have an electronic contact on the LTO layer. On the other hand, the shorter plateau during the charge, indicated that not all the Li ions inserted during the discharge were de-inserted back during the charge. However, despite being above 1 V, electrolyte decomposition could also be related with this effect. Same conclusion was obtained from the capacity results in figure 3.17c, where the discharge capacity of the first cycle was higher than the charge one. Described electrochemical process was reversibly reproduced in the successive cycles (figure 3.17b), with a capacity stabilization at around 35 μAh cm$^{-2}\mu$m^{-1} (almost 60% of the theoretical capacity) both for discharge and charge (figure 3.17c). Note that μAh cm$^{-2}\mu$m^{-1} was used as the magnitude to quantify the capacity, since it is more useful than mAh g^{-1} or mAh cm^{-3}, usually used in bulky electrodes. In the magnitude used cm^2 and μm^1 correspond to the thin-film area and thickness, respectively.

3.3 Surface evolution upon cycling

In order to fulfill the aim of this study, the verification of the formation of the electrochemically stable/inactive $\alpha-Li_2TiO_3$ thin layer on top of the LTO (111) upon cycling, both pristine and cycled samples were analyzed by synchrotron XRD. Measurements were carried out in the BM25 Spanish CRG Beamline, at the European Synchrotron (ESRF, in Grenoble), with a radiation energy of 20 keV (λ=0.62 Å). As the possible formation process of the $\alpha-Li_2TiO_3$ phase remains unclear, cycled sample was analyzed for six cycles (meaning by cycle one insertion followed by de-insertion), in case the formation process needs several electrochemical cycles.

The general diffraction pattern obtained for the pristine (figure 3.18), showed the reflections of the first two orders for the (111) plane corresponding to TiO_2 substrate, as well as the first five-order reflections of the (111) plane for LTO film. There were also some small traces related to (400) and (800) reflections. The best fit of the experimental data obtained, resulted in a unit cell parameter of a=8.135 Å. This value is 2.6% lower if compared with to crystallographic database, which could involve the existence of tensile stress on the LTO crystal. For the TiO_2 peaks, the obtained cell param-

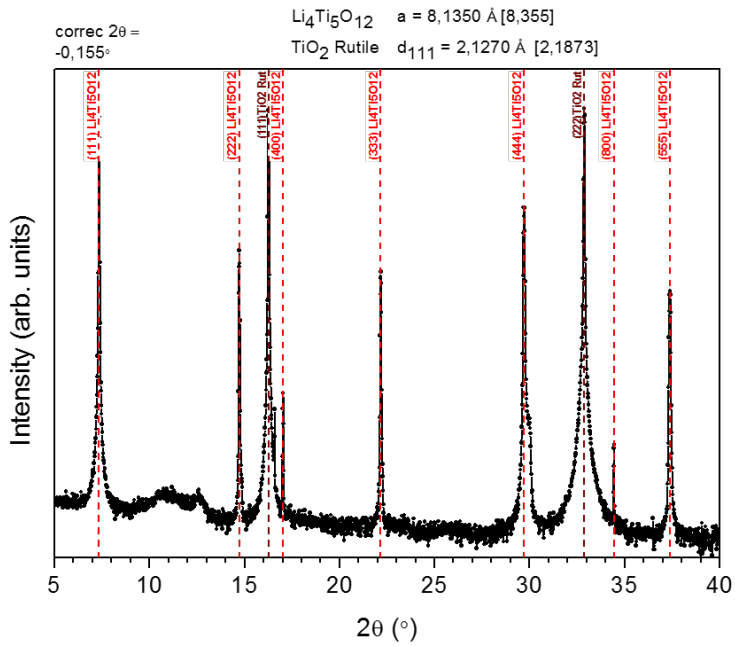

Figure 3.18: General XRD spectra from the pristine LTO sample recorded at the BM25 Spanish CRG Beamline of the ESRF.

eter was d_{111}=2.127 Å, 2.7% lower than the database value, meaning that would be under tensile stress as well. This stress could be an effect of the synthesis method used, in which the Li source reacts with the TiO_2 rutile single crystal, being this last one not just the substrate, but also the reactive for forming the LTO layer. The big difference in the unit cell volume between TiO_2 and LTO (62.43 $Å^3$ vs 583.23 $Å^3$), could explain the stress. The fractures observed on the surface (figure 2b), might be another indication of the same effect. Finally, less intense contributions were present on the diffraction pattern (figure 3.19), at $2\theta = 14.7°$ and $2\theta = 30.0°$, which could be related to the first and second order of a diffraction plane, with an interplanar distance of d=4.03 Åbased on the fitted data. This would be in good agreement with the expected values for the (111) and (222) reflections for $\alpha-Li_2TiO_3$, with a cell parameter reduced also in 1.7% due to a possible tensile stress. The presence of this phase in the pristine sample (non cycled), indicated that $\alpha-Li_2TiO_3$ was a product of the synthesis process, and not a consequence of the reactions occurring upon the first electrochemical cycles.

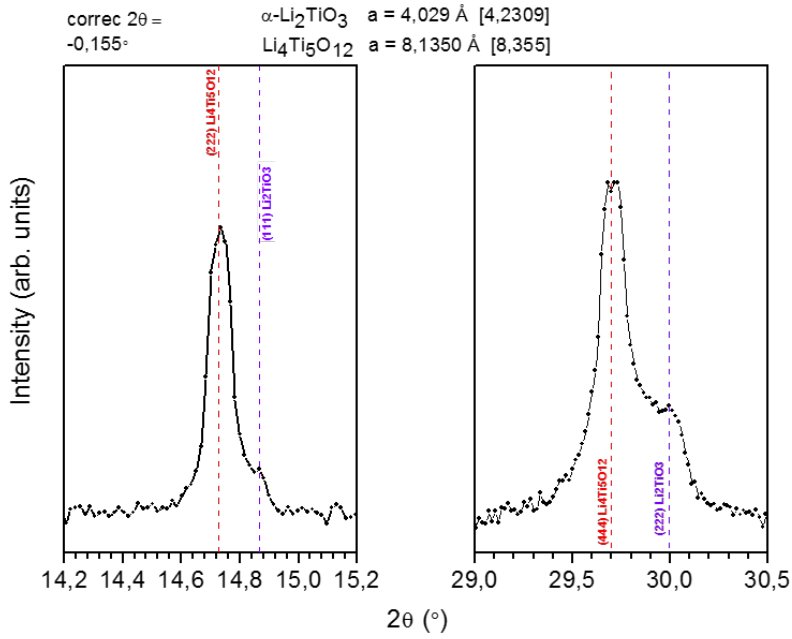

Figure 3.19: Detail of the less intense synchrotron XRD contribution, attributed to $\alpha-Li_2TiO_3$ phase.

Same reflections were present in x-ray diffraction patterns for the cycled electrodes (figure 3.20a), and the fit of such data gave similar results. Thus, no new phases were formed over the LTO (111) surface upon the first electrochemical cycles. In particular, the $\alpha-Li_2TiO_3$ phase contribution to the XRD spectra did not increase for the cycled sample (figure 3.20b), meaning that this phase was not being further formed during the electrochemical process. Moreover, no remarkable change of the cell parameter was observed, indicating that no change on the strain/stress was present after the electrochemistry was performed, and the tensile stress of the different phases remained the same. This is something that would have been expected, as the zero-strain property of LTO upon cycling is of general knowledge [12–16].

As the interest of this study was focused on the evolution of the outermost surface of the prepared samples, High Resolution Electron Backscattered Diffraction (HREBSD) was used, allowing for the analysis of the outermost 50 nm of the LTO layer. Diffraction data obtained by this technique, called Kikuchi patterns, are represented in figure 3.21. The fitting of the pattern corresponding to the pristine sample gave 99% of indexation reliability with

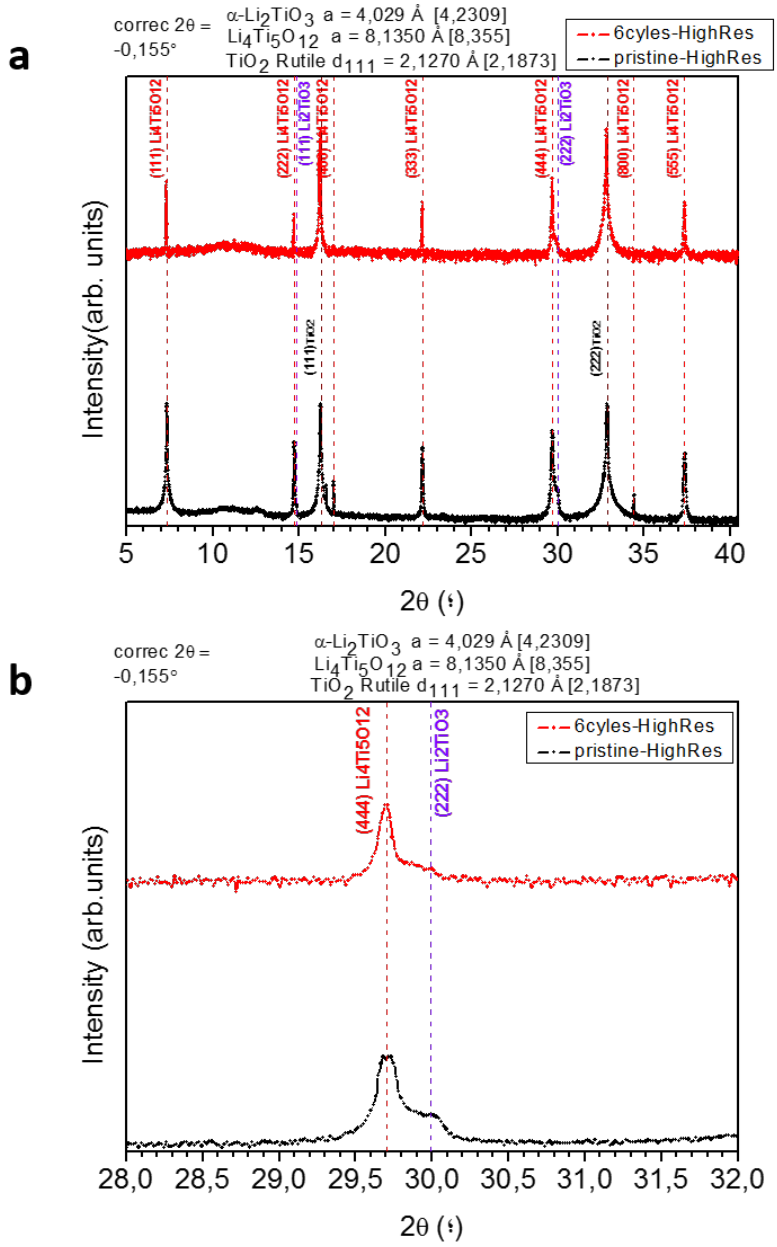

Figure 3.20: Comparison of the synchrotron XRD spectra corresponding to pristine and cycled sample (6 electrochemical cycles): full spectra (a); and, zoom of the $\alpha-Li_2TiO_3$ signal (b).

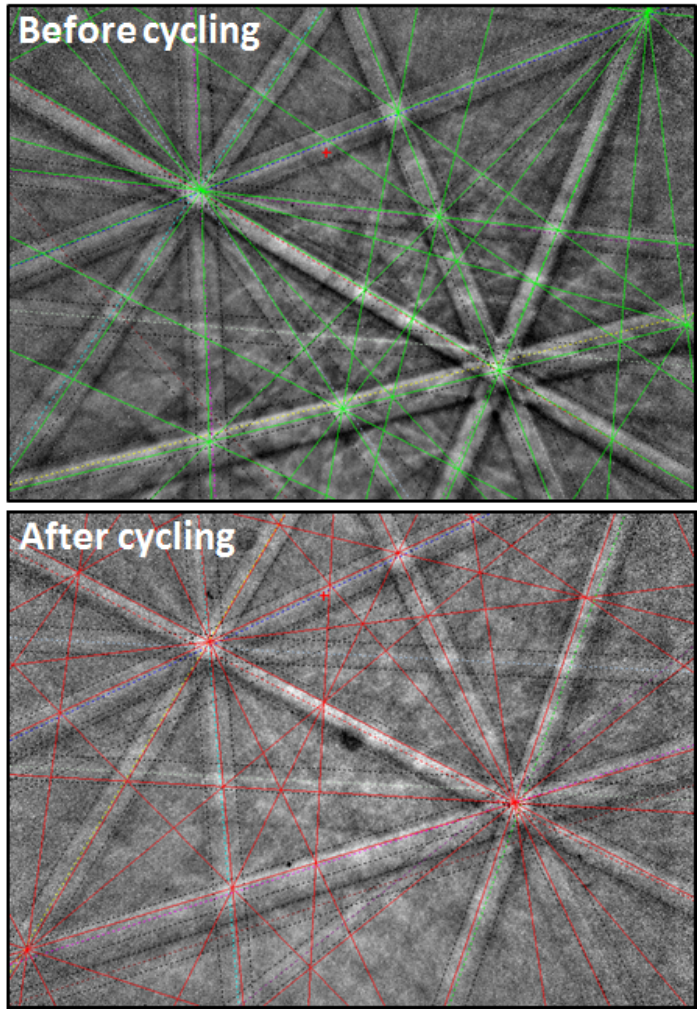

Figure 3.21: Comparison of the Kikuchi pattern obtained by HREBSD for the LTO pristine and cycled sample.

the LTO phase. After electrochemical cycles, the Kikuchi pattern did not change, matching again perfectly (99% reliability) with the expected spectra from LTO. In the results obtained by HREBSD, there was no trace of the $\alpha-Li_2TiO_3$ phase in any of the samples. This could be because the amount of $\alpha-Li_2TiO_3$ was below the detection limit of the technique.

To prove the presence and study the distribution of the $\alpha-Li_2TiO_3$ phase

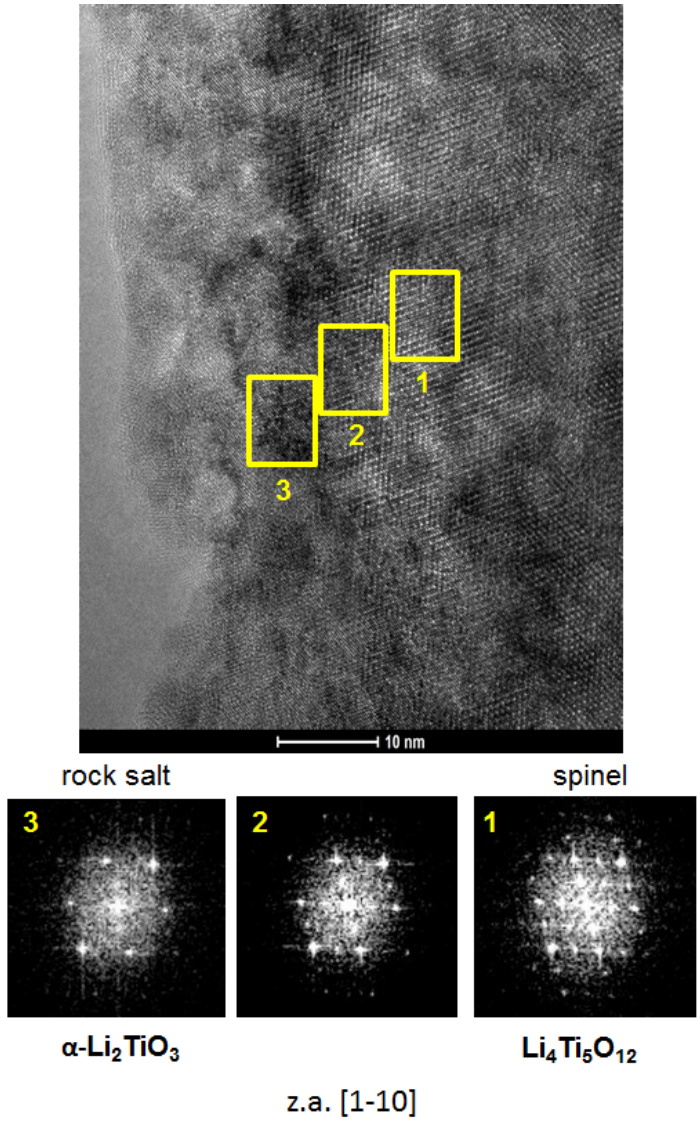

Figure 3.22: HRTEM image around the pristine LTO sample's surface obtained from the cross-section preparation. The three indicated areas (yellow squares) in the HRTEM presented different diffraction patterns as seen in the Fast Fourier Transforms (FFT) images at the bottom part of the figure.

in the synthesized sample, cross-section analysis was carried out by TEM. Images and diffraction were obtained by a FEI Tecnai G2 TEM instrument,

with a 200kV field emission gun. Sample preparation procedure has been already described in chapter 2.

Although $Li_4Ti_5O_{12}$ and $\alpha-Li_2TiO_3$ present different crystalline structures, Spinel and Rock-salt respectively, they have several interplanar distances in common. Thereby they have similar electron diffraction patterns with some particular diffraction specific for each crystal phase allowing to validate the presence of $\alpha-Li_2TiO_3$. As shown in figure 3.22, a difference on the crystal structure could be discerned at around 15 nm from the surface, which is the detection limit of HREBSD. When performing the Fourier Transform in the outermost area of the surface (first 10 nm), only the diffraction signal of a rock salt structure was observed suggesting the presence of the $\alpha-Li_2TiO_3$ phase. On the other hand, looking the diffraction in a deeper sample regions (around 20 nm), there was a good agreement with what was expected for $Li_4Ti_5O_{12}$ phase. The Fourier Transform in the intermediate region suggests a transition from one structure to the other.

The spatial phase transition is represented in figure 3.23. These images were obtained from a filtering procedure using masks in the FFTs. By means of these masks, it is possible to select one or several areas, and subsequently diffraction spots, in the diffraction patterns. Once the mask is over the spot of interest (i.e. the spot corresponding to an interplanar distance unique for the $\alpha-Li_2TiO_3$ or the LTO), the inverse of the FFT is computed and the result is an image in the real space only containing information about the family planes previously selected. Thus, the two images in figure 3.23 revealed the spatial distribution of two different phases. For the cases where those diffractions corresponding to $\alpha-Li_2TiO_3$ were present, area was colored in cyan. The areas containing only diffraction signal from LTO, were colored in red. These regions can overlap, white areas, representing the common diffractions for LTO and $\alpha-Li_2TiO_3$.

Therefore, from the filtered images in figure 3.23, the transition from $\alpha-Li_2TiO_3$ to $Li_4Ti_5O_{12}$ was confirmed, hence, demonstrating that $\alpha-Li_2TiO_3$ phase is a product of the synthesis and is not formed during the electrochemical cycling. Moreover, it was observed that $\alpha-Li_2TiO_3$ was present in approximately the first 15 nm from the surface. Thus, being such a superficial phase, the detection limit of HREBSD could not be excluded as the reason for the absence of $\alpha-Li_2TiO_3$ phase on the Kikuchi patterns.

Going back to HREBSD, besides the study of Kikuchi lines, the variation

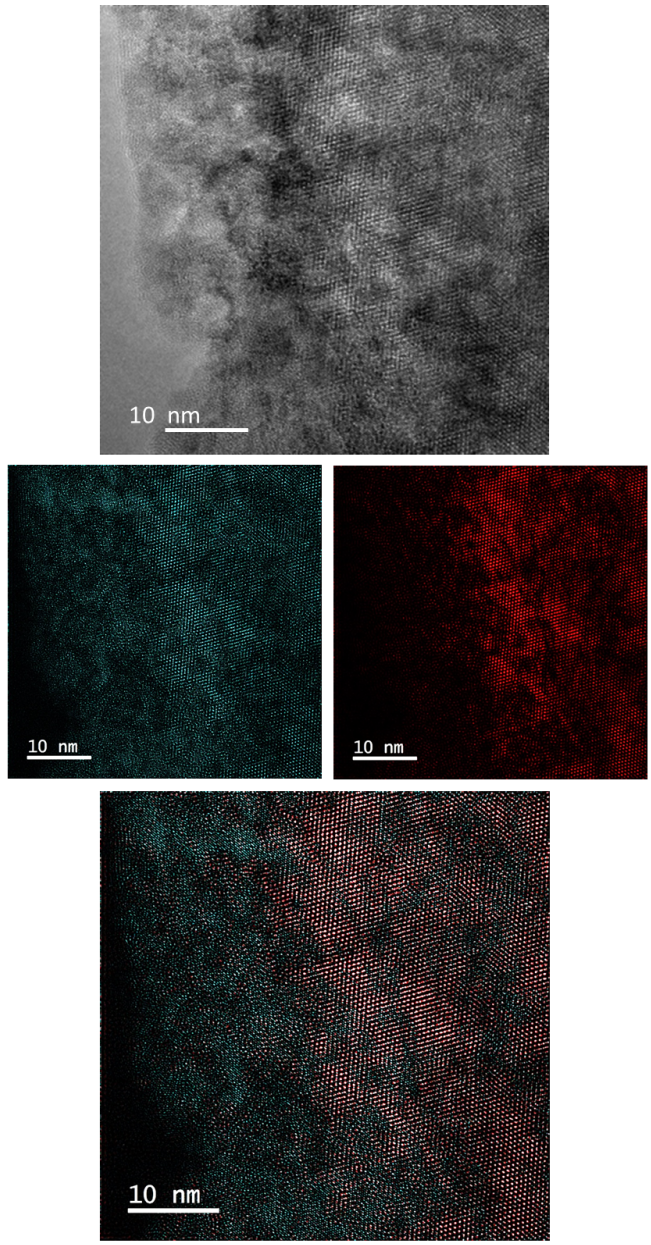

Figure 3.23: TEM image of the area analyzed for the pristine LTO sample (top); color representation of the area where each diffraction was detected (center), in cyan for $\alpha-Li_2TiO_3$ (left) and in red for LTO (right); and, distribution of each phase when adding both results (bottom).

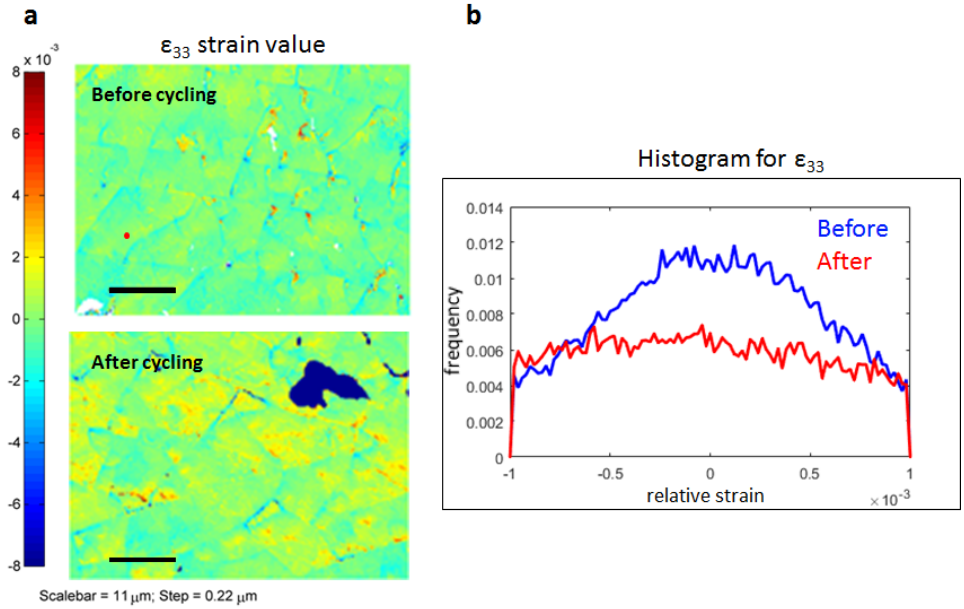

Figure 3.24: Surface normal strain (ϵ_{33}) evolution upon cycling. (a) Comparison of the ϵ_{33} value before and after cycling represented by color map of the scanned area. Values are relative to the reference point, indicated by the red spot. (b) Histogram comparing the ϵ_{33} value distribution before and after cycling.

of surface strain can be evaluated with this technique, before and after cycling. To do so, a reference point on the sample was chosen, the strain value was scanned in each point of the area analyzed and compared to this reference point. In the color map representation of the normal strain results (ϵ_{33} value of the strain tensor) presented in figure 3.24a, green would mean zero strain. Any color change implies strain variation; blue means compressive strain and red means tensile strain. Thus, a general tensile strain in normal direction (111 direction in this case) was present in the cycled sample, as a general color change towards yellowish was observed. This type of analysis is usually also represented by histograms (figure 3.24b), where relative strain value versus the occurrence frequency is represented. Before cycling, strain values gave a Gaussian-like curve centered around 0, indicating that almost all strain values were around zero. After cycling, however, there was a wider distribution of strain values, which, indeed, meant an overall increase of the non-zero strain values. Therefore, a significant increase of normal strain on the surface for the cycled LTO sample in comparison with the non-cycled one

was present, which could be related to the corrugation calculated by DFT that was mentioned in the introduction.

3.4 Conclusions

Micron-thick highly oriented LTO (111) layer was successfully synthesized, once initial problems related to Na contamination and substrate orientation were avoided. LTO layer was electrochemically cycled reversibly versus Li metal, in spite of the limitation of the system in terms of electronic conductivity, which was overcome via direct connection to the surface.

From the characterization carried out in pristine and cycled samples, by means of surface specific techniques, several conclusions related to the evolution of (111) surface on LTO material were obtained. From synchrotron XRD, it was concluded that no new crystalline phase is formed on the surface upon the electrochemical process. Besides, HREBSD results were in good agreement with this, since no change was detected from pristine to cycled sample in Kikuchi patterns. In particular, synchrotron XRD results suggested that $\alpha-Li_2TiO_3$ phase is present from the pristine sample, and, thus, is a product of the synthesis process.

Moreover, from cross-section TEM analysis of pristine LTO (111) layer, presence of $\alpha-Li_2TiO_3$ phase on the pristine sample was further confirmed, and it was delimited to the outermost 15 nm. Hence, the presence of $\alpha-Li_2TiO_3$ on pristine LTO sample was verified, confirming that it is formed during the synthesis process, and not during cycling as stated in previous studies.

Finally, a significant increase of normal strain on the surface for the cycled sample was measured by HREBSD, in comparison with the non-cycled one. This increase in strain could be related with the corrugation of the surface mentioned before, that was both calculated by DFT and detected experimentally by AFM in previous studies. Controlling the surface strain, particularly being present on the electrode-electrolyte interface, might help to improve even more the already good electrochemical properties of LTO material.

Bibliography

[1] J.M. Tarascon and M. Armand. Issues and challenges facing rechargeable lithium batteries. *Nature*, 414(6861):359-367, 2001.

[2] K. Ozawa. Lithium Ion Rechargeable Batteries: Materials, Technology and New Applications. John Wiley & Sons, 2012.

[3] O.K. Park, Y. Cho, S. Lee, H.C. Yoo, H.K. Song and J. Cho. Who will drive electric vehicles, olivine or spinel? *Energy & Environmental Science*, 4(5):1621-1633, 2011.

[4] F.T. Wagner, B. Lakshmanan and M.F. Mathias. Electrochemistry and the future of the automobile. *J. Phys. Chem. Lett*, 1(14):2204-2219, 2010.

[5] B. Dunn, H. Kamath and J.M. Tarascon. Electrical energy storage for the grid: a battery of choices. *Science*, 334(6058):928-935, 2011.

[6] Z. Yang, J. Zhang, M.C. Kintner-Meyer, X. Lu, D. Choi, J.P. Lemmon and J. Liu. Electrochemical energy storage for green grid. *Chemical Reviews*, 111(5):3577-3613, 2011.

[7] M.S. Whittingham. Ultimate limits to intercalation reactions for lithium batteries. *Chemical Reviews*, 114(23):11414-11443, 2014.

[8] N. Nitta, F. Wu, J.T. Lee and G. Yushin. Li-ion battery materials: present and future. *Materials Today*, 18(5):252-264, 2015.

[9] A. Deschanvres, B. Raveau and Z. Sekkal. Mise en evidence et etude cristallographique d'une nouvelle solution solide de type spinelle $Li_{1+x}Ti_{2-x}O_4$ $0 \leq x \leq 0.333$. *Materials Research Bulletin*, 6(8):699-704, 1971.

[10] D.C. Johnston. Superconducting and normal state properties of $Li_{1+x}Ti_{2-x}O_4$ spinel compounds. Preparation, crystallography, superconducting properties, electrical resistivity, dielectric behavior, and mag-

netic susceptibility. *Journal of Low Temperature Physics*, 25(1-2):145-175, 1976.

[11] K.M. Colbow, J.R. Dahn and R.R. Haering. Structure and electrochemistry of the spinel oxides $LiTi_2O_4$ and $Li_{4/3}Ti_{5/3}O_4$. *Journal of Power Sources*, 26(3-4):397-402, 1989.

[12] S. Scharner, W. Weppner and P. Schmid-Beurmann. Evidence of two-phase formation upon lithium insertion into the $Li_{1.33}Ti_{1.67}O_4$ spinel. *Journal of the Electrochemical Society*, 146(3):857-861, 1999.

[13] T. Ohzuku, A. Ueda and N. Yamamoto. Zero-strain insertion material of $Li[Li_{1/3}Ti_{5/3}]O_4$ for rechargeable lithium cells. *Journal of the Electrochemical Society*, 142(5):1431-1435, 1995.

[14] S. Panero, P. Reale, F. Ronci, B. Scrosati, P. Perfetti and V. Rossi-Albertini. Refined in-situ EDXD structural analysis of the $Li[Li_{1/3}Ti_{5/3}]O_4$ electrode under lithium insertion-extraction. *Physical Chemistry Chemical Physics*, 3(5):845-847, 2001.

[15] F. Ronci, P. Reale, B. Scrosati, S. Panero, V. Rossi-Albertini, P.Perfetti, M. Di Michiel and J.M. Merino. High-resolution in-situ structural measurements of the $Li_{4/3}Ti_{5/3}O_4$ zero-strain insertion material. *The Journal of Physical Chemistry B*, 106(12):3082-3086, 2002.

[16] M. Wagemaker, D.R. Simon, E.M. Kelder, J. Schoonman, C. Ringpfeil, U. Haake, D. Lützenkirchen-Hecht, R. Frahm and F.M. Mulder. A kinetic two-phase and equilibrium solid solution in spinel $Li_{4+x}Ti_5O_{12}$. *Advanced Materials*, 18(23):3169-3173, 2006.

[17] H. Wu, I. Belharouak, H. Deng, A. Abouimrane, Y.K. Sun and K. Amine. Development of $LiNi_{0.5}Mn_{1.5}O_4/Li_4Ti_5O_{12}$ system with long cycle life. *Journal of The Electrochemical Society*, 156(12):A1047-A1050, 2009.

[18] J. Haetge, P. Hartmann, K. Brezesinski, J. Janek and T. Brezesinski. Ordered large-pore mesoporous $Li_4Ti_5O_{12}$ spinel thin film electrodes with nanocrystalline framework for high rate rechargeable lithium batteries: relationships among charge storage, electrical conductivity, and nanoscale structure. *Chemistry of Materials*, 23(19):4384-4393, 2011.

[19] K. Zaghib, M. Dontigny, A. Guerfi, P. Charest, I. Rodrigues, A. Mauger and C.M. Julien. Safe and fast-charging Li-ion battery with long shelf life for power applications. *Journal of Power Sources*, 196(8):3949-3954, 2011.

[20] D. Peramunage and K.M. Abraham. Preparation of micron-sized $Li_4Ti_5O_{12}$ and its electrochemistry in polyacrylonitrile electrolyte-based lithium cells. *Journal of the Electrochemical Society*, 145(8):2609-2615, 1998.

[21] Z. Yang, D. Choi, S. Kerisit, K.M. Rosso, D. Wang, J. Zhang, G. Graff and J. Liu. Nanostructures and lithium electrochemical reactivity of Lithium Titanites and Titanium Oxides: A review. *Journal of Power Sources*, 192(2):588-598, 2009.

[22] J. B Goodenough. Energy storage materials: a perspective. *Energy Storage Materials*, 1:158-161, 2015.

[23] J. Christensen, V. Srinivasan and J. Newman. Optimization of lithium titanate electrodes for high-power cells. *Journal of The Electrochemical Society*, 153(3):A560-A565, 2006.

[24] A. Singhal, G. Skandan, G. Amatucci, F. Badway, N. Ye, A. Manthiram, H. Ye and J.J. Xu. Nanostructured electrodes for next generation rechargeable electrochemical devices. *Journal of Power Sources*, 129(1):38-44, 2004.

[25] K. Amine, I. Belharouak, Z. Chen, T. Tran, H. Yumoto, N. Ota, S.T. Myung and Y.K. Sun. Nanostructured anode material for high-power battery system in electric vehicles. *Advanced Materials*, 22(28):3052-3057, 2010.

[26] H.G. Jung, M.W. Jang, J. Hassoun, Y.K. Sun and B. Scrosati. A high-rate long-life $Li_4Ti_5O_{12}/Li[Ni_{0.45}Co_{0.1}Mn_{1.45]O_4}$ lithium-ion battery. *Nature Communications*, 2:516, 2011.

[27] J.B. Goodenough and K.S. Park. The Li-ion rechargeable battery: a perspective. *Journal of the American Chemical Society*, 135(4):1167-1176, 2013.

[28] Y.J. Hao, Q.Y Lai, J.Z. Lu, H.L. Wang, Y.D. Chen and X.Y. Ji. Synthesis and characterization of spinel $Li_4Ti_5O_{12}$ anode material by oxalic acid-assisted sol-gel method. *Journal of Power Sources*, 158(2):1358-1364, 2006.

[29] M. Ganesan, M.V.T. Dhananjeyan, K.B. Sarangapani and N.G. Renganathan. Solid state rapid quenching method to synthesize micron size $Li_4Ti_5O_{12}$. *Journal of Electroceramics*, 18(3-4):329-337, 2007.

[30] J. Kim and J. Cho. Spinel $Li_4Ti_5O_{12}$ nanowires for high-rate Li-ion intercalation electrode. *Electrochemical and Solid-State Letters*, 10(3):A81-A84, 2007.

[31] C. Jiang, E. Hosono, M. Ichihara, I. Honma and H. Zhou. Synthesis of nanocrystalline $Li_4Ti_5O_{12}$ by chemical lithiation of Anatase nanocrystals and postannealing. *Journal of The Electrochemical Society*, 155(8):A553-A556, 2008.

[32] E. Matsui, Y. Abe, M. Senna, A. Guerfi and K. Zaghib. Solid-state synthesis of 70 nm $Li_4Ti_5O_{12}$ particles by mechanically activating intermediates with amino acids. *Journal of the American Ceramic Society*, 91(5):1522-1527, 2008.

[33] A.S. Prakash, P. Manikandan, K. Ramesha, M. Sathiya, J.M. Tarascon and A.K. Shukla. Solution-combustion synthesized nanocrystalline $Li_4Ti_5O_{12}$ as high-rate performance Li-ion battery anode. *Chemistry of Materials*, 22(9):2857-2863, 2010.

[34] Junjie Huang and Zhiyu Jiang. The synthesis of hollow spherical $Li_4Ti_5O_{12}$ by macroemulsion method and its application in Li-ion batteries. *Electrochemical and Solid-State Letters*, 11(7):A116-A118, 2008.

[35] S.L. Chou, J.Z. Wang, H.K. Liu and S.X. Dou. Rapid synthesis of $Li_4Ti_5O_{12}$ microspheres as anode materials and its binder effect for Lithium-ion battery. *The Journal of Physical Chemistry C*, 115(32):16220-16227, 2011.

[36] L. Shen, E. Uchaker, X. Zhang and G. Cao. Hydrogenated $Li_4Ti_5O_{12}$ nanowire arrays for high rate Lithium-ion batteries. *Advanced Materials*, 24(48):6502-6506, 2012.

[37] L. Yu, H.B. Wu and X.W. Lou. Mesoporous $Li_4Ti_5O_{12}$ hollow spheres with enhanced lithium storage capability. *Advanced Materials*, 25(16):2296-2300, 2013.

[38] S. Zhao, O.Ka, X. Xian, L. Sun and Jing Wang. Effect of primary crystallite size on the high-rate performance of $Li_4Ti_5O_{12}$ microspheres. *Electrochimica Acta*, 206:17-25, 2016.

[39] Z. Ding, L. Zhao, L. Suo, Y. Jiao, S. Meng, Y.S. Hu, Z. Wang and L. Chen. Towards understanding the effects of carbon and nitrogen-doped carbon coating on the electrochemical performance of $Li_4Ti_5O_{12}$ in Lithium-ion batteries: a combined experimental and theoretical study. *Physical Chemistry Chemical Physics*, 13(33):15127-15133, 2011.

[40] L. Zhao, Y.S. Hu, H. Li, Z. Wang and L. Chen. Porous $Li_4Ti_5O_{12}$ coated with N-doped carbon from ionic liquids for Li-ion batteries. *Advanced Materials*, 23(11):1385-1388, 2011.

[41] L. Shen, X. Zhang, E. Uchaker, C. Yuan and G. Cao. $Li_4Ti_5O_{12}$ nanoparticles embedded in a mesoporous carbon matrix as a superior anode material for high rate Lithium-ion batteries. *Advanced Energy Materials*, 2(6):691-698, 2012.

[42] Y.Q. Wang, L. Gu, Y.G. Guo, H. Li, X.Q. He, S. Tsukimoto, Y. Ikuhara and L.J. Wan. Rutile-TiO_2 nanocoating for a high-rate $Li_4Ti_5O_{12}$ anode of a Lithium-ion battery. *Journal of the American Chemical Society*, 134(18):7874-7879, 2012.

[43] C.H. Chen, J.T. Vaughey, A.N. Jansen, D.W. Dees, A.J. Kahaian, T. Goacher and M.M. Thackeray. Studies of Mg-substituted $Li_{4-x}Mg_xTi_5O_{12}$ spinel electrodes ($0 < x < 1$) for lithium batteries. *Journal of the Electrochemical Society*, 148(1):A102-A104, 2001.

[44] K.S. Park, A. B., D.J. Kang and S.G. Doo. Nitridation-driven conductive $Li_4Ti_5O_{12}$ for Lithium-ion batteries. *Journal of the American Chemical Society*, 130(45):14930-14931, 2008.

[45] H. Zhao, Y. Li, Z. Zhu, J. Lin, Z. Tian and R. Wang. Structural and electrochemical characteristics of $Li_{4-x}Al_xTi_5O_{12}$ as anode material for Lithium-ion batteries. *Electrochimica Acta*, 53(24):7079-7083, 2008.

[46] J. Shu. Study of the interface between $Li_4Ti_5O_{12}$ electrodes and standard electrolyte solutions in 0.0-5.0 V. *Electrochemical and Solid-State Letters*, 11(12):A238-A240, 2008.

[47] L. El-Ouatani, R. Dedryvere, C. Siret, P. Biensan and D. Gonbeau. Effect of Vinylene Carbonate additive in Li-ion batteries: Comparison of $LiCoO_2/c$, $LiFepO_4/c$ and $LiCoO_2/Li_4Ti_5O_{12}$ systems. *Journal of The Electrochemical Society*, 156(6):A468-A477, 2009.

[48] R. Dedryvere, D. Foix, S. Franger, S. Patoux, L. Daniel and D. Gonbeau. Electrode/electrolyte interface reactivity in high-voltage spinel $LiMn_{1.6}Ni_{0.4}O_4/Li_4Ti_5O_{12}$ Lithium-ion battery. *The Journal of Physical Chemistry C*, 114(24):10999-11008, 2010.

[49] Y.B. He, B. Li, M. Liu, C. Zhang, W. Lv, C. Yang, J. Li, H. Du, B. Zhang, Q.H. Yang. Gassing in $Li_4Ti_5O_{12}$-based batteries and its remedy. *Scientific Reports*, 2:913, 2012.

[50] Y.B. He, F. Ning, B. Li, Q.S. Song, W. Lv, H. Du, D. Zhai, F. Su, Q.H. Yang and F. Kang. Carbon coating to suppress the reduction decomposition of electrolyte on the $Li_4Ti_5O_{12}$ electrode. *Journal of Power Sources*, 202:253-261, 2012.

[51] I. Belharouak, G.M. Koenig, T. Tan, H. Yumoto, N. Ota and K. Amine. Performance degradation and gassing of $Li_4Ti_5O_{12}/LiMn_2O_4$ Lithium-ion cells. *Journal of The Electrochemical Society*, 159(8):A1165-A1170, 2012.

[52] V. Borgel, G. Gershinsky, T. Hu, M.G. Theivanayagam and D. Aurbach. $LiMn_{0.8}Fe_{0.2}PO_4/Li_4Ti_5O_{12}$, a possible Li-ion battery system for load-leveling application. *Journal of The Electrochemical Society*, 160(4):A650-A657, 2013.

[53] Y.B. He, M. Liu, Z.D. Huang, B. Zhang, Y. Yu, B. Li, F. Kang and J.K. Kim. Effect of Solid Electrolyte Interface (SEI) film on cyclic performance of $Li_4Ti_5O_{12}$ anodes for Li-ion batteries. *Journal of Power Sources*, 239:269-276, 2013.

[54] T. Nordh, R. Younesi, D. Brandell and K. Edström. Depth profiling the Solid Electrolyte Interphase on Lithium Titanate ($Li_4Ti_5O_{12}$) using synchrotron-based Photoelectron Spectroscopy. *Journal of Power Sources*, 294:173-179, 2015.

[55] J.B. Gieu, C. Courrèges, L. El-Ouatani, C. Tessier and H. Martinez. Temperature effects on $Li_4Ti_5O_{12}$ electrode/electrolyte interfaces at the first cycle: A X-ray Photoelectron Spectroscopy and Scanning Auger Microscopy study. *Journal of Power Sources*, 318:291-301, 2016.

[56] M. Kitta, T. Akita, Y. Maeda and M. Kohyama. Study of surface reaction of spinel $Li_4Ti_5O_{12}$ during the first lithium insertion and extraction processes using Atomic Force Microscopy and analytical Transmission Electron Microscopy. *Langmuir*, 28(33):12384-12392, 2012.

[57] M. Kitta, T. Akita, Y. Maeda and M. Kohyama. Preparation of a spinel $Li_4Ti_5O_{12}$ (111) surface from a Rutile TiO_2 single crystal. *Applied Surface Science*, 258(7):3147-3151, 2012.

[58] T.L. Barr and S. Seal. Nature of the use of adventitious carbon as a binding energy standard. *Journal of Vacuum Science & Technology A: Vacuum, Surfaces, and Films*, 13(3):1239-1246, 1995.

[59] P. Swift. Adventitious carbon-the panacea for energy referencing? *Surface and Interface Analysis*, 4(2):47-51, 1982.

[60] R.J. Ward and B.J. Wood. A comparison of experimental and theoretically derived sensitivity factors for XPS. *Surface and Interface Analysis*, 18(9):679-684, 1992.

[61] J. Chastain, R.C. King and J.F. Moulder. Handbook of X-ray Photoelectron Spectroscopy: a reference book of standard spectra for identification and interpretation of XPS data. Physical Electronics Eden Prairie, MN, 1995.

[62] J.F. Moulder, W.F. Stickle, P.E. Sobol and K.D. Bomben. Handbook of X-ray Photoelectron Spectroscopy. Perkin Elmer corporation, physical electronic division, USA. Technical Report, ISBN 0-9627026-2-5, 1992.

[63] G. Beamson, D. Briggs, et-al. High resolution XPS of organic polymers. Wiley, 1992.

[64] M.C. Biesinger, L.W.M. Lau, A.R. Gerson and R.S.C. Smart. Resolving surface chemical states in XPS analysis of first row transition metals, oxides and hydroxides: Sc, Ti, V, Cu and Zn. *Applied Surface Science*, 257(3):887-898, 2010.

[65] C. Kim, N.S. Norberg, C.T. Alexander, R. Kostecki and J. Cabana. Mechanism of phase propagation during lithiation in carbon-free $Li_4Ti_5O_{12}$ battery electrodes. *Advanced Functional Materials*, 23(9):1214-1222, 2013.

[66] M.G. Verde, L. Baggetto, N. Balke, G.M. Veith, J.K. Seo, Z. Wang and Y.S. Meng. Elucidating the phase transformation of $Li_4Ti_5O_{12}$ lithiation at the nanoscale. *ACS Nano*, 10(4):4312-4321, 2016.

[67] C. Lai, Y.Y. Dou, X. Li and X.P. Gao. Improvement of the high rate capability of hierarchical structured $Li_4Ti_5O_{12}$ induced by the pseudocapacitive effect. *Journal of Power Sources*, 195(11):3676-3679, 2010.

Bibliography

[1] H.M. Wu, I. Belharouak, H. Deng, A. Abouimrane, Y.K. Sun and K. Amine. Development of $LiNi_{0.5}Mn_{1.5}O_4/Li_4Ti_5O_{12}$ system with long cycle life. *Journal of The Electrochemical Society*, 156(12):A1047-A1050, 2009.

[2] J. Haetge, P. Hartmann, K. Brezesinski, J. Janek and T. Brezesinski. Ordered large-pore mesoporous $Li_4Ti_5O_{12}$ spinel thin film electrodes with nanocrystalline framework for high rate rechargeable lithium batteries: relationships among charge storage, electrical conductivity, and nanoscale structure. *Chemistry of Materials*, 23(19):4384-4393, 2011.

[3] K. Zaghib, M. Dontigny, A. Guerfi, P. Charest, I. Rodrigues, A. Mauger, and C.M.Julien. Safe and fast-charging Li-ion battery with long shelf life for power applications. *Journal of Power Sources*, 196(8):3949-3954, 2011.

[4] T. Ohzuku, A. Ueda and N. Yamamoto. Zero-strain insertion material of $Li[Li_{1/3}Ti_{5/3}]O_4$ for rechargeable lithium cells. *Journal of the Electrochemical Society*, 142(5):1431-1435, 1995.

[5] F. Ronci, P. Reale, B. Scrosati, S. Panero, V. Rossi-Albertini, P. Perfetti, M. Di-Michiel and J.M. Merino. High-resolution in-situ structural measurements of the $Li_{4/3}Ti_{5/3}O_4$ zero-strain insertion material. *The Journal of Physical Chemistry B*, 106(12):3082-3086, 2002.

[6] M. Wagemaker, D.R. Simon, E.M. Kelder, J. Schoonman, C. Ringpfeil, U. Haake, D. Lützenkirchen-Hecht, R. Frahm and F.M. Mulder. A kinetic two-phase and equilibrium solid solution in spinel $Li_4Ti_5O_{12}$. *Advanced Materials*, 18(23):3169-3173, 2006.

[7] J. Shu. Study of the interface between $Li_4Ti_5O_{12}$ electrodes and standard electrolyte solutions in 0.0-5.0 V. *Electrochemical and Solid-State Letters*, 11(12):A238-A240, 2008.

[8] Y.B. He, M. Liu, Z.D. Huang, B. Zhang, Y. Yu, B. Li, F. Kang and J.K. Kim. Effect of Solid Electrolyte Interface (SEI) film on cyclic performance of $Li_4Ti_5O_{12}$ anodes for Li-ion batteries. *Journal of power sources*, 239:269-276, 2013.

[9] M.S. Song, R.H. Kim, S.W. Baek, K.S. Lee, K. Park and A. Benayad. Is $Li_4Ti_5O_{12}$ a Solid Electrolyte Interphase-free electrode material in Li-ion batteries? reactivity between the $Li_4Ti_5O_{12}$ electrode and electrolyte. *Journal of Materials Chemistry A*, 2(3):631-636, 2014.

[10] T. Nordh, R. Younesi, D. Brandell and K. Edström. Depth profiling the Solid Electrolyte Interphase on Lithium Titanate ($Li_4Ti_5O_{12}$) using synchrotron-based Photoelectron Spectroscopy. *Journal of Power Sources*, 294:173-179, 2015.

[11] R. Dedryvere, D. Foix, S. Franger, S. Patoux, L. Daniel and D. Gonbeau. Electrode/electrolyte interface reactivity in high-voltage spinel $LiMn_{1.6}Ni_{0.4}O_4/Li_4Ti_5O_{12}$ Lithium-ion battery. *The Journal of Physical Chemistry C*, 114(24):10999–11008, 2010.

[12] I. Belharouak, G.M. Koenig, T. Tan, H. Yumoto, N. Ota and K. Amine. Performance degradation and gassing of $Li_4Ti_5O_{12}/LiMn_2O_4$ Lithium-ion cells. *Journal of The Electrochemical Society*, 159(8):A1165-A1170, 2012.

[13] V. Borgel, G. Gershinsky, T. Hu, M.G. Theivanayagam and D. Aurbach. $LiMn_{0.8}Fe_{0.2}PO_4/Li_4Ti_5O_{12}$, a possible Li-ion battery system for load-leveling application. *Journal of The Electrochemical Society*, 160(4):A650-A657, 2013.

[14] J. Gao, B. Gong, Q. Zhang, G. Wang, Y. Dai, and W. Fan. Study of the surface reaction mechanism of $Li_4Ti_5O_{12}$ anode for Lithium-ion cells. *Ionics*, 21(9):2409-2416, 2015.

[15] T. Nordh, R. Younesi, M. Hahlin, R.F. Duarte, C. Tengstedt, D. Brandell and K. Edstrom. Manganese in the SEI layer of $Li_4Ti_5O_{12}$ studied by combined NEXAFS and HAXPES techniques. *The Journal of Physical Chemistry C*, 120(6):3206-3213, 2016.

[16] J.B. Gieu, C. Courrèges, L. El-Ouatani, C. Tessier and H. Martinez. Temperature effects on $Li_4Ti_5O_{12}$ electrode/electrolyte interfaces at the first cycle: A X-ray Photoelectron Spectroscopy and Scanning Auger Microscopy study. *Journal of Power Sources*, 318:291-301, 2016.

[17] L. El-Ouatani, R. Dedryvere, C. Siret, P. Biensan and D. Gonbeau. Effect of Vinylene Carbonate additive in Li-ion batteries: Comparison of $LiCoO_2/C$, $LiFePO_4/C$, and $LiCoO_2/Li_4Ti_5O_{12}$ systems. *Journal of The Electrochemical Society*, 156(6):A468-A477, 2009.

[18] J.B. Gieu, C. Courrèges, L. El-Ouatani, C. Tessier and H. Martinez. Influence of Vinylene Carbonate additive on the $Li_4Ti_5O_{12}$ electrode/electrolyte interface for Lithium-ion batteries. *Journal of The Electrochemical Society*, 164(6):A1314-A1320, 2017.

[19] D. Brandell, F. Jeschull, T. Nordh, R. Younesi, K. Edström, C. Tengstedt and T. Kocak. Different shades of $Li_4Ti_5O_{12}$ composites: The impact of the binder on interface layer formation. *ChemElectroChem*, 4:2683-2692, 2017.

[20] Z. Ding, L. Zhao, L. Suo, Y. Jiao, S. Meng, Y.S. Hu, Z. Wang and L. Chen. Towards understanding the effects of carbon and nitrogen-doped carbon coating on the electrochemical performance of $Li_4Ti_5O_{12}$ in Lithium-ion batteries: a combined experimental and theoretical study. *Physical Chemistry Chemical Physics*, 13(33):15127-15133, 2011.

[21] L. Zhao, Y.S. Hu, H. Li, Z. Wang and L. Chen. Porous $Li_4Ti_5O_{12}$ coated with N-doped carbon from ionic liquids for Li-ion batteries. *Advanced Materials*, 23(11):1385-1388, 2011.

[22] L. Shen, X. Zhang, E. Uchaker, C. Yuan and G. Cao. $Li_4Ti_5O_{12}$ nanoparticles embedded in a mesoporous carbon matrix as a superior anode material for high rate Lithium-ion batteries. *Advanced Energy Materials*, 2(6):691-698, 2012.

[23] C. Kim, N.S. Norberg, C.T. Alexander, R. Kostecki and J. Cabana. Mechanism of phase propagation during lithiation in carbon-free $Li_4Ti_5O_{12}$ battery electrodes. *Advanced Functional Materials*, 23(9):1214-1222, 2013.

[24] Y.B. He, B. Li, M. Liu, C. Zhang, W. Lv, C. Yang, J. Li, H. Du, B. Zhang, Q.H. Yang. Gassing in $Li_4Ti_5O_{12}$-based batteries and its remedy. *Scientific Reports*, 2:913, 2012.

[25] Y.B. He, F. Ning, B. Li, Q.S. Song, W. Lv, H. Du, D. Zhai, F. Su, Q.H. Yang and F. Kang. Carbon coating to suppress the reduction decomposition of electrolyte on the $Li_4Ti_5O_{12}$ electrode. *Journal of Power Sources*, 202:253-261, 2012.

[26] J. Cho, Y.J. Kim, T.J. Kim and B. Park. Zero-strain intercalation cathode for rechargeable Li-ion cell. *Angewandte Chemie International Edition*, 40(18):3367-3369, 2001.

[27] J.S. Kim, C.S. Johnson, J.T. Vaughey, S.A. Hackney, K.A. Walz, W.A. Zeltner, M.A. Anderson and M.M. Thackeray. The electrochemical stability of spinel electrodes coated with ZrO_2, Al_2O_3 and SiO_2 from colloidal suspensions. *Journal of The Electrochemical Society*, 151(10):A1755-A1761, 2004.

[28] L.J. Fu, H. Liu, C. Li, Y.P. Wu, E. Rahm, R. Holze and H.Q. Wu. Surface modifications of electrode materials for Lithium-ion batteries. *Solid State Sciences*, 8(2):113-128, 2006.

[29] N. Nitta, F. Wu, J.T. Lee and G. Yushin. Li-ion battery materials: present and future. *Materials today*, 18(5):252-264, 2015.

[30] J. Cho, Y.J. Kim and B. Park. Novel $LiCoO_2$ cathode material with Al_2O_3 coating for a Li-ion cell. *Chemistry of Materials*, 12(12):3788–3791, 2000.

[31] Lijun Liu, Liquan Chen, Xuejie Huang, Xiao-Qing Yang, Won-Sub Yoon, HS Lee, and James McBreen. Electrochemical and in situ synchrotron XRD studies on Al_2O_3-coated $LiCoO_2$ cathode material. *Journal of The Electrochemical Society*, 151(9):A1344-A1351, 2004.

[32] Y.S. Jung, A.S. Cavanagh, A.C. Dillon, M.D. Groner, S.M. George and S.H. Lee. Enhanced stability of $LiCoO_2$ cathodes in Lithium-ion batteries using surface modification by Atomic Layer Deposition. *Journal of The Electrochemical Society*, 157(1):A75-A81, 2010.

[33] J. Liu and A. Manthiram. Understanding the improvement in the electrochemical properties of surface modified 5 V $LiMn_{1.42}Ni_{0.42}Co_{0.16}O_4$ spinel cathodes in Lithium-ion cells. *Chemistry of Materials*, 21(8):1695-1707, 2009.

[34] L. Baggetto, N.J. Dudney and G.M. Veith. Surface chemistry of metal oxide coated Lithium Manganese Nickel oxide thin film cathodes studied by XPS. *Electrochimica Acta*, 90:135-147, 2013.

[35] S.Y. Kim and Y. Qi. Property evolution of Al_2O_3 coated and uncoated Si electrodes: A first principles investigation. *Journal of The Electrochemical Society*, 161(11):F3137-F3143, 2014.

[36] T. Feng, Y. Xu, Z. Zhang, X. Du, X. Sun, L. Xiong, R. Rodriguez and R. Holze. Low-cost Al_2O_3 coating layer as a preformed SEI on natural graphite powder to improve coulombic efficiency and high-rate cycling stability of Lithium-ion batteries. *ACS Applied Materials & Interfaces*, 8(10):6512-6519, 2016.

[37] D. Ahn and X. Xiao. Extended Tithium titanate cycling potential window with near zero capacity loss. *Electrochemistry Communications*, 13(8):796-799, 2011.

[38] Y. Wang, W. Zou, Z. Huang and J. Li. Al_2O_3 coated $Li_4Ti_5O_{12}$ electrode with enhanced cycle performance for Lithium-ion battery. *ECS Transactions*, 59(1):35-43, 2014.

[39] Y.S. Jung, A.S. Cavanagh, L.A. Riley, S.H. Kang, A.C. Dillon, M.D. Groner, S.M. George and S.H. Lee. Ultrathin direct Atomic Layer Deposition on composite electrodes for highly durable and safe Li-ion batteries. *Advanced Materials*, 22(19):2172-2176, 2010.

[40] Y. Kim, N.J. Dudney, M. Chi, S.K. Martha, J. Nanda, G.M. Veith and C. Liang. A perspective on coatings to stabilize high-voltage cathodes: $LiMn_{1.5}Ni_{0.5}O_4$ with sub-nanometer LiPON cycled with $LiPF_6$ electrolyte. *Journal of The Electrochemical Society*, 160(5):A3113-A3125, 2013.

[41] G. Tan, F. Wu, L. Li, R. Chen and S. Chen. Coralline glassy lithium phosphate-coated $LiFePO_4$ cathodes with improved power capability for Lithium-ion batteries. *The Journal of Physical Chemistry C*, 117(12):6013-6021, 2013.

[42] X. Dai, A. Zhou, J. Xu, B. Yang, L. Wang and J. Li. Superior electrochemical performance of $LiCoO_2$ electrodes enabled by conductive Al_2O_3-doped ZnO coating via magnetron sputtering. *Journal of Power Sources*, 298:114-122, 2015.

[43] J.E. Greene. Tracing the recorded history of thin-film sputter deposition: From the 1800s to 2017. *Journal of Vacuum Science & Technology A: Vacuum, Surfaces and Films*, 35(5):05C204, 2017.

[44] S. Hao and C. Wolverton. Lithium transport in amorphous Al_2O_3 and AlF_3 for discovery of battery coatings. *The Journal of Physical Chemistry C*, 117(16):8009-8013, 2013.

[45] L. Baggetto, R.R. Unocic, N.J. Dudney and G.M. Veith. Fabrication and characterization of Li-Mn-Ni-O sputtered thin film high voltage cathodes for Li-ion batteries. *Journal of Power Sources*, 211:108-118, 2012.

[46] C.L. Wang, Y.C. Liao, F.C. Hsu, N.H. Tai and M.K. Wu. Preparation and characterization of thin film $Li_4Ti_5O_{12}$ electrodes by magnetron sputtering. *Journal of The Electrochemical Society*, 152(4):A653-A657, 2005.

[47] F. Wunde, F. Berkemeier and G. Schmitz. Lithium diffusion in sputter-deposited $Li_4Ti_5O_{12}$ thin films. *Journal of Power Sources*, 215:109–115, 2012.

[48] Z. Yu, G. Zhu, H. Xu and A. Yu. Amorphous $Li_4Ti_5O_{12}$ thin film with enhanced lithium storage capability and reversibility for lithium-ion batteries. *Energy Technology*, 2(9-10):767-772, 2014.

[49] A. Kumatani, S.Shiraki, Y. Takagi, T. Suzuki, T. Ohsawa, X. Gao, Y. Ikuhara and T. Hitosugi. Epitaxial growth of $Li_4Ti_5O_{12}$ thin films using RF magnetron sputtering. *Japanese Journal of Applied Physics*, 53(5):058001, 2014.

[50] Z.Z. Yu, H.R. Xu, G.S. Zhu and A.B. Yu. Preparation and characterisation of porous Lithium Titanate thin film by magnetron sputtering. *Materials Research Innovations*, 19(sup9):S9-302, 2015.

[51] S.Y. Tsai, K.Z. Fung and C.-T. Ni. Conductivity enhancement and thin-film processing of $Li_4Ti_5O_{12}$ (LTO) spinel for Li battery applications. *ECS Transactions*, 68(2):37-43, 2015.

[52] S. Özen, V. Şenay, S. Pat, and Şadan Korkmaz. Optical, morphological properties and surface energy of the transparent $Li_4Ti_5O_{12}$ (LTO) thin film as anode material for secondary type batteries. *Journal of Physics D: Applied Physics*, 49(10):105303, 2016.

[53] M.G. Verde, L. Baggetto, N. Balke, G.M. Veith, J.K. Seo, Z. Wang and Y.S. Meng. Elucidating the phase transformation of $Li_4Ti_5O_{12}$ lithiation at the nanoscale. *ACS Nano*, 10(4):4312-4321, 2016.

[54] M. Hirayama, K. Kim, T. Toujigamori, W. Cho and Ryoji K. Epitaxial growth and electrochemical properties of $Li_4Ti_5O_{12}$ thin-film lithium battery anodes. *Dalton Transactions*, 40(12):2882-2887, 2011.

[55] J. Deng, Z. Lu, C.Y. Chung, X. Han, Z. Wang and H. Zhou. Electrochemical performance and kinetic behavior of lithium ion in $Li_4Ti_5O_{12}$ thin film electrodes. *Applied Surface Science*, 314:936-941, 2014.

[56] P. Schichtel, M. Geiß, T. Leichtweiß, J. Sann, D.A. Weber and J. Janek. On the impedance and phase transition of thin film all-solid-state batteries based on the $Li_4Ti_5O_{12}$ system. *Journal of Power Sources*, 360:593-604, 2017.

[57] J. Xie, P.P. Harks, D. Li, L. Raijmakers and P. Notten. Planar and 3D deposition of $Li_4Ti_5O_{12}$ thin film electrodes by MOCVD. *Solid State Ionics*, 287:83-88, 2016.

[58] N. Li, T. Katase, Y. Zhu, T. Matsumoto, T. Umemura, Y. Ikuhara and H Ohta. Solid-liquid phase epitaxial growth of $Li_4Ti_5O_{12}$ thin film. *Applied Physics Express*, 9(12):125501, 2016.

[59] S. Leroy, F. Blanchard, R. Dedryvere, H. Martinez, B. Carré, D. Lemordant and D. Gonbeau. Surface film formation on a Graphite electrode in Li-ion batteries: AFM and XPS study. *Surface and Interface Analysis*, 37(10):773-781, 2005.

[60] L. El-Ouatani, R. Dedryvère, J.B. Ledeuil, C. Siret, P. Biensan, J. Desbrières and D. Gonbeau. Surface film formation on a carbonaceous electrode: Influence of the binder chemistry. *Journal of Power Sources*, 189(1):72-80, 2009.

[61] T.L. Barr and S. Seal. Nature of the use of adventitious carbon as a binding energy standard. *Journal of Vacuum Science & Technology A: Vacuum, Surfaces and Films*, 13(3):1239-1246, 1995.

[62] L. Castro, R. Dedryvère, J.B. Ledeuil, J. Bréger, C. Tessier and D. Gonbeau. Aging mechanisms of $LiFePO_4$/Graphite cells studied by XPS: redox reaction and electrode/electrolyte interfaces. *Journal of the Electrochemical Society*, 159(4):A357-A363, 2012.

[63] S.W. Gaarenstroom, A.V. Naumkin, A. Kraut-Vass and C.J. Powell. NIST X-ray Photoelectron Spectroscopy database. *https://srdata.nist.gov/xps/Default.aspx*.

[64] B. Simon and J.P. Boeuve. Rechargeable lithium electrochemical cell, May 6 1997. US Patent 5,626,981.

[65] X. Zhang, R. Kostecki, T.J. Richardson, J.K. Pugh and P.N. Ross. Electrochemical and infrared studies of the reduction of organic carbonates. *Journal of The Electrochemical Society*, 148(12):A1341-A1345, 2001.

[66] J. Chastain, R.C. King and J.F. Moulder. *Handbook of X-ray Photoelectron Spectroscopy: a reference book of standard spectra for identification and interpretation of XPS data.* Physical Electronics Eden Prairie, MN, 1995.

[67] J.F. Moulder, W.F. Stickle, P.E. Sobol and K.D. Bomben. Handbook of X-ray Photoelectron Spectroscopy, Perkin Elmer corporation, physical electronic division, USA. Technical Report, ISBN 0-9627026-2-5, 1992.

[68] S.-T. Myung, K. Amine and Y.-K. Sun. Surface modification of cathode materials from nano to microscale for rechargeable Lithium-ion batteries. *Journal of Materials Chemistry*, 20(34):7074-7095, 2010.

[69] R.J. Ward and B.J. Wood. A comparison of experimental and theoretically derived sensitivity factors for XPS. *Surface and Interface Analysis*, 18(9):679-684, 1992.

[70] M.C. Biesinger, L.W. Lau, A.R. Gerson and R.C. Smart. Resolving surface chemical states in XPS analysis of first row transition metals, oxides and hydroxides: Sc, Ti, V, Cu and Zn. *Applied Surface Science*, 257(3):887-898, 2010.

[71] S. Scharner, W. Weppner and P. Schmid-Beurmann. Evidence of two-phase formation upon lithium insertion into the $Li_{1.33}Ti_{1.67}O_4$ spinel. *Journal of the Electrochemical Society*, 146(3):857-861, 1999.

Chapter 5

Optimization of sputter deposited thin-film LNMO electrode & sputterability study of ceramic solid electrolyte

5.1 Introduction

$LiCoO_2$ (LCO) transition metal oxide [1], introduced by Goodenough in 1980, was the active material in the positive electrode for the first Li-ion batteries commercialized by SONY in 1991 [2]. Since then, it has widely been used in commercial Li-ion batteries, being its success nested in the compromise between high theoretical capacity (274 mAh/g), low self-discharge and good cycling performance [3]. Nonetheless, the scarcity and high cost of cobalt [4, 5], as well as the low thermal stability [6] and fast capacity fade of LCO at high current rates or deep cycling [7], pushed the scientific community to search for alternative materials. During the last years, research was oriented to tackle several key issues related to cathode materials, such as cost reduction, availability of raw materials, environmental impact, higher energy density and improved safety [8, 9]. Nowadays, a variety of compounds are present as active material on the positive electrode in the battery market, which can be classified based on their crystallographic structure in layered, olivine and spinels. Layered oxides referred as NMC [4, 10, 11] and NCA [5, 11] ($LiNi_{1/3}Mn_{1/3}Co_{1/3}O_2$ and $LiNi_{0.8}Co_{0.15}Al_{0.05}O_2$ in the most typical compositions respectively) are some of the most known. Indeed they were chosen by

Tesla company for their home storage system and electric vehicle (EV). These materials attracted the attention due to the lower price (they contain less Co) and the higher specific capacity they can practically achieve (170 mAh/g for NMC and 200 mAh/g for NCA vs 145 mAh/g for LCO) [5], although their thermal instability is a problem that has not been settled yet [11]; limitation that has been overcome with olivine $LiFePO_4$ (LFP) [12], which is known for its thermal stability [13, 14] and high power capability [15, 16]. However, LFP has other drawbacks, namely, the relatively low average potential (which involves lower energy density) as well as low electrical and ionic conductivity [17, 18].

Spinel $LiMn_2O_4$ (LMO) [19] is another of the materials that has attracted the attention as cathode material. Although it has slightly lower energy density (the specific capacity is 120 mAh/g) [5], in view of its favorable properties like low cost, environmental friendliness and satisfactory thermal stability [20–24], LMO is a very good option as it overcomes the limitations of the materials mentioned so far. Moreover, the spinel structure contains three-dimensional (3D) channels [2] that should enhance the Li-ion diffusion through the structure, and, thus, show better electrochemical behavior than two-dimensional (2D) layered materials [25]. As a matter of fact, it has been the choice of some battery manufacturers for different applications, such as automotive and cell phones [26]. However, LMO shows poor cycling stability and capacity fading, mainly due to Jahn-Teller effect and manganese dissolution. The former is induced by the increase of Mn^{3+} ions during intercalation of lithium in the 3V region that lead to structural fatigue and microcracks [27, 28]. The manganese dissolution, on the other hand, is ascribed to the disproportionation reaction of Mn^{3+} with Mn^{2+} and Mn^{4+} ions, which is a result of reactions with the electrolyte components [29, 30].

One of the ways to improve the electrochemical performance of LMO is partially substituting the Mn cations with other transition metal (TM), with a general formula $LiM_xMn_{2-x}O_4$. Several TM were studied as dopants, e.g. Cr, Co, Fe, Ti, Zr, Ni or Cu [31–33]. Among the different options, the $LiNi_{0.5}Mn_{1.5}O_4$ (LNMO) phase is the most promising [9, 19, 34]. The role of the dopant TM is to compensate the capacity loss from Mn^{3+} to Mn^{4+} below 4.5 V by oxidizing dopant from M^{2+} to M^{4+}, while manganese is maintained at Mn^{4+} state, as an electrochemical spectator. In this manner, disproportionation reaction (and consequently the capacity loss related to it) is avoided, at the same time that the beneficial aspects of Mn are maintained (environmental friendliness, cost, safety,...). Furthermore, dopant provides higher redox

voltage close to 5 V vs Li metal, increasing considerably the energy density and mostly avoiding the Jahn-Teller distortion that occurs mainly below 3 V.

As mentioned before, LNMO stands out among this family of doped materials. It has a theoretical capacity of 147 mAh/g and a high potential around 4.7 V from the $Ni^{2+} \leftrightarrow Ni^{4+}$ redox process. Thus, it has a remarkably high specific energy of around 650 Wh/kg, which is higher than most of the other state of the art materials mentioned above (table 5.1). This property, along with the low cost, environmental friendliness, safety, excellent rate capability and the high electronic and Li-ion conductivity [33, 34], turn LNMO onto a promising cathode material for high performance Li-ion batteries. However, LNMO still suffers from some drawbacks that have to be overcome if this material is to be used in the real market. Performance is highly dependent on the stoichiometry and cation ordering [35, 36] and, consequently, on the synthesis process [25]. Indeed, LNMO can crystallize in two different structures called ordered ($P4_332$ spatial group) and disordered (Fd-3m). The main structural difference between them, is that in the ordered phase Ni and Mn atoms are regularly ordered in 16d octahedral sites while, in the disordered structure, they are randomly occupying the 16d sites [34]. Another difference is the presence of Mn^{3+} in the disordered phase whereas, in the ordered phase, all Mn remains in 4+ state. This effect stems from the loss of oxygen, so part of the Mn is reduced in order to maintain the charge neutrality. Given that Mn^{3+} has higher ionic radius than Mn^{4+}, the disordered phase results in larger unit cell than the ordered one [37]. The higher cell volume implies better diffusion path for the Li ions [35, 38]. In addition, electronic conductivity is also much better (two orders of magnitude) in the case of the disordered phase [39], due to the presence of Mn^{3+}. These two properties, are thought to be the main reason for the better electrochemical performance of the disordered phase, with respect to that of the ordered one, specially at high c-rates [37, 39]. Nevertheless, contradictory conclusions can be found in the bibliography regarding which phase is better from the electrochemical point of view. In fact, another problem associated to LNMO is the dissolution of Mn into the electrolyte, in which Mn^{3+} is involved, and is partially responsible of the capacity fade in the long term. Thus, interest on the ordered phase has also been reported, claiming that only having Mn^{4+} avoids the aging phenomena [9].

Finally, there is an intrinsic limitation when conventional carbonate-based liquid electrolytes are used in combination with high voltage positive electrodes: their narrow electrochemical stability window. Redox reactions in-

Table 5.1: Specific energy values for the state of the art positive electrode materials [33].

Material	Energy density(Wh/kg))
LNMO	650
LMO	400
LCO	518
NMC	576
NCA	680
LFP	495

volved in LNMO charge-discharge processes occur about 0.4 V above the upper stability voltage limit of these electrolytes [40,41]. Therefore, oxidative decomposition of electrolyte occurs upon cycling, with the continuous formation of a non-stable SEI. This results in low Coulombic Efficiency [42,43] and in very limited cycle life in cells [44].

The most promising way to solve all the problems related to LNMO is the development of all solid state batteries [45], which would enable the full utilization of high-voltage cathode materials. Besides overcoming the voltage limitation related to organic electrolytes and the dissolution of Mn, this approach would also avoid the safety concerns arisen from the use of metallic lithium and liquid electrolytes in conventional batteries [46,47]. The bottleneck for all solid state Li-ion batteries is their low power density [48], along with their high interfacial resistances [49]. The former stems from the low ionic conductivity of the solid electrolytes, while, the origin of the later can be ascribed to the poor interfacial contact delivered by current processing methods. Lately, attention has been attracted by certain ceramic electrolytes due to their increased ionic conductivity, with particular focus on garnet-type oxides with general formula $Li_xLa_3M_2O_{12}$, where M=Zr, Nb or Ta [50].

Among the these garnet-type family, $Li_7Zr_2La_3O_{12}$(LLZO) has attracted special attention, due to its high ionic conductivity, which has been reported to be as high as 1.3 mS/cm [51]. This high conductivity is obtained when the LLZO is crystallized in a metastable cubic structure, while the thermodynamically more stable tetragonal phase has low ionic conductivity [52]. Highly conductive cubic phase can be stabilized by introducing aliovalent dopants in the Li sites, such as Ga [53]. Another important property of LLZO is its wide electrochemical stability window of around 6 V [54], enabling the use of Li and high voltage cathodes, such as LNMO. Furthermore, it does not react

with oxygen, which is not the case for other solid electrolytes [55] (although it is moisture-sensitive). Thus, LLZO is one of the potential solid electrolytes that stands out for all solid state batteries. In fact, successful application of several micrometric LLZO layer at cell level has recently been reported [56]. In spite of this promising results, there are several reports evidencing metallic lithium dendrite growth inside LLZO, producing failure in bulky samples and under higher current densities. Works studying this phenomenon, have concluded that it occurs either via transgranular Li metal propagation [57] or/and grain-boundary electrodeposition [58], with grain boundary inhomogeneity and poor interfaces being recurrently referred as the responsible of the deleterious effect.

Considering the potential of magnetron sputtering (described in chapter chapter 2), deposition of LLZO thin-films by means of this technique could help to overcome the Li propagation problem by producing high quality and dense LLZO layers with upgraded interfaces. In fact, magnetron sputtering is the technology behind the fabrication of thin-film batteries, which are based on the all solid state approach, as described in subsection 1.2.1.

5.1.1 Main objectives

The aim of the work carried out in this chapter was twofold: to develop a high performing LNMO thin-film positive electrode while studying the processing parameters and interface role on the electrochemical performance (from section 5.2 to section 5.6); and to study the deposition conditions of sputtered Li-La-Zr-O layers so highly conductive LLZO layers can be grown on top of LNMO thin-film electrodes (Section 5.7). Different techniques have been demonstrated suitable to produce LNMO thin-films, such as Electrostatic Spray Deposition (ESD) [59], Sol-gel [60–62] or PLD [63–67], although magnetron sputtering is the preferred deposition technique [68–74]. RF is the usual source of choice for sputter depositions, while LNMO thin-films deposited using AC power source have not been reported up to date. Few reports were published on sputter deposited LNMO thin-film prior to the beginning of this thesis work, focused on the influence of certain deposition conditions [71] and study of coatings as passivation layers [68–70]. Thus, a thorough study of different parameters on LNMO thin-film preparation and interface phenomena was missing, although recently related works were published [73, 74].

Few works have been reported regarding the preparation of thin-film LLZO, most of them published during the development of this thesis. Some

of them were based in CVD techniques [75, 76], while others use PVD techniques, being PLD the most reported one [77–79]. To the best of the author's knowledge, there is only one publication reporting crystalline LLZO thin-film deposited by magnetron sputtering [80]. That research work by Lobe et al. [81] presents the successful growth of cubic LLZO thin-films by RF magnetron sputtering at high substrate temperature (700°C), which, despite displaying the aimed crystalline structure, delivered out of plane ionic conductivity values far below the expected ones (2.0×10^{-9} S cm^{-1}). Besides the crystalline LLZO, amorphous Li-La-Zr-O thin-films were deposited by Kalita et al. [82], with a highest ionic conductivity reported of 4×10^{-7} S cm^{-1}.

Up to now, only individual thin-film cell components (cathode, anode and electrolyte) have been obtained. Therefore, a thin-film battery based on high voltage LNMO cathode, highly conductive LLZO electrolyte and Li metal anode, would strongly boost the advent of all solid state Li-ion batteries in general and of thin-film microbatteries in particular. It is expected from these batteries that much higher energy density values and outstanding power performance are obtained; hence becoming the choice for a wide range of applications such as aeronautics, Internet of Things, automotive and biomedical industry. The research activities shown in this chapter were carried out within European H2020 project MONBASA (Monolithic Batteries for Spaceship Applications, No. 687561).

5.2 Deposition of LNMO thin-films

LNMO thin-films were deposited in the Mid-Frequency AC dual technology based magnetron sputtering system available in Tecnalia (group of A. García Luis), one of the partners in the MONBASA project with large experience in magnetron sputtering processing. The used AC sputtering method is based on the same concept than the DC method, with the difference that, in the former, cathode and anode switch their polarity every half cycle. As the potential continuously changes polarity, the deposition of electrically non-conductive materials, like metal oxides, can be performed; otherwise impossible by means of DC sputtering. If two targets are used, AC sputtering results in a more efficient use of the power being supplied to the process, in contrast to RF sputtering, where only 50% of the applied power is effectively transferred to the target material. Thus, AC mode can lead to increased deposition rates, which is an important parameter from the industrial application point of view.

The initial deposition conditions were chosen from previous experience

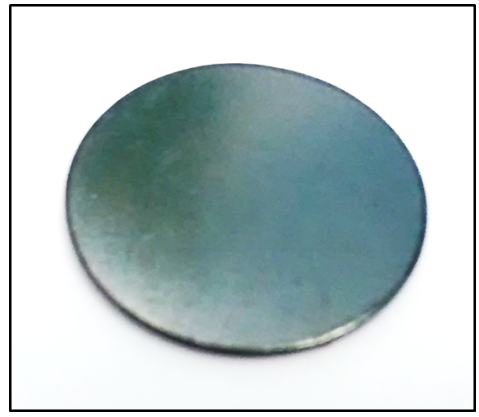

Figure 5.1: Picture of deposited LNMO thin-film on stainless steel substrate.

that Tecnalia had with this type of ceramic targets, and were optimized based on the results obtained for the first depositions. The final deposition conditions used were a maximum AC power of 300 W applied to the targets and an argon flow of 250 sccm, which corresponds to an absolute pressure of the process chamber of 1.05 $\times 10^{-2}$ mbar. The estimated deposition rate for this process was about 0.5 - 0.6 μm/h. As substrate, 316 stainless steel (SS) discs (Hohsen Corp., diameter 16 mm, thickness 0.5 mm) were chosen, which are commonly used as spacers in CR2032 coin cells for electrochemical tests. In fact, the main reason for using such substrate was to facilitate the subsequent electrochemical testing while avoiding the use of more expensive Cu or Al foil current collector.

LNMO-coated substrates had an homogeneous grey surface, as can be observed in figure 5.1. Being the coating thickness of around 2 μm, based on the cross-section SEM analysis (figure 5.2) performed by means of FEI Quanta 200FEG microscope with an accelerating voltage of 30 kV.

5.3 Determination of annealing atmosphere

Once the LNMO thin-film cathodes were successfully deposited, the need for a post-deposition thermal process was studied at CIC-energiGUNE, in order to obtain the desired crystalline structure (described in section section 5.1) and an optimal electrochemical performance. Out of plane XRD was performed on as deposited LNMO sample, to verify its crystallinity and phase identification. For the measurement, a Bruker Advance D8 instrument with Cu radiation (Cu $K_{\alpha 1,2}$, λ= 1.5406 Å, 1.5444 Å) was used. The de-

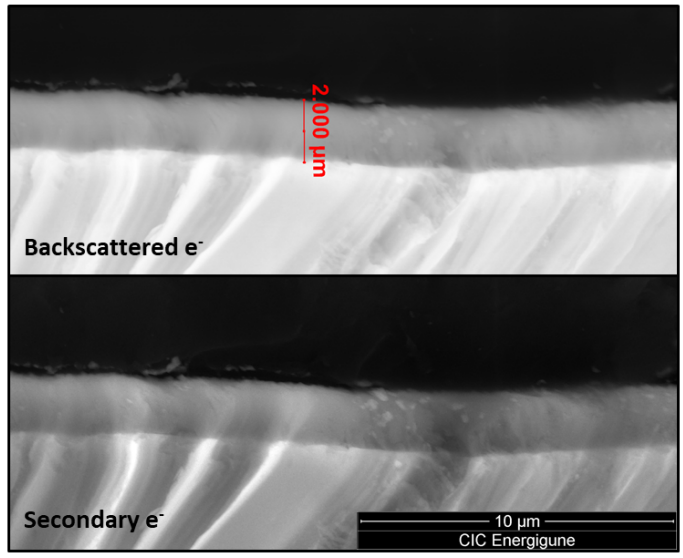

Figure 5.2: SEM cross-section image of deposited LNMO thin-film on stainless steel substrate.

posited layer was not crystalline, based on the absence of any reflection apart from those related to the SS substrate (figure 5.3). Broad and weak peaks can be intuited in the diffractogram of figure 5.3 around $2\theta = 18°$ and $2\theta = 36°$, which would correspond to crystalline LNMO. However, no clear diffraction peaks that could be ascribed to a long range order structure are present.

In order to induce crystallization of the deposited thin-film, annealing of the sample was performed under two different atmospheres: air and Ar. Both annealing processes were carried out in an oven, using an alumina crucible as sample container: up to a temperature of 600°C, with a heating ramp of 5°C/min, and keeping the maximum temperature for 1 hour. Once the process was finished, sample was left to cool down naturally, without any cooling ramp.

XRD patterns of the two annealed samples (both in air and Ar atmosphere), compared to the as deposited one, are presented in figure 5.4. Similar results were obtained for both annealing processes. There is a clear evidence of the crystallization of the thin layer, as several new reflections appear in the XRD patterns of the annealed samples in comparison with the as deposited one. In fact, these new reflections are in good agreement with the diffraction lines expected for the LNMO for different (hkl) Miller indices, as indicated

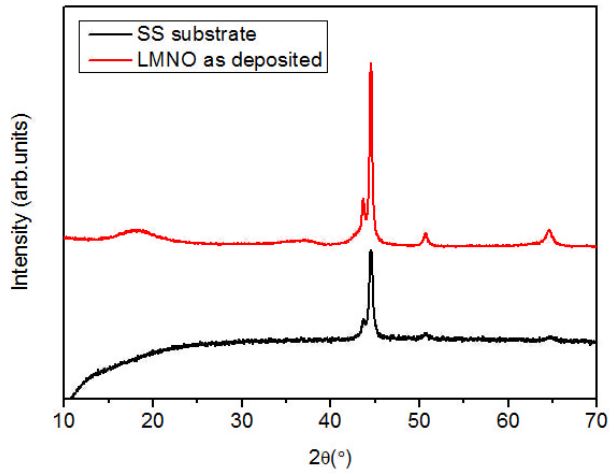

Figure 5.3: XRD pattern of LNMO thin-film as deposited (red) and the SS substrate (black).

in figure 5.4. Moreover, as both Ar and air annealed samples showed similar XRD pattern, both annealing processes were, apparently, successful.

Raman spectroscopy was used to further characterize the thin-film samples, as a complementary technique to XRD. Indeed, conventional XRD cannot easily differentiate between the ordered ($P4_332$) and the disordered (Fd-3m) structures of LNMO, and neutron diffraction and Raman spectroscopy have been commonly used for that purpose [34, 83]. Measurements were performed with a Renishaw InVia microscope, with a 50x objective and 532 nm wavelength laser source. First, a general spectra was acquired (from 3000 to 100 cm^{-1}), followed by a more accurate acquisition increasing the counting time on the region of interest. Results obtained for as deposited, Ar annealed and air annealed LNMO samples are shown in figure 5.5.

In the case of air annealed sample Raman spectra obtained was in good agreement with that expected for LNMO, based on the literature [84]. Peaks at 640, 600, 500, 404 and 343 cm^{-1} are usually assigned to A_{1g}, $F_{2g(1)}$, $F_{2g(2)}$, E_g, $F_{2g(3)}$ vibrational modes, being the main features at 640 and 500 cm^{-1} related to Mn-O stretching and Ni^{2+}-O stretching modes, respectively [39,84,85]. Nonetheless, assignment of the modes has also been reported to be speculative and not rigorous, and different approaches can be found in

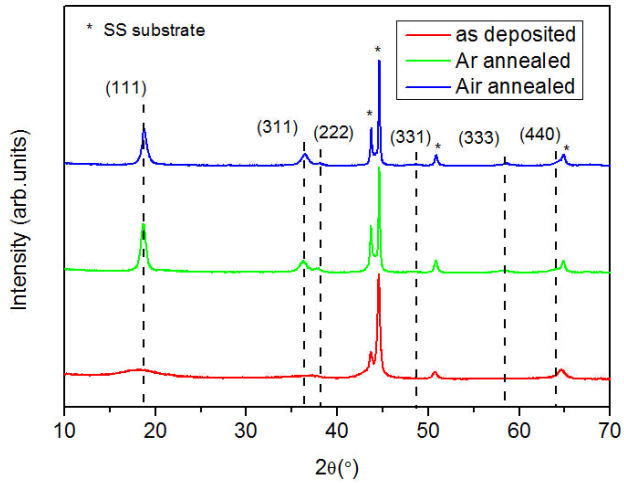

Figure 5.4: Comparison of the XRD pattern for LNMO thin-films with different thermal treatments: as deposited (red), annealed in Ar (green), and annealed in air (blue).

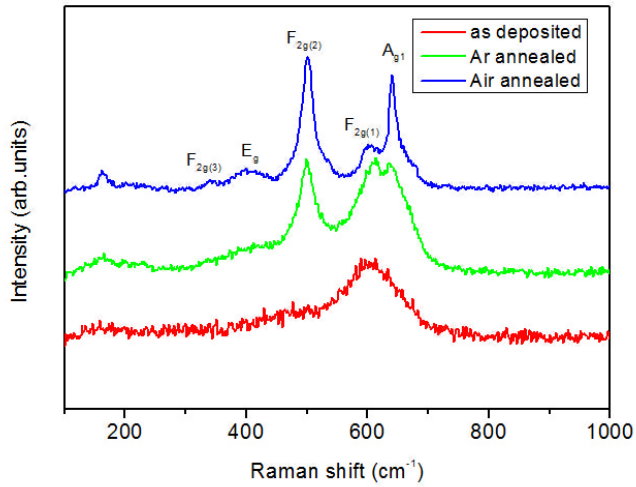

Figure 5.5: Raman spectra obtained for as deposited (red), Ar annealed (green), and air annealed (blue) LNMO thin-films.

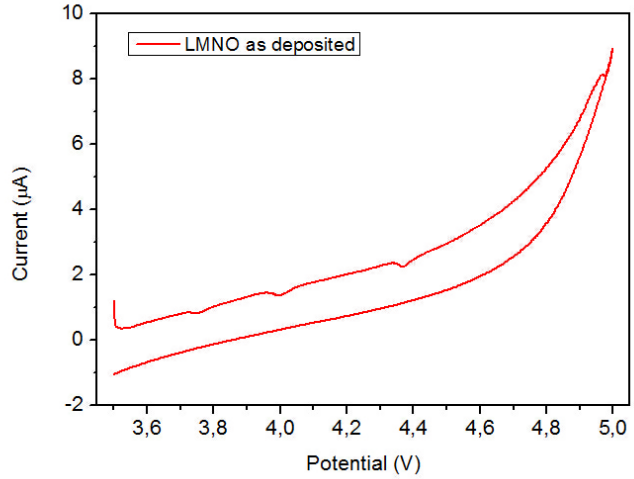

Figure 5.6: CV in the case of the as deposited LNMO sample.

the literature [86]. In any case, independently of the correct symmetry and bindings involved in each band, what is evident is that the Raman spectra obtained for the air annealed thin-film corresponded to that commonly obtained for LNMO. In summary, it can be concluded that the disordered Fd-3m phase was obtained; grounded on the low intensity of the peaks at 162 and 404 cm^{-1}, as well as the lack of definition of a double peak at 600 cm^{-1} [39].

For the case of the Ar annealed sample, Raman spectra was different to the air annealed one. Although they had peaks at similar Raman shifts, all peaks were sharper and better resolved in the case of the air annealed sample, at the same time that the main contribution came from the peak at 612 cm^{-1} in the case of Ar annealed sample, which is not representative of LNMO phase. Thus, despite having observed similar XRD patterns for both annealed samples, Raman spectroscopy revealed a difference between the two annealing processes, being the air annealed sample the one with the desired phase and structure. Finally, the Raman spectra obtained for the as deposited sample showed a single broad peak at around 604 cm^{-1} which does not correspond to a LNMO phase. This, on line with XRD results, confirms the need of a heating treatment on the deposited layers in order to obtain the desired phase.

Cyclic Voltammetry tests tests were performed in order to check the electrochemical response of the different thin-films. Samples were kept overnight

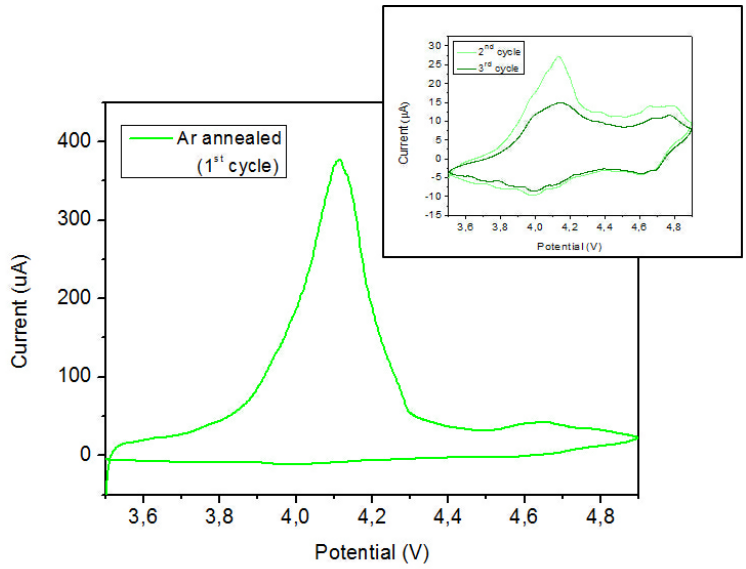

Figure 5.7: CV in the case of the Ar annealed LNMO sample.

at 120°C in vacuum oven before mounting the cells, in order to avoid any adsorbed moisture. LNMO samples were cycled versus metallic lithium (Rockwood Lithium, battery grade, 99.8%), with glass fiber as separator (GE Healthcare, GF/D grade) and $LiPF_6$ EC:DMC (1:1 v/v) as electrolyte (Solvionic, 99.9%). CR2032 type coin cells were assembled in MBraun Ar filled globe box (H_2O and O_2 values below 0.1 ppm) and cycled in Biologic VMP3 Potenciostats. CV measurements were carried out at a rate of 0.05 mV/s in the 3.5-4.9 V voltage range.

As shown in figure 5.6, the as deposited LNMO sample, did not present any redox activity in the selected potential window, as shown in figure 5.6. Only a slight increase of the current could be observed as the voltage was increased, most probably related to the decomposition of the electrolyte, as the stability window of the electrolyte was below the analyzed voltage range [70]. In fact, looking at the results obtained from XRD and Raman characterization on this sample, the absence of any electrochemical activity was somehow expected. Indeed, this was the outright proof of the need of an annealing process to electrochemically activate the LNMO thin-films.

In the case of the sample annealed in Ar atmosphere, massive oxidation peak appeared during the first cycle at around 4.1V (figure 5.7). When the

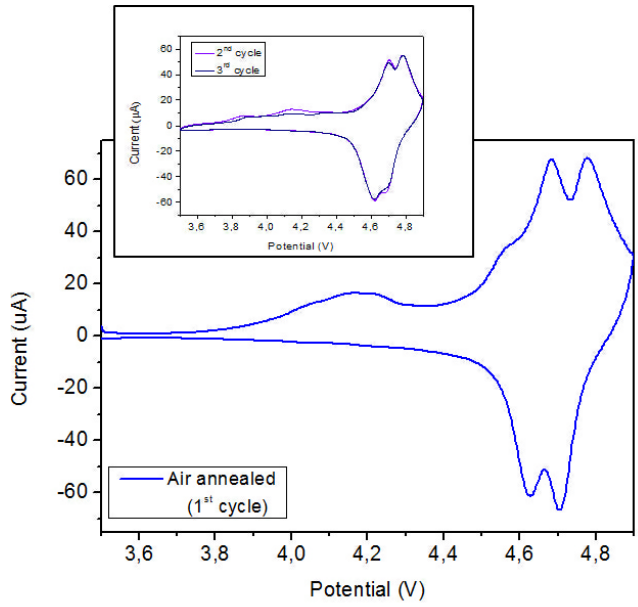

Figure 5.8: CV in the case of the air annealed LNMO sample.

voltage scan was reversed, there was no presence of the equivalent reduction process, indicating the irreversible nature of this reaction. In subsequent cycles, the oxidation peak continuously decreased until no clear redox activity could be observed. Taking into account that Li-ion exchange occurs around 4.7 V for LNMO, this oxidation process should not be related to LNMO. Moreover, based on the high current measured, the oxidation reaction was unlikely to be related to possible impurities or similar reasons. Most probably, this irreversible process is related with the SS substrate used for the LNMO thin-film deposition; this phenomena is further detailed later in this chapter. Nevertheless, the main conclusion obtained from the CV analysis of the Ar annealed sample was its electrochemical inactivity.

Finally, as shown in Figure 5.8, CV experiments were performed on air-annealed LNMO thin-films. In this case, two clear reversible redox peaks can be observed around 4.7 V, in good agreement with the expected electrochemical activity of disordered Fd-3m LNMO. While in ordered LNMO a single redox peak is detected in the CV measurements, double redox peak is representative of the disordered structure. The presence of a double peak is nested in the subsequent oxidation of Ni from 2+ to 3+ and from 3+ to 4+ oxidation states, as mentioned in the introduction section. Similar redox peaks

were observed also in the reverse scan, as well as in subsequent cycles, indicating that lithium was reversibly inserted and extracted from the structure. The broad small peak around 4.1-4.2 V, which corresponded to an irreversible process, could be related either to Mn^{3+} presence on the LNMO (common in disordered LNMO) or to a similar effect (but much less intense) than that observed in Ar annealed sample. In any case, from the second cycle on, this redox activity at low voltage was much less intense, almost disappearing.

As a summary of this section, from the XRD data, the need for a thermal treatment to induce the crystallization of the deposited layer was determined. From the Raman spectra, differences in the material after annealing under different atmospheres were evidenced, being the annealing in air the most appropriate for the formation of disordered LNMO phase. The cyclic voltammetry revealed that only the air-annealed LNMO resulted in proper electrochemical performance.

5.4 Determination of annealing temperature

Once the need for an annealing process and the atmosphere for obtaining the desired phase and structure were identified, an study about the effect of different annealing temperatures on the sample was carried out. Dependence and evolution of different characteristics were studied such as surface morphology, roughness, crystallinity and structural changes, as well as identification of possible impurities or additional phases. To obtain truthful and contrasted information about all of them, a wide range of characterization techniques were used, namely, AFM, SEM, XPS, Raman spectroscopy and XRD. As the formation of the LNMO phase was demonstrated for 600°C in the previous step, for this analysis the temperature window was widen below and above, from 300°C to 900°C. The temperatures chosen for SEM, AFM, XPS and Raman characterization were 300°C, 550°C, 600°C, 750°C and 900°C, with an annealing duration of 30 minutes at the maximum temperature selected, and natural cooling. In the case of the XRD, thermal *in-situ* analysis was performed, acquiring the diffraction pattern at 13 different temperatures in the range between 200°C to 900°C.

5.4.1 Morphology and composition evolution

Surface morphology evolution with different annealing temperatures was tracked by SEM, using FEI Quanta-200FEG model microscope with an acceleration voltage of 30 kV. As it is observed in figure 5.9, the surface of the sample evolved continuously with the temperature, with progressive crys-

tallization and increase of the crystal size. The images of the as-deposited sample showed a granular morphology with grains below 100 nm in size, with no evidence of crystallite formation. At 300°C, still no clear crystallite formation was present, although certain evolution of the grains could be intuited.

Surface morphology was completely different at 550°C. At that temperature, small flake shaped crystallites were present all over the surface. This kind of surface morphology was previously reported for LNMO thin-films [67]. No big differences were detected when the LNMO was annealed to 600°C, an expected outcome if one looks at the small increase in temperature from the previous step. However, flakes were not so clearly defined as in the sample annealed at 550°C, and particles looked to be more compacted. The aggregation of smaller particles to form larger ones has been reported up to 800°C [62].

The continuous evolution of the morphology was evident at 750°C. At such temperature, bigger crystallites were visible with a dominating triangular shape, although particles were not well defined yet. Annealing at 900°C resulted in big crystallites (¿1 um) with perfectly defined edges. Most of the particles presented diamond-like shape, with triangular faces, which is typically obtained for LNMO annealed at high temperatures [87], as well as for other spinel structured phases [88,89]. Therefore, a continuous crystallization of the thin layer, along with an increase on particle size, was observed as the annealing temperature was raised.

Following with the morphological analysis, this samples were also studied by AFM, in order to have more detailed information of the evolution of the surface morphology and roughness. Measurements were performed with an Agilent 5500 microscope, in tapping mode, and a Si tip (NT-MDT). Due to the local nature of the AFM, several points over the sample surface were measured, in order to be sure that the result obtained was representative of the whole sample. Analysis of the images and roughness calculation was done using the Gwyddion program. AFM images of the topography are shown in figure 5.10, while amplitude is represented in figure 5.11. The first is representative for the roughness of the surface, while the second provides much better resolved particle shape and edges. Thus, topography was used to obtain quantitative information of the roughness, whereas amplitude is represented to have a better insight of the particle morphology. In terms of roughness values, which results are gathered in table 5.2, progressive increase was detected upon increasing of the annealing temperature. From the visual qualitative point of view, conclusions obtained by SEM were reinforced, although higher

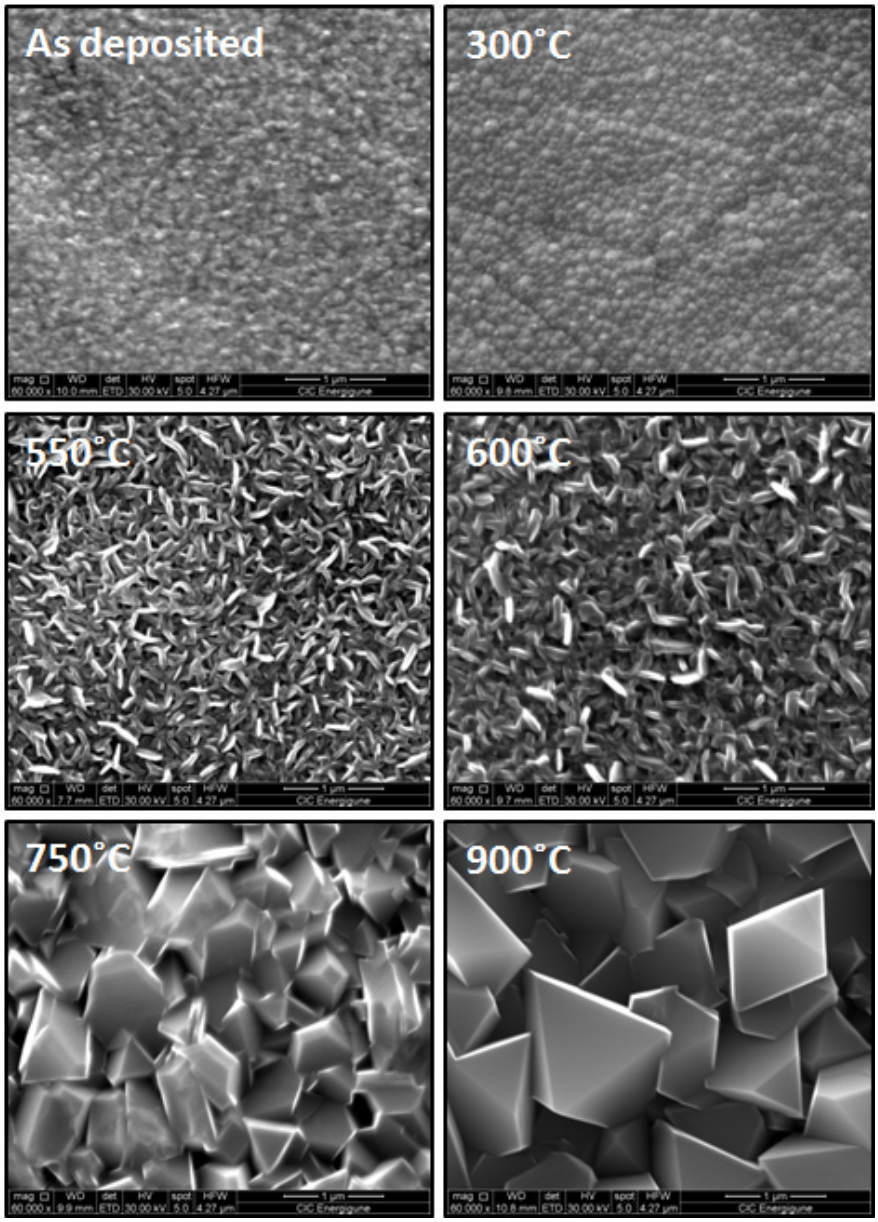

Figure 5.9: SEM images for LNMO samples annealed at different temperatures, from 300°C to 900°C. Images from as deposited sample are also included.

degree of detail was obtained by AFM.

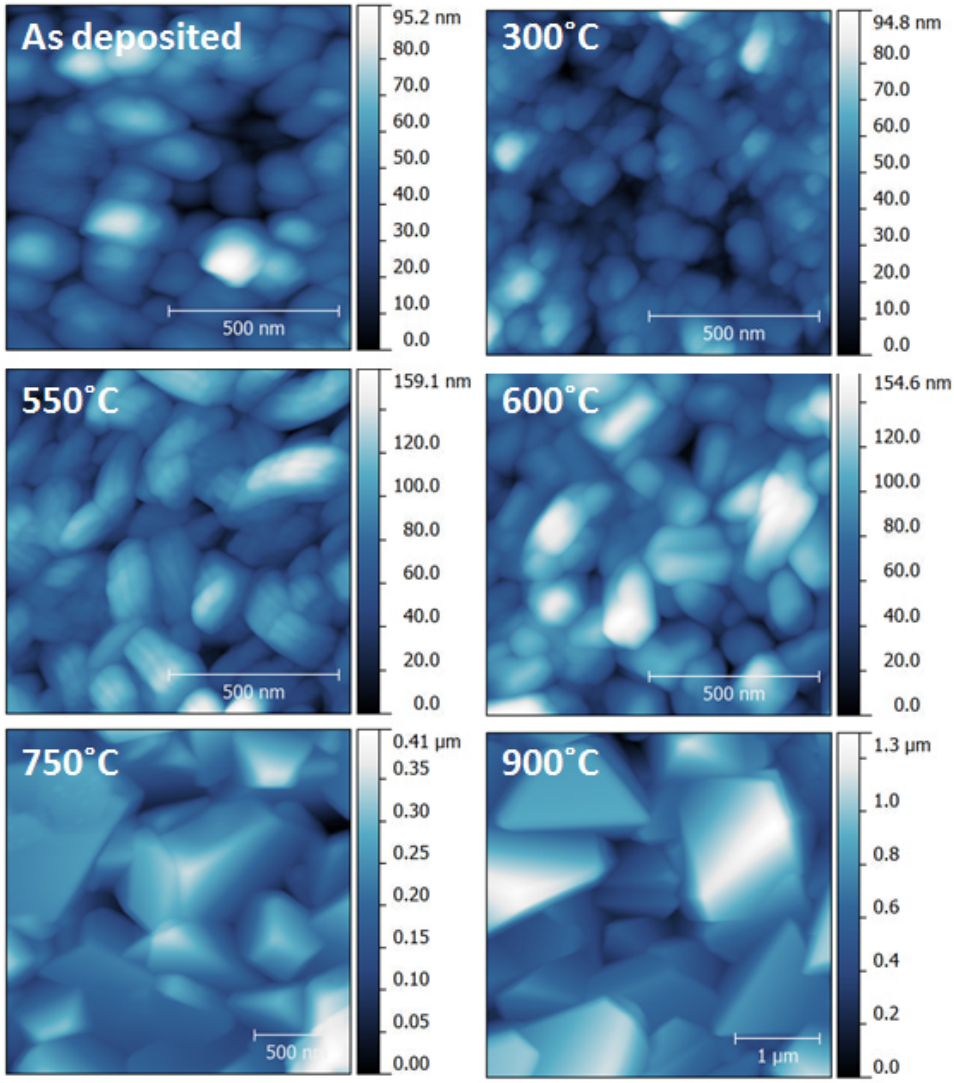

Figure 5.10: AFM topography images for LNMO samples annealed at different temperatures, from 300°C to 900°C, as deposited sample are also included.

Differences between the as deposited and 300°C were clearly visible, with smaller particles at 300°C, most probably indicating the beginning of a crystallization process, which would be on the line of the results obtained by XRD. Apart from the change on particle shape and size, a slight decrease of the roughness (both average and maximum) was detected (table 5.2) between as deposited and 300°C.

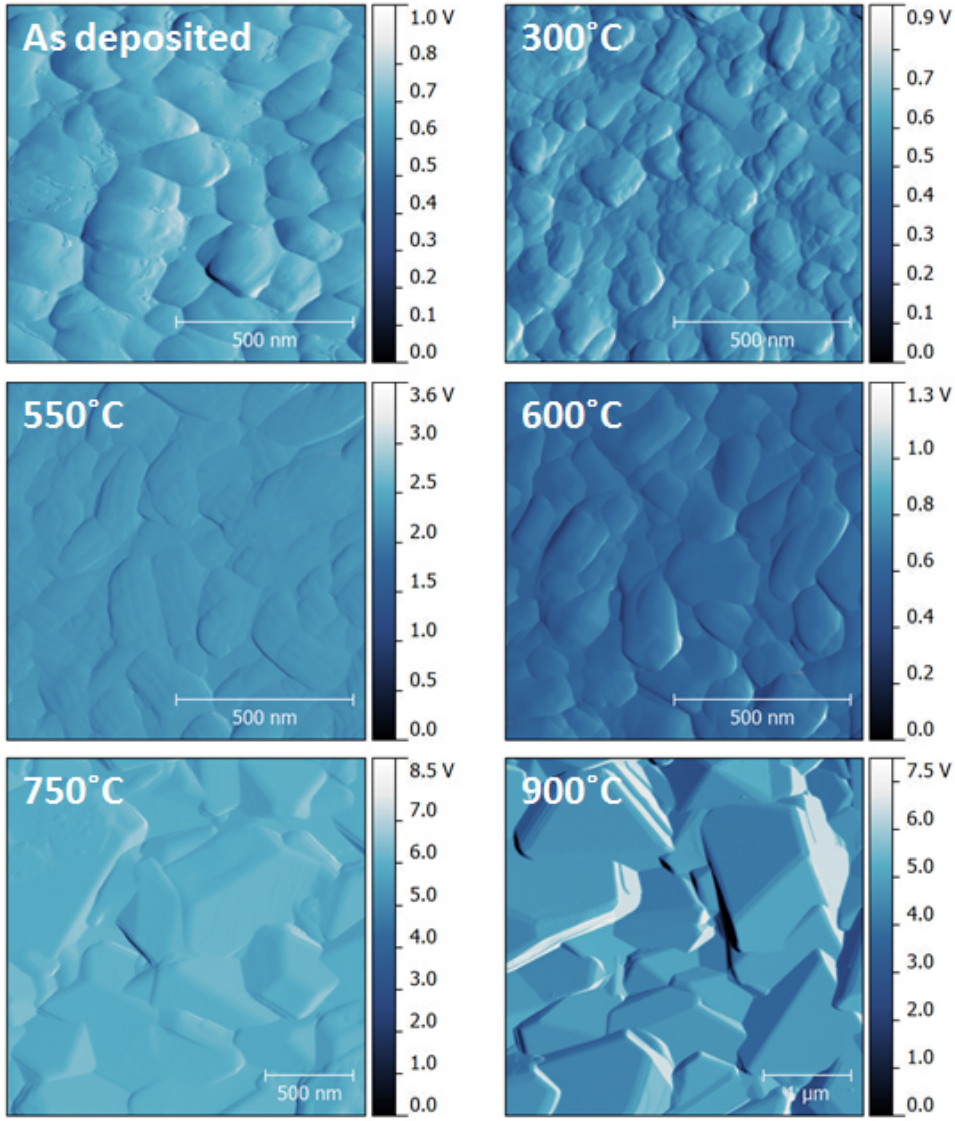

Figure 5.11: AFM amplitud images for LNMO samples annealed at different temperatures, from 300°C to 900°C. Images from as deposited sample are also included.

Features present at 550°C were more discernible by AFM, where shape and sizes of flakes (around 200-300 nm long, and 100 nm wide) were more clear. Moreover, the compactness and lack of definition of the flakes at 600°C

intuited by SEM was perfectly represented in AFM images. With the formation of flake-like crystallites at 550°C, an increase of the roughness values was measured which decreased again at 600°C, in good agreement with the compactness evolution observed by SEM.

For the high annealing temperatures, there was a big increase in roughness values, in particular at 900°C, where values of 13.7 nm for the average roughness (R_a) and 19.0 nm for the root mean square roughness (R_q) were obtained, which represents a one order of magnitude increase with respect to the other samples. This was related to the formation of big crystallites, already described by the SEM experiments and also confirmed by the AFM results. For the sake of clarity, it is worth noting that for the samples annealed at 750°C and 900°C the scanned areas were wider. This was necessary to obtain a representative region of the surface and, thus, to have a realistic value of the roughness. Looking at the AFM results as a whole, those confirmed and completed the observations of SEM and, a general trend towards increased corrugation of the surface was identified and quantified (table 5.2).

Table 5.2: Surface roughness values for LNMO samples annealed at different temperature.

Sample	**R_a(nm)**	**R_q(nm)**
As deposited	1.1±0.2	1.5±0.1
300°C	1.0±0.2	1.3±0.3
550°C	2.2±0.1	3.1±0.1
600°C	2.0±0.2	2.5±0.1
750°C	3.6±0.7	5±1
900°C	13±2	19±2

The composition evolution of the LNMO surfaces was analyzed by XPS using a Phoibos 150 XPS spectrometer in Fixed Analyzer Transmission (FAT) mode and a non monochromatic Mg K_α source ($h\nu$ =1253.6 eV). Survey spectra were obtained with 0.5 eV step size, pass energy of 60 eV, dwell time of 0.1 s and 1 scan. Particular regions for the photoelectrons of the elements present on the survey signal were acquired with higher resolution. These regions were measured with step size of 0.1 eV, pass energy of 30 eV, dwell time of 1 second and 3 cumulative scans. For the Li 1s region, 18 scans were recorded, owing to the very low sensitivity factor of Li 1s orbitals to the Mg K_α photons [90]. Experimental data was treated with CasaXPS program. All the spectra were calibrated using the aliphatic carbon signal which was set

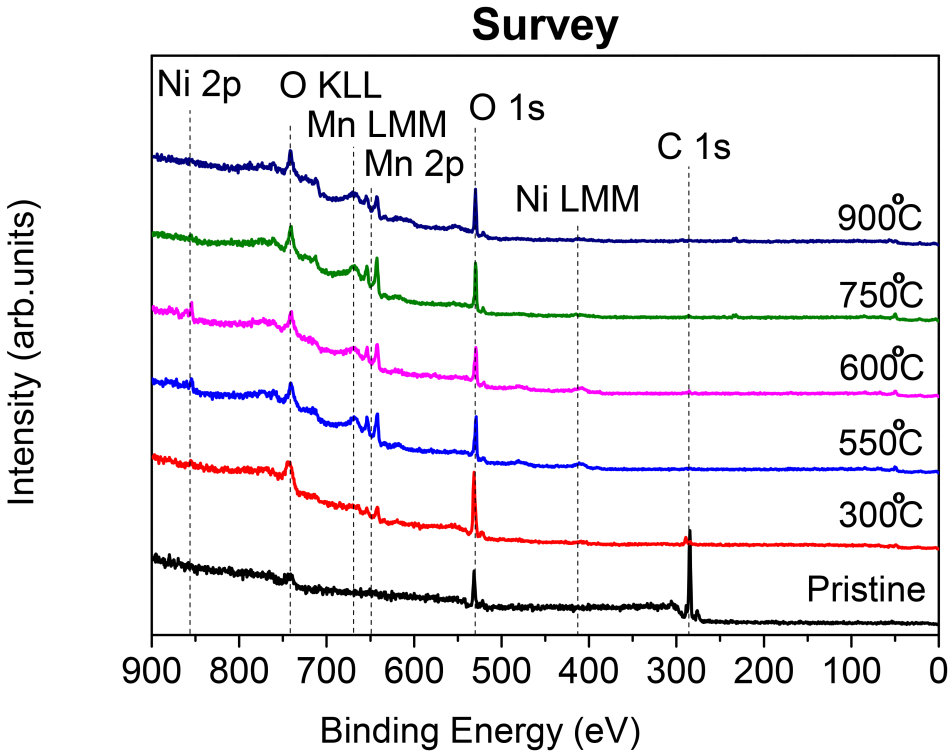

Figure 5.12: Comparison of the XPS survey spectra obtained for LNMO layers annealed at different temperatures.

at 284.8 eV. Results are shown in figure 5.12 and 5.13 where survey spectra and core electron regions are represented, respectively.

For the as deposited sample, only C and O were identified by XPS as can be observed in the survey spectra. Some small amount of Li was also detected when Li 1s photoelectron region was measured, which was most probably present in form of carbonate. C 1s core electron peak was typical of adventitious carbon, which is common in samples exposed to air [91, 92]. O 1s spectra was associated with surface oxides species and carbonate signals. The absence of any signal related to Ni and Mn, or to O in form of transition metal oxide, implies that the thin-film surface was covered by a nanometric layer (more than 10 nm which is approximately the detection limit of the technique) mainly composed of organic species. The presence of such a layer is justified, specially considering that the samples were deposited in a different laboratory and stored in air during relatively long time before they were

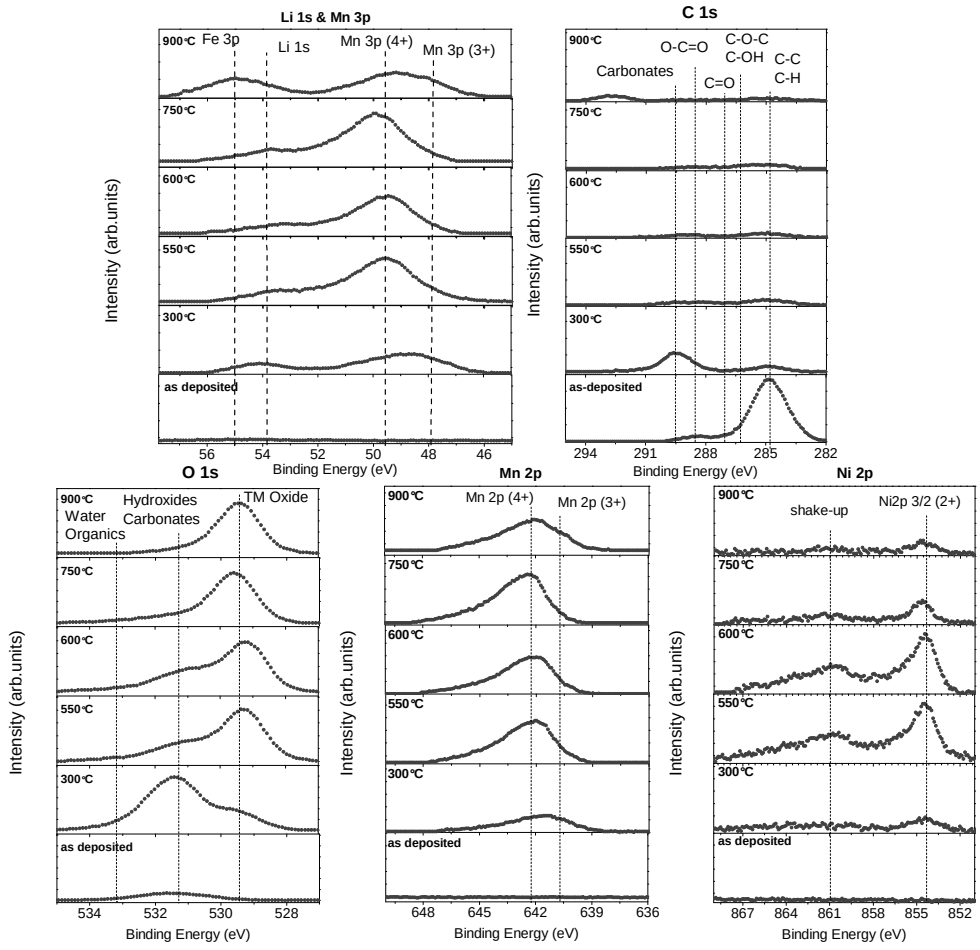

Figure 5.13: Comparison of the XPS spectra obtained for LNMO layers annealed at different temperatures. Particular regions for Ni 2p, Mn 2p, O 1s, C 1s, and Li 1s core electrons.

transferred to the UHV system for XPS analysis. There are several possibilities to get rid of the surface contamination in order to measure the underlying material. The first option is to calcine the sample which, considering that the outermost layer is mainly formed by organic species, would result in a clean surface. However, we were interested on studying the evolution of the sample with the temperature, which means that this was not an option. The second option is the ultrasonic cleaning of the sample in ethanol or a similar solvent, however, owing to the presence of Li, the LNMO thin-film could probably react with the solvent. The last option was to proceed with the typical ion

etching with Ar ions. This option was considered, although post-etching measurements demonstrated that Ar ions were reducing the Mn, thus, rendering this method useless to get reliable information. Therefore, the use of any of the mentioned methods was discarded and the already described spectra was considered for the as deposited sample, having only the contribution from the surface contamination layer.

After annealing the sample at 300°C, C contribution decreased considerably, while O signal increased, and Ni and Mn were also detected in survey spectra. Analyzing the C 1s region, adventitious carbon signal clearly decreased, indicating that these species were removed during the annealing process. Main contribution to the C 1s peak appeared at higher binding energies that correspond to carbonates, which could be present as contamination on the surface of the sputter deposited layer. At low binding energies, carbonate species were also the most important in Li 1s signal (around 54.5 eV) [93], same as the main contribution in the O 1s photoelectron peak around 531.5 eV which corresponds to carbonates as well [69, 93]. In addition, a new contribution appeared at this annealing temperature in the O 1s signal at around 529.5 eV, which is typically related with transition metal oxides. In the same line, Mn and Ni 2p signals were discernible, confirming that at 300°C we were measuring the sputter deposited film that was below the surface contamination layer. It is worth noting that, Mn signal was a bit broad, with contributions from two different oxidation states, namely, Mn^{3+} and Mn^{4+}. In the case of LNMO, Mn is supposed to be in 4+ oxidation state, although some Mn^{3+} is always present in its disordered form. However, in this case Mn^{3+} contribution is, apparently, higher than Mn^{4+} contribution, which would not be the case for LNMO. Same conclusion is obtained from the Mn 3p signal, which is also broaden due to the presence of Mn in 3+ state. Hence, this result suggests that at this annealing temperature some other Mn oxide could be present, at least on the outermost surface region. Moreover, the atomic concentration ratios between the Mn, Ni and O were not in good agreement with the expected ones for LNMO. These concentration ratios, calculated from the quantitative analysis of the XPS data, are gathered in table 5.3 for the different annealing temperatures. In the case of annealing at 300°C, Mn concentration is slightly above the expected one for LNMO, while Ni is clearly below, if we compare them to oxygen concentration as estimated from the transition metal oxide component.

For the sample annealed at 550°C, differences in the XPS results were present. C 1s contribution related to carbonates decreased, as well as the sig-

Table 5.3: Relative concentrations between O, Mn and Ni for LNMO samples annealed at different temperature, as calculated from XPS data.

Sample	**O/Mn**	**O/Ni**	**Mn/Ni**
Nominal $LiNi_{0.5}Mn_{1.5}O_4$	2.7	8.0	3.0
300°C	2.5	12.3	4.9
550°C	2.8	8.2	2.9
600°C	2.8	8.4	3.0
750°C	2.8	31.2	11.0
900°C	4.0	58.7	14.7

nal related to surface species, meaning that little amount of surface contamination was detected. Same conclusion could be obtained from O 1s spectra, where peak related to carbonates decreased and contribution from transition metal oxides was dominating. In addition, Ni and Mn were more clearly visible in the survey spectra and, from the quantification obtained from the recorded regions, concentrations determined to be much closer to the nominal stoichiometry of LNMO. Moreover, the shape of the Mn 2p peak changed, becoming narrower and related to Mn^{4+} component. Same behavior was observed for the Mn 3p peak, with no contribution at lower binding energies from Mn^{3+}. Regarding the Li 1s signal, the contribution from lower binding energies (around 53.6 eV) gained intensity in comparison with the contribution that was higher at 300°C (around 54.5 eV), which would be in good agreement with the decrease of carbonate signal and increase of the oxide signal, presumably related to LNMO. Very similar results were obtained for the sample annealed at 600°C. Same contributions were detected, and the concentrations were very close to those calculated for the sample annealed at 550°C, thus, being in good agreement with the LNMO in terms of stoichiometry.

The results obtained for the sample annealed at 750°C were different in certain points. C 1s signal continued with the decreasing tendency as the annealing temperature was increased, and the same was observed for O 1s core level where the peak related to transition metal oxide was the main contribution while the other components, related to different carbon species were less intense. Signal related to Li 1s did not have alterations either. However, Ni signal intensity was decreased, and relative concentrations were far from the ones calculated for the previous two cases. Mn signal, did not suffer big changes, neither in concentration nor in terms of oxidation.

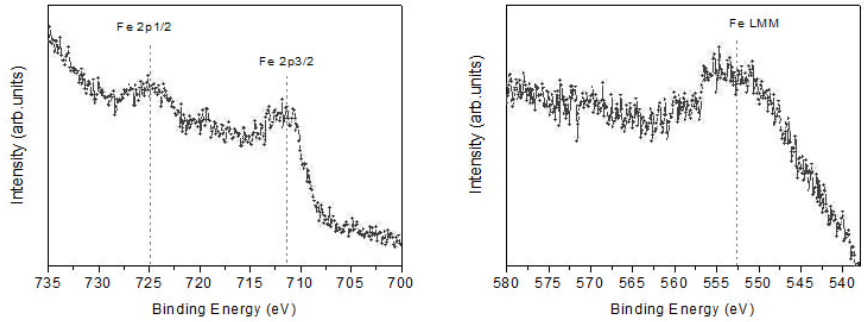

Figure 5.14: Fe detection by XPS in LNMO sample annealed at 900°C. Panel on the left corresponds to the Fe 2p core level while panel on the right shows the Fe LMM Auger electron peak.

At the highest annealing temperature, 900°C, the changes were much more evident. Decrease on the Ni 2p signal was more pronounced and relative concentrations of Ni, Mn and O were far from those expected for LNMO. Moreover, Mn signals, both 2p and 3p, were broadened indicating the presence of Mn^{3+} again. In addition, the appearance of two new contributions should be remarked. First, in the C 1s region, a new peak was detected around 292.7 eV. At such high binding energy, it could be related to fluorinated species, which was not an option based on the absence of F in the survey spectra. The other feasible option was ascribing this signal to K 2p photoelectron, which would be originated by cross contamination from the annealing performed in the oven. In any case, this contamination would be negligible since its contribution to the whole signal was below 0.5%. The second new contribution, much more important, was the appearance of a new peak on the Li 1s region around 55.3 eV. Although it could be related to lithium in the form of some impurity formed during annealing, based on the high intensity and the position, it could also be assigned to Fe 3p. The presence of Fe on the surface would stem from the diffusion of this element through the whole thin-film, coming from the SS substrate. To confirm this extent, particular regions where Fe 2p core electron and Fe LMM Auger electron signals should be detected were scanned with XPS. The result, shown in figure 5.14, verifies the presence of Fe on the surface. This diffusion effect, was further studied and is discussed later on the text. In any case, the XPS results obtained from the sample annealed at 900°C suggested an evolution of the sample surface in terms of composition.

Therefore, from the overall analysis of the XPS results, it was concluded

that, in terms of composition, the nominal composition of LNMO was obtained for the intermediate annealing temperatures, namely 550°C and 600°C, with almost identical results in both cases. For lower annealing temperatures, contamination in form of organic surface species and carbonates was detected. In the case of the highest annealing temperatures, deviations from the expected composition, contribution of the Mn^{3+} and presence of Fe was noticed, suggesting that some changes were occurring on the sample surface.

5.4.2 Phase and structural evolution

Continuing with the analysis of the thin-film evolution with the annealing temperature, further structural characterization was performed on the material. Following the same characterization procedure described in section section 5.3, XRD was used to get accurate information of the crystalline structure and phase at bulk level, whilst Raman spectroscopy provided structural information of crystalline and amorphous phases at surface level [86]. Details of the experimental setup and acquisition conditions have been already explained (chapter chapter 2 and section section 5.3).

Raman spectroscopy results are displayed in figure 5.15. As expected, for the as deposited, the same result as the one shown in Section section 5.3 was obtained. An asymmetric broad band appeared centered around 600 cm^{-1}, with a long tail down to 400 cm^{-1}, without the presence of a well defined band. A similar spectra was recorded for the sample annealed at 300°C, showing no clear bands on the pattern.

The main difference appeared at 550°C where several bands were detected on the spectra. The peaks obtained were the same contributions described for the air annealed sample in section section 5.3, thus, indicating the presence of LNMO phase already at that temperature. At 600°C, the bands were better defined, suggesting that further structuring of LNMO phase occurred from 550°C to 600°C. After annealing the sample at 750°C, the detected bands were not as well defined as in the previous step, which could suggest that an inflection point was already reached towards a loss of crystallinity of the LNMO phase.

The structural change and the formation of impurities with temperature was clear for the final measurement, annealing at 900°C. In this case, the change on band distribution was drastic: spectra was broaden, with the overlapping of several peaks on the 500-750 cm^{-1}, new bands were detected around 575 cm^{-1} and 710 cm^{-1}, while the band at 500 cm^{-1} related to Ni^{2+}-O

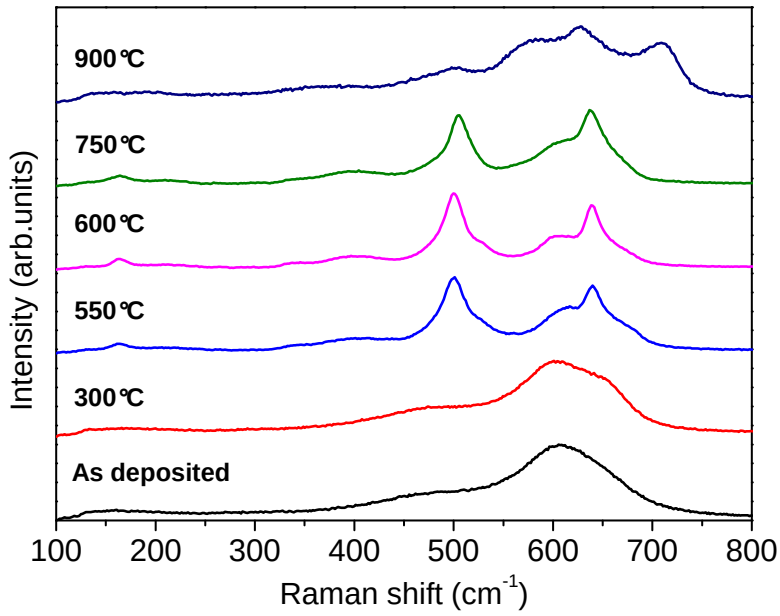

Figure 5.15: Raman spectra obtained for the LNMO samples at different annealing temperatures.

stretching mode, almost disappeared, as well as the small contribution at low energies related to the LNMO.

Analyzing the Raman results as a whole, three main conclusions were obtained: first, no clear bands, and, hence, no signal of LNMO structure was detected on the as deposited and 300°C measurements, suggesting the need of higher temperature for the formation of this phase. Secondly, between 550°C and 750°C, Raman bands commonly related to LNMO appeared being 600°C the best annealing temperature according to the better definition of the Raman bands. Finally, when the sample was annealed at the highest temperature (i.e. 900°C), typical LNMO Raman spectra was lost, with the presence of non identified new peaks, and fading of the previous ones. Thus, at 900°C, the LNMO pure phase was lost.

Regarding the XRD thermal *in-situ* analysis, measurements were performed using Advance D8 diffractometer (Co $K_{\alpha 1,2}$, λ= 1.78897 Å, 1.79285 Å). As deposited LNMO thin-film sample was placed on an alumina holder, which was introduced in a high temperature oven chamber (Anton Paar HTK 1200, Rigaku). Temperature was increased from room temperature (20-25°C)

to 900°C at 5°C/min. Temperature was hold for 30 minutes at 200°C 300°C, 400°C, 450°C, 500°C, 550°C, 600°C, 650°C, 700°C, 750°C, 800°C, 850°C, 900°C, and XRD patterns were acquired at each point after the holding time.

Results obtained from the XRD thermal in-situ analysis are presented in figure 5.16. For the low temperature region, from as deposited sample up to 300°C, there were no signals of crystallization on the LNMO phase, being present only the peaks related to the SS substrate. At 300°C, a broad peak started to be visible around $2\theta = 21.5°$, presumably related to the (111) diffraction line of LNMO, as already mentioned in section section 5.3, and indicating the beginning of a crystallization process of the deposited material. From 300°C to 550°C, evolution of that reflection was observed, with increasing intensity and slow narrowing of the peak suggesting further crystallization process. Less intense reflections, probably related to (311) and (222) diffraction lines, were also present just above $2\theta = 42°$ and $2\theta = 44°$, respectively.

After annealing at 600°C, the main diffraction peak was clearly narrowed, suggesting a better crystallization of the phase. (311) and (222) reflections were also better defined, although a shoulder was present at lower angles for (311) reflection. At 650°C, (311) reflection was clearly splitted in two different reflections, suggesting that a structural/phase change was starting. Although the main reflection continued sharpening, indicating better crystallization level, a shoulder at the low angle side was also present for this reflection, further supporting the idea of a structural change going on. Moreover, all reflections were shifted to lower angles, indicating an increase in lattice parameter which could be related to thermal expansion. Same tendency was observed at 700°C and 750°C, where all reflections kept shifting to lower angles. Besides the shift, the main difference was the evolution of the newly formed reflections, gaining intensity and dominating in the case of the (311) region, and progressively dominating also the signal for the (111) region. Moreover, another reflection, presumably corresponding to (220) diffraction line appeared, gaining intensity with the temperature.

At 800°C, the newly formed reflections were dominating the whole diffraction pattern, with no contribution from the original reflections ascribed to LNMO. After further increasing the annealing temperature at 850°C and 900°C, new diffraction lines appeared around $2\theta = 28°$, $2\theta = 38.5°$ and $2\theta = 47.5°$, indicating the formation of new phases. Furthermore, the rest of the peaks were still present, although some broadening and lack of definition

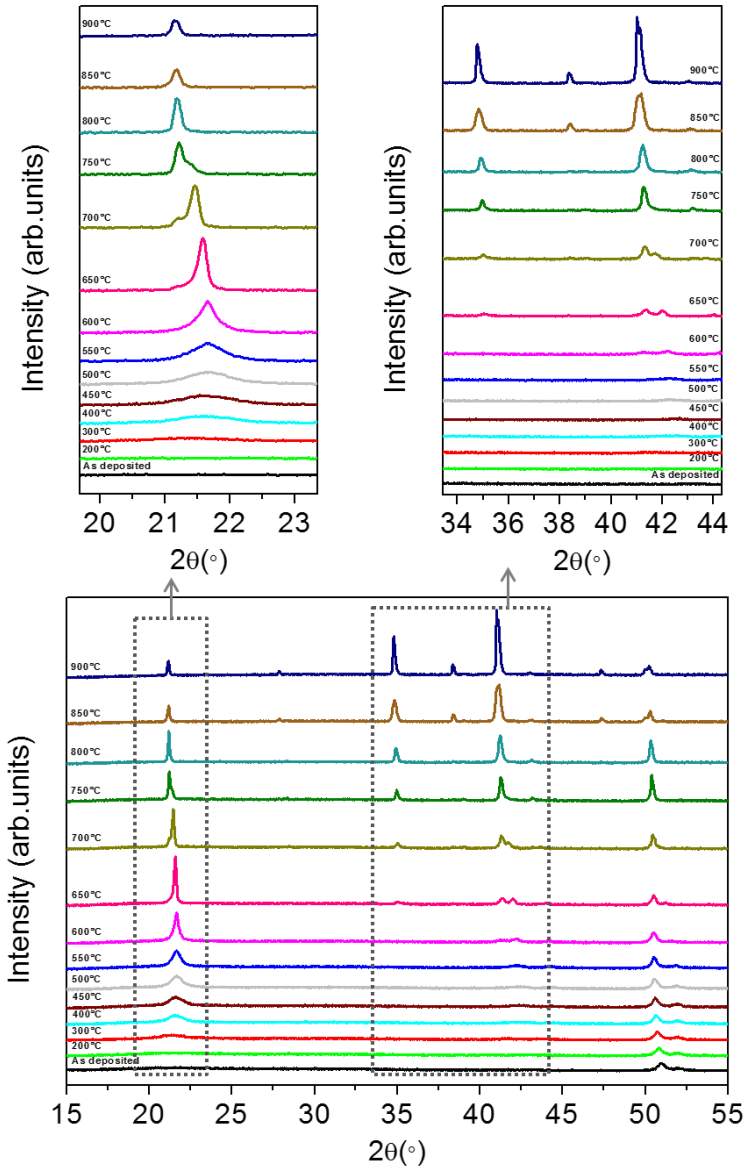

Figure 5.16: XRD patterns obtained for different temperatures in the *in-situ* thermal measurements.

was detected on them.

Table 5.4: Lattice parameter and χ^2 values obtained from the XRD data refinement.

Phase	**LNMO** (S.G.: Fd-3m)	**phase 2** (S.G.: Fd-3m)	χ^2
300°C	a = 8.189(5)	-	1.32
400°C	a = 8.186(2)	-	1.33
450°C	a = 8.183(1)	-	1.30
500°C	a = 8.180(1)	-	1.47
550°C	a = 8.1800(7)	-	1.30
600°C	a = 8.2355(7)	a = 8.409(5)	2.70
650°C	a = 8.2902(2)	a = 8.409(1)	3.0
700°C	a = 8.331(1)	a = 8.4152(3)	4.83
750°C	a = 8.3584(3)	a = 8.4215(5)	5.33
800°C	-	a = 8.4357(3)	6.37

FullProf program [94] was used for pattern refinement by Le Bail method (pattern matching), in order to determine crystal structure (space group), lattice parameters, and their evolution with temperature. The space group and lattice parameter values obtained for the different phases with the best refinement achieved, along with their standard uncertainties and reliability factor χ^2, are detailed in table 5.4. At the beginning of the crystallization process, from 300°C to 550°C, the best fit was obtained for a single phase with Fd-3m space group and unit cell of a=8.18 Å, in good agreement with what would be expected for LNMO spinel phase (8.17-8.21 Å, based on the ICSD database). At 600°C, although with very small contribution to the total signal, an additional phase had to be included for an optimal refinement. This additional phase had the same space group (Fd-3m) but slightly higher cell parameters (a=8.41 Å). For the following annealing temperatures, up to 750°C, XRD pattern was refined using the two phases, with the second one increasing its contribution to the total pattern as annealing temperature was increased. Additionally, a progressive increase of the lattice parameter values was estimated for both phases which was more prominent for the first phase than for the second. This effect might be related, at least partially, to a dilatation of the crystal structure due to the thermal expansion. In the case of 800°C annealing, proper refinement was only obtained when using the second spinel phase, meaning that first original phase was not detected. As mentioned before, for the last two temperatures (850°C and 900°C) extra peaks were present on the XRD pattern which were related to the formation of new phases, not identified at that moment. Indeed, for the last two patterns no good refinement was achieved. However, identification of those new phases

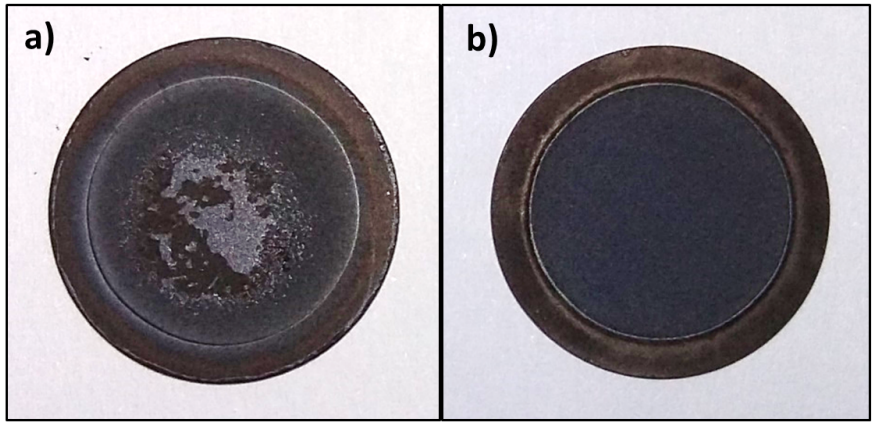

Figure 5.17: Visual differences between LNMO samples after being annealed to 900°C with different thermal treatments: a) sample used for XRD thermal *in-situ* experiment, and, b) sample used for the other characterization methods used.

was later clarified in this work.

Looking at the results as a whole, some conclusions can be obtained comparing the results obtained by the different techniques for the analyzed annealing temperatures. First of all, XPS and Raman results showed the same tendency. The best results, in terms of formation of LNMO phase and proper composition, were obtained for the intermediate temperatures, while big changes were only detected for the highest annealing temperature. From the XRD thermal in-situ results, however, changes on structure were noticed from 600°C on. Couple of things can be deduced from this difference. First, changes with temperature were occurring from bulk level towards the surface and, hence, were first detected by XRD and later, at higher temperatures, by Raman and XPS, which are more surface specific techniques. Secondly, the thermal treatment was not exactly the same for the XRD experiment than for the rest of characterization. As the XRD thermal experiment was performed *in-situ*, it was not cooled down at each step. Moreover, besides the 30 minutes temperature holding time in the case of XRD measurements, temperature was hold during the acquisition of the diffraction pattern, which was not the case for the rest of characterizations. Therefore, this difference on the thermal treatment could have accelerated and magnified the effects that temperature was producing on the sample. Indeed, certain difference was visually obvious when comparing the sample's surface appearance between the

XRD experiment sample and the one used for all other characterization. This difference can be observed in figure 5.17.

Regarding the diffraction reflection evolution observed in the XRD patterns above 600°C, there are several explanations for this effect. Choi et al. reported the evolution of the structure for LixNi0.5Mn1.5O4 for different x [95]. In the XRD measurements, they observed a progressive shift of the diffraction lines to lower angles as the value of x was decreasing from 1 to 0. They also observed a change in the ratio between (111)/(220) and (111)/(311) reflections, with continuous increase of the (220) and (311) diffraction lines and decrease of the (111) upon lowering of Li amount on the structure. Therefore, the evolution observed in our case might be related to a progressive loss of Li in the structure. Nonetheless, there are two issues that render this explanation rather unlikely for our case. First, Choi et al. did not report the presence of two coexisting phases, but a transition in the structure indicated by the progressive displacement of the reflections. Moreover, the XPS result did not indicate any remarkable evolution of the Li 1s signal that would suggest a change in the Li distribution on the sample.

Another effect that could explain the changes in the XRD pattern would be the progressive occupation of 8a tetrahedral sites in the spinel structure by a transition metal, which normally preclude lithium ion transportation in the spinel-framework [96]. Ohzuku et al. reported how in Fe doped LMO, Fe atoms can occupy the tetrahedral sites, which is indicated by a continuous augment of (220) and (311) diffraction intensities as the occupancy of 8a sites by Fe atoms increases [96]. Furthermore, they also reported an increase in the lattice parameters as the Fe occupies the tetrahedral sites. This would be in line with the results observed in our XRD, particularly if Fe is diffused from the SS substrate through the LNMO thin-film. In this case, the splitting of the peaks could be justified by the progressive doping of the material with Fe as the diffused area increased with the higher temperatures. Moreover, as a process starting from the bottom of the thin-film towards the surface, it would be logical to be first detected by XRD, and later by the further surface sensitive techniques like Raman and XPS. In addition, the idea would be more supported by the Fe detection on the LNMO surface by XPS at the highest annealing temperature. Nevertheless, Fe diffusion would not explain the new peaks that appeared in the XRD pattern for the highest annealing temperature.

A third possible origin of the evolution observed by different experimental

techniques could be nested on the instability of the substrate itself, via an oxidation process or similar. For instance, oxidation of SS substrate could lead to the formation of Fe_3O_4, which, in fact, has an spinel structure and a cell parameter a=8.39 Å, based on ICSD crystallographic database. Thus, the second spinel structure identified on the XRD analysis could be related to an oxidation process of the substrate itself. In the same line, the new peaks appearing on the XRD pattern at 900°C could be linked to other sub-products coming from substrate reactions at this temperature. Formation of these oxidized phases in the LNMO-current collector interface would have detrimental consequences in terms of adhesion of the LNMO layer and electronic conductivity, which would negatively affect the performance as electrode.

It goes without saying that the features observed in the characterization of the material could be driven by a mixture of the different effects mentioned so far, being more likely the last two. Those two hypothesis, related to effects coming from the SS substrate, are further investigated later in this chapter. In any case, whatever the explanation is, none of the effects mentioned above would be beneficial for the electrochemical properties of the LNMO layer. Therefore, from the point of view of obtaining an optimal LNMO phase from the annealing process, such effects should be avoided.

In conclusion, from the extensive analysis of the effects of the annealing temperature on the deposited thin-film LNMO, using a wide range of techniques that gave complementary information at different levels of the sample, an annealing temperature of 600°C was determined to be the optimal for obtaining the desired disordered spinel LNMO phase.

5.5 Study of the electrochemical performance

Once the thermal process to obtain optimized LNMO phase was determined, the electrochemical response of LNMO thin-films (annealed at 600°C) was determined. For the electrochemical tests, CR2032 cells were assembled following the protocol already described in this chapter. Cycling at room temperature was performed in Maccor Series 4000 battery tester, while the tests at higher temperatures were run in Biologic VMP3 potentiostats attached to Binder climatic chamber. Electrochemical behavior of the samples was studied by Galvanostatic cycling: charge-discharge cycles were run at different current rates to analyze the capacity retention of the material at different currents. The effect of the film thickness on the electrochemical response and the performance of the thin-film at high temperature in comparison with

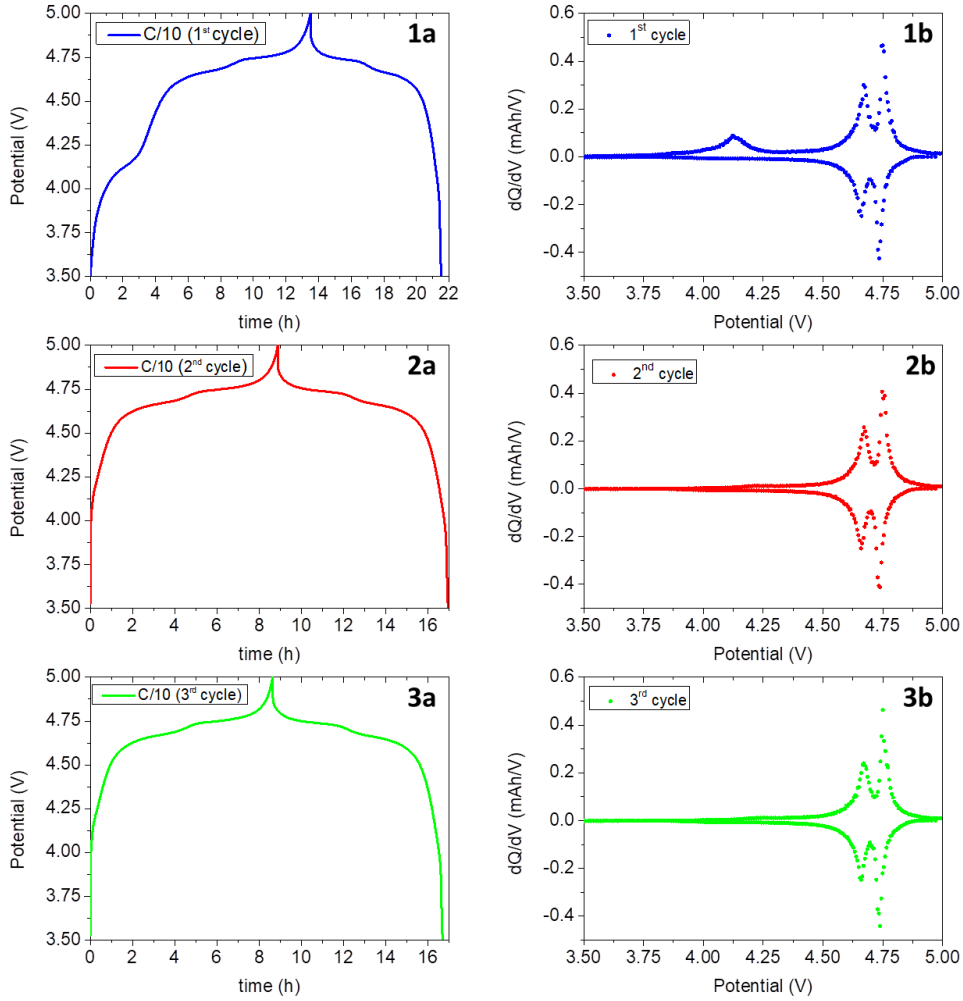

Figure 5.18: First (blue), second (red) and third (green) charge-discharge cycle for LNMO thin-film cycled at C/10. Potential evolution over the time (left column) and differential capacity vs potential (right column) are represented for each cycle.

commercial conventional LNMO electrodes was also investigated. Finally, the long cycling stability of the thin-film electrodes was tested.

First of all, the electrochemical response at low currents (C/10 rate) for LNMO thin-films was studied. The results are shown in figure 5.18, where potential evolution over time and differential capacity vs potential are dis-

played for the first three cycles. As can be observed, oxidation and reduction reversible reactions are present in the three first cycles. On the charge process in figure 5.18 1a, from 3.5 V to 5.0 V, two successive *plateaus* are present in the 4.67-4.75 V range. They are related to the $Ni^{2+} \rightarrow Ni^{3+}$ and $Ni^{3+} \rightarrow Ni^{4+}$ oxidation processes occurring during LNMO charge. These two processes are better discerned in figure 5.18 1b, where two peaks corresponding to the two oxidation processes appear at 4.67 V and 4.75 V. During discharge, equivalent *plateaus* can be observed (figure 5.181a) indicating that Ni is reversibly reduced. These reduction peaks are situated at 4.73 V and 4.66 V (figure 5.18 1b), with a low voltage hysteresis of 0.01-0.02 V between oxidation and reduction. The other feature present in the first cycle is a small *plateau* around 4.1 V (figure 5.18 1a) and the equivalent redox peak in figure 5.18 1b, which is most probably related to some traces of Mn^{3+} that is commonly seen for this phase [68]. It could also be related to the SS substrate, as will be shown later in this chapter. This oxidation process is irreversible as only occurs during the charge. During the second (figure 5.18 2) and third (figure 5.18 3) cycles, redox reactions related to Ni were reproduced in a very similar way, while the last oxidation reaction linked to Mn^{3+} did not appear anymore. Thus, deposited LNMO thin-films showed reversible electrochemical response, in good agreement with what is reported [64, 70, 97].

In terms of specific capacity, values obtained both for charge and discharge are detailed in figure 5.19. In this figure, specific capacity obtained for different C-rates are plotted for charge and discharge, along with the Coulombic efficiency (CE) of each cycle. In the first cycle, at a rate of C/10, charge capacity was 199 $mAhg^{-1}$, while the discharge capacity was 118 $mAhg^{-1}$, resulting in a CE as low as 59.2%. This low value of the efficiency in the first cycle was mainly nested in the irreversible oxidation process observed in the first charge. This discharge capacity value corresponds to an 80% of the theoretical capacity of the material (146.5 $mAhg^{-1}$). For the rest of the cycles, charge capacity decreased, reaching a value of 125 $mAhg^{-1}$ for the fifth cycle, whereas the discharge capacity was stabilized at 118 $mAhg^{-1}$. The CE value for that cycle was 94.6% which, despite being much higher value than in the first cycle, was still a low value. The reason of the low CE at C/10, stems from the instability of the liquid electrolyte used above 4.3 V as already explained in the introduction.

For higher C-rates (higher current intensities), the CE progressively improves as the current is increased. The increase in CE is a consequence of the decrease of the electrolyte decomposition parasitic reactions owing to high

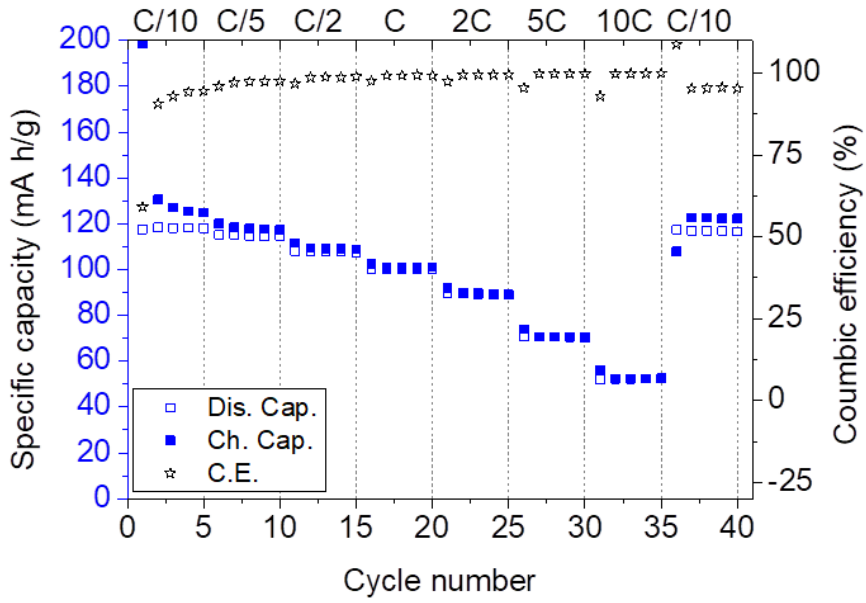

Figure 5.19: LNMO thin-film cycled at different C rates. Specific capacity of charge and discharge processes, along with the Coulombic Efficiency are represented for each cycle.

C-rate cycling; the reduced charge-discharge times affect those undesired decomposition reactions which also occur over a short time, thus, contributing in less amount to the total charge capacity. Therefore, CE of 97.6% is achieved in the fifth cycle at C/5, is improved to 99.2% at C, 99.8% at 5C, and even 100% at 10C. Regarding the capacity retention, as expected, the higher the C-rate the lower the capacity. This behavior is typical for any electrode material and it is originated by Li-ion diffusivity limitations within the crystal lattice. In the case of our LNMO thin-film electrodes, discharge specific capacity at C/10 rate was 118 $mAhg^{-1}$. When current was increased, retained capacity continuously decreased to 114 $mAhg^{-1}$ at C/5, 108 $mAhg^{-1}$ at C/2 and 100 $mAhg^{-1}$ at C rate, corresponding to 96.6%, 91.5%, and 84.7% of the initial capacity, respectively. For cycling rates above C, capacity loss continued decreasing even more pronouncedly. A capacity of 89 $mAhg^{-1}$, 70 $mAhg^{-1}$, and 53 $mAhg^{-1}$ was obtained for 2C, 5C and 10C rates, corresponding to 75.4%, 59.3%, and 44.9% of the initial capacity. After cycling at 10C rate, once the cell was cycled back at C/10 rate, almost full initial capacity was recovered (117 $mAhg^{-1}$, 99.1% of the initial capacity).

Thereby, good electrochemical performance of the LNMO thin-films was observed, with reversible charge-discharge cycles demonstrated up to a C rate of 10C, and recovery of the initial capacity once back in lower C-rate. In terms of CE, improved efficiency at higher rates was measured, in good agreement with previous reports [73]. Regarding the specific capacity, our results did not reach the best capacity reported up to date, which is close to theoretical for rates up to 1C [74], and capacity retention above 90% of the initial capacity up to 10C [72]. However, for the sake of clarity, it is worth mentioning certain differences in the method used for the calculation of the capacity and the electrochemical cycling:

- In most of the works reporting the cycling behavior of LNMO thin-films, specific capacity is calculated based on the thickness of the film [63, 68, 74]. To do so, certain value for the density of the material is assumed. Taking into account that the density strongly depends on the material porosity, which, in fact, can be different for different deposition conditions, errors in the calculation of the capacity can be induced. Moreover, sometimes, homogeneity of the film thickness is also assumed, and capacity values are based on estimated thicknesses. In our case, calculations were based on direct measurement of the thin-film mass.

- In some cases, among which the best reported capacity retentions are included [68, 70, 72], despite using the same galvanostatic techniques used in this work, different electrochemical methods were used which could induce better capacity retentions. As an example, Constant Current Constant Voltage (CCCV) cycling, or the use of lower charging C-rates compared to the discharge rate, can help to overcome Li-ion diffusivity limitations at high rates, and, thus, to obtain better capacity values.

Therefore, these differences with other works reporting similar studies render difficult the comparison of the capacity values obtained. However, our capacity and CE values were better than the values recently reported for LNMO thin-films using direct active material mass quantification [73].

5.5.1 Effect of layer thickness

Next step within the electrochemical characterization of the thin-film LNMO electrodes was to analyze the effect of the electrode thickness. From

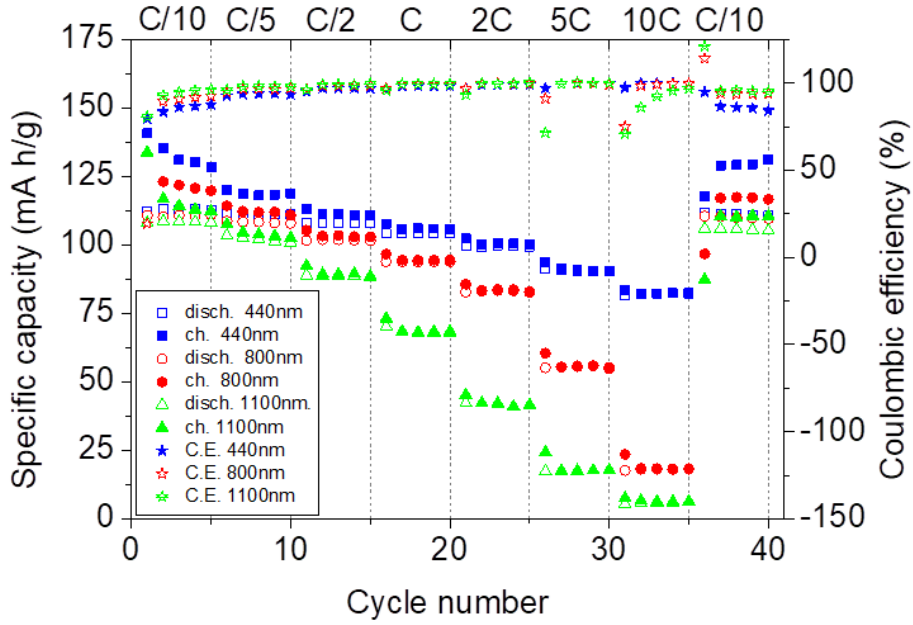

Figure 5.20: LNMO thin-films with different thicknesses cycled at different C-rates. Specific capacity of charge and discharge processes, along with the Coulombic Efficiency on each cycle, for 1100 nm thick (green triangle), 800 nm thick (red circle), and 440 nm thick (blue square) electrodes.

the theoretical point of view, the thicker the electrode, the higher the areal mass loading and, thus, more capacity. However, in reality, the thicker the electrode, the longer is the distance the ion and the electron have to travel in the intercalation/de-intercalation process during discharge/charge of the electrode, hence, limiting the electrochemical. Therefore, LNMO thin-film electrodes with different thicknesses were cycled in order to study the electrochemical response as a function of the thickness.

Results obtained are gathered in figure 5.20, where capacity obtained for charge and discharge cycles at different C-rates are represented for several thickness of the LNMO electrode. CE of each cycle is also indicated. Three different thickness were analyzed, namely, 440 nm, 800 nm, and 1100 nm. Thickness values were determined by a stylus profiler over a masked Si wafer piece that was simultaneously deposited with each of the electrode samples.

Initial discharge specific capacity was similar for the different samples

(108-112 $mAhg^{-1}$), indicating that at low C-rates the Li-ion diffusion through the spinel lattice is not a limiting factor for the electrochemical performance. The CE was low in the first cycle and, in general, at C/10, similar to what was observed from figure 5.19. Lower CE values were obtained for thinner electrodes, although this outcome is not surprising [74]. As stated before, the inefficiency is caused by the electrolyte decomposition process occurring predominantly during the charge. Since electrode area and electrolyte volume are roughly the same for all samples, the inefficiency will be similar for all of them. Then, in terms of specific values, the absolute inefficiency will be higher for the thinnest electrode due to the higher surface/bulk ratio.

When the current was increased, differences in specific capacity were evidenced. Although all the samples followed the usual behavior, losing capacity at higher C-rates, the thinner the electrode, the better was the capacity retention. Moreover, the capacity loss was not linear with the thickness, being much strong the effect in the thickest electrode (1100 nm) than in the intermediate one (800 nm). At C/2, the capacity retention was 95.7%, 91.5% and 81.6% of the initial value for the 440 nm, 800 nm, and 1100 nm electrodes, respectively. At 2C rate, capacity retention values were 88.2%, 74.8%, and 38.4% from the thinnest to the thickest electrode, respectively. Thus, the capacity decay was not linear with the thickness of the LNMO layer, being the effect more pronounced in the thickest electrode. For even higher C-rates, the decay effect on the 800 nm sample was accelerated, as can be seen in figure 5.20, with a specific capacity of 16.4% at 10C. Moreover, for the thickest electrode (1100 nm), capacity retention at 10C was only 5.8%. Nevertheless, for the thinnest electrode (440 nm) very good retention was observed: 73.0% of the initial capacity. Therefore, at the highest C-rates, even with less active material, higher overall capacity was obtained by the electrode with a thickness of 440nm, compared to those of 800 nm and 1100nm.

After cycling at high currents, when the current was set back to C/10 rate, all the electrodes recovered above 97% of the initial capacity. In terms of CE, the evolution upon C-rate increasing followed the same trend previously described in figure 5.19.

Based on these rate capability studies, the effect of the electrode thickness on the electrochemical performance was confirmed. In spite of having a similar initial specific capacity at low C-rates (C/10), for higher currents the difference in specific capacity started to be significant mainly for the electrode with a thickness above 1 μm. For the highest C-rates (5C and 10C), the dif-

ference was notorious, with remarkable differences between the thinnest electrode (440 nm) and the other two (800 nm and 1100 nm). For those C-rates, even with less material, higher total capacity was obtained. Therefore, the best electrochemical performance was obtained for the 440 nm thick electrode.

5.5.2 Effect of temperature

Continuing with the electrochemical evaluation of the LNMO thin-films, the effect of the temperature on the electrochemical response was investigated. It has been mentioned several times in the text, that one of the main degradation mechanisms in LNMO electrodes is the decomposition of the electrolyte in the high voltage region. At elevated temperatures the kinetics of this chemical reactions are accelerated, thus enhancing such deleterious effects [98]. Solid electrolyte should tackle the decomposition problem associated to organic solvents, being, hence clearing out any safety problem for the battery concept pursued in this project. However, in order to perform a thorough study of our electrodes in comparison with commercial LNMO, their performance at higher temperatures was investigated.

For that purpose, thin-film and commercial LNMO electrodes (Custom-cells) were used to assemble coin cells under the same conditions described before. Cells were introduced in an oven (Binder, model 115) at 50°C, and tested in Biologic VMP3 potentiostat with galvanostatic techniques. Results from both electrodes are shown in figure 5.21, where the electrochemical performance of a thin-film, compared with a commercial LNMO electrode, cycled at different C-rates, is represented. As can be observed, although initial specific capacity of the thin-film electrode was higher (112 $mAhg^{-1}$ vs 84 $mAhg^{-1}$ for the commercial electrode), upon C-rate increase, loss of capacity was much higher for thin-film electrodes than for the commercial LNMO. At a current intensity equivalent to a rate of C, thin-film electrode only retained 36.6% of the initial capacity (41 $mAhg^{-1}$), while the commercial electrode retained 87.0% (73 $mAhg^{-1}$). Nonetheless, at the highest rates tested, namely 5C and 10C, no capacity was obtained for the commercial electrode, whereas the thin-film electrode was still showing some electrochemical response (although as low as 15$mAhg^{-1}$ at 5C and 9 $mAhg^{-1}$ at 10C).

In terms of Coulombic efficiency, results were on the same line than for the specific capacity. Better CE was measured for the commercial cell at any C-rate, and, in particular, really low CE was delivered by the thin-film electrode at C/10 rate: the first two cycles, CE was below 35% (charge capacity of 1114 $mAhg^{-1}$ and 334 $mAhg^{-1}$, out of the scale in figure 5.21) and, despite

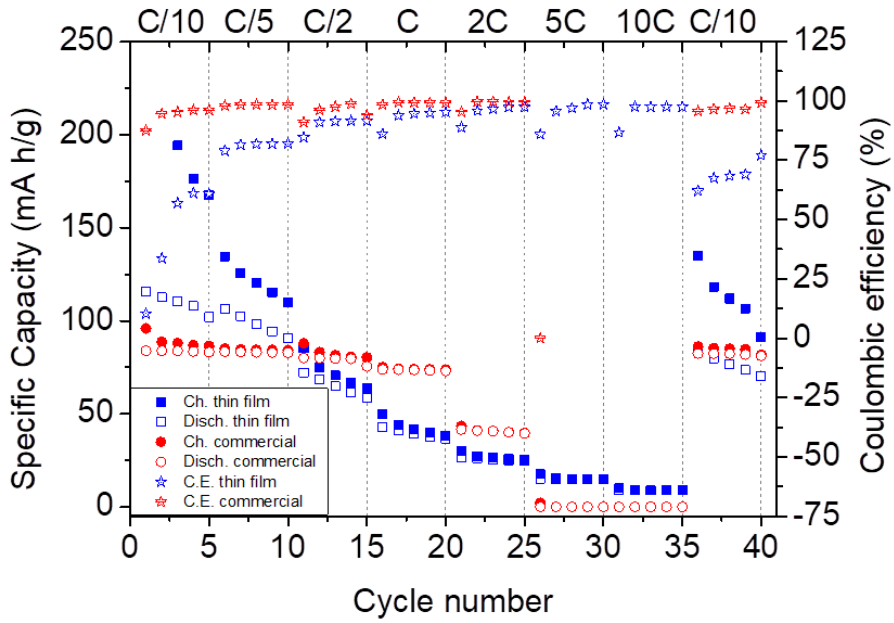

Figure 5.21: Electrochemical performance of LNMO thin-films and commercial electrodes cycled at 50°C at different C-rates.

improving for subsequent cycles, it was below 80% for all the cycles performed at the lowest rate.

5.5.3 Long cycling behavior

Last, but not least, long cycling performance of the deposited LNMO was investigated. Once more, our thin-film electrode was compared with commercial electrode under the same conditions. Formation cycles were performed first, followed by long cycling period with a current corresponding to C. Formation cycling procedure was defined as two cycles at C/10, C/5 and C/2.

Results are shown in figure 5.22, where normalized discharge capacity is represented vs the cycle number. Thin-film LNMO electrode had much more stable capacity retention upon cycling compared to the commercial electrode. Battery life of thin-film electrode (which is usually considered while more than 80% of initial capacity is kept) was around 2000 cycles, whereas for the commercial one was below 150 cycles. Hence, much better long cycling elec-

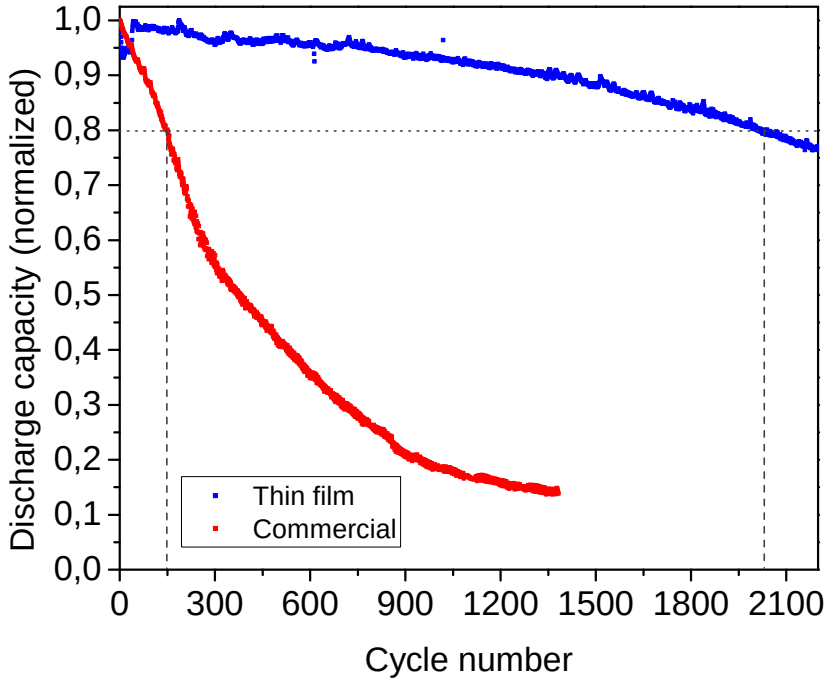

Figure 5.22: Discharge capacity evolution of LNMO thin-film and commercial electrodes at 1C for long cycling.

trochemical performance was obtained for thin-film LNMO electrodes than for commercial conventional electrodes, which is an outstanding result from the point of view of applicability. In addition, it is worth noting that using solid electrolyte cycle life of the electrode would improve considerably, as deleterious effect arisen from liquid electrolyte decomposition would be avoided. Thus, as using the thin-film LNMO electrodes in all solid state battery is the final goal of the project, its cycle life should dramatically improve in this kind of configuration.

5.6 Substrate oxidation and diffusion effect

In a previous section (section 5.4), the effect of the annealing temperature in the LNMO sample was studied. Although a conclusive result about some features present in Raman and XRD data at high annealing temperatures was not obtained, some of the speculative possibilities proposed were related to an effect occurring with the temperature in the substrate. From XPS results on the films annealed at at 900°C, Fe diffusion at that temperatures was con-

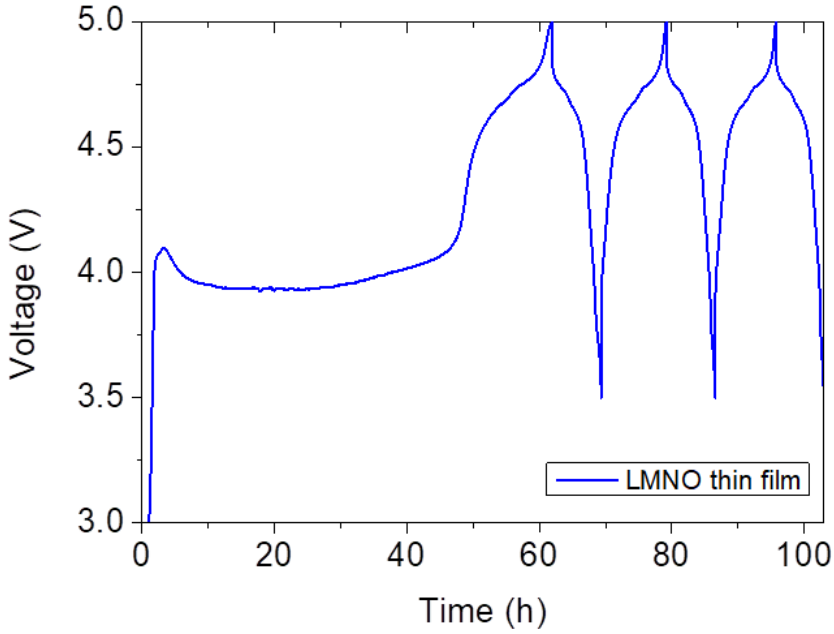

Figure 5.23: Non reversible electrochemical process on LNMO thin-film sample during the first charge. First 3 charge discharge cycles at C/10 rate.

firmed. In spite of the absence of Fe on the XPS spectra from films lower temperatures, the possibility of diffusion should not be discarded. Moreover, XRD and Raman results from the samples annealed at the highest annealing temperatures might also have a correlation with the effects of temperature in the SS substrate, as suggested in section subsection 5.4.2. In addition, during the electrochemical characterization of the LNMO thin-films, another phenomena was observed in some of the cycled samples. During the first charge, or in the second charge in extraordinary cases, a long non-reversible electrochemical process was detected (figure 5.23). In order to elucidate the origin of this feature and clarify the stability of the substrate at high temperatures, electrochemical characterization was performed on the bare SS substrate.

First, SS discs, identical to those used for the deposition of the LNMO, were heated in the oven at 600°C, 750°C and 900°C for 1 hour, and characterized by XRD and Raman spectroscopy. Results are represented in figure 5.24. In spite of some change for the reflection related to Fe on the SS, there was no

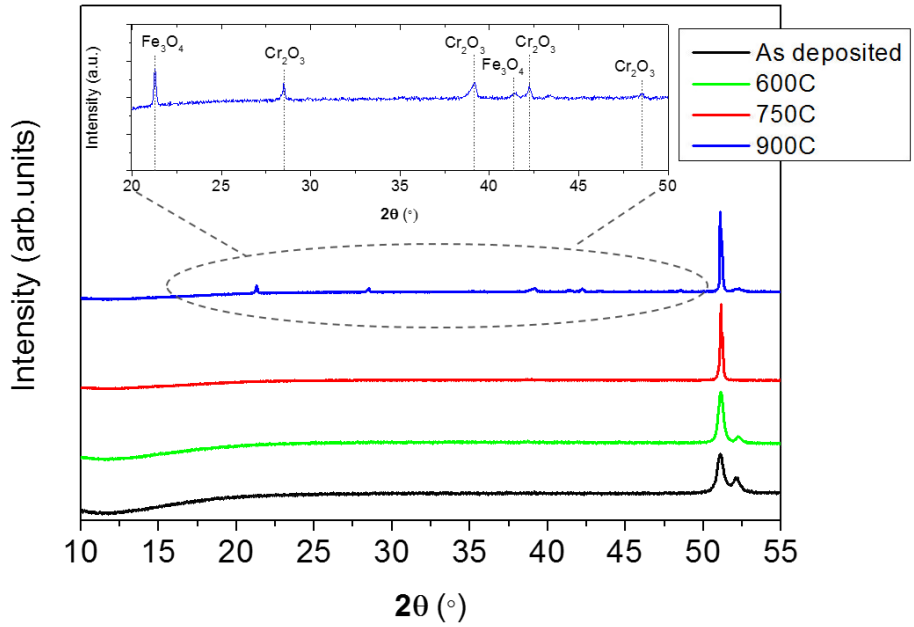

Figure 5.24: XRD of SS substrate annealed at different temperatures. Inset of the substrate annealed at 900°C, with the identification of new reflections.

presence of new reflections indicating the formation of new phases that could be related to the changes observed in the T-chamber experiment described previously (section subsection 5.4.2). However, at 900°C, new peaks appeared as identified in figure 5.24. Therefore, at the highest annealing temperature, SS substrate suffered an oxidation effect that was partially responsible of the changes detected by XRD in the thermal *in-situ* experiment.

Despite of the fact that no considerable changes were detected by XRD at lower temperatures, sample was also characterized by Raman to identify eventual effects at surface level. Indeed, as can be seen from figure 5.25, differences appear starting at 600°C upwards, with different spectra obtained for all other temperatures. Pristine SS substrate showed only baseline Raman spectra, owing to its metallic nature. At 600°C several Raman transitions were detected, indicating that some non-metallic phase was formed on the surface. Comparing with the data obtained from database (Rruff project), at this annealing temperature a mix of two iron oxides are formed, namely, hematite (Fe_2O_3) and magnetite (Fe_3O_4). At 750°C, the bands related to hematite disappear and only bands corresponding to magnetite remain. Fi-

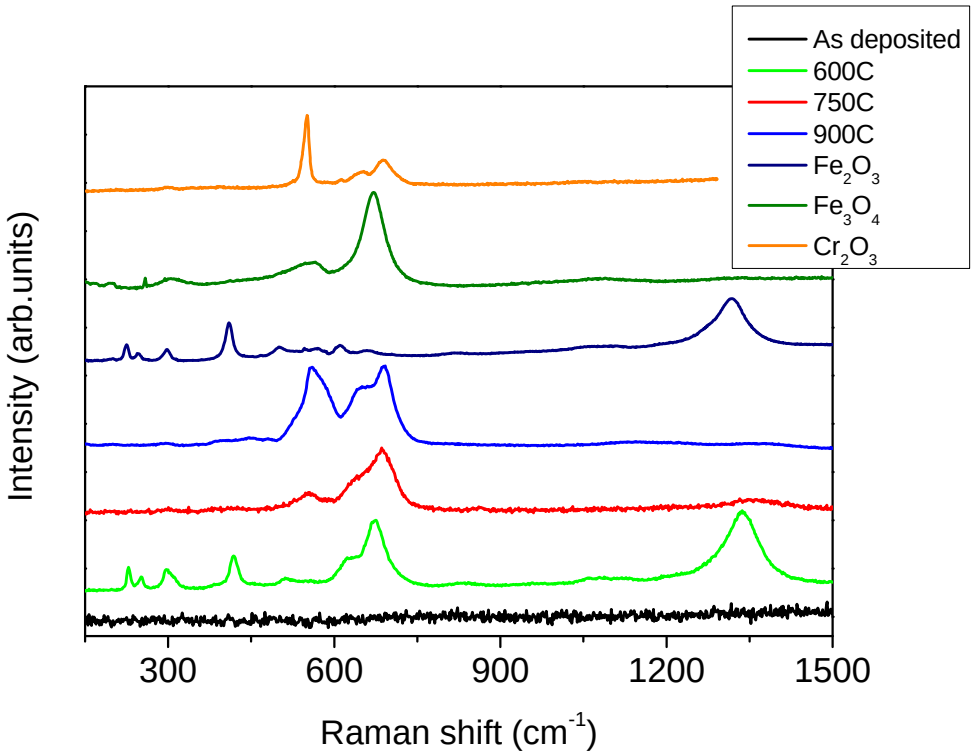

Figure 5.25: Raman spectra of SS substrate annealed at different temperatures, along with Fe_2O_3, Fe_3O_4, Cr_2O_3 spectra obtained from database.

nally, at 900°C, eskolaite (Cr_2O_3) is also detected, being the spectra formed by overlapping signal of magnetite and eskolaite. Therefore, it is clear that the outermost surface of the SS suffers from oxidation when it is annealed in air, forming an oxide layer even at 600°C which was the temperature chosen for the crystallization of the LNMO thin-film. This oxide layer, being present in the electrode-current collector interface, could affect the electrochemical performance.

In order to verify the effect that the oxide layer formed on the SS surface may have on electrochemistry and, in particular, to elucidate if the irreversible process detected in the first charge for several samples stemmed from this oxide layer, an SS substrate was electrochemically cycled. The SS disc was annealed in air at 600°C and assembled in a coin cell following the same procedure used for any other electrochemical characterization. Charge-discharge program was set with similar currents used for a C/10 rate for LNMO thin-films. The electrochemical response obtained is included in figure 5.26. The

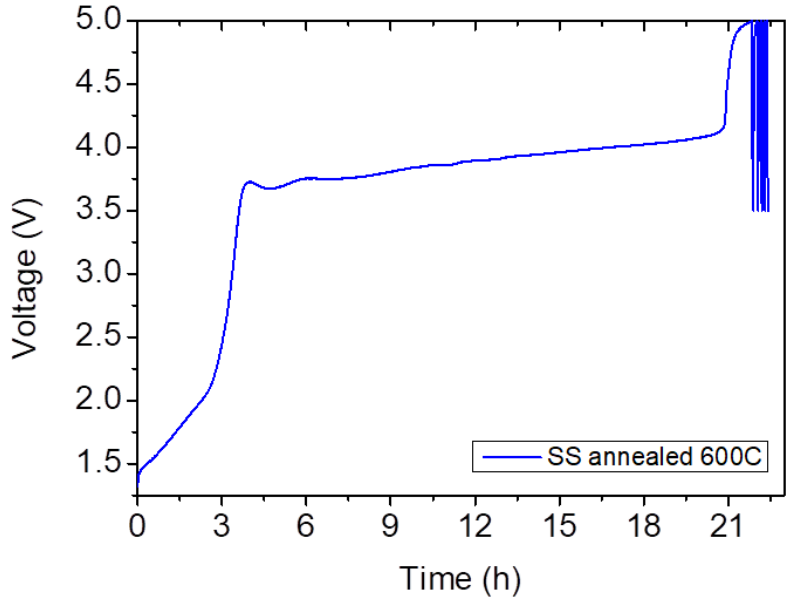

Figure 5.26: Electrochemical test on SS substrate after being annealed at 600°C in air.

irreversible process of the first cycle was similar to those obtained for the LNMO samples shown in figure 5.23. Hence, not only the oxidation of the substrate during the annealing process, but also its influence on the electrochemical process was demonstrated.

Besides the oxidation of the SS, the possible diffusion along the LNMO layer was unclear. The diffusion towards the surface was confirmed by XPS for an annealing temperature of 900°C, but progressive diffusion upon temperature increase could also be happening. Cross section SEM measurements were performed to clarify if diffusion was occurring at the selected annealing temperature (600°C). Thick LNMO layer, about 2 μm in thickness, was used to facilitate the characterization and have reliable results. EDS measurements were carried out to detect the different elements present along the LNMO films.

EDS mapping results are represented in figure 5.27. Detected elements were C, O, Ni, Mn, Cr, and Fe. C signal was limited to the upper region of the image, corresponding to the epoxy where the sample was embedded.

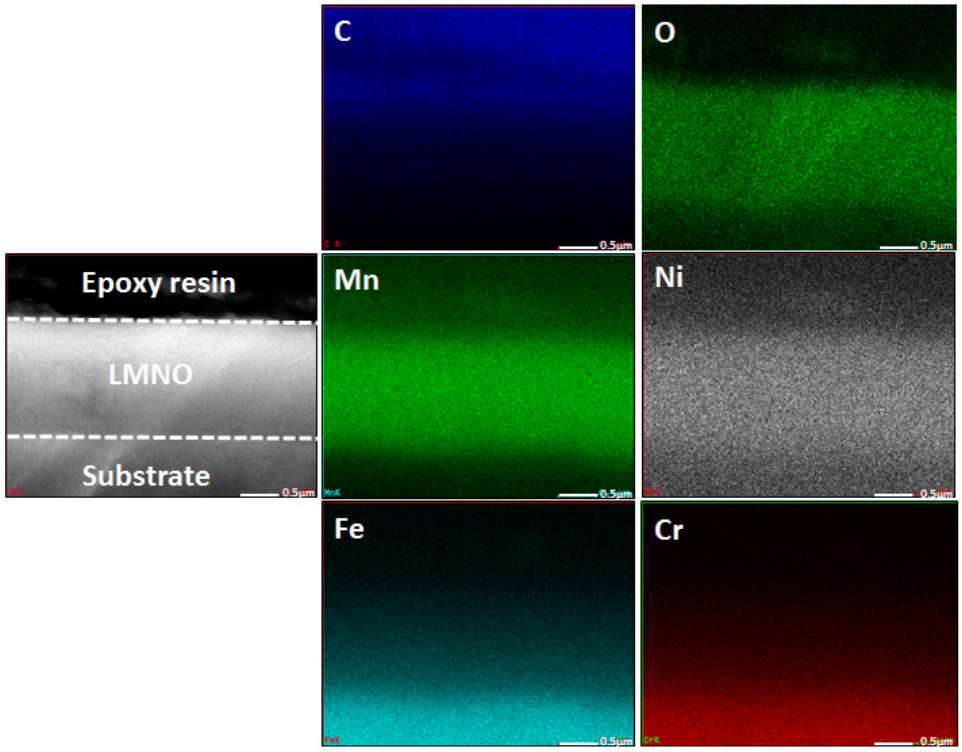

Figure 5.27: EDS mapping images obtained for C, O, Mn, Ni, Fe, and Cr in the LNMO cross-section analysis.

O was limited almost exclusively to the central region, corresponding to the LNMO film, similar to Mn signal, which was also very intense in the intermediate layer. Despite being more intense on the LNMO region, Ni was also present on the substrate, which is normal considering it is present in some stainless steel compositions. Fe and Cr were delimited to the lower part of the scanned area, corresponding to the SS side, although a progressive decrease of the signal from the SS towards the LNMO layer could be intuited.

Line mapping EDS analysis was also measured to obtain better resolved results (figure 5.28). EDS was measured along the line indicated in figure 5.28. Limiting interfaces between substrate, electrode and epoxy resin used for sample preparation are indicated by dashed lines. Such limits match with changes observed in the EDS intensity detected for the different elements, in good agreement with the transition between different layers present on the sample. In particular, for Fe and Cr, high concentration is detected in the

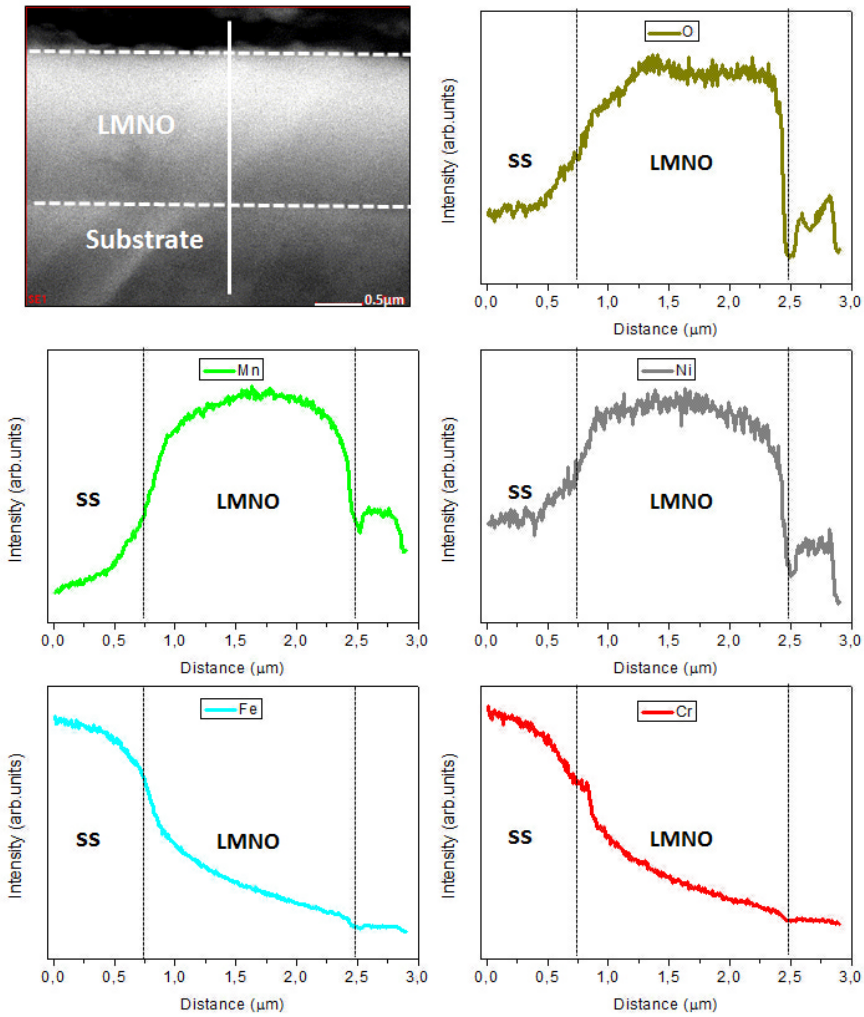

Figure 5.28: EDS detection evolution of O, Mn, Ni, Fe, and Cr accross the line indicated in SEM LNMO cross-section image (top left).

region corresponding to SS layer, while it is progressively decreasing in the LNMO side, suggesting a slight diffusion process from the SS to the LNMO layer.

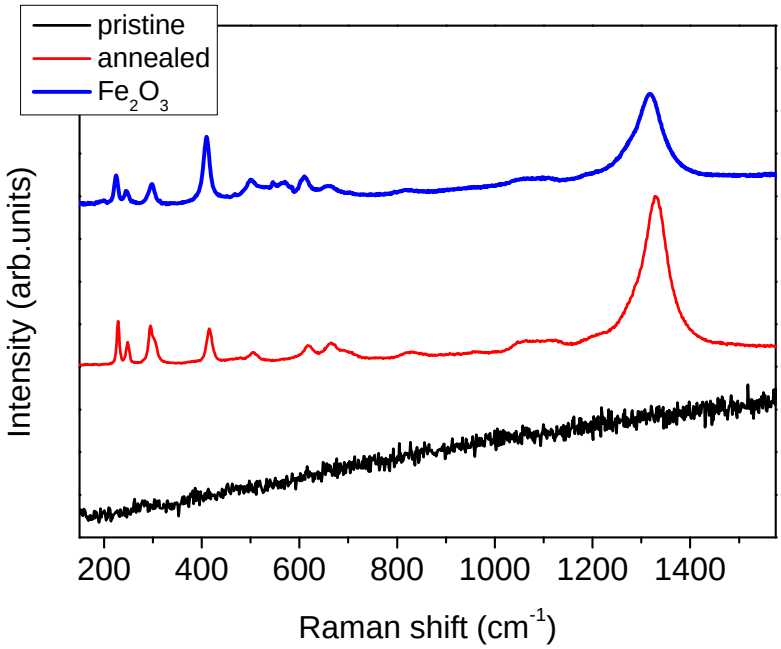

Figure 5.29: Raman spectroscopy on gold coated SS substrates, before and after annealing at 600°C in air, as well as Fe_2O_3 spectra, from database.

5.6.1 Deposition of protective layer

Interface between SS substrate and LNMO thin-film was demonstrated to be critical point, since formation of interphase oxides and diffusion of metals across the LNMO film was detected. Deposition of buffer layers with protective purpose could be the solution to stop those interface processes. Gold was chosen as first tentative coating material, based on its good conductivity and stability. In fact, it was already used as current collector in previously reported works [97]. Besides, Gellert et al. reported the formation of mixed oxides interlayer in gold coated SS substrate, although they claimed that no deleterious effect was produced by this layer on the electrochemical performance of LNMO thin-films [60]. Hence, based on previous reports, Au coating layer, although not free of reactions, should be a valid protective layer between SS substrate and LNMO thin-film.

Substrates were coated with 1.5 μm thick layer by electroplating. Au deposited substrates were characterized and annealed at 600°C, in order to study the effect of the temperature on the coated surface. Surface was analyzed by means of Raman spectroscopy. Since Au is a metal, it should be free

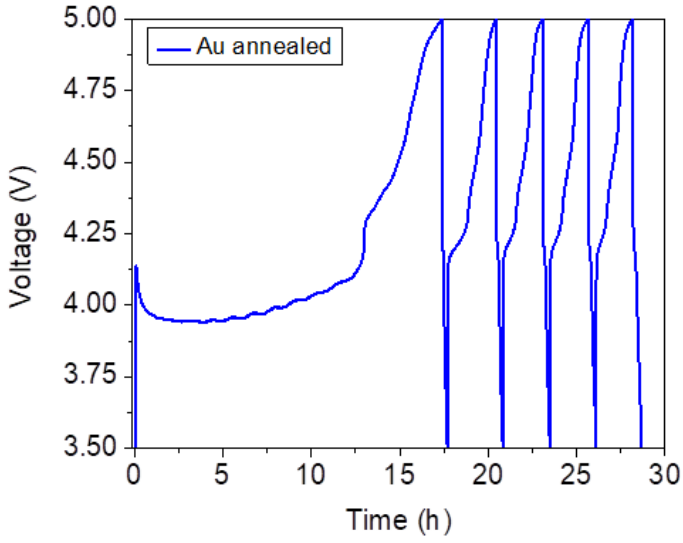

Figure 5.30: Electrochemical test on gold coated substrate after being annealed at 600°C in air.

any Raman transition. Thus, the presence of oxide formation on the surface due to the annealing process should be detectable by Raman spectroscopy.

In figure 5.29, results obtained for as received gold coated substrate and annealed counterpart are represented. As it was expected, only baseline Raman signal was detected in the as received coated substrate. On the other hand, once it was annealed, it showed several Raman bands resembling to the result obtained for bare SS substrate. Indeed, detected bands correspond to hematite, same as in the case of the of bare SS substrate annealed at that temperature. Hence, Au layer did not stop neither the diffusion, nor the formation of oxides.

Electrochemical test was performed on Au coated substrate, in order to verify its electrochemical (in)activity. Sample was cycled under the same conditions described before for the bare SS substrate. Obtained results are represented in figure 5.30. In contrast to what was claimed by Gellert et al., the electrochemical activity of the oxide layer formed on gold coated SS substrate surface was demonstrated. Thereby, such interlayer would affect to the overall electrochemical response of the cell, meaning that Au is not a proper

option as a protective buffer layer between SS substrate and LNMO thin-film electrode.

Other potential buffer layers should be investigated to obtain upgraded interfaces, free of interphases that could hinder the overall electrochemical performance of the cell. Recently, Filippin et al. reported the use of chromium nitride as a stable cathode current collector for all solid state thin-film Li-ion batteries [73]. Hence, CrN could also be a potential material to be used as protective layer in the case of study.

5.7 Sputtered Li-La-Zr-O thin-films

The final objective of this thesis project, as mentioned in the introduction, was the development of different layers composing a thin-film all solid state battery. LLZO was chosen as alternative to usual LiPON electrolyte, due to its advantageous properties already described. Since almost no information was available on the growth of LLZO thin-films by magnetron sputtering, a sputterability assessment of LLZO had to be performed. This was followed by an optimization of the sputtering system itself and the analysis of the deposited film properties under different conditions.

5.7.1 Sputterability of Li-La-Zr-O thin-films

First, the sputterability of Li-La-Zr-O thin-films in our system was studied. Pfeiffer Classic 500 SP instrument was used, with 2'' magnetron sputtering head. An LLZO stoichiometric target (Toshima Manufacturing Co, Cu backing plate and In bonding) was used for the initial tests. Since the LLZO is an electronic insulator material, an RF power supply was required. Due to the brittleness of ceramic targets, applied power had to be slowly increased when initiating the sputtering process, following a ramp up of 10-20 W/min. Plasma was ignited at 0.5 W/cm^2 with a chamber pressure of 8.5 $\times 10^{-3}$ mbar, in pure Ar atmosphere. Next step was to perform a screening of different deposition parameters in order to find the best deposition conditions for good deposition-rate, adhesion of the film and desired stoichiometry and morphology. Several films were grown on Si(100) substrates changing sputtering conditions. Target-substrate distance and orientation was optimized within the limits of the system and the effect of applied power and Ar flux was studied. Optimal conditions were found to be a power density of 1.5 W/cm^2 and an Ar flux of 45 sccm, corresponding to a chamber pressure of 8.5 $\times 10^{-3}$ mbar. The low value of the power density was selected to avoid target fracture under higher power.

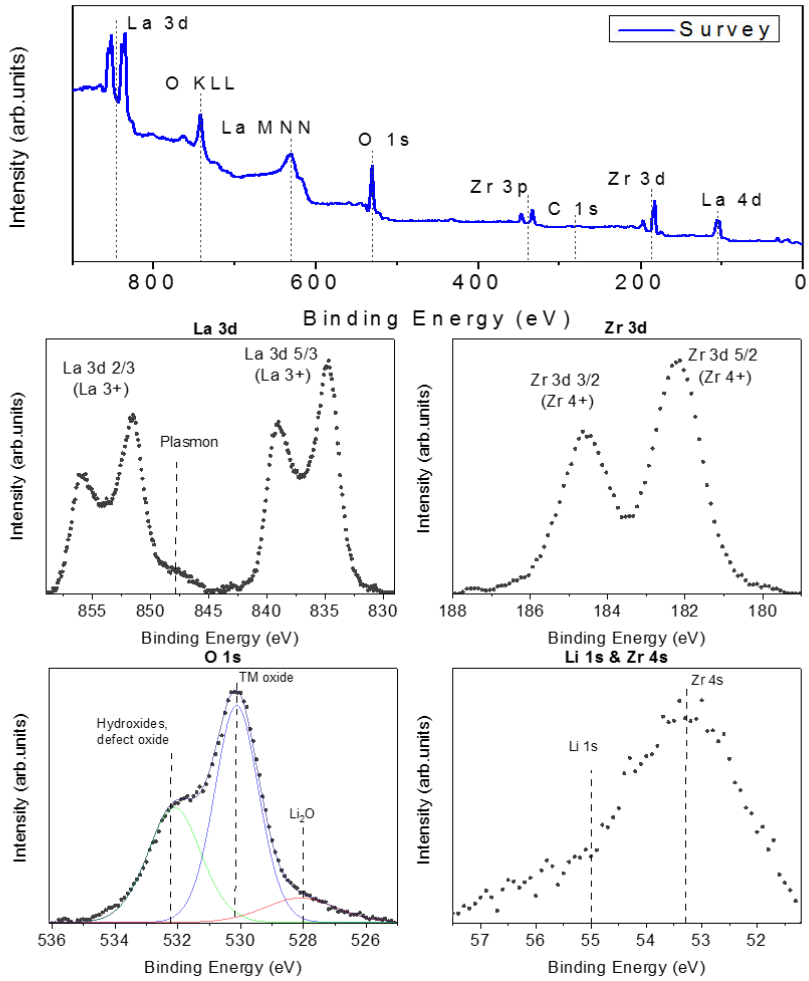

Figure 5.31: XPS results of the Li-La-Zr-O layer deposited. Survey spectra with the elements detected (top), and, particular regions of the elements of interest, with experimental data (dotted curves), deconvolution of peaks in colored areas, and overall fitting (line).

Table 5.5: La, Zr and O relative ratios obtained for the deposited Li-La-Zr-O layer, as determined from the quantification of XPS data.

Sample	O/La	O/Zr	La/Zr
Li-La-Zr-O film	3.7	4.1	1.1

Deposited films were characterized by means of XPS to determine the composition, using a Phoibos 150 XPS spectrometer and a non monochromatic Mg Kα source (hν =1253.6 eV). First a survey spectra was recorded, for the overall detection of the elements. Specific regions for each detected element were also measured with higher resolution. Regions were measured with the following conditions: 0.5 eV step size, pass energy value of 30 eV, dwell time of 0.5 s and 3 scans. XPS results are represented in figure 5.31. CasaXPS was used to analyze the collected XPS data: O 1s spectrum was deconvoluted with Gaussian-Lorentzian functions, and Shirley type background was used. Expected elements for this material were detected in the survey spectra with no impurities or contamination from other elements. As can be observed, C is barely present on the survey spectra. As described previously along this work C is usually present in samples exposed to air and it is useful for binding energy calibration. The absence of C 1s signal stems from the use of a transfer tool that allowed transferring the samples from the sputtering chamber into the XPS chamber under ultra high vacuum. Thus, binding energy was calibrated in a different way: Zr 3d 5/2 peak was set to 182.2 eV, which is the energy commonly reported for zirconium in oxide form (ZrO_2) [99], all other peaks were shifted accordingly. Particular regions of the elements, also represented in figure 5.31, were used for the quantification of the relative concentration. Looking at the results gathered in table 5.5, ratio between La and Zr elements was close to nominal LLZO, although marginally poor in Zr. La 3d region showed the typical spectra for La^{3+} in oxide form [100, 101]. Moreover, oxygen deficiency was detected, suggesting the need for reactive sputtering to obtain desired stoichiometry. Besides, for the O 1s region, best fit was obtained for a deconvolution using three components. Transition metal oxide's contribution is typically present around 530 eV, although there are exceptions and it can vary depending on the oxide. Furthermore, for the LLZO, we would expect a single peak. Therefore, the presence of different contributions, in particular taking into account the fact that only La, Zr and Li were detected apart from O, could suggest the mix of three different oxides. In addition, there might be a deficiency of lithium, although it was difficult to reach a conclusion on this regard, due to the low relative sensitivity factor of Li and the overlapping of Li 1s and Zr 4s photoelectron signals.

In order to determine the deposition rate of the sputtering process, a cross section SEM measurement was performed. Images (figure 5.32) were taken with an accelerating voltage of 30 kV in a FEI Quanta microscope. Since the electronic conductivity of the sample was rather low, it was gold-coated (few

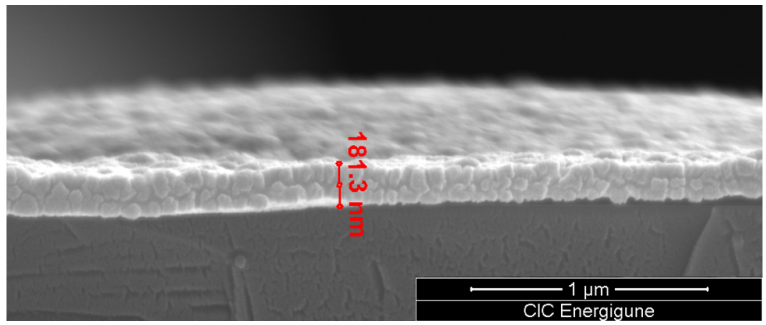

Figure 5.32: SEM cross-section image of the Li-La-Zr-O layer deposited by magnetron sputtering.

nanometers) with a SPI-Module sputter coater, so that the layer could be properly focused. Film thickness was around 180 nm, which involved a deposition rate of approximately 14 nm/h. The reason to have such a low value was twofold. First, the intrinsic limitation of the RF mode along with the low power used to avoid damaging the target. Secondly, the substrate-target configuration which was limited by the design of system itself. In fact, the distance from the target to the substrate was above 15 cm, while standard values in sputtering deposition are below 10 cm.

5.7.2 Improvement of deposition rate and film quality

Before continuing with the optimization of the deposited thin-film in terms of stoichiometry and structure of the material, the limitations of the deposition process, arisen from the properties of the system itself, were addressed. For that purpose, within the framework of the MONBASA project, a collaboration with the UK company Gencoa Ltd. was established to design and commission the integration of three new technologies into the sputtering vacuum chamber.

The first one was a circular 3-inch target size full face erosion magnetron (FFE75). This magnetron was intended to increase deposition rate while taking advantage of two facts: on the one hand, target to substrate distance was decreased below 10 cm, which should considerably increase the amount of material deposited on the substrate. On the other hand, owing to the full face erosion technology, whole target surface is sputtered via motor driven dynamic plasma scanning which directly implies an increase of the deposited material. Moreover, higher homogeneity over a larger area and higher quality

Figure 5.33: FFE75 full face erosion magnetron (left) and IMC75 Ion Source (right) in operation.

films should be obtained along with an optimization of the target use.

Second element introduced was a circular ion source (IMC75) for ion etching: convenient for pre-sputtering of the surfaces for upgraded adhesion or surface activation. Moreover, it could also be used during the deposition, which would supply energy into the growing film as high density low energy bombardment, hence influencing the way the deposition and crystallization is induced.

Last new feature introduced into the vacuum chamber was the Penning-PEM sensor with the Speedflo feedback controller. This is a control system for high speed automatic adjustment of the reactive gas during the deposition process. It is based on a sensor that sniffs into the plasma and calculates the partial pressure by optical analysis. The sensor is connected to a controller that drives a mass flow meter to regulate the reactive gas intake. This element was very useful for the accurate regulation of the oxygen flow during the sputtering of LLZO.

Therefore, with all these three new elements integrated, several improvements were expected, such as, the increase in deposition rate ant the improvement of the quality, homogeneity and adhesion of the thin-films. In figure 5.33, new FFE75 magnetron and IMC75 ion source are shown operating together in the sputtering chamber. As can be observed, the created plasma is intense and it homogeneously covers a wide area.

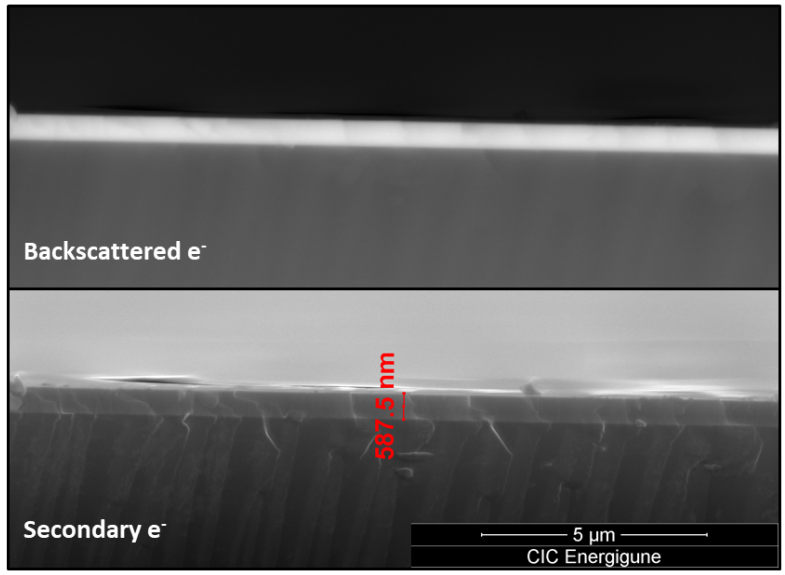

Figure 5.34: SEM cross-section image of the Li-La-Zr-O layer deposited with the new FFE75 magnetron.

A new oxygen-deficient LLZO target ($Li_7La_3Zr_2O_{3.5}$) was acquired for the new 3-inch size FFE75 magnetron from the US company Super Conductor Materials Inc. The reason to get an oxygen deficient target was twofold: first, to plan new reactive sputtering processes using different oxygen inset sources with the feedback control system; secondly, oxygen deficiency should increase the conductivity of the target, thus, allowing the use of DC sputtering mode, which is much more efficient than RF mode with increased deposition rates. However, when DC mode was tried in the new target, surface charging and arcing was noticed, hence, indicating that the material was not conductive enough for using this mode.

The increase on the deposition rate was studied via deposition on Si (100) substrate single crystal. Deposition conditions for initial test were 100 W power (2.2 W/cm^2), 55 sccm Ar flux, chamber pressure of 1.0 $\times 10^{-2}$, and magnetron rotation speed of 40 rpm. Non-reactive sputtering was used for this first test. Pretreatment of the Si substrate surface was performed with the IMC75 ion source, which was set to constant voltage mode, at 1500V, a current of 30 mA, and pure Ar gas mode at 35-40%, for a duration of 15 minutes. SEM cross-section measurement was carried out to determine the

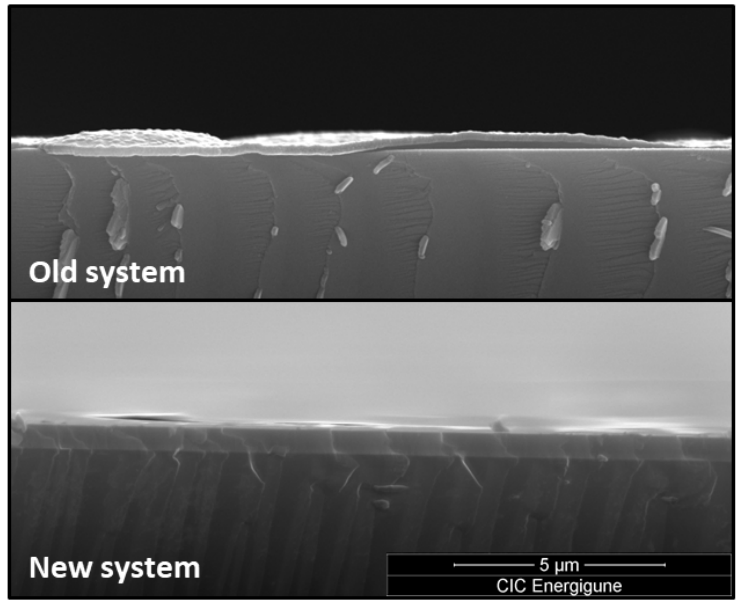

Figure 5.35: Comparison of the Li-La-Zr-O layers deposited with the old and new magnetron, by SEM cross-section images.

deposition rate obtained with the new setup. As shown in figure 5.34, a thickness around 590 nm was obtained after 5 hours deposition, which gives a deposition rate of 117 nm/h. Thereby, deposition rate with the new magnetron was demonstrated to be much higher, in fact, one order of magnitude higher than before. Moreover, a better adhesion of the layer was also observed in comparison with the layers obtained with the previous magnetron (figure 5.35), with no signs of thin-film delamination.

5.7.3 Optimization of deposition conditions

Once the initial test with the new magnetron was done, a scanning of different sputtering parameters was performed in order to find the optimal conditions for obtaining the desired stoichiometry on the deposited film. For that purpose, several sputtering processes were carried out under different reactive atmospheres. Oxygen partial pressure was incremented from 0% to 70%, meaning by partial pressure the percentage of oxygen gas out of the total gas present in the chamber. Oxygen partial pressure in the chamber was adjusted by the feedback control system: penning-PEN sensor and Speedflo controller. With this system, a better control of the reactive atmosphere

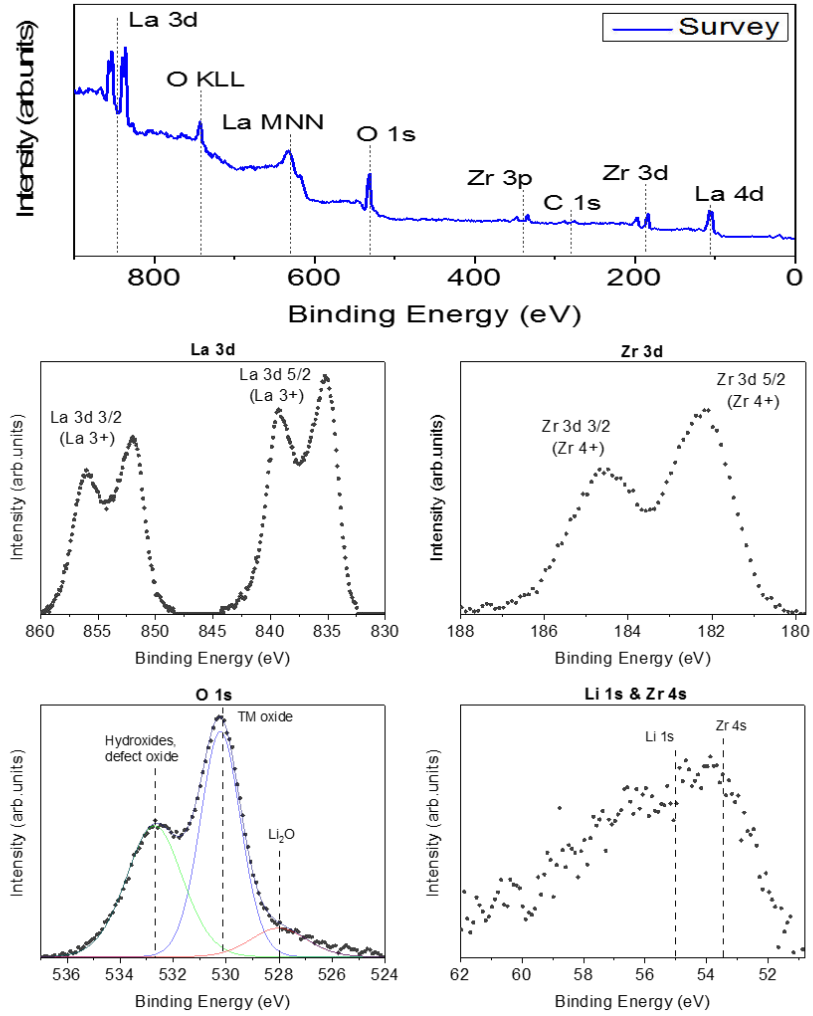

Figure 5.36: XPS results of the Li-La-Zr-O layer deposited with the new magnetron head. Survey spectra with the identification of the elements detected (top), and, particular regions of the elements of interest which include experimental data (dotted curves), deconvolution of peaks in coloured areas and overall fitting (line).

during the whole deposition process was obtained. Films were deposited on Si (100) single crystal substrates, applying a power of 100 W from the RF source. The substrates surface was conditioned with the ion source using the parameters described before to ensure a good adhesion of the deposited film.

Compositional analysis of the deposited films was carried out by means of XPS under the same conditions used for previous samples. Results, corresponding to the sample deposited under the most reactive conditions with 70% of oxygen partial pressure, are represented in figure 5.36 and are representative for all the measurements performed. For the rest of samples, the same measuring and data treatment conditions were used and same elements with similar peak shape and contributions were detected. Therefore, only final results based on the quantitative calculation from the XPS data are presented here (figure 5.37).

In the survey spectra in figure 5.36, the detected elements are indicated being the composition very similar to the one obtained previously (figure 5.31). Again, due to the absence of adventitious carbon, the Zr 3d 5/3 peak was used for binding energy calibration. As can be observed in figure 5.36, peaks and components for the particular regions of the different elements present on the sample were similar to those obtained in the first depositions. Hence, conclusions drawn for XPS results in section subsection 5.7.1 are also valid in this case, in terms of the composition of the deposited Li-La-Zr-O layer.

The evolution of the oxygen, lanthanum and zirconium ratios detected on the sample upon change of the reactive sputtering atmosphere is shown in figure 5.37. Nominal ratios corresponding to stoichiometric LLZO are indicated with dashed lines. Starting from non-reactive atmosphere up to 20% relative oxygen concentration, certain tendencies are observed: O/Zr ratio tends to decrease approaching to the nominal value of 6, although O/La and La/Zr ration tend to deviate with the increase of oxygen amount, suggesting a continuous increase of relative La concentration. Similar results were obtained for 30% relative oxygen concentration while tendency is reversed for higher oxygen concentrations. Despite being still far from the nominal value pursued, the best overall result was obtained with a partial oxygen concentration of 70% during the sputtering process, as can be observed in figure 5.37.

Apart from the compositional analysis of the Li-La-Zr-O thin-films, additional characterization was performed in order to obtain complementary information about the surface morphology and structure. In this case Li-La-Zr-O was sputtered directly on top of the LNMO thin-film electrodes, since the substrate has a huge impact on the surface morphology of sputtered thin-films and the final goal was to deposit directly the ceramic electrolyte layer on top of the thin-film cathodes. In figure 5.38, surface of deposited Li-La-Zr-O thin-film analyzed by AFM is shown. As in previous cases, topography pro-

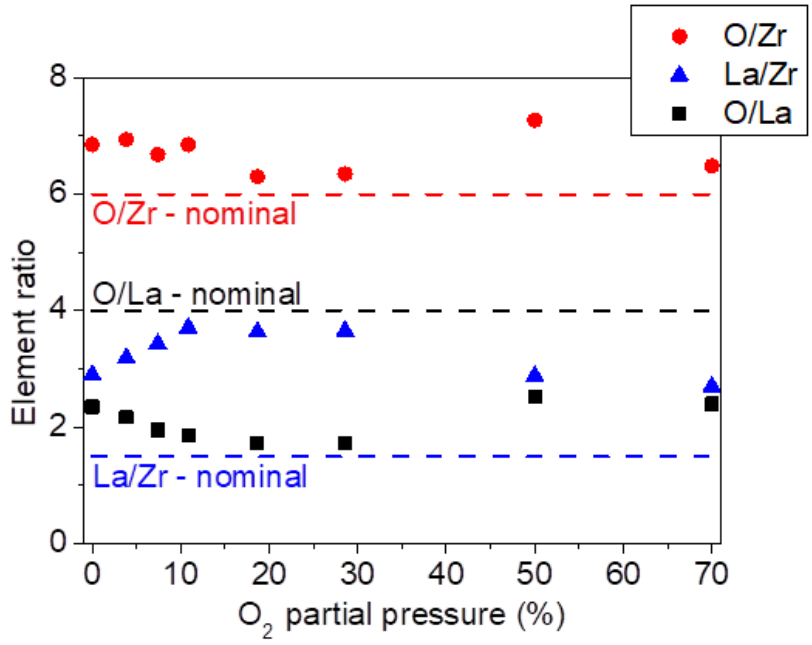

Figure 5.37: Evolution of O, Zr and La ratios with the different relative concentration of oxygen during sputtering process.

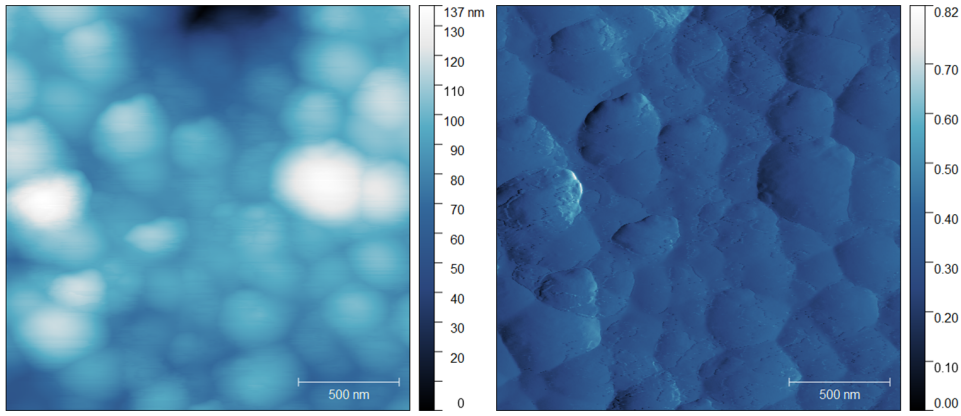

Figure 5.38: Surface of deposited LLZO layer, characterized by AFM.

vides information about the roughness, while amplitude is represented to have a better insight of the surface morphology. Measurements were performed using an Agilent 5500 microscope in tapping mode with Si tip (NT-MDT).

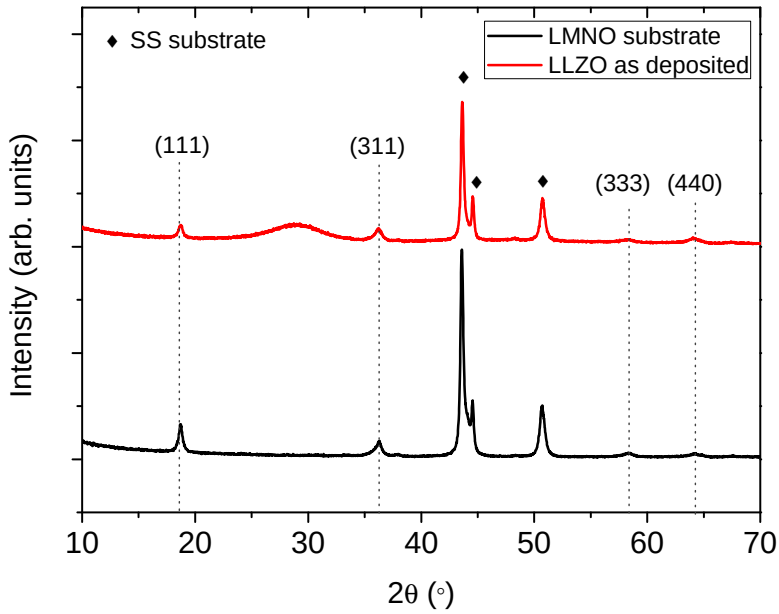

Figure 5.39: XRD pattern of deposited LLZO on top of a LNMO layer. In black, LNMO thin-film sample used as substrate before the deposition; in red, same sample after LLZO deposition.

Analysis of the images and roughness calculation was carried out with Gwyddion program. As can be observed in figure 5.38, surface was conformed by grains with a size of hundreds of nanometers. Average roughness value was calculated to be 0.5 nm, whereas maximum height of roughness was 7.9 nm.

The crystallinity of the layer (deposited on LNMO thin-film electrodes) was studied by means of XRD, using the same instrument and data acquisition conditions as reported before in this work. As can be observed in figure 5.39, where XRD patterns of a LNMO thin-film sample before and after LLZO deposition are represented, detected reflections are related to the substrate, both LNMO and SS. There is only one change in the pattern, a very broad peak just below 30°. Hence, at room temperature deposition, the amorphous structure of the sputtered film was confirmed, indicating the need of thermal post-processing to obtain the desired crystalline phase.

Therefore, sputterability of LLZO target was verified, although desired phase and structure was not obtained. Ion source could be used during the deposition, in order to check if it would help in terms of composition, as well as inducing crystallization of the deposited layer. Besides, based on the amor-

phous nature of the deposited Li-La-Zr-O thin-film, a thermal post-processing might be required so as to obtain the highly conductive cubic phase of LLZO. Heating the substrate upon deposition might also be a route to obtain crystalline layer.

5.8 Conclusions

The research activity carried out in this chapter helped to elucidate several aspects related to LNMO thin-film electrodes. Successful deposition was achieved by means of AC magnetron sputtering, obtaining homogeneous electrodes on stainless steel (SS) substrates. From the characterization performed on the as deposited samples, the need of an annealing process to obtain desired structure and electrochemical reversible reactions was confirmed. Such annealing process was demonstrated to be successful in air atmosphere, while in Ar the desired atomic structure and redox behavior were not observed, based on Raman spectroscopy and electrochemical measurements.

A scanning of the optimal temperature for the annealing process was also done using a wide range of characterization techniques. From SEM and AFM measurements, a continuous crystallization with higher particle size and roughness was detected as the annealing temperature was increased. From the compositional point of view, the best results were obtained for the intermediate annealing temperatures, namely, 550°C and 600°C. Moreover, at 900°C, Fe was detected on the surface of the sample. Besides, in terms of structural evolution, crystallization was observed above 300°C, being the optimal annealing temperature between 550°C and 600°C as identified from the combination of Raman spectroscopy and XRD results. Above that temperature new phases were detected. The temperature of 600°C was chosen as the optimal for the annealing of LNMO thin-films, since a better defined crystalline structure was observed. However, electrochemical analysis of samples annealed at different temperatures could help to definitely determine the best temperature.

The electrochemical response of the LNMO thin-film electrodes was studied with positive results. Electrodes were reversibly cycled at different C rates, with good capacity retentions and Coulombic efficiency values compared to published reports. Best reported values were not reached, although this might be related to differences on the electrochemical methods used. Furthermore, the effect of several parameters on the electrochemical response of the electrodes was studied. For instance, thickness of the thin-film was

demonstrated to play a critical role, in particular at high C-rates, where huge difference was observed between the thinnest (400 nm) and the other electrodes, being the capacity retention much better in the former one. Effect of temperature and long cycling was also studied, comparing the performance of the deposited thin-film LNMO electrodes with that from acquired commercial LNMO casted electrodes. Regarding the temperature, at 50°C, despite having better initial specific capacity at C/10, at higher C-rates capacity retention of the commercial electrodes was better than in thin-films. Nevertheless, at the highest C-rates, commercial electrodes failed, while thin-film electrodes were still having some capacity retained. Besides, in the long term cycling, thin-film electrodes showed much better behavior compared to that of commercial ones. Cycle life of the commercial electrodes at 1C did not reach 150 cycles, while the thin-film electrodes hold for over 2000 cycles.

In addition, SS substrate was observed to suffer oxidative reactions during annealing process that had influence at least on the first electrochemical cycle via irreversible processes. Surface of the SS was detected to be oxidized, being identified the surface phases like hematite, magnetite and eskolaite. Moreover, diffusion of Fe from the SS substrate through the LNMO layer was measured by means of cross section electron microscopy analysis and XPS measurements. Au gold interlayer was tried as protective coating to block the oxidation and diffusion of Fe, although it was demonstrated not to be the appropriate material. Other materials, such as TiN or CrN might have better properties to fulfill this role.

Finally, sputterability of LLZO solid electrolyte material was studied. Li-La-Zr-O layers were successfully deposited on top of thin-film LNMO electrodes, although desired composition and crystalline structure were not obtained. Full face erosion system was demonstrated to improve deposition efficiency, while IMC75 ion source and Penning pen were found to be really useful for improving film quality and reactive atmosphere conditions, respectively. In fact, when reactive sputtering was performed, under high relative oxygen concentration, surface composition was detected to be closer to the desired one. In terms of crystallinity of deposited Li-La-Zr-O films, they were observed to be amorphous when deposited at room temperature, indicating the need of higher temperatures in order to obtain highly conductive cubic phase. Such thermal treatment could be applied either directly during the sputtering deposition, or via post deposition annealing process.

Bibliography

[1] K. Mizushima, P.C. Jones, P.J. Wiseman and J.B. Goodenough. Li_xCoO_2 (0<x<1): A new cathode material for batteries of high energy density. *Materials Research Bulletin*, 15(6):783-789, 1980.

[2] K. Ozawa. Lithium Ion Rechargeable Batteries: Materials, Technology and New Applications. John Wiley & Sons, 2012.

[3] A. Du-Pasquier, I. Plitz, S. Menocal and G. Amatucci. A comparative study of Li-ion battery, supercapacitor and nonaqueous asymmetric hybrid devices for automotive applications. *Journal of Power Sources*, 115(1):171-178, 2003.

[4] M.S. Whittingham. Lithium batteries and cathode materials. *Chemical Reviews*, 104(10):4271-4302, 2004.

[5] N. Nitta, F. Wu, J.T. Lee and G. Yushin. Li-ion battery materials: present and future. *Materials Today*, 18(5):252-264, 2015.

[6] J.R. Dahn, E.W. Fuller, M. Obrovac and U. Von-Sacken. Thermal stability of Li_xCoO_2, Li_xNiO_2 and $\lambda - MnO_2$ and consequences for the safety of Li-ion cells. *Solid State Ionics*, 69(3-4):265-270, 1994.

[7] J.N. Reimers and J.R. Dahn. Electrochemical and in situ X-ray diffraction studies of lithium intercalation in Li_xCoO_2. *Journal of The Electrochemical Society*, 139(8):2091-2097, 1992.

[8] J.B. Goodenough. Energy storage materials: a perspective. *Energy Storage Materials*, 1:158-161, 2015.

[9] P. Axmann, G. Gabrielli and M. Wohlfahrt-Mehrens. Tailoring high-voltage and high-performance $LiNi_{0.5}Mn_{1.5}O_4$ cathode material for high energy Lithium-ion batteries. *Journal of Power Sources*, 301:151-159, 2016.

[10] B. Scrosati and J. Garche. Lithium batteries: Status, prospects and future. *Journal of Power Sources*, 195(9):2419-2430, 2010.

[11] M.S. Whittingham. Ultimate limits to intercalation reactions for lithium batteries. *Chemical Reviews*, 114(23):11414-11443, 2014.

[12] A.K. Padhi, K.S. Nanjundaswamy and J.B. Goodenough. Phospho-Olivines as positive-electrode materials for rechargeable lithium batteries. *Journal of the Electrochemical Society*, 144(4):1188-1194, 1997.

[13] A.S. Andersson, J.O. Thomas, B. Kalska and L. Häggström. Thermal stability of $LiFePO_4$-based cathodes. *Electrochemical and Solid-State Letters*, 3(2):66-68, 2000.

[14] M. Takahashi, H. Ohtsuka, K. Akuto and Y. Sakurai. Confirmation of long-term cyclability and high thermal stability of $LiFePO_4$ in prismatic Lithium-ion cells. *Journal of the Electrochemical Society*, 152(5):A899-A904, 2005.

[15] H. Huang, S.C. Yin and L.F. Nazar. Approaching theoretical capacity of $LiFePO_4$ at room temperature at high rates. *Electrochemical and Solid-State Letters*, 4(10):A170-A172, 2001.

[16] H.Y. Kim, B.W. Cho and W. Cho. Electronically conductive Phospho-Olivines as lithium storage electrodes. *Journal of Power Sources*, 132(1-2):235-239, 2004.

[17] S.Y. Chung, J.T. Bloking and Y.M. Chiang. From our readers: On the electronic conductivity of Phospho-Olivines as lithium storage electrodes. *Nature Materials*, 2(11):702-703, 2003.

[18] Y. Abu-Lebdeh and I. Davidson. *Nanotechnology for Lithium-ion batteries*. Springer Science & Business Media, 2012.

[19] M.M. Thackeray. Manganese Oxides for lithium batteries. *Progress in Solid State Chemistry*, 25(1):1-71, 1997.

[20] G.A. Nazri and G. Pistoia. *Lithium batteries: science and technology*. Springer Science & Business Media, 2008.

[21] O.K. Park, Y. Cho, S. Lee, H.C. Yoo, H.K. Song and J. Cho. Who will drive electric vehicles, Olivine or Spinel? *Energy & Environmental Science*, 4(5):1621-1633, 2011.

[22] H. Ishikawa, O. Mendoza, Y. Nishikawa, Y. Maruyama and M. Umeda. Thermal characteristics of lithium ion secondary cells in high temperature environments using an accelerating rate calorimeter. *Journal of Renewable and Sustainable Energy*, 5(4):043122, 2013.

[23] O.S. Mendoza-Hernandez, H. Ishikawa, Y. Nishikawa, Y. Maruyama and M. Umeda. Cathode material comparison of thermal runaway behavior of Li-ion cells at different state of charges including over charge. *Journal of Power Sources*, 280:499-504, 2015.

[24] C. Schilcher, C. Meyer and A. Kwade. Structural and electrochemical properties of calendered Lithium Manganese Oxide cathodes. *Energy Technology*, 4(12):1604-1610, 2016.

[25] L. Quispe, M.A. Condoretty, H. Kawasaki, S. Tsuji, H. Visbal, H. Miki, K. Nagashima and K. Hirao. Synthesis of spinel $LiNi_{0.5}Mn_{1.5}O_4$ by a wet chemical method and characterization for Lithium-ion secondary batteries. *Journal of the Ceramic Society of Japan*, 123(1433):38-42, 2015.

[26] R. Garcia-Valle and J.A. Peças-Lopes. *Electric vehicle integration into modern power networks*. Springer Science & Business Media, 2012.

[27] M.M. Thackeray, Y. Shao-Horn, A.J. Kahaian, K.D. Kepler, E. Skinner, J.T. Vaughey and S.A. Hackney. Structural fatigue in spinel electrodes in high voltage (4V) $Li/Li_xMn_2O_4$ cells. *Electrochemical and Solid-State Letters*, 1(1):7-9, 1998.

[28] K.Y. Chung and K.B. Kim. Investigations into capacity fading as a result of a Jahn-Teller distortion in 4V $Li_xMn_2O_4$ thin film electrodes. *Electrochimica Acta*, 49(20):3327-3337, 2004.

[29] A. Blyr, C. Sigala, G. Amatucci, D. Guyomard, Y. Chabre and J.M. Tarascon. Self-discharge of $Li_xMn_2O_4/C$ Li-ion cells in their discharged state understanding by means of three-electrode measurements. *Journal of The Electrochemical Society*, 145(1):194-209, 1998.

[30] K. Raju, F.P. Nkosi, E. Viswanathan, M.K. Mathe, K. Damodaran and K.I. Ozoemena. Microwave-enhanced electrochemical cycling performance of the $LiNi_{0.2}Mn_{1.8}O_4$ spinel cathode material at elevated temperature. *Physical Chemistry Chemical Physics*, 18(18):13074-13083, 2016.

[31] C. Sigala, D. Guyomard, A. Verbaere, Y. Piffard and M. Tournoux. Positive electrode materials with high operating voltage for lithium batteries: $LiCr_yMn_{2-y}O_4$ ($0 \leq y \leq 1$). *Solid State Ionics*, 81(3-4):167-170, 1995.

[32] T. Ohzuku, S. Takeda and M. Iwanaga. Solid-state Redox potentials for $Li(Me_{1/2}Mn_{3/2})O_4$ (Me:3d-transition metal) having spinel-framework structures: a series of 5 Volt materials for advanced Lithium-ion batteries. *Journal of Power Sources*, 81:90-94, 1999.

[33] D. Liu, W. Zhu, J. Trottier, C. Gagnon, F. Barray, A. Guerfi, A. Mauger, H. Groult, C.M. Julien, J.B. Goodenough. Spinel materials for high-voltage cathodes in Li-ion batteries. *Rsc Advances*, 4(1):154-167, 2014.

[34] T.F. Yi, J. Mei and Y.R. Zhu. Key strategies for enhancing the cycling stability and rate capacity of $LiNi_{0.5}Mn_{1.5}O_4$ as high-voltage cathode materials for high power Lithium-ion batteries. *Journal of Power Sources*, 316:85-105, 2016.

[35] J. Xiao, X. Chen, P.V. Sushko, M.L. Sushko, L. Kovarik, J. Feng, Z. Deng, J. Zheng, G.L. Graff, Z. Nie. High-performance $LiNi_{0.5}Mn_{1.5}O_4$ spinel controlled by Mn^{3+} concentration and site disorder. *Advanced Materials*, 24(16):2109-2116, 2012.

[36] J. Cabana, M. Casas-Cabanas, F.O. Omenya, N.A. Chernova, D. Zeng, M.S. Whittingham and C.P. Grey. Composition-structure relationships in the Li-ion battery electrode material $LiNi_{0.5}Mn_{1.5}O_4$. *Chemistry of Materials*, 24(15):2952-2964, 2012.

[37] M. Kunduraci, J.F. Al-Sharab and G.G. Amatucci. High-power nanostructured $LiMn_{2-x}Ni_xO_4$ high-voltage Lithium-ion battery electrode materials: Electrochemical impact of electronic conductivity and morphology. *Chemistry of Materials*, 18(15):3585-3592, 2006.

[38] M. Atanasov, J.L. Barras, L. Benco and C. Daul. Electronic structure, chemical bonding, and vibronic coupling in Mn^{iv}/Mn^{iii} mixed valent $Li_xMn_2O_4$ spinels and their effect on the dynamics of intercalated Li: A cluster study using DFT. *Journal of the American Chemical Society*, 122(19):4718-4728, 2000.

[39] M. Kunduraci and G.G. Amatucci. Synthesis and characterization of nanostructured 4.7V $LiNi_{0.5}Mn_{1.5}O_4$ spinels for high-power Lithium-

ion batteries. *Journal of The Electrochemical Society*, 153(7):A1345-A1352, 2006.

[40] D. Aurbach. Review of selected electrode-solution interactions which determine the performance of Li and Li-ion batteries. *Journal of Power Sources*, 89(2):206-218, 2000.

[41] L. Yang, B. Ravdel and B.L. Lucht. Electrolyte reactions with the surface of high voltage $LiNi_{0.5}Mn_{1.5}O_4$ cathodes for Lithium-ion batteries. *Electrochemical and Solid-State Letters*, 13(8):A95-A97, 2010.

[42] S.R. Li, C.H. Chen, J. Camardese and J.R. Dahn. High precision coulometry study of $LiNi_{0.5}Mn_{1.5}O_4/Li$ coin cells. *Journal of The Electrochemical Society*, 160(9):A1517-A1523, 2013.

[43] S. Brutti, G. Greco, P. Reale and S. Panero. Insights about the irreversible capacity of $LiNi_{0.5}Mn_{1.5}O_4$ cathode materials in lithium batteries. *Electrochimica Acta*, 106:483-493, 2013.

[44] N.P.W. Pieczonka, Z. Liu, P. Lu, K.L. Olson, J. Moote, B.R. Powell and J.H. Kim. Understanding transition-metal dissolution behavior in $LiNi_{0.5}Mn_{1.5}O_4$ high-voltage spinel for Lithium-ion batteries. *The Journal of Physical Chemistry C*, 117(31):15947-15957, 2013.

[45] A. Manthiram, X. Yu and S. Wang. Lithium battery chemistries enabled by solid-state electrolytes. *Nature Reviews Materials*, 2:16103, 2017.

[46] J.G. Kim, B. Son, S. Mukherjee, N. Schuppert, A. Bates, O. Kwon, M.J. Choi, H.Y. Chung and S. Park. A review of lithium and non-lithium based solid state batteries. *Journal of Power Sources*, 282:299-322, 2015.

[47] J.C. Bachman, S. Muy, A. Grimaud, H.H. Chang, N. Pour, S.F. Lux, O. Paschos, F. Maglia, S. Lupart, P. Lamp. Inorganic solid-state electrolytes for lithium batteries: mechanisms and properties governing ion conduction. *Chemical Reviews*, 116(1):140-162, 2015.

[48] K. Takada. Progress and prospective of solid-state lithium batteries. *Acta Materialia*, 61(3):759-770, 2013.

[49] W.D. Richards, L.J. Miara, Y. Wang, J.C. Kim and G. Ceder. Interface stability in solid-state batteries. *Chemistry of Materials*, 28(1):266-273, 2015.

[50] V. Thangadurai, S. Narayanan and D. Pinzaru. Garnet-type solid-state fast Li-ion conductors for Li batteries: critical review. *Chemical Society Reviews*, 43(13):4714-4727, 2014.

[51] R. Murugan, V. Thangadurai and W. Weppner. Fast lithium ion conduction in Garnet-type $Li_7La_3Zr_2O_{12}$. *Angewandte Chemie International Edition*, 46(41):7778-7781, 2007.

[52] J. Awaka, N. Kijima, H. Hayakawa and J. Akimoto. Synthesis and structure analysis of tetragonal $Li_7La_3Zr_2O_{12}$ with the Garnet-related type structure. *Journal of Solid State Chemistry*, 182(8):2046-2052, 2009.

[53] C. Bernuy-Lopez, W. Manalastas, J.M. Lopez-del-Amo, A. Aguadero, F. Aguesse and J.A. Kilner. Atmosphere controlled processing of Ga-substituted Garnets for high Li-ion conductivity ceramics. *Chemistry of Materials*, 26(12):3610-3617, 2014.

[54] T. Thompson, S. Yu, L. Williams, R.D. Schmidt, R. Garcia-Mendez, J. Wolfenstine, J.L. Allen, E. Kioupakis, D.J. Siegel and J. Sakamoto. Electrochemical window of the Li-ion solid electrolyte $Li_7La_3Zr_2O_{12}$. *ACS Energy Letters*, 2(2):462-468, 2017.

[55] J.T.S. Irvine. Ar west in high conductivity ionic conductors, recent trends and application. *World Scientific*, 1989.

[56] X. Yan, Z. Li, Z. Wen and W. Han. $Li/Li_7La_3Zr_2O_{12}/LiFePO_4$ all-solid-state battery with ultrathin nanoscale solid electrolyte. *The Journal of Physical Chemistry C*, 121(3):1431-1435, 2017.

[57] Asma Sharafi, Harry M Meyer, Jagjit Nanda, Jeff Wolfenstine, and Jeff Sakamoto. Characterizing the $Li - Li_7La_3Zr_2O_{12}$ interface stability and kinetics as a function of temperature and current density. *Journal of Power Sources*, 302:135-139, 2016.

[58] E.J. Cheng, A. Sharafi and J. Sakamoto. Intergranular Li metal propagation through polycrystalline $Li_{6.25}Al_{0.25}La_3Zr_2O_{12}$ ceramic electrolyte. *Electrochimica Acta*, 223:85-91, 2017.

[59] K. Dokko, M. Mohamedi, N. Anzue, T. Itoh and I. Uchida. In situ Raman spectroscopic studies of $LiNi_xMn_{2-x}O_4$ thin film cathode materials for Lithium-ion secondary batteries. *Journal of Materials Chemistry*, 12(12):3688-3693, 2002.

[60] M. Gellert, K.I. Gries, J. Zakel, A. Ott, S. Spannenberger, C. Yada, F. Rosciano, K. Volz and B. Roling. $LiNi_{0.5}Mn_{1.5}O_4$ thin-film cathodes on gold-coated stainless steel substrates: Formation of interlayers and electrochemical properties. *Electrochimica Acta*, 133:146-152, 2014.

[61] J.H. Lee and K.J. Kim. Structural and electrochemical evolution with post-annealing temperature of solution-based $LiNi_{0.5}Mn_{1.5}O_4$ thin-film cathodes for microbatteries with cyclic stability. *Electrochimica Acta*, 137:169-174, 2014.

[62] J.C. Arrebola, A. Caballero, M. Cruz, L. Hernán, J. Morales and E. Rodríguez-Castellón. Crystallinity control of a nanostructured $LiNi_{0.5}Mn_{1.5}O_4$ spinel via polymer-assisted synthesis: A method for improving its rate capability and performance in 5V lithium batteries. *Advanced Functional Materials*, 16(14):1904-1912, 2006.

[63] H. Xia, Y.S. Meng, L. Lu and G. Ceder. Electrochemical properties of non-stoichiometric $LiNi_{0.5}Mn_{1.5}O_{4-\delta}$ thin-film electrodes prepared by Pulsed Laser Deposition. *Journal of the Electrochemical Society*, 154(8):A737-A743, 2007.

[64] H. Xia, S.B. Tang, L. Lu, Y.S. Meng and G. Ceder. The influence of preparation conditions on electrochemical properties of $LiNi_{0.5}Mn_{1.5}O_4$ thin film electrodes by PLD. *Electrochimica Acta*, 52(8):2822-2828, 2007.

[65] H. Konishi, K. Suzuki, S. Taminato, K. Kim, S. Kim, J. Lim, M. Hirayama and R. Kanno. Structure and electrochemical properties of $LiNi_{0.5}Mn_{1.5}O_4$ epitaxial thin film electrodes. *Journal of Power Sources*, 246:365-370, 2014.

[66] H. Konishi, K. Suzuki, S. Taminato, K. Kim, Y. Zheng, S. Kim, J. Lim, M. Hirayama, J.Y. Son and Y. Cui. Effect of surface Li_3PO_4 coating on $LiNi_{0.5}Mn_{1.5}O_4$ epitaxial thin film electrodes synthesized by Pulsed Laser Deposition. *Journal of Power Sources*, 269:293-298, 2014.

[67] L. Wang, H. Li, M. Courty, X. Huang and E. Baudrin. Preparation and characterization of $LiNi_{0.5}Mn_{1.5}O_{4-\delta}$ thin films taking advantage of correlations with powder samples behavior. *Journal of Power Sources*, 232:165-172, 2013.

[68] L. Baggetto, R.R. Unocic, N.J. Dudney and G.M. Veith. Fabrication and characterization of Li-Mn-Ni-O sputtered thin film high voltage cathodes for Li-ion batteries. *Journal of Power Sources*, 211:108-118, 2012.

[69] L. Baggetto, N.J. Dudney and G.M. Veith. Surface chemistry of metal oxide coated Lithium Manganese Nickel Oxide thin film cathodes studied by XPS. *Electrochimica Acta*, 90:135-147, 2013.

[70] J. Li, L. Baggetto, S.K. Martha, G.M. Veith, J. Nanda, C. Liang and N.J. Dudney. An artificial Solid Electrolyte Interphase enables the use of a $LiNi_{0.5}Mn_{1.5}O_4$ 5V cathode with conventional electrolytes. *Advanced Energy Materials*, 3(10):1275-1278, 2013.

[71] S.H. Su, K-F. Chiu and H.J. Leu. Structural evolution of bias sputtered $LiNi_{0.5}Mn_{1.5}O_4$ thin film cathodes for lithium-ion batteries. *Thin Solid Films*, 572:15-19, 2014.

[72] J. Li, C. Ma, M. Chi, C. Liang and N.J. Dudney. Solid electrolyte: the key for high-voltage lithium batteries. *Advanced Energy Materials*, 5(4), 2015.

[73] A.N. Filippin, M. Rawlence, A. Wäckerlin, T. Feurer, T. Zünd, K. Kravchyk, M.V. Kovalenko, Y.E. Romanyuk, A.N. Tiwari and S. Buecheler. Chromium Nitride as a stable cathode current collector for all-solid-state thin film Li-ion batteries. *RSC Advances*, 7(43):26960-26967, 2017.

[74] M. Letiche, M. Hallot, M. Huve, T. Brousse, P. Roussel and C. Lethien. Tuning the cation ordering with the deposition pressure in sputtered $LiNi_{0.5}Mn_{1.5}O_4$ thin film deposited on functional current collectors for Li-ion microbattery applications. *Chemistry of Materials*, 29(14):6044-6057, 2017.

[75] E. Kazyak, K.H. Chen, K.N. Wood, A.L. Davis, T. Thompson, A.R. Bielinski, A.J. Sanchez, X. Wang, C. Wang, J. Sakamoto. Atomic Layer Deposition of the solid electrolyte Garnet $Li_7La_3Zr_2O_{12}$. *Chem. Mater*, 29(8):3785-3792, 2017.

[76] C. Loho, R. Djenadic, M. Bruns, O. Clemens and H. Hahn. Garnet-type $Li_7La_3Zr_2O_{12}$ solid electrolyte thin films grown by CO_2-laser assisted CVD for all-solid-state batteries. *Journal of The Electrochemical Society*, 164(1):A6131-A6139, 2017.

[77] J. Tan and A. Tiwari. Fabrication and characterization of $Li_7La_3Zr_2O_{12}$ thin films for Lithium-ion battery. *ECS Solid State Letters*, 1(6):Q57-Q60, 2012.

[78] S. Kim, M. Hirayama, S. Taminato and R. Kanno. Epitaxial growth and lithium ion conductivity of lithium-oxide Garnet for an all solid-state battery electrolyte. *Dalton Transactions*, 42(36):13112-13117, 2013.

[79] M. Rawlence, I. Garbayo, S. Buecheler and J.L.M. Rupp. On the chemical stability of post-lithiated Garnet Al-stabilized $Li_7La_3Zr_2O_{12}$ solid state electrolyte thin films. *Nanoscale*, 8(31):14746-14753, 2016.

[80] I. Garbayo, M. Struzik, W.J. Bowman, R. Pfenninger, E. Stilp and J.L.M. Rupp. Glass-type polyamorphism in Li-Garnet thin film solid state battery conductors. *Advanced Energy Materials*, 2018.

[81] S. Lobe, C. Dellen, M. Finsterbusch, H.G. Gehrke, D. Sebold, C.L. Tsai, S. Uhlenbruck and O. Guillon. Radio Frequency magnetron sputtering of $Li_7La_3Zr_2O_{12}$ thin films for solid-state batteries. *Journal of Power Sources*, 307:684-689, 2016.

[82] D.J. Kalita, S.H. Lee, K.S. Lee, D.H. Ko and Y.S. Yoon. Ionic conductivity properties of amorphous Li-La-Zr-O solid electrolyte for thin film batteries. *Solid State Ionics*, 229:14-19, 2012.

[83] A. Bhaskar, N.N. Bramnik, A. Senyshyn, H. Fuess and H. Ehrenberg. Synthesis, characterization, and comparison of electrochemical properties of $LiM_{0.5}Mn_{1.5}O_4$ (M= Fe, Co, Ni) at different temperatures. *Journal of The Electrochemical Society*, 157(6):A689-A695, 2010.

[84] L. Wang, H. Li, X. Huang and E. Baudrin. A comparative study of Fd-3m and P4332 $LiNi_{0.5}Mn_{1.5}O_4$. *Solid State Ionics*, 193(1):32-38, 2011.

[85] K. Saravanan, A. Jarry, R. Kostecki and G. Chen. A study of room-temperature $Li_xMn_{1.5}Ni_{0.5}O_4$ solid solutions. *Scientific Reports*, 5, 2015.

[86] L. Boulet-Roblin, C. Villevieille, P. Borel, C. Tessier, P. Novák and M. Ben-Yahia. Versatile approach combining theoretical and experimental aspects of Raman spectroscopy to investigate battery materials: The case of the $LiNi_{0.5}Mn_{1.5}O_4$ spinel. *The Journal of Physical Chemistry C*, 120(30):16377-16382, 2016.

[87] H.B. Lin, Y.M. Zhang, H.B. Rong, S.W. Mai, J.N. Hu, Y.H. Liao, L.D. Xing, M.Q. Xu, X.P. Li and W.S. Li. Crystallographic facet and size-controllable synthesis of spinel $LiNi_{0.5}Mn_{1.5}O_4$ with excellent cyclic stability as cathode of high voltage Lithium-ion battery. *Journal of Materials Chemistry A*, 2(30):11987-11995, 2014.

[88] N.M. Hagh and G.G. Amatucci. A new solid-state process for synthesis of $LiNi_{0.5}Mn_{1.5}O_{4-\delta}$ spinel. *Journal of Power Sources*, 195(15):5005-5012, 2010.

[89] J. Sato, M. Kobayashi, H. Kato, T. Miyazaki and M. Kakihana. Hydrothermal synthesis of Magnetite particles with uncommon crystal facets. *Journal of Asian Ceramic Societies*, 2(3):258-262, 2014.

[90] R.J. Ward and B.J. Wood. A comparison of experimental and theoretically derived sensitivity factors for XPS. *Surface and Interface Analysis*, 18(9):679-684, 1992.

[91] P. Swift. Adventitious carbon—the panacea for energy referencing? *Surface and Interface Analysis*, 4(2):47-51, 1982.

[92] T.L. Barr and S. Seal. Nature of the use of adventitious carbon as a binding energy standard. *Journal of Vacuum Science & Technology A: Vacuum, Surfaces and Films*, 13(3):1239-1246, 1995.

[93] H. Duncan, D. Duguay, Y. Abu-Lebdeh and I.J. Davidson. Study of the $LiNi_{0.5}Mn_{1.5}O_4$/electrolyte interface at room temperature and 60C. *Journal of The Electrochemical Society*, 158(5):A537-A545, 2011.

[94] L.C. Chapon and J. Rodrıguez-Carvajal. Fullprof: a program of the fullprof suite developed for Rietveld analysis of neutron or X-ray powder diffraction data. *https://www.ill.eu/sites/fullprof /php/programs8809.html?pagina=FullProf.*

[95] H.W. Choi, S.J. Kim, Y.H. Rim and Y.S. Yang. Effect of lithium deficiency on Lithium-ion battery cathode $LiNi_{0.5}Mn_{1.5}O_4$. *The Journal of Physical Chemistry C*, 119(49):27192-27199, 2015.

[96] T. Ohzuku, K. Ariyoshi, S. Takeda and Y. Sakai. Synthesis and characterization of 5V insertion material of $Li(Fe_yMn_{2-y})O_4$ for Lithium-ion batteries. *Electrochimica Acta*, 46(15):2327-2336, 2001.

[97] J.C. Arrebola, A. Caballero, L. Hernán, M. Melero, J. Morales and E.R. Castellón. Electrochemical properties of $LiNi_{0.5}Mn_{1.5}O_4$ films prepared by spin-coating deposition. *Journal of Power Sources*, 162(1):606-613, 2006.

[98] D. Aurbach, Y. Talyosef, B. Markovsky, E. Markevich, E. Zinigrad, L. Asraf, J.S. Gnanaraj and H.J. Kim. Design of electrolyte solutions for Li and Li-ion batteries: a review. *Electrochimica Acta*, 50(2):247-254, 2004.

[99] S.W. Gaarenstroom, A.V. Naumkin, A. Kraut-Vass and C.J. Powell. NIST X-ray Photoelectron Spectroscopy database. *https:// srdata.nist.gov/xps/Default.aspx.*

[100] M. Burriel, S. Wilkins, J.P. Hill, M.A. Muñoz-Márquez, H.H. Brongersma, J.A. Kilner, M.P. Ryan and S.J. Skinner. Absence of Ni on the outer surface of Sr doped La_2NiO_4 single crystals. *Energy & Environmental Science*, 7(1):311-316, 2014.

[101] S. Wenzel, T. Leichtweiss, D. Krüger, J. Sann and J. Janek. Interphase formation on lithium solid electrolytes—an in situ approach to study interfacial reactions by photoelectron spectroscopy. *Solid State Ionics*, 278:98-105, 2015.

Chapter 6

General conclusions & future perspectives

The comprehensive study of electrode surfaces and interfaces carried out along this work, confirmed the assumption made on the introduction about the importance of interfaces and interphases on Li-ion batteries. Likewise, the research work performed on thin-films of different battery materials corroborated their potential both as model systems for surface studies of battery components, as electrodes for microbatteries and coatings for casted electrodes. From the particular research activities developed and presented in different chapters, several conclusions were drawn.

The study of the surface evolution upon electrochemical cycling on highly oriented LTO (111) layer (chapter 3), helped to elucidate several issues:

- First of all, the possibility of cycling LTO material without the need of a conductive additive was confirmed in agreement with previous studies, in spite of the insulating nature of LTO.

- Previous studies suggested that $\alpha-Li_2TiO_3$ was formed on the LTO surface during cycling. However, the XRD results and cross-sectional TEM analysis performed in this work confirmed that $\alpha-Li_2TiO_3$ was present in the outermost 15 nm of the pristine LTO surface as impurity. Hence, demonstrating that $\alpha-Li_2TiO_3$ is not formed on LTO upon electrochemical cycling.

- The identification of $\alpha-Li_2TiO_3$ in previous works was done on the basis of a surface roughness increase. However, in this work, the analysis of surface strain by means of HREBSD revealed an increase on normal strain during cycling. This evolution upon electrochemical cycling, could explain the corrugation of the LTO surface reported before. Controlling such effect, which occurs on the electrode-electrolyte interface, may help to improve the electrochemical properties of LTO material. Besides, the presence of this interface phenomena, further supports the idea of the benefits that surface engineering of the electrodes may have on their cycling performance.

From the results and conclusions obtained in this chapter, some issues remain unclear and new ideas for future work arise:

- The study was only performed on the (111) surface of LTO. Similar study could be carried out on surfaces with different orientation, such as (100) or (110). This would allow to verify either if $\alpha-Li_2TiO_3$ phase is exclusively formed on studied surface, or is also common in other orientations. The study of the strain evolution on different surfaces could help to identify which orientation suffers less variations, directly striking in the long term electrochemical performance.

- The electronic conductivity of LTO material and its change upon discharge have attracted the attention of research community during the last years. LTO samples described in this work, with highly oriented flat surfaces and free of any additive, in contrast to conventional electrodes, would be the ideal platform for direct conductivity measurements and their evolution upon electrochemical cycling. Comparison between different orientations, as stated in the previous point, could also be done.

- Based on the interesting results obtained in this chapter, the particular synthesis method used for producing LTO layers could be used for the preparation of other electrode materials. It would be of special interest in the cases where understanding of surface reactions is critical for their implementation as electrodes. As an example, preparation of $LiMn_2O_4$ layers using this synthesis method has already been reported [1].

In regard to the study developed in chapter 4, where the effect of different coatings on LTO electrodes was studied, the following conclusions were reached:

- Our study has concluded that the SEI-free LTO is not such. A SEI-like surface layer starting at OCV is formed in both conventional and thin-film LTO electrodes.

- RF magnetron sputtering was proved to be a suitable and useful method for the deposition of surface coatings directly on conventionally casted electrodes. It was confirmed that electrodes do not suffer any variation or degradation effect when exposed to the ultra high vacuum conditions, ignition of plasma, and sputtering process in general.

- Carbon and aluminum oxide coatings were demonstrated to enhance the electrochemical performance of casted LTO electrodes, being the improvement in specific capacity more prominent at higher current intensities. Results obtained for Al_2O_3 coated electrodes were particularly noteworthy, since the specific capacity of LTO electrodes increased in almost 30% at 10C rate. The better C-rate performance of insulating Al_2O_3 coatings if compared with conductive C-coatings is an unexpected result. At this point, the most plausible explanation is the presence of defects, e.g. oxygen vacancies, in the Al_2O_3 that render the coating electronically conductive. Moreover, observed electrochemical improvement could stem from the recognized scavenger function of Al_2O_3. Coating material would react with traces of HF and H_2O present on the electrolyte during the initial phase of electrochemical process, avoiding deleterious reactions on the active material that would hamper the electrochemical response. On the other hand, the improved electrochemical performance in the case of carbon coatings must have a different origin, based on XPS measurements. In this case the improvement most probably stems from the improved electronic conductivity of the particles on the surface.

- Usefulness of thin-films as an ideal system for the analysis of the phenomena occurring on the electrode-electrolyte interface was confirmed, since the contribution of the surface reactions is enhanced due to the higher surface to core ratio, at the same time that compositional and

geometrical complexity of conventional electrodes is avoided. However, it is worth noting that avoiding such complexity may impact the results obtained. Indeed, the effect of coatings in conventional and thin-film electrodes was observed to be different. Al_2O_3 coated LTO thin-film electrodes did not mimic the enhancement on the electrochemical performance observed on casted electrodes. This could be nested on the geometrical differences among the two systems. Despite having same coating in terms of composition and thickness, a possible lack of homogeneity in the coating deposited in conventional casted electrodes, due to its geometrical complexity, could result beneficial. On thin-film electrodes, although Al_2O_3 worked as scavenger agent, the homogeneous layer could limit the Li ion diffusion into the LTO structure. On the other hand, on casted electrodes, Al_2O_3 still played the same role, but the non-coated free areas and pores made a direct connection between electrolyte and active material possible, which enabled better ionic diffusion. Therefore, the compromise reached between coating homogeneity and free spots for direct electrolyte-LTO contact, would strongly foster the electrochemical response of LTO electrodes.

From these conclusions, the following ideas are proposed as future research work:

- Scanning of different thickness Al_2O_3 coatings on conventional LTO electrodes could be performed, in order to optimize the thickness and obtain the best electrochemical performance.

- Perform direct measurements of electronic conductivity on the deposited coatings.

- Following the success of Al_2O_3 as coating material for LTO electrodes, other oxides could be investigated following the same procedure for coating deposition. Among others, ZrO could be tried, based on the positive results obtained in similar works performed in cathode materials [2].

Finally, from the extensive research developed in chapter 5, related to LNMO thin-film cathodes and sputterability study of solid electrolyte, obtained conclusions are described below:

- AC magnetron sputtering was demonstrated to be a suitable and convenient deposition technique for LNMO thin-film electrodes. Moreover, the need for a post-deposition annealing process in air at 600°C in order to obtain desired phase and electrochemical properties was confirmed. Fe diffusion from the current collector to the LNMO surface was detected, caused by the annealing process. Gold coatings were unsuccessfully investigated as a barrier layer for the diffusion effect.

- LNMO thin-films were successfully cycled as positive electrodes in Li-ion half cells, using conventional electrolytes. 400 nm-thick LNMO electrodes were found to be the best performing ones. Thin-film electrodes are more sensitive to high temperature (50°C) cycling in terms of capacity retention at low C-rates, although they can still be cycled above 5C in contrast to commercial electrodes. On the other hand, thin-film LNMO electrodes showed much longer cycle life (above 2000 cycles) compared to the commercial casted ones (below 150 cycles) which demonstrates a better stability of the thin-film electrodes in the long term.

- Sputterability of LLZO material was demonstrated to be possible, although desired phase and structure for deposited Li-La-Zr-O was not obtained. Benefits of FFE75 magnetron, IMC75 ion source and Penning pen feedback controller were confirmed in terms of deposition efficiency, film quality and control of reactive atmosphere conditions, respectively. Finally, amorphous nature of deposited films was observed, hence confirming the need for higher annealing temperatures to obtain highly conductive cubic LLZO phase.

These conclusions reveal several issues to be addressed while opening new research possibilities:

- Despite the fact that 600°C was chosen as the optimal annealing temperature for LNMO, the results obtained for 550° were also promising. Hence, comparative electrochemical characterization should be done, in order to determine possible differences and choose the best option. From the production point of view, the lower the temperature of the thermal processes, the better.

- New materials should be investigated to avoid interfacial phenomena occurring on SS-LNMO interface. TiN and CrN could be suitable candidates, particularly the last one, based on latest reports [3]. Alternatively, other conductive substrates for LNMO deposition could be used.

- Further research should be carried out to find the proper conditions for the deposition of highly conductive LLZO films, both from the compositional and structural point of view. Scanning of different temperatures upon deposition and post-deposition annealing processes could help to reach this objective. Obtaining highly oriented LNMO thin-films instead of current policrystalline ones could help on the crystallization of deposited LLZO films. Besides, ionic conductivity measurement of LLZO films deposited at different temperatures could be done, since latest reports suggest that LLZO could be potentially used in microbatteries in amorphous or glass-type phase [4].

Therefore, all along this thesis work several issues related to surfaces and interfaces of conventional and thin-film electrodes were addressed. Confirming that their study is critical to continue with the on-going development of next generation Li-ion batteries. Fundamental knowledge of phenomena occurring on electrode surfaces has been generated, promising upgraded electrochemical results nested on interface engineering have been obtained, and optimization of thin-film electrodes and analysis of different interfaces present on thin-film batteries have been performed. Nevertheless, to reach the outstanding properties necessary to match the wide range of requirements that current and near-future multiple applications demand, intensive research effort will have to be devoted in surface and thin-film fields, in order to tackle all the challenges that still remain an issue.

Bibliography

[1] M. Kitta, T. Akita and M. Kohyama. Preparation of a spinel $LiMn_2O_4$ single crystal film from a MnO wafer. *Journal of Power Sources*, 232:7-11, 2013.

[2] L. Baggetto, N.J. Dudney and G.M. Veith. Surface chemistry of metal oxide coated Lithium Manganese Nickel Oxide thin film cathodes studied by XPS. *Electrochimica Acta*, 90:135-147, 2013.

[3] A.N. Filippin, M. Rawlence, A. Wäckerlin, T. Feurer, T. Zünd, K. Kravchyk, M.V. Kovalenko, Y.E. Romanyuk, A.N. Tiwari and S. Buecheler. Chromium Nitride as a stable cathode current collector for all-solid-state thin film Li-ion batteries. *RSC Advances*, 7(43):26960-26967, 2017.

[4] I. Garbayo, M. Struzik, W.J. Bowman, R. Pfenninger, E. Stilp and J.L.M. Rupp. Glass-type polyamorphism in Li-Garnet thin film solid state battery conductors. *Advanced Energy Materials*, 2018.

Acknowledgment

Lehenik eta behin eskerrak eman behar dizkiot Miguel Angeli tesi hau burutzeko aukera emateagatik, egindako lanagatik eta baita irakatsitako guztiagatik ere. Baita, nola ez, urte hauetan zehar CIC-energiGUNEn lan hau aurrera eramaten era batera edo bestera lagundu didaten beste guztiei. Jende askorekin lan egiteko, kafea hartzeko, eztabaidatzeko, barre egiteko eta abarrerako aukera izan dut bertan. Plazerra izan da bertan pasatako denbora jende guzti horrekin bizitzea, baina ezin denak banan-banan aipatu. Mila esker jende guzti horri. CICean nire lehen pausuak Montse G. eta Montse C.-ren eskutik eman nituen, haien "erruz" hasi nintzen ni gerora benetan disfrutatu dudan ikerkuntzaren munduan; eskerrik asko, hortaz, lehen aukera hori emateagatik. Tesi honetan aurkezten den lana hainbat urtetan zehar burututako ikerkuntza projektu ezberdinen eta jende askorekin egindako elkarlanaren emaitza da: milesker Maider, Juan Luis, Begoña, Elena, Fred, William, Aitor,... Baita Liverpooleko jendeari ere, Laurence eta Laurari gehienbat, bertan izandako hiru hilabeteko esperientzia posible egiteagatatik, harreragatik eta dedikazioagatik. Aipatu nahi ditut, halaber, hainbat eta hainbat neurketekin lagundu didaten instrumentu ezberdinen arduradunak (Fran, Maria, Egoitz, Nuria...) beti laguntzeko izandako prestutasunagatik. Bereziki eskertu behar diot Alexi, tesian zehar ikasitakoaren parte handi bat berarengandik izan da eta; zorretan nago harekin, zalantzarik gabe. Esker berezienak taldekide gertukoen izan ditudanei: Iñakiri, egunero elkarlanean pasatako momentuengatik (ez sekula galdu espiritu hori gero!); gauza anitzetarako eredu izan dudan Giorgiori; eta, Aneri, nahita ere ezingo bainuen lan eta mahai-kide hoberik aukeratu. Mila-mila esker hiruroi. Nola ez, lankide eta lagunetaz gain, familiari ere asko diot eskertzeko. Tesia bizitza guztian zeharreko ikasketen ibilbide luzearen azken puntua baino ez den heinean, bihotzez eskerrak eman behar dizkiet ama, aita eta arrebari, haiei esker iritsi bainaiz puntu honetara. Ezagun batek esan zidan behin, zuzen esan ere, tesia errusiar mendi horietako baten modukoa dela, gora-behera luze eta etengabez osatutako bide bat. Hala izan da, nire kasuan bederen. Gora-behera horien mareoa sufritzea tokatu zaio Paulari, eta bertan egon da beti. Horregatik, eta

guztiagatik, mila esker bihotzaren barrenetik. Aipatutako guztioi, eta seguruena ahaztu zaizkidan horiei (memoria, zoritxarrez, ez da nire bertuteetako bat) esker mila! Aupa zuek!